博士論文

# Direct and indirect local deformation measurements of sand specimen in undrained cyclic triaxial and torsional shear tests

（非排水繰返し三軸・ねじりせん断試験における砂供試体の局所変形挙動の直接・間接的計測）

趙闖

# Abstract

Liquefaction is always accompanied by the increasing of pore water pressure, that is, one of the most important reasons for losing strength and ground sediment during earthquakes. In the recent two earthquakes, extensive liquefactions occurred in loose deposit. For example, liquefactions took place over a wide range area of the reclaimed lands along Tokyo bay area in 2011Tohoku earthquake. Based on reconnaissance project, more than 184 liquefaction sites were found in total. There are two main problems confronting researchers when dealing with a situation where liquefaction takes place. One is the condition of specimen required to trigger liquefaction, the other is the evaluation of potential deformations during and after liquefaction.

The loose deposits formed by hydraulic filling (dredging and pumping) and natural deposits near rivers have large potential to liquefy during seismic event. Related researches have been conducted in recent decades. The complicated geology indicates that there are some less permeable layers intercepting the stratum. This may be affected by the sediment of sand particles through water with different velocities, which is determined by the particle size. This segregation phenomenon will have a significant affection on the liquefaction stabilities of layered deposits. Past relevant studies based on shaking table tests, centrifuge tests and model tests indicated that water film underneath the less permeable layer was generated during shaking. The water film lasted for a while after the cease of shaking. Moreover, the existence of water film decreased the stability of slope in the model test. The generation of water film resulted in lateral displacement of liquefied ground.

The deformation of sand specimen in laboratory tests, such as triaxial tests, torsional shear tests and plane strain compression tests, maybe not uniform, in particular on heterogeneous specimen. Therefore, the deformations measured at the boundaries of specimen could not be valid parameters to present the behaviors of soil. In drained element tests, local deformation has been widely investigated by continuously updated techniques such as image analysis, Particle Image Velocimetry, Digital Correlation, photogrammetry and X-ray and so on. However, since the deformations along the specimen are always assumed to be uniform during testing, little attention has been paid on the local deformations of sand specimen in undrained element test. Some researchers also supposed that strain localization would not occur in the liquefaction tests. Up to now, there is discrepancy between researchers when dealing with strain localization in undrained element test. It is urgent to conduct researches on local deformation of sand specimen in undrained test. Further, the mechanism of water film generation on heterogeneous specimen in liquefaction test could be studied to some extent.

Toyoura sand specimen specked by blue colored Silica sand was employed in undrained triaxial test to investigate the local deformations directly and indirectly by

image analysis method. In order to increase the color contrast for image analysis, Toyoura sand specimen was replaced by mixed white and black colored Silica sand at a mass ratio of 10 to 1. The Silica sand specimen was speckled by black colored Silica sand, with a diameter of 75 mm and a height of 150 mm. These two colored Silica sand had the same physical properties, with a mean particle size of 0.52 mm, a uniformity coefficient of 2.0, a gradation coefficient of 0.92 and a specific gravity of 2.633. The maximum and minimum void ratios of mixed sand were 1.047 and 0.688, respectively. Both air pluviation and moist tamping methods were applied to prepare the sand specimens in triaxial liquefaction test. The mixed Silica sand specimens were also used in the undrained hollow cylindrical torsional shear tests, with an outer diameter of 200 mm, inner diameter of 120 mm and a height of 300 mm. Only air pluviation method was used to make uniform sand specimens in undrained torsional shear tests. In addition, a disturbed sand named as Katori sand from reclaimed area was used to prepare segregated sand specimens. Only water sediment method was applied to prepare the segregated specimens.

For all the undrained triaxial and torsional shear tests, the double vacuuming method was used to obtain a B value larger than 0.96. After saturation, the specimen was consolidated to an effective confining stress of 100 kPa. Undrained cyclic axial loading with a constant single amplitude of deviator stress was applied. The relative density and amplitude of deviator stress were changed in different undrained triaxial liquefaction tests. On the other hand, undrained cyclic torsional loading with a constant single amplitude of shear stress was implemented in the torsional shear test while the vertical displacement was not allowed.

In addition, image analysis was applied in these tests for capturing the local deformations of sand specimen through a transparent membrane. Black latex dots were pasted on the surface of membrane by perfect grids with 5 mm intervals on horizontal and vertical directions. LED lights were added to increase the brightness of specimen surface. The side view of specimen was recorded by using a digital camera in front of cell with a prescribed time interval. The coordinates of dots on membrane and sand particles patterns were obtained respectively by a software named Move-Tr2D.

Since the rays were refracted twice by two interfaces among three mediums, the image was distorted largely, especially at the boundary areas of image. No coordinate correction was considered in the triaxial liquefaction tests. A coordinate correction procedure was developed in torsional shear tests to eliminate the distortion effects. Theoretical analysis and calibration tests were employed to verify the validity of proposed coordinate correction method. The resolutions of current image analysis are around 0.025 mm/pixel in triaxial test and 0.05 mm/pixel in torsional shear test, respectively. In the calibration test, the calculation errors of two neighboring dots were less than 0.2 mm on horizontal and vertical directions even when the rotation displacement was larger than 46 mm. The effects from lens, curvature of cell and specimen and refractions had been taken into consideration in the proposed coordinate correction method. The local strains of each grid at specimen surface were computed and finally plotted by local strain distributions, by which the local deformations of specimen could be displayed visually and clearly.

Based on the direct and indirect evaluations of local deformations of sand specimen in triaxial liquefaction tests, the relative displacements between dots on membrane and sand particles named slippage would not be zero and could not remain constant along cyclic loading. The vertical slippage had a significant leap when excess pore water pressure reached 1.0 at each time during cyclic mobility, which indicated that sand particles sunk during liquefaction. Regardless of air pluviation and moist tamping sample preparation methods, vertical slippage always occurred. Moreover, necking phenomenon of specimen prepared by moist tamping was found at small axial strains. From local strain distributions, the local strains of specimen prepared by air pluviation method were more uniform than the local strains of specimen prepared by moist tamping method.

Similarly, vertical slippage also occurred when excess pore water pressure reached 1.0 in undrained torsional shear tests. In addition, there was no slippage before initial liquefaction. Therefore, the local deformation results from indirect evaluation (from dots on membrane) could represent those from direct evaluation (sand particles) before initial liquefaction. Horizontal slippage existed throughout the test and varied with the cyclic shearing under a limited value. There was almost no vertical slippage when relative density of Silica sand specimen was larger than 60%, which meant the potential of vertical slippage would decrease due to a smaller void ratio of specimen. There was another factor affecting the quantity of vertical slippage which was the accumulated movement of the measured point. The vertical slippage would be small when loose specimen was sheared under a relatively large shear stress by which the specimen reached 15% double amplitude of shear strain with little shear movement (accumulated). Meanwhile, the condition of excess pore water pressure determined when the vertical slippage would happen during liquefaction tests.

Segregated sand specimen in undrained torsional shear test induced different increments of excess pore water pressure at two sides of less permeable layer. Through image analysis results and original photos taken during the tests, relatively large local strains were observed at the less permeable layer. The thickness of fine layer had a significant affection on the concentration of pore water beneath the fine layer. The difference of pore water pressures between bottom and top of specimen, which was intercepted by fine layers, increased with the absolute value of shear stress. Near the status of initial liquefaction, this variation rule of differential pore pressure changed and the maximum value of the differential pore pressure was obtained when the initial liquefaction occurred. Under such circumstance, the largest potential to form water films was generated. A local water film was found at the interface between sand layer and

above fine layer when the initial liquefaction was reached. However, these water films were generated in membrane wrinkles where the sand might be looser than other positions outside of wrinkles. The migration of pore water from the bottom of specimen to the upper part created the generation condition of water film. Based on the results from image analysis, large local strains at fine layer were observed both from the direct and indirect evaluations of local deformations. Since the stiffness of fine layer was smaller than the sand layer during consolidation, serious membrane penetration was observed at the fine layer by the local strain distributions. Interestingly, due to pore water concentration at fine layer, the effect of membrane penetration disappeared gradually and shear strain localization was observed at the interface between fine layer and sand layer.

# Acknowledgement

First and foremost, I would like to express my sincere gratitude to my supervisor, Prof. Junichi Koseki, for the continuous support of my PhD study and related research, for the patient guidance, encouragement and advice he has provided. His guidance helped me in all the time of my research and writing this thesis. I am extremely lucky to be a student under his supervision.

Besides my supervisor, I am deeply grateful to the PhD thesis committee members: Prof. Reiko Kuwano (Institute of Industrial Science, The University of Tokyo), Prof. Tsutomu Namikawa (Shibaura Institute of Technology), Associate Prof. Taro Uchimura (Saitama University) and Associate Prof. Takashi Kiyota (Institute of Industrial Science, The University of Tokyo), for their insightful comments, encouragement and suggestions.

My special appreciation goes to Mr. Takeshi Sato, for his meticulous help and support on teaching me the basic procedures of laboratory testing and adjusting the testing apparatus. His contribution to our laboratory is immensurable. Many thanks to Assistant Prof. Hiroyuki Kyokawa who gave precious suggestions on my thesis and defense.

I would like to thank Ms. Yukika Miyashita, the technician of Koseki and Kuwano laboratories, for teaching me how to conduct image analysis and triaxial test. Without her help, I could not understand the image analysis so quickly and easily.

I would like to thank Dr. Usama Juniansyah Fauzi and Mr. Ryoichiro Hoshino who taught me the experimental procedures step by step. Moreover, they shared the experiences on image analysis with me.

I would like to thank Mr. Yudai Aoyagi who picked me up at Tokyo Station at the first time when I came to Japan. As my tutor, he gave me lots of help on life and studies.

I would like to thank Dr. Wang Hailong, Dr. Mao Wuwei, Dr. Yang Yang and Dr. Chen Yulong, who gave me much of support on my research. They always shared their study experience with me and tried to help me conduct my research effectively.

My sincere appreciation also goes to both Geotechnical Engineering Laboratory (Hongo), Koseki Laboratory, Kuwano Laboratory and Kiyota Laboratory members. Thanks to Mr. Shane and Miss Luisa who will graduate together with me at September of this year, for always shearing ideas and experiment experience. In addition, thanks to Mr. Zain and Mr. Fad who came to Koseki lab at the same time as Shane and me, for helping me deal with study problem. I hope Zain could slow down the rhythm of study and take care of his ‘heart’. Thanks to Miss Wang, I hope everything goes well for her. Thanks to Mr. Tao, Dr. Huang, Ms. Lin and Mr. Xie who always celebrated Chinese holidays together and helped me a lot. Thanks to Jay who always worked hard until middle night. Many thanks to Dr. Naveed, Mr. Shahid, Mr. Babar, Mr. Ali, Mr. Hamada, Mr. Nakamura, Mr. Ahmed, Miss. Catherine, Mr. Tanaka, Mr. Kapila, Ms. Thanuja, Miss Okabe, Mr. Hemakanth, Mr. Jimbo, Mr. Hamaguchi, Miss Sasaki, Dr. Matsumaru, Mr.

Ishihara, Mr. Ahsan, Miss Elise, Mr. Morimoto, Mr. Nunokawa and the others, for having great time with you.

I would like to thank the friends who lived in the dormitory which belongs to the Japan-China Friendship Center (日中友好会館). The dormitory provided very comfortable environment for me in the first two years.

I sincerely acknowledge the China Scholarship Council (CSC) for providing the financial assistance to support my studies in Japan.

Last but not least, I would like to thank all my family members for their support.

26th, July, 2017
The University of Tokyo
Tokyo, Japan

# Table of Contents

# List of Tables

# List of Figures

# 1. INTRODUCTION

## 1.1 Background

It is well known that liquefaction is deemed as a serious issue by engineers after the Niigata Earthquake in 1965. The damage induced by liquefaction can be seen as a combination of subsidence, floating and lateral displacement. It is summarized that the displacement and deformation are the causes of these damages (Towhata, 2008). In recent years, liquefaction has been extensively investigated in the worldwide researchers. The fundamental mechanism of liquefaction is clear and has been applied into the practical constructions for increasing the liquefaction resistance. Even so, related tests such as element tests, model tests, in-situ tests and numerical simulation are continuously investigated for satisfying the requirement of more complicated projects. Generally, the deformation of foundation is triggered by the loss of strength and stiffness. During the seismic events, the external loading condition around the foundation is not changed. The losses of strength and stiffness are induced by the rising of excess pore water pressure. The damage will be serious when loose sandy ground is saturated. The pore water pressure will share the external force while the contact force between grains decreases. If the shear stress induced by external force becomes larger than the shear strength of foundation, failure or damage will be triggered. Theoretically, without considering the external force, zero effective stress status could be achieved. Hence, the grains are actually floating in the pore water without constraint from neighboring particles. This is the main reason why subsidence of foundation and lateral displacement occur during earthquake.

Based on the site investigation after earthquake, liquefaction frequently occurs in loose sandy deposits which are observed in abandoned river channels, young alluvial and reclamations. They have one common characteristic that the deposits are loose. For example, most of reclamations are constructed by dredging and pumping. The sand is excavated from river or sea bay area and filled in the site where is occupied by water before the construction. Partial researchers also name this as hydraulic filling. The large size sand particles settle faster than the smaller one, which will result in layered deposits. Without sufficient compaction, the loose sandy deposit with high ground water level is of large potential to liquefy during earthquake. In addition, the stratification is another issue confronted by researcher when dealing with liquefaction resistance of layered deposit.

Detailed soil investigation was carried out at two sand deposits by Kokusho and Kojima (2002). One was a reclaimed land in Tokyo Bay area which was constructed by hydraulic filling method. The soil was excavated by step on a straight line along the excavation slope for conducting sieve analysis. The results indicated that the soil along the depth was highly variable in terms of particle size. The percentages of fine were distinctly large at some layers, and the intervals of these layers were around 1.5 m. In order to obtain the mechanical characteristics of fine layer, one dimensional and model tests with silt seams were conducted by Kokusho (1999), respectively. Water films were generated during the shaking and still existed even after shaking ceased. If a water film was formed underneath a low permeability layer with inclination, discontinuous deformation would be induced. More seriously, lateral flow would be triggered only by the force of gravity, as it was sometimes observed in the field. Additionally, dynamic centrifuge tests were performed to investigate the seismic performance of embankments by various liquefiable foundations (Maharjan and Takahashi, 2014). In the tests, multiple layered sand foundation was intercepted by discontinuous low permeability layers. The results indicated that pore water was accumulated beneath the low permeability layers. Significant shear strain was also observed below the silty layer which might result in lateral spreading of heterogeneous foundation. Therefore, the local deformations near low permeability layer dominated the stability of layered deposit during seismic events.

It has been addressed particular attention in the past decades that strain localization in drained element test is considered as a major factor, which has a great impact on the stress-strain response of sand specimen. Several techniques are applied for quantifying the local strains or internal failure of sand specimen with a reasonable degree of accuracy such as stereo-photography technique (Desrues et al., 1985; Tatsuoka et al., 1986), X-ray radiographs (Scarpelli and Wood, 1982), tomography (Desrues et al., 1996), photogrammetry (White et al., 2003; Zhang et al., 2015) and digital correlation technique (Bhandari et al., 2012; Li et al., 2015; Lin and Penumadu, 2006; Macari et al., 1997; Mokni and Desrues, 1999; Rechenmacher et al., 2011; Rechenmacher and Finno, 2003; Sadrekarimi and Olson, 2010; Shao et al., 2016). In the above researches, strain localization, shear banding and volume change had been intensively investigated in the drained laboratory tests. However, little attention was paid on the strain localization in undrained laboratory tests. Because researchers usually assumed that only uniform strains were formed in the undrained tests. Han and Vardoulakis (1991) presented that strain localization did not develop in undrained compression of loose sand, whereas results from Mokni (1999) indicated the contrary. Kiyota et al. (2008) and Chiaro et al. (2013) claimed that specimen deformation became non-uniform after exceeding a certain level of overall shear strain, which was named as strain localization in undrained torsional shear test. The initiation of strain localization was related to the sudden decrease of deviator stress when the vertical displacement was prohibited in undrained torsional shear test. Moreover, based on the modification of effective stress and shear strain, strain softening was observed from the evolution curves of stress ratio versus shear strain.

In addition, Kokusho et al. (2003) had concluded that water film beneath cap pedestal was formed in undrained torsional shear test once the excess pore water pressure ratio reached 100%.

The distinct void redistribution was observed during test due to the settlement of sand particles. The water film might have served as sliding surface for the lateral flow during 1964 Niigata earthquake. The potential of this type flow failure would be high when the relative density of sand was around 40% or less. Since the mechanism of water film information was still poorly understood, segregated sand specimen was employed in undrained torsional shear test by Fauzi et al. (2015; 2014). The sand was excavated from Katori city at Chiba prefecture in Japan to prepare the specimen which was intercepted by two fine layers through water sediment method. These two fine layers acted as low permeability layers in the layered deposits. Meanwhile, Particle Image Velocimetry was used to observe the local deformation evolution of segregated specimen. The results indicated that pore water was concentrated beneath the fine layers, which was confirmed by the extended local vertical strains near the fine layer.

In order to observe the local deformation of sand specimen directly, a transparent membrane was employed in undrained triaxial liquefaction tests by Hoshino (2015). Through the membrane, sand particles could be seen clearly. In order to trace the movement of membrane, black latex dots were pasted on the membrane by a constant interval of 5 mm. Based on the Particle Image Velocimetry method, the dots and sand particles patterns could be tracked respectively, namely indirect and direct evaluations. The results indicated that local strains from dots were almost same as those from sand particles patterns. Importantly, slightly different local strains were found at the top and bottom of specimen when the double amplitude of axial strain was around 5%.

Literature reviews indicate that it remains a major challenge to obtain an accurate description of local deformations of specimen in undrained element test, affected by the distortion of image due to the refractions at the interfaces among specimen surface, water, cell and atmosphere. Another issue is that the specimen in the image is rotating during shearing. A suitable correction method determines the validity of the results obtained from image analysis. Thus, Fauzi et al. (2015; 2014) had developed a coordinate correction method in the undrained torsional shear test where the vertical displacement was prohibited during shearing. However, this method was not appropriate to correct the coordinate of sand particles patterns. Therefore, a new coordinate correction method is urgent to satisfy the requirements of indirect and direct evaluations.

The target of this thesis is to study the local deformations of sand specimen in undrained triaxial and torsional shear tests by direct and indirect evaluations, respectively. Mixed colored silica sand is employed in this study to increase the accuracy of image analysis method. The results of local deformation on silica sand specimen will be referred to the test on segregated sand specimen. Katori sand used in this study is excavated from reclaimed land where extensive liquefaction occurred during 2011 East Japan Great Earthquake. It is hoped that the results of this study will help to clarify some discrepancies which exist among geotechnical researchers currently with regard to strain localization and its effects in undrained laboratory tests.

## 1.2 Objectives of this study

Based on the introduced background, the objectives of this study are summarized as follows:

**1. To establish a methodology for measuring the local deformation directly**

Since the geometry of specimen in digital image is very complicated, an appropriate correction method is the foundation of image analysis results. Numbers of coordinate correction methods have been proposed by researchers for the local deformation calculation. However, the scope of application was limited due to the different experimental conditions. In present experiment condition, one digital camera is set in front of the cell and the vertical displacement is not allowed during undrained torsional shearing. The displacement information parallel to the perpendicular line of camera lens would be missed during shearing. Another fact is that the camera is fixed, by which the specimen inside of the image is rotated during torsional shearing. In this study, the coordinate obtained from digital image directly will be converted into the coordinate in a plane condition. It also means that geometry relations on the surface of cylinder are converted into the relations in plane condition.

Calibration tests are applied by using a plastic mold which has the same size as sand specimen. The plastic mold is suspended beneath the top cap and rotated freely without local deformations. The accuracy of proposed coordinate correction method could be computed. Further, the coordinate correction method can be verified and confirmed.

**2. To compare the direct and indirect observations of local deformations in undrained tests by triaxial and torsional apparatuses**

Air Pluviation and moist tamping methods are employed in the undrained triaxial tests. The local deformations are compared between indirect and direct evaluations. As for the undrained torsional shear tests, only uniform sand specimens prepared by air pluviation method are used to study the local deformations. Based on the indirect and direct evaluations, the local deformations are compared along the height of specimen and the relative displacements between membrane and sand specimen are analyzed. By varying the relative densities of sand specimen, the liquefaction resistances are evaluated properly, and the settlement of sand particles in different tests will be calculated and compared.

**3. To investigate the local deformations of segregated specimen directly in undrained torsional shear tests**

The segregated sand specimens are prepared by water sediment method. Thus, the sand specimen will be intercepted by fine layers. In this study, the specimens with thin fine layers and thick fine layer are employed in the undrained torsional shear tests, respectively. The thicker fine layer will increase the potential to observe water film. The local deformations of segregated sand specimen between sand layers and fine layers are compared. The differential pore pressure between top and bottom of specimen is measured during the tests.

## 1.3 Organization of thesis

Base on the background and objectives of this study, this thesis is arranged as follows:

| | |
|---|---|
| Chapter 1 | This chapter introduces the background and motivation of this study. Subsequently, the objectives are divided into three catalogs. In the last section, the arrangement of this thesis is presented. |
| Chapter 2 | This chapter presents the test materials, apparatus and testing procedures in undrained triaxial and torsional shear tests, respectively. The physical properties of Toyousa sand, colored silica sand and Katori sand are introduced. The sample preparation methods for uniform and segregated sand specimens are described in order. The procedures of saturation, consolidation and undrained loading are introduced. |
| Chapter 3 | This chapter gives the basic soil mechanics, mainly focusing on the stress and strain calculations in triaxial and torsional shear tests. |
| Chapter 4 | This chapter presents the image analysis technique applied in this study. It consists of the following sections:<br>---Scale and origin setting<br>---Dot and sand particles pattern tracking<br>---Coordinate correction<br>---Calibration test for the proposed coordinate correction method<br>---Interpolation method and strain computation<br>---Local strain distributions |
| Chapter 5 | This chapter gives the local deformation comparison between indirect and direct evaluations in different undrained triaxial tests. It includes the experiment results under the following conditons:<br>---Toyoura sand specimen (Moist tamping method)<br>---Colored silica sand specimen (Moist tamping and air pluviation methods)<br>---Vertical slippage analysis |
| Chapter 6 | This chapter presents the local deformation comparison between indirect and direct evaluations in undrained torsional shear tests on uniform sand specimens. |

| | |
|---|---|
| | The tests are divided into three catalogs by the relative density of specimen, loose, middle dense and dense. The slippages of each test are analyzed. Meanwhile, the onset of strain localization is described. At last, the quantities of slippage on vertical and horizontal directions are explained under the variations of relative density and accumulated movement of measure point. |
| Chapter 7 | This chapter shows the comparison of local deformations between indirect and direct evaluations on segregated specimen in undrained torsional shear tests. The specimens are prepared by water sediment method to simulate the layered deposits in field. The local deformations of specimen intercepted by thin fine layers and thick fine layer are introduced, respectively. The pore water and sand particle migrations are explained by the evolutions of local strains and differential pore pressures between top and bottom of specimen. At last, the observation of water films is presented. |
| Chapter 8 | This chapter summarizes the conclusions of this study and gives the possible recommendations for the future researches. |

## Reference

1. Bhandari, A., Powrie, W. and Harkness, R. (2012). A digital image-based deformation measurement system for triaxial tests. *Geotechnical Testing Journal, 35*(2), 1-18.
2. Chiaro, G., Kiyota, T. and Koseki, J. (2013). Strain localization characteristics of loose saturated Toyoura sand in undrained cyclic torsional shear tests with initial static shear. *Soils and Foundations, 53*(1), 23-34.
3. Desrues, J., Chambon, R., Mokni, M. and Mazerolle, F. (1996). Void ratio evolution inside shear bands in triaxial sand specimens studied by computed tomography. *Géotechnique, 46*(3), 529-546.
4. Desrues, J., Lanier, J. and Stutz, P. (1985). Localization of the deformation in tests on sand sample. *Engineering fracture mechanics, 21*(4), 909-921.
5. Fauzi, U. J. (2015). *Local Deformation and Repeated Liquefaction Properties of Segregated Sand Specimen in Hollow Cylindrical Torsional Shear Tests.* The University of Tokyo.
6. Fauzi, U. J. and Koseki, J. (2014). Local deformation properties of segregated sand specimen in hollow cylindrical torsional shear tests. *Bulletin of ERS*(47), 27-36.
7. Han, C. and Vardoulakis, I. (1991). Plane-strain compression experiments on water-saturated fine-grained sand. *Géotechnique, 41*(1), 49-78.

8. Hoshino, R., Miyashita, Y., Sato, T. and Koseki, J. (2015). Local deformation properties of sand specimens in triaxial liquefaction tests evaluated by direct and indirect observations. *Bulletin of ERS, 48,* 63-71.

9. Kiyota, T., Sato, T., Koseki, J. and Abadimarand, M. (2008). Behavior of liquefied sands under extremely large strain levels in cyclic torsional shear tests. *Soils and Foundations, 48*(5), 727-739.

10. Kokusho, T. (1999). Water film in liquefied sand and its effect on lateral spread. *Journal of Geotechnical and Geoenvironmental Engineering, 125*(10), 817-826.

11. Kokusho, T. (2003). Current state of research on flow failure considering void redistribution in liquefied deposits. *Soil Dynamics and Earthquake Engineering, 23*(7), 585-603.

12. Kokusho, T. and Kojima, T. (2002). Mechanism for postliquefaction water film generation in layered sand. *Journal of Geotechnical and Geoenvironmental Engineering, 128*(2), 129-137.

13. Li, L., Zhang, X., Chen, G. and Lytton, R. (2015). Measuring unsaturated soil deformations during triaxial testing using a photogrammetry-based method. *Canadian Geotechnical Journal, 53*(3), 472-489.

14. Lin, H. and Penumadu, D. (2006). Strain localization in combined axial-torsional testing on kaolin clay. *Journal of engineering mechanics, 132*(5), 555-564.

15. Macari, E. J., Parker, J. K. and Costes, N. C. (1997). Measurement of volume changes in triaxial tests using digital imaging techniques. *Geotechnical Testing Journal, 20*(1), 103-109.

16. Maharjan, M. and Takahashi, A. (2014). Liquefaction-induced deformation of earthen embankments on non-homogeneous soil deposits under sequential ground motions. *Soil Dynamics and Earthquake Engineering, 66,* 113-124.

17. Mokni, M. and Desrues, J. (1999). Strain localization measurements in undrained plane-strain biaxial tests on Hostun RF sand. *Mechanics of Cohesive ‐ frictional Materials, 4*(4), 419-441.

18. Rechenmacher, A. L., Abedi, S., Chupin, O. and Orlando, A. D. (2011). Characterization of mesoscale instabilities in localized granular shear using digital image correlation. *Acta Geotechnica, 6*(4), 205-217.

19. Rechenmacher, A. L. and Finno, R. J. (2003). Digital image correlation to evaluate shear banding in dilative sands. *Geotechnical Testing Journal, 27*(1), 13-22.

20. Sadrekarimi, A. and Olson, S. M. (2010). Particle damage observed in ring shear tests on sands. *Canadian Geotechnical Journal, 47*(5), 497-515.

21. Scarpelli, G. and Wood, D. M. (1982). Experimental observations of shear patterns in direct shear tests. *NASA STI/Recon Technical Report N, 83*.

22. Shao, L., Liu, G., Zeng, F. and Guo, X. (2016). Recognition of the Stress-Strain Curve Based on the Local Deformation Measurement of Soil Specimens in the Triaxial Test. *Geotechnical Testing Journal, 39*(4), 658-672.

23. Tatsuoka, F., Sakamoto, M., Kawamura, T. and FUKUSHIMA, S. (1986). Strength and deformation characteristics of sand in plane strain compression at extremely low pressures. *Soils and Foundations, 26*(1), 65-84.

24. Towhata, I. (2008). *Geotechnical earthquake engineering*: Springer Science & Business Media.

25. White, D., Take, W. and Bolton, M. (2003). Soil deformation measurement using particle image velocimetry (PIV) and photogrammetry. *Géotechnique, 53*(7), 619-631.

26. Zhang, X., Li, L., Chen, G. and Lytton, R. (2015). A photogrammetry-based method to measure total and local volume changes of unsaturated soils during triaxial testing. *Acta Geotechnica, 10*(1), 55.

# 2. MATERIAL, APPARATUS AND TESTING PROCEDURES

## 2.1 Introduction

This chapter introduces the testing materials, apparatus and test procedures of this study. Since the intention of this study is evaluating the local deformations of homogeneous and heterogeneous sand specimens in undrained triaxial and torsional shear tests, both triaxial apparatus and torsional shear apparatus will be employed. By applying a transparent membrane and Particle Image Velocimetry, the local deformations of membrane and sand specimen could be evaluated indirectly and directly. Toyoura sand, colored silica sand and Katori sand will be used in this study. Subsequently, triaxial and torsional shear apparatuses are presented with their corresponding testing procedures, respectively.

## 2.2 Testing Material

### 2.2.1 Toyoura sand

Toyoura sand, from Toyoura Beach area of Yamakuchi prefecture in Japan, has been widely used as a standard sand in laboratory experiments due to its uniformity and negligible of fine content. The grain size distribution of Toyoura sand is shown in Fig. 2.1 with a mean particle size of 0.28 mm, a uniformity coefficient of 2.31, curvature coefficient of 1.24 and a specific gravity of 2.634. Its maximum and minimum void ratios are 0.948 and 0.619, respectively.

### 2.2.2 Colored Silica sand

In order to speckle the specimen, the blue colored silica sand (No. 5) shown in Fig. 2.1 was mixed in Toyoura sand at a mass ratio of 5%. Its maximum and minimum void ratios are 1.047 and 0.688 respectively, with a mean particle size of 0.50 mm, a uniformity coefficient of 2.0, curvature coefficient of 0.97 and a specific gravity of 2.633.

Another two colored silica sand (No. 5) with white and black colors, which had the same physical properties with blue colored silica sand, were mixed at a mass ratio of 10 to 1. The largest contrast between black and white colors was formed and shown in Fig. 2.2.

### 2.2.3 Katori sand

Since relcaimed land area in Katori city near Tone river (Chiba prefecture of Japan) suffered from extensive liquefaction during the 2011 Tohoku Earthquake, a disturbed sand, named Katori sand, was excavated from the reclaimed region at the depth of 2-3 m below the ground surface. The localtion of excavated sand is marked in the map in Fig. 2.3 with corresponding excavation photo.

Before preparing segregaed sand specimen, the Katori sand was put into the oven (50℃) to dry firstly with a cut-off diameter of 4.75 mm. The grain size distritbution of Katori sand is shown in Fig. 2.4, with a mean particle size of 0.13 mm, a uniformity coefficient of 4.55, a curvature coefficient of 1.94 and specific gravity of 2.688. Its maximun and minimun void ratios are 1.377 and 0.791, respectively. The fines content of Katori sand is around 15%.

# 2.3 Triaxial apparatus and corresponding test procedure

## 2.3.1 Triaxial apparatus

Fig. 2.5 shows the triaxial apparatus which is employed in this study. The triaxial apparatus mainly consists of vertical loading system, Cell pressure, measurement devices, computer, digital camera and the control system. The schematic diagram of triaxial apparatus is shown in Fig. 2.6.

### 2.3.1.1 Vertical loading system

The axial loading system in triaxial apparatus includes an AC servomotor, a reduction gear system, electromagnetic clutches and brackes. During the test, axial strain rate was kept constant, which meant the axial load could be applied to the cylinder specimen by a constant speed of servomotor. In the cyclic loading test, the loading direction was controled and reversed by a pair of electro-magnetic clutches when axial load reached the target value. The feedback information was controled and record by the computer program, namely Digital Show Basic.

### 2.3.1.2 Cell pressure

A 700 kPa house pressure is supplyed by the air pressure pump. There are several air tanks connected to the air pump by which the output of air pressure from tank will become stable. As needed, the positive pressure could be adjusted by a regular which is connected to the air supply system. By connecting to a positive pressure gage, an accurate positive pressure could be produced. In the undrained triaxial tests, all the positive pressures were controled manually.

### 2.3.1.3 Measurement devices

In order to obtain the important parameters of sand specimen during test, several transducers are employed in the test as shown below. Each transducer will generate millivolt which is not enough to adapt to the condition of A/D converter. Therefore, the millivolt from each transducer will be amplified by amplifiers at first, by which the output of voltage could reach a certain value which is suitable for the test (-5 to 5 V). Then the analog singles would be converted into digital electronic signals by a 16-bit AD converter board. Through the Digital Show Basic, the input voltages will be recorded by the program as well as the physical value of each parameters after calculation. The sampling time could be adjusted manually through the program. Thus, output files consist of voltage and physical results will be saved automatically.

*Load cell*

A load cell with a capacity of 2 kN is used in this apparatus, which was fixed at the bottom of loading shaft. Four electronic resistant strain gauges are fixed on the copper block with one pair at compression side, the other on extension side. Through the amplifier, the millivolt of load cell will be amplified. By a proper magnification ratio, the accuracy of load cell could be adjusted. Before testing, several known weights are applied to the load cell. The relationship between amplified voltage and weight will be built as shown in Fig. 2.8. The slope of the line will be typed into the program. Without the changing the magnification ratio, the physical value of weight applied by loading motor can be obtained accurately.

*EDT*

The External Displacement Transducer (EDT) measures the vertical displacement of top gap during loading. The EDT used in this study has a capacity of 25 mm, calibrated by measuring the voltage and known displacement. The calibration curve of EDT is illustrated in Fig. 2.9.

*HCDPT*

High Capacity Differential Pressure Transducer measures the different pore water pressures between cell water and specimen, which is used as the effective confining pressure. The connecting method is plotted in Fig. 2.6. The calibration curve between known pressure and voltage is demonstrated in Fig. 2.10.

*LCDPT*

Low Capacity Differential Pressure Transducer measures the volume change of specimen during test. As shown in Fig. 2.6, the water height in reference burette remains constant and the measurement burette is connected to the specimen. In the consolidation stage, water could flow out and into the specimen, which will induce the change of water height in the measurement burette. Since the LCDTP is very sensitive with the different pore pressure, the change of water height in measurement burette referring to the reference burette could be measured accurately. The calibration curve between volume change of water in the measurement burette and voltage is shown in Fig. 2.11.

## 2.3.2 Specimen preparation

### 2.3.2.1 Moist tamping method for Toyoura sand

Being different from ordinary membrane with a thickness of 0.3 mm, a transparent membrane with the thickness of 0.5 mm was employed in this study as shown in Fig. 2.12. Therefore, the mould used for ordinary membrane was not suitable for the transparent membrane. A plastic board with 0.3 mm thickness was applied into the sample preparation. Since sand would be mixed with water before preparing the specimen by moist tamping method, the sand specimen after preparation could be frozen by freezer. Through this method, the sand specimen could be set in the transparent membrane with the thickness of 0.5 mm.

The mould, consisted of two symmetrical metal parts, was fixed and tightened together. The plastic board was put into the model as shown in Fig. 2.13 firstly. Naturally dry sand (Toyoura sand with 5% blue colored sand) was mixed with 15% water before sample preparation. Then the specimen was prepared by moist tamping method with 5 layers. In order to obtain the target relative density and relatively uniform specimen, the weight of each layer was controlled and kept same to each other. After completing the tamping of 5 layers, top surface of specimen was leveled horizontally by a metal strip. The sand leveled from the top will be put into the over and used to calculate the relative density. A metal plate was put at the top of metal mould to prevent the losing sand and specimen volume expanding during freezing.

After the preparation of specimen, the mould and specimen were put into the refrigerator for at least 24 hours.

Another mould which was larger than the specimen size (75 mm in diameter and 150 mm in height) was used as shown in Fig. 2. 14. The transparent membrane was put over the plastic mould, and a partial vacuum of 30 kPa was applied between the membrane and plastic mould to make the membrane be sealed to the plastic mould perfectly. Then, the plastic mould and transparent membrane ringed the freezing specimen which has been taken out from the metal mould and put on the pedestal with bottom porous stone and filter paper. The top filter paper and porous stone were put on the freezing specimen. When the specimen reached the position of blue line drawn on the membrane, the 30 kPa vacuum pressure was released. The transparent membrane was taken off from the mould to the specimen.

The Top cap and bottom pedestal were smeared by vacuum grease and ringed by bandages. The weight of top cap including the loading shaft was balanced using counter weight. The local cell was connected to the amplifier and then from the amplifier to the computer. After adjusting the same magnification time as the calibration test of load cell, the physical value of load cell was set to 0 N when the load cell was suspended in the air. Then the loading shaft was locked by screws, by which the top cap would be fixed. The top and bottom parts of membrane would be sealed on the top cap and pedestal by bandages. The drainage tubes of specimen should be connected to the top cap and pedestal. After this, load shaft was unlocked and balanced by the counter balance. The 30 kPa vacuum pressure was applied to the sand specimen gradually.

In order to melt the specimen under indoor temperature, the specimen was kept at 30 kPa vacuum pressure for 2-3 hours. After that, the diameter and height of specimen were measured by micrometers. Each parameter should be measured at least three times at three different positions. The average values of diameter and height of specimen were typed into the computer program.

For applying image analysis, a plastic board with 5 mm interval holes on horizontal and vertical directions was designed. Then the dots with 5 mm intervals both on horizontal and vertical direction were painted on the surface of membrane. The photos of painting and after painting are shown in Fig. 2.15 and Fig. 2.16, respectively.

#### 2.3.2.2 Mosit tamping method for colored Silica sand

All the preparation procedures of moist tamping method for colored silica sand were almost same as the moist tamping method for Toyoura sand, except for two steps:

1) Backed colored sand was mixed in the white colored silica sand at a mass ratio of 1 To 10. 15% of water by weight was also added to the mixed colored sand.
2) Dots were pre-produced by a factory with accurate 5 mm intervals both on horizontal and vertical directions. The dots were pasted on the membrane surface before the transparent membrane was put over the plastic mould. The photo of pasting pre-produced dots on membrane is shown in Fig. 2.17.

#### 2.3.2.3 Air pluviation method for colored Silica sand

Being different from Toyoura sand mixed with colored silica sand, the black and white colored silica sand have the same physical properties. Therefore, air pluviation (AP) method (Tatsuoka et al., 1986) could be applied into the specimen preparation. If the air pluviation method was applied into the Toyoura sand specimen preparation, the blue colored silica sand would be separated during the pluviation.

The method of setting dots on the surface of membrane was same as the one described in the section of air pluviation method for colored silica sand.

Naturally dry colored silica sand with black and white colors was mixed at a mass ratio of 1 to 10. A funnel with an appropriate opening was used to preparation the specimen. During the preparation, the falling height of sand from the opening to the top surface of prepared specimen was maintained. The target relative density could be changed by adjusting the falling height of mixed colored sand.

After completing the pluviation, the top surface of specimen was leveled by a metal strip. The extra sand which was flowing away during the pluviation was collected and weighted to recalculate the relative density.

A metal plate was put at the top of metal mould. The specimen, metal plate and the metal mould were put into a bowl or bucket which was filled with appropriate height of water. Additionally, there was a hole at the bottom of the mould, from which water could flow into the specimen. There was a filter pater at the top of specimen. The water height in the bowl was increased until the filler paper became wet. Under this condition, the specimen was put in the water for 2-3 hours to obtain a uniform water content. The photo of putting specimen in a bowl is shown in Fig. 2.18.

Then the specimen was put into the refrigerator for at least 24 hours. The following procedures were same as those described in the mosit tamping method of Toyoura sand. The photo of mixed colored silica sand before saturation is shown in Fig. 2.19.

## 2.3.3 Test procedure in undrained triaxial liquefaction tests

### 2.3.3.1 Saturation process

Step1

The black O-rings of top and bottom of cell were smeared by vacuum grease. The cell was cleaned by alcohol and assembled carefully after locking the load shaft and removing the counter balance. The cell was fixed safely and the air inside of cell should be released during the assembly. The top part of cell should be locked carefully. The counter balance was installed again to keep isotropic stress condition. The load shaft was connected to another shaft under the loading system. Before connecting, the load shaft should be locked to avoid disturbance. After connection, the loading shaft was unlocked and the computer controlling program was set to keep the isotropic stress condition (pre-consolidation). The physical value of q was adjust by the servomotor automatically under the range of -1 kPa to 1 kPa.

Step 2

The cell was filled with water until the water level reached the middle position of top cap. During filling water, the cell should be connected to the air outside for releasing the air.

Step 3

Double vacuuming method (Ampadu and Tatsuoka, 1993) was applied in this study. Another vacuum resource was connected to the cell. Two water tanks filled with de-aired water were connected to the sand specimen as shown in Fig. 2.20. The air was vacuumed only before water flowing into the specimen. The vacuum pressures inside and outside of specimen increased together from 30 kPa and 0 kPa to 100 kPa and 70 kPa, respectively. The effective confining pressure remained constant which was equal to 30 kPa. After 3 hours, a stable difference of water height was informed between top and bottom water tanks. Then the switch for vacuuming air was closed and water started flowing into the specimen, the status of switches to fill water are shown in Fig. 2.20. During the saturation, water flowed from the bottom of specimen to the top to replace the air in the voids. The expelled air was vacuumed out from the top of specimen to the water tank.

Step 4

The saturation process stopped when there was no bubble flowing out from the specimen. The vacuum pressure of specimen would be decreased from 100 kPa to 30 kPa, vacuum cell pressure from 70 kPa to 0 kPa. Then positive pressure was added to the cell by the regulater. The vacuum pressure of specimen continuously decreased to 0 kPa, while the positive cell pressure increased from 0 kPa to 30 kPa. During the process of reversing vacuum pressure to positive pressure, the isotropic stress condition was always kept by the pre-consolidation program.

#### 2.3.3.2 B Value measurement

Step 5

After closing all the drainage valves, the water tanks were taken out. Meanwhile, the de-aired water in the tank could be used to the saturate the HCDPT and LCDPT. There should be no air inside of HCDPT and LCDPT. After the saturation, HCDPT and LCDPT would be checked when there was no differential pressure of each transducer, which meant the voltage of each transducer should be 1.0 V. Then the physical values of HCDPT and LCDPT were set to be zero. After that the switch of each transducer changed to the measuring status.

Step 6

The water heights in the reference and measurement burettes were almost same to each other, which should be at the middle height level of specimen. The positive back pressure could be transformed from the water in the burette to the specimen.

Step 7

The back pressure increased from 0 kPa to 200 kPa while keeping the effective confining stress constant. Under this circumstance, the value connected to LCDPT was closed. The cell pressure increased from the 230 kPa to 280 kPa, while effective stress measured by HCDPT should be recorded manually. Then cell pressure decreased from 280 kPa to 230 kPa. The B value could be calculated by equation 3.1. During the all the process of measuring B value, the isotropic stress condition was always kept.

$$B = \frac{\Delta u}{\Delta \sigma_3} \quad (2.1)$$

$\Delta$u = Increment of pore water pressure of specimen

$\Delta\sigma_3$ =Increment of minor total principle stress (isotropic stress condition)

Step 8

Fully saturation could be achieved when the B value was larger than 0.96. 0.95 is the boundary of fully saturation in Japanese experimental standard (地盤工学会, 2009).

#### 2.3.3.3 Consolidation

Since the diameter and height were measured when the isotropic effective stress was 30 kPa, it was assumed that no change occurred when the isotropic effective stress was kept.

Step 9

External Displacement Transducer was fixed with the tip touching to the rigid plate which would movement together with the loading shaft. The physical value of EDT should be set as 0 before increasing the effective confining stress.

Step 10

The drainage value from specimen to measurement burette was opened before increasing effective confining stress. The The cell pressure increased from 230 kPa to 300 kPa, while the back pressure remained at 200 kPa. The consolidation data was saved by the computer automatically with pre-set sampling time.

#### 2.3.3.4 Undrained cyclic loading

Step 11

After the isotropic consolidation at an effective stress of 100 kPa, undrained cyclic axial loading with a constant single amplitude deviator stress was applied. Fig. 2.21 shows the typical stress path in the undrained triaxial liquefaction test. The axial strain rate was controlled to be 0.1%/min.

Step 12

Digital images were taken by a prescribed interval time of 10 seconds during the undrained cyclic loading. The apparatus would stop automatically when the double amplitude of axial strain reached 15%. Based on the test procedure described above, the undrained tiraxial tests conducted in this study were summarized in table 2.1 and table 2.2.

## 2.4 Torsional shear apparatus and corresponding test procedure

In this study, a high capacity torsional shear test apparatus developed at the Institute of Industrial Science, the University of Tokyo was employed. The schematic diagram of this torsional shear apparatus is shown in Fig. 2.22. In order to investigate the local deformations of sand specimen directly and indirectly during undrained torsional shear tests, a camera was set in front of cell to take photos.

### 2.4.1 Torsional shear apparatus

The hollow cylindrical torsional shear apparatus is schematically shown in Fig. 2.23 and Fig. 2.24. This apparatus is capable of testing specimen with various dimensions ranging from 160 mm in inner-diameter, 200 mm in outer-diameter and 300 mm in height to 60 mm in inner-diameter, 120 mm in outer-diameter and 200 mm in height. In this study, a hollow cylindrical specimen with 120 mm in inner-diameter, 200 mm in outer diameter and 300 mm in height was employed. In order to avoid the repetitive description, some similar sections to triaxial apparatus which has been described above will be skipped.

#### 2.4.1.1 Vertical and torsional loading systems

In Fig. 2.24, the vertical loading system and torsional loading system are schematically described. The vertical and torsional loading capacities of this apparatus are 15 kN and 0.3 kN•m, respectively. The axial loading system is similar to the triaxial apparatus, which consists of AC servo-motor, a reduction gear system, electro magnetic clutches, brakes and a ball screw with a pre-pressured nut. The motor always drives in one direction. Simultaneously, the upper gear is rotating in one direction and the lower gear is rotating in the opposite direction. Therefore, the loading direction is decided by which gear the loading shaft are using. The loading direction could be reversed without any backlash by the electric clutches.

The torsional loading system also consists of similar devices. Torque is transmitted to the load shaft by controlling two metal bands on clockwise and anti-clockwise directions, respectively. In addition, the vertical and torsional loadings are controlled independently by these two loading systems. These two loading devices are a displacement-controlled type from a mechanical point of view. Meanwhile, deviator stress and shear stress by keeping a specific amplitude could be conducted by utilizing computer which monitors the physical values of stress from load cell and controls the loading systems accordingly.

#### 2.4.1.2 Cell pressure

Being different from the cell pressure in triaxial apparatus which was controlled manually, the electro-pneumatic transducer (E/P) with a capacity of 1000 kPa was employed in the torsional shear apparatus. The pressure in the inner hollow of specimen was always kept as same as the cell pressure during each test. There is one relationship between voltage of E/P and the real cell pressure, which means the cell pressure supplied by the E/P remains constant when a constant voltage value of E/P is kept. Form the beginning of using positive pressure to the end of measuring B value, the positive pressure in cell was controlled manually. After that, E/P would control the cell pressure. It should be noted that the positive pressures from EP and regulator needed to be equal during the replacement.

#### 2.4.1.3 Measurement devices

The A/D convert system has 16 measuring channels to measure the stresses, strains and other important parameters. In this study, 8 channels were used , which are two channels for load cell, two channels for potentiometer, one channel for HCDPT, one channel for LCDPT, one channel for EDT and the last one for electronic balance. Each transducer is introduced as follows:

*Load cell*

As described by Koseki (2005), the load cell fixed between top cap of specimen and loading shaft is capable of measuring deviator load and torque without coupling effect between each other. The capacities of load cell are 15 kN in axial load and 0.3 kN•m in torque, respectively. The photo of load cell is shown in Fig. 2.25, as well as the calibration curves in Fig. 2.26.

*Potentiometers*

Fig. 2.27 shows the two potentiometers which were used to measure the corresponding rotation angles of loading shaft and top cap. The potentiometer 1 attached to loading shaft could detect the maximum shear strains of 38%. Meanwhile, the potentiometer 2 with the capacity of 10% shear strain is attached to the top cap. Their calibration curves are plotted in Fig. 2.28.

*EDT*

The External Displacement Transducer measures the vertical displacement of specimen. The position of EDT in this study is shown in Fig. 2. 29, with its max range of 30 mm. The calibration curve of EDT is plotted in Fig. 2.30.

*HCDPT*

Similar to the description in traxial apparatus section, The High Capacity Differential Pressure Transducer measures the different pore water pressure between cell water and specimen, which is used as the effective confining stress. The photo of HCDPT and its calibration curve are plotted in Fig. 2.31 and Fig. 2.32, respectively.

*LCDTP*

Being different from the purpose of using Low Capacity Differential Pressure Transducer in triaxial apparatus, the LCDPT used herein measures the different pore water pressure between the top and bottom of specimen. The photo of LCDPT and its calibration curve are plotted in Fig. 2.33 and Fig. 2.34, respectively.

*High sensitive electronic balance*

In this study, a high sensitive electronic balance (AND FX-500i) with a capacity of 520 g was employed, which is capable of measuring the volume change of saturated specimen with a precision of 0.001g (Fauzi and Koseki, 2014). The load cell of the balance was removed from the produced and installed into a pressure chamber which is connected to the back pressure of specimen. The weight weighed by the balance was converted into electrical signals and recorded by the computer program. The photos of balance are shown in Fig. 2.35.

*Camera and Control unit*

Digital images are taken by the commercial camera and lens, Nikon D810 and Nikkor 24 mm f/1.4G ED, respectively. The status of camera during test is shown in Fig. 2.36. Moreover, the camera is connected to the camera control unit, which is connected to the computer visa D/A board converter. The photo of camera control unit is shown in Fig. 2.37. During test, photos can be taken by the pre-described time interval. It should be noticed that the maximum photo number in one control step is 2014. If the number exceeds 2014, the camera will stop taking photo or the testing program will jump to the next control step.

*LED light*

As shown in Fig. 2.36, LED light is employed to increase the brightness of specimen surface.

## 2.4.2 Specimen preparation

Two kinds of materials are employed in this study with different sample preparation method. One is air pluviation method for colored silica sand, the other is water sediment method for Katori sand.

### 2.4.2.1 Air pluviation method for colored silica sand

The inner membrane with 0.3 mm thickness was cut into proper length and attached on the inner metal ring, which had a rubber O-ring at the top as shown in Fig. 2.38. The metal ring together with membrane was inserted to the outer metal pedestal. Then the inner module consisting of four parts was installed. The pedestal was fixed to the base by 6 bolts and the inner module should be set at the central positions as shown in Fig. 2.39.

The outer membrane (transparent membrane) was cut into a proper length and the pre-produced dots were pasted on the surface of membrane. The dots have an interval of 5 mm both on vertical and horizontal directions as shown in Fig. 2.40. In order to make the membrane stand vertically after specimen preparation, lines were drawn at the top and bottom of membrane in advance. Vacuum grease was smeared at the bottom pedestal in advance. The outer membrane was attached to the metal pedestal and the position of drawn bottom line on membrane should be same as the top of pedestal. A rubber O-ring was placed outside of the outer membrane to seal the gap between membrane and outer mould, another function of the O-ring was protecting the membrane from being broken by the outer mould. The outer mould consisting of two symmetrical metal parts was tightened by clamps. Then the extra outer membrane was put over the mould as shown in Fig. 2.41. A partial vacuum pressure of 30 kPa was applied to make the membrane perfectly sealed to the mould.

Before pouring the sand into the mould, a plastic bag attached to the outer mould was used to collect the sand particles which might drop un-intentionally during the pluviation. After the specimen preparation, the sand in the plastic bag would be used to correct the relative density of specimen.

Being similar with the procedure of air pluviation method in triaxial test, the hollow cylindrical specimen was also prepared by air pluviation method. As suggested by De Sliva (De Silva, 2008), the pluviation method started with moving the nozzle towards inner and outer perimeter of mould in the radial direction while moving in clockwise direction instantaneously. After one cycle pluviation, the nozzle changed to anti-clockwise direction. These steps were repeated until the height of sand exceeding the height of outer mould. As introduced in triaxial section, the height of falling sand should be kept constant during the whole process.

After completion of sand pluviation, the extra sand higher than the mould was leveled horizontally by a metal strip. By collecting the waste sand, the relative density of specimen was revised properly.

Subsequently, the top cap clamps were fixed to two of the four steel poles with a proper height. The top cap was placed on the clamps whose heights were higher than the specimen and inner membrane was inserted through the hollow of top cap carefully. Then counter balance was used to balance the weight of top cap. After loosing the clamps, the top cap moved downward to the top surface of specimen. The clamps were locked with the condition that the top cap touched the top of specimen without force. The dead weight of top cap would be supported by the clamps after removing the counter balance. As shown in Fig. 2.42, the top cap was fixed on the two clamps and should be placed horizontally.

The top cap was smeared by vacuum grease carefully. The outer membrane was placed over the top cap and the top cap was ringed by the bands gently. Similarly, the inner membrane was pulled over the top cap and perfectly sealed by bands.

Before applying the vacuum pressure to the specimen, the counter balance was set again and the clamps were removed.

After the specimen was vacuumed by a 30 kPa pressure, the specimen was placed for a while to obtain a stable status. Then the outer mould and inner mould were removed carefully. The outer diameter and height of specimen were measured and typed into the computer program. The status of specimen under such circumstance is shown in Fig. 2.43.

The clamps were fixed to the bottom of top cap again and counter balance was removed. The load cell cap was placed and fixed on the four steel poles carefully. Meanwhile, another counter balance was installed to balance the weight of load cell cap. Before connecting the top cap and load cell cap, the setting of load cell should be finished in advance and the physical value of load cell was set to be 0 kPa.

After connecting the load cell and top cap by 6 bolts, the load shaft was locked and the load cell was disconnected. The cell was placed, followed by fill water into the cell. Meanwhile, the air inside of cell should be released properly. As shown in Fig. 2.44, the cell was connected to the load shaft of servomotor and the pre-consolidation was applied to the specimen to keep isotropic stress condition.

Since the double amplitude of shear strain would be larger than 15%, potentiometer 2 was not used in this study. The potentiometer 1 and EDT were installed to the load shaft while the control program should be stopped temporarily during installment.

#### 2.4.2.2 Water sediment method for Katori sand

Before installing the acrylic pipes, all the procedures were same as those in the AP method for colored silica sand. The following illustrations mainly focus on the water sediment method.

After the inner and outer membranes were placed over the inner and outer moulds, two acrylic pipes shown in Fig. 2.45 were used to elongate the height of mould for specimen preparation. The inner pipe was installed firstly and fixed by a steel rod, which was connected to the inner metal mould. The outer pipe was fixed on the four steel poles and these two pipes were sealed, respectively.

Subsequently, the hollow space was filled with water at an initial water height of 50 cm from the bottom as shown in Fig. 2.46. Then a mixture of Katori sand and water at a mass ratio of 1 to 2 was poured into the hollow pipes once by a funnel. As shown in Fig. 2.47, more than 6 hours was needed for the complete sediment. After the first time of sediment, 10 cm water was extracted from the pipe. Then another same amount of mixture of Katori sand and water was poured again. By repeating this procedures three times totally, a specimen segregated by fine layers was prepared and shown in Fig. 2.48.

After the complete sediment, the acrylic pipes were removed carefully. As shown in Fig. 2.49, the extra part which exceeded the height of metal mould was leveled. The sand, which was wasted during preparation, was collected to revise the relative density.

The next step was to install the load cell which had been described in the AP method for colored silica sand specimen. Since the following procedures are same as the AP method, more details could be referred to the above section. The segregated specimen in the cell that filled with water is displayed in Fig. 2.50.

### 2.4.3 Test procedure in undrained torsional shear tests

Since the test procedures in torsional shear test are similar to those in triaxial test, the following illustrations mainly focus on the different parts.

#### 2.4.3.1 Saturation process

Similar to the procedures in triaxial tests, the connection between water tanks during saturation is shown in Fig. 2.51. The double vacuuming method was already introduced in the triaxial test section, the same procedures will not be repeated herein.

#### 2.4.3.2 B value measurement

Being different from triaxial apparatus, the back pressure of specimen in the torsional shear apparatus was transformed from the chamber in which there was an electronic balance. The final back pressure for the saturation of colored silica sand was 200 kPa, under which the B value was larger than 0.96. However, the B value of Katori sand was lower than 0.95 with the back pressure of 200 kPa. In order to achieve the full saturation requirement, the 300 kPa was applied to the specimen as the back pressure. Under this circumstance, the B value of Katori sand after saturation could reach 0.95. During saturation when applied double vacuum method, the de-air water from top water tank should be kept flowing to the lower tank until all the original water in the specimen for water sediment was replaced by the de-air water. This measure was very important for guaranteeing the B value larger than 0.95.

#### 2.4.3.3 Consolidation

After achieving a B value larger than 0.95, the potentiometer 1 and EDT were installed. During the installment, the pre-consolidation program should be stopped. The E/P was opened and adjusted to reach the same pressure as the pressure in the cell. Then the pressure resource was replaced by the E/P.

The camera was set in front of the cell and the LED lights were connected to increase the brightness of specimen surface. In order to eliminate the reflection from other light resources, a piece of white cloth covered the camera and part of cell as shown in Fig. 2.52.

The cell pressure was increased and controlled by the computer program from 330 kPa to the target pressure around 400 kPa, at which the effective confining stress was 100 kPa perfectly. During the consolidation, the camera took photos at an interval of 1 minute and the isotropic stress condition was kept.

#### 2.4.3.4 Undrained cyclic loading

After the isotropic consolidation at an effective stress of 100 kPa, undrained cyclic torsional shear was applied under these connections of transducers as shown in Fig. 2.23. HCDPT was used for measuring the effective confining pressure, while LCDPT measured the different pore water pressure between top and bottom of specimen. During the undrained cyclic loading, the vertical displacement was not allowed. The shear strain rate was controlled to be 0.025%/min and 0.8%/min for the tests on colored silica sand specimen and Katori sand specimen, respectively. Different amplitudes of shear stress were applied to obtain the liquefaction resistance curves of colored silica sand and Katori sand.

Digital images were taken during the undrained cyclic loading by different time intervals which was corresponding to the rate of shearing. The setting between shear strain rate and time interval of taking photo is shown in table 2.3. The test was terminated automatically when the double amplitude of shear strain reached 15%. Based on the test procedure described above, the undrained torsional shear tests conducted in this study were summarized in table 2.4 and table 2.5. Meanwhile, table 2.6 gives the details of calibration tests for image analysis, which will be introduced in chapter 4.

# References

1. Ampadu, S. and Tatsuoka, F. (1993). Effect of setting method on the behaviour of clays in triaxial compression from saturation to undrained shear. *Soils and Foundations, 33*(2), 14-34.
2. De Silva, L. I. N. (2008). *Deformation characteristics of sand subjected to cyclic drained and undrained torsional loadings and their modelling.* 東京大学.
3. Fauzi, U. J. and Koseki, J. (2014). Local deformation properties of segregated sand specimen in hollow cylindrical torsional shear tests. *Bulletin of ERS*(47), 27-36.
4. Koseki, J., Yoshida, T. and Sato, T. (2005). Liquefaction properties of Toyoura sand in cyclic tortional shear tests under low confining stress. *Soils and Foundations, 45*(5), 103-113.
5. Tatsuoka, F., Ochi, K., Fujii, S. and Okamoto, M. (1986). Cyclic undrained triaxial and torsional shear strength of sands for different sample preparation methods. *Soils and Foundations, 26*(3), 23-41.
6. 地盤工学会. (2009). 地盤材料試験の方法と解説-二分冊の 1: 丸善.

**Table 2.1 Undrained cyclic triaxial tests on Toyoura sand specimen prepared by moist tamping method**

| Test | Type | Specimen preparation | Mixed colored sand | Dr | CSR | Loading speed | Transparent membrane |
|---|---|---|---|---|---|---|---|
| Test 1 | UC | MT, Freezing | 5% (silica) | 53~54% | 0.2 | 0.1%/min | Yes |
| Test 2 | UC | MT, Freezing | 5% (silica) | 49~50% | 0.2 | 0.1%/min | Yes |
| Test 3 | UC | MT, Freezing | 5% (silica) | 52~53% | 0.2 | 0.1%/min | Yes |
| Test 4 | UC | MT, Freezing | 5% (silica) | 41~42% | 0.2 | 0.1%/min | Yes |
| Test 5 | UC | MT, Freezing | 5% (silica) | 52~53% | 0.2 | 0.1%/min | Yes |
| Test 6 | UC | MT, Freezing | 5% (silica) | 53~54% | 0.25 | 0.1%/min | Yes |
| Test 7 | UC | MT, Freezing | 5% (silica) | 52~53% | 0.25 | 0.1%/min | Yes |
| Test 8 | UC | MT, Freezing | 5% (silica) | 74~75% | 0.25 | 0.1%/min | Yes |
| Test 9 | UC | MT, Freezing | 5% (silica) | 72~73% | 0.25 | 0.1%/min | Yes |

Test 1~9: Toyoura sand specimen, Moist tamping method, Undrained cyclic loading

**Table 2.2 Undrained cyclic triaxial tests on Silica sand specimen prepared by moist tamping and air pluviation methods**

| Test | Type | Specimen preparation | Mixed sand (W to B) | Dr | CSR | Loading speed | Transparent membrane |
|---|---|---|---|---|---|---|---|
| Test 10 | UC | MT, Freezing | 10:1 | 53~54% | 0.29 | 0.1%/min | Yes |
| Test 11 | UC | MT, Freezing | 10:1 | 67~68% | 0.43 | 0.1%/min | Yes |
| Test 12 | UC | MT, Freezing | 10:1 | 42~43% | 0.4 | 0.1%/min | Yes |
| Test 13 | UC | AP, Freezing | 10:1 | 79~80% | 0.4 | 0.1%/min | Yes |
| Test 14 | UC | AP, Freezing | 10:1 | 69~70% | 0.4 | 0.1%/min | Yes |
| Test 15 | UC | MT, Freezing | 10:1 | 63~64% | 0.4 | 0.1%/min | Yes |
| Test 16 | UC | AP, Freezing | 10:1 | 53~54% | 0.29 | 0.1%/min | Yes |

Test 10, 11, 12 and 15: Silica sand specimen, moist tamping method, undrained cyclic loading

Test 13, 14 and 16: Silica sand specimen, Moist tamping method, Undrained cyclic loading

**Table 2.3 The setting of time interval for taking photos in undrained torsional shear tests**

| Shear strain rate (%/min) | Photo number/min |
|---|---|
| 0.025 | 1 |
| 0.8 | 10 |
| 0.8 | 20 |

**Table 2.4 Undrained cyclic torsional shear tests on silica sand specimen prepared by air pluviation method**

| Test | Type | Specimen preparation | Relative density | CSR | Loading speed | Transparent membrane |
|---|---|---|---|---|---|---|
| SAUC1 | Cyclic undrained | Air pluviation | 39~40% | 0.2 | 0.025%/min | No |
| SAUC2 | Cyclic undrained | Air pluviation | 55~56% | 0.2 | 0.025%/min | No |
| SAUC3 | Cyclic undrained | Air pluviation | 53~54% | 0.3 | 0.025%/min | No |
| SAUC4 | Cyclic undrained | Air pluviation | 56~57% | 0.4 | 0.025%/min | No |
| SAUC5 | Cyclic undrained | Air pluviation | 57~58% | 0.15 | 0.025%/min | No |
| SAUC6 | Cyclic undrained | Air pluviation | 57~58% | 0.18 | 0.025%/min | No |
| SAUC7 | Cyclic undrained | Air pluviation | 55~56% | 0.25 | 0.025%/min | Yes |
| SAUC8 | Cyclic undrained | Air pluviation | 53~54% | 0.23 | 0.025%/min | Yes |
| SAUC9 | Cyclic undrained | Air pluviation | 31~32% | 0.23 | 0.025%/min | Yes |
| SAUC10 | Cyclic undrained | Air pluviation | 84~85% | 0.23 | 0.025%/min | Yes |
| SAUC11 | Cyclic undrained | Air pluviation | 26~27% | 0.18 | 0.025%/min | Yes |
| SAUC12 | Cyclic undrained | Air pluviation | 80~81% | 0.45 | 0.025%/min | Yes |
| SAUC13 | Cyclic undrained | Air pluviation | 59~60% | 0.35 | 0.025%/min | Yes |
| SAUC14 | Cyclic undrained | Air pluviation | 42~43% | 0.35 | 0.025%/min | Yes |
| SAUC15 | Cyclic undrained | Air pluviation | 74~75% | 0.35 | 0.8/min | Yes |

SAUC: Silica sand (mixed), Air pluviation method, undrained cyclic loading

**Table 2.5 Undrained cyclic torsional shear tests on segregated sand specimen prepared by water sediment method**

| Test | Type (Trans) | Specimen preparation | Fine | | Dr | CSR | Loading speed | Stages |
|---|---|---|---|---|---|---|---|---|
| | | | Content | Layers | | | | |
| KWUC1 | UC | Water sediment | 15% | 3 (thin) | 26% | 0.15 | 0.8%/min | 3 |
| KWUC2 | UC | Water sediment | 15% | 3 (thin) | 24% | 0.1 | 0.8%/min | 3 |
| KWUC3 | UC | Water sediment | 15% | 1(thick) | 26% | 0.13 | 0.8%/min | 3 |
| KWUC4 | UC | Water sediment | 15% | 1(thick) | 25% | 0.14 | 0.8%/min | 3 |

KWUC: Katori sand, Water sediment method, Undrained cyclic loading

**Table 2.6 Calibration tests for verifying image analysis technique**

| Test | Type | Specimen | Purpose | Rotation speed | Maximum rotation |
|---|---|---|---|---|---|
| C1 | Calibration | Suspended model | Image analysis accuracy | 0.025%/min | 46mm |
| C2 | Calibration | | | 0.025%/min | 46mm |

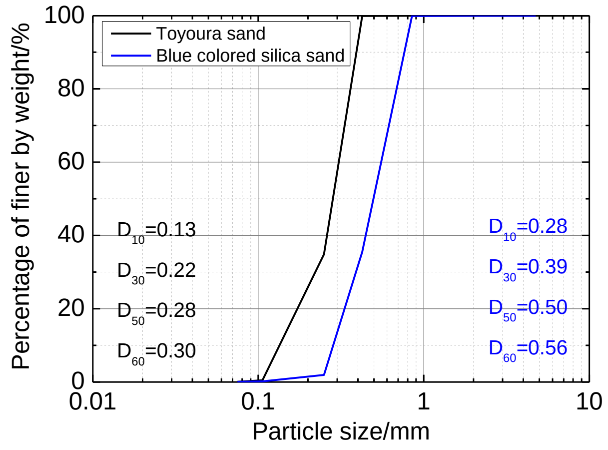

**Fig. 2.1 Grain size distribution of Toyoura sand and colored Silica sand**

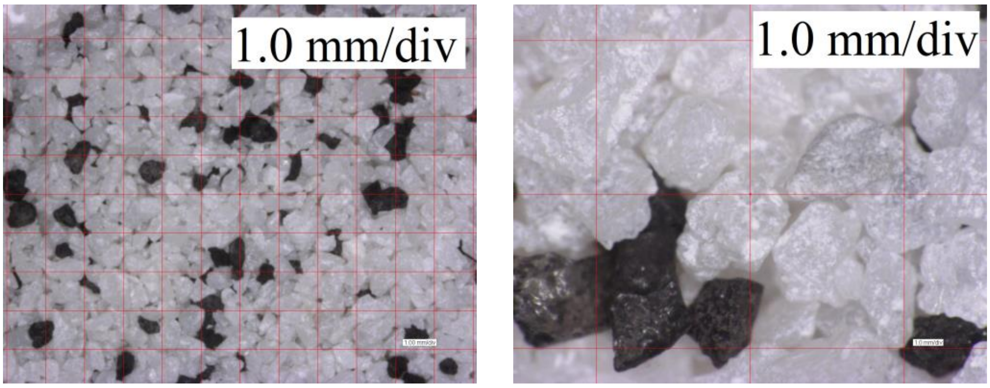

**Fig. 2.2 Photos of Silica sand**

**Fig. 2.3 Maps and excavation of Katori sand**

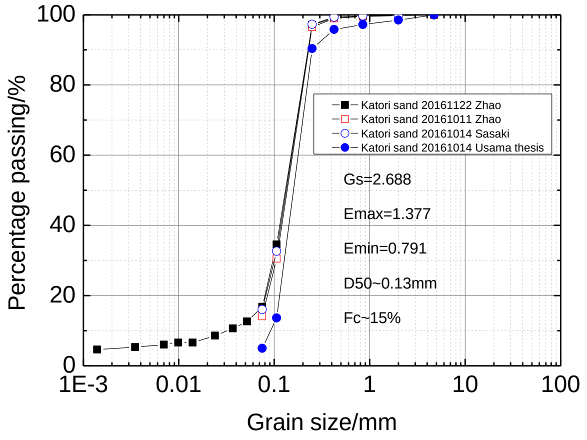

Fig. 2.4 Grain size distribution of Katori sand

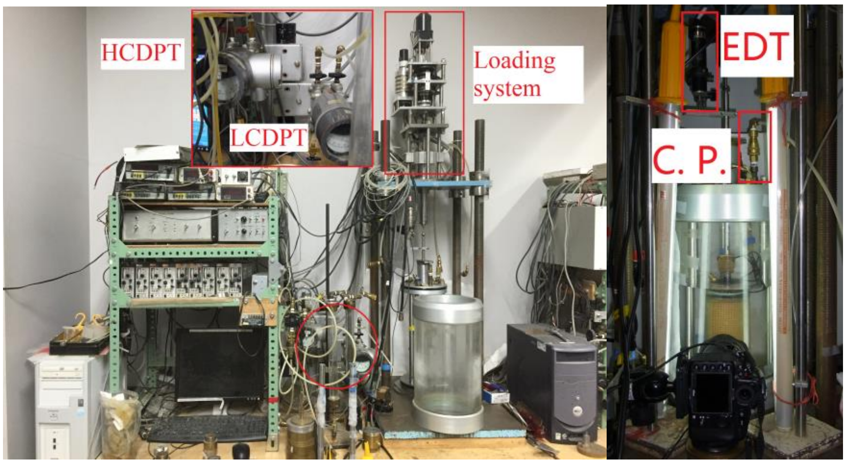

Fig. 2.5 Triaixal apparatus used in this study

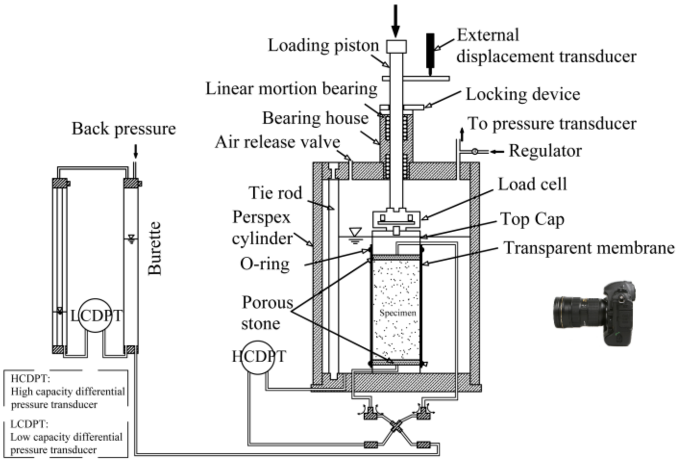

Fig. 2.6 Schematic diagram of triaxial apparatus

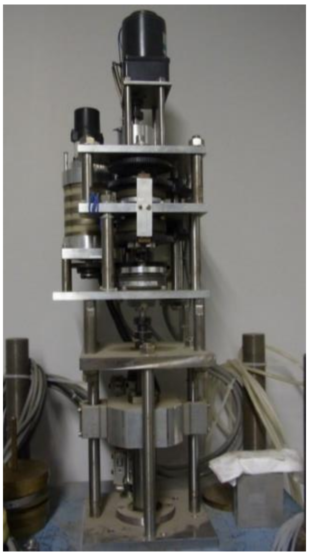

Fig. 2.7 Vertical loading system

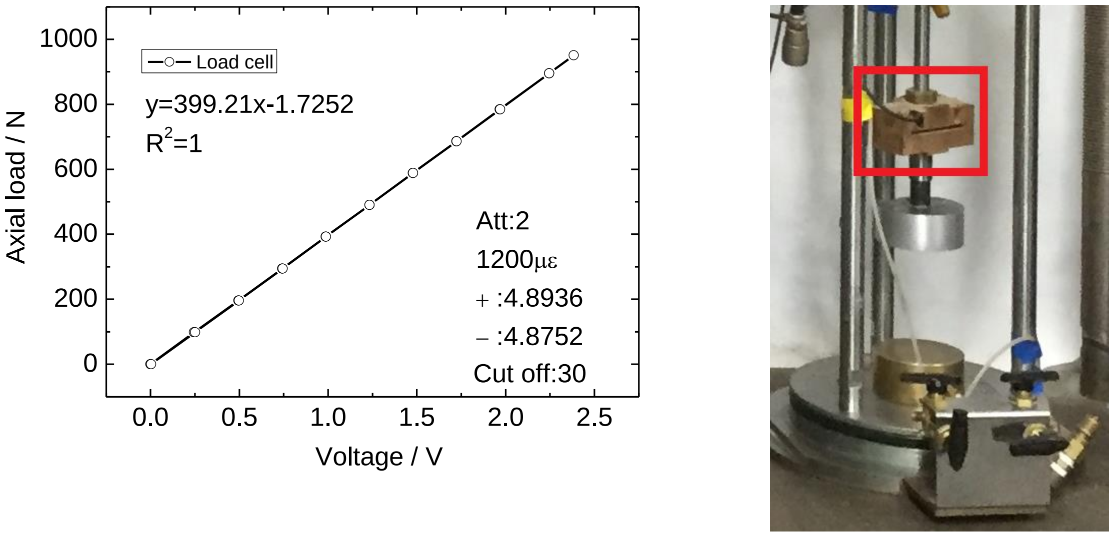

Fig. 2.8 Calibration of load cell and its photo

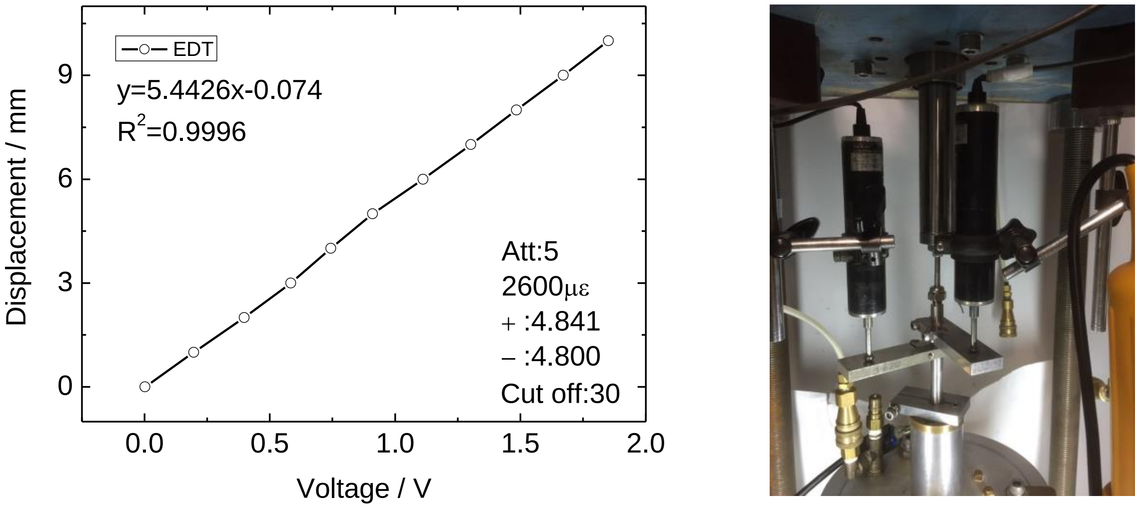

Fig. 2.9 Calibration of external displacement transducer and its photo

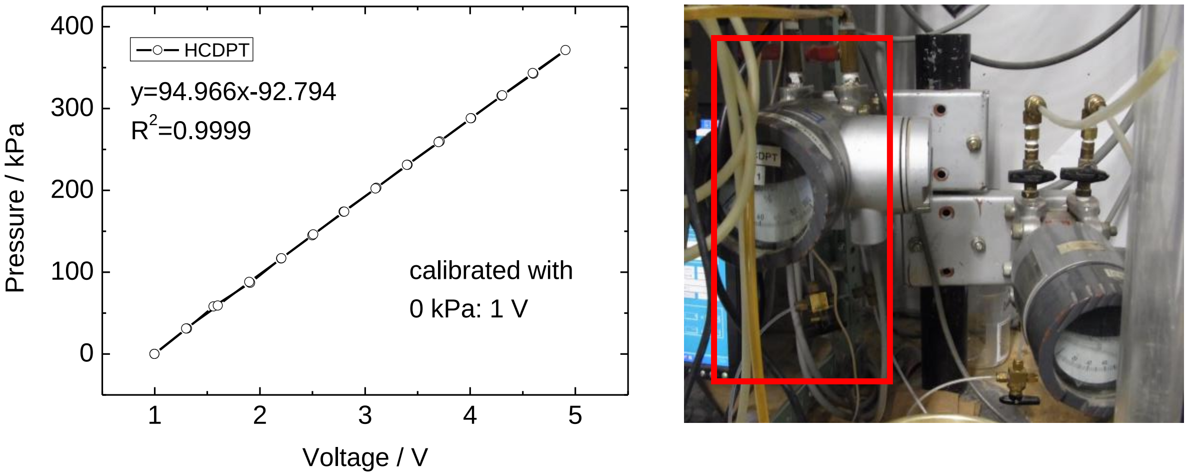

Fig. 2.10 Calibration of HCDPT and its photo

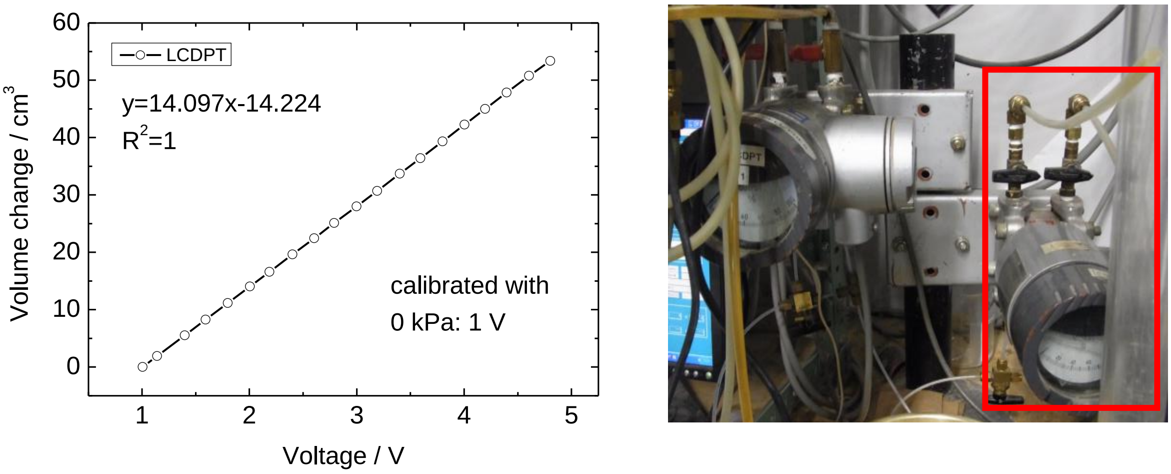

**Fig. 2.11 Calibration of LCDPT and its photo**

**Fig. 2.12 Transparent membrane used in triaxial liquefaction tests**

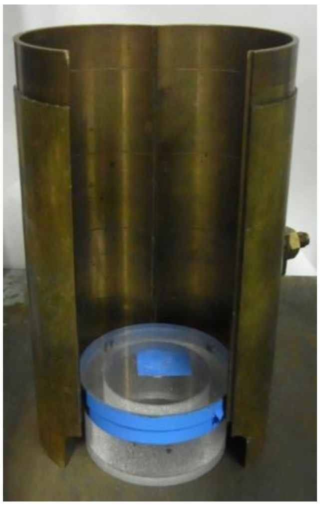

**Fig. 2.13 Mould for sample preparation in triaxial tests**

**Fig. 2.14 Mould for vacuuming the membrane**

**Fig. 2.15 Painting for making dots on membrane**

**Fig. 2.16 The sample after painting**

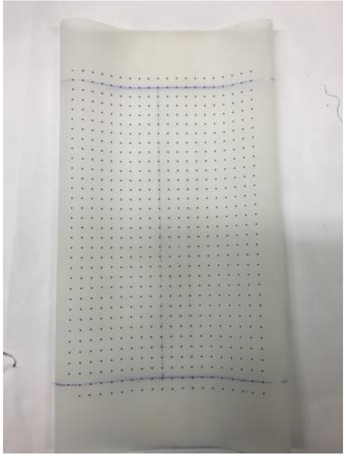

**Fig. 2.17 Precast dots pasted on membrane**

**Fig. 2.18 Absorbing water in the air pluviation method**

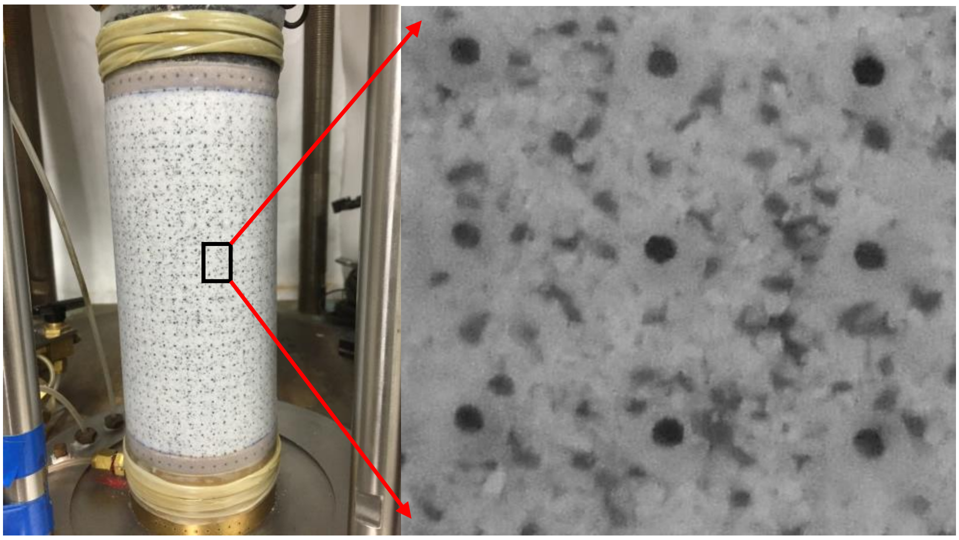

**Fig. 2.19 Silica sand specimen with dots on membrane**

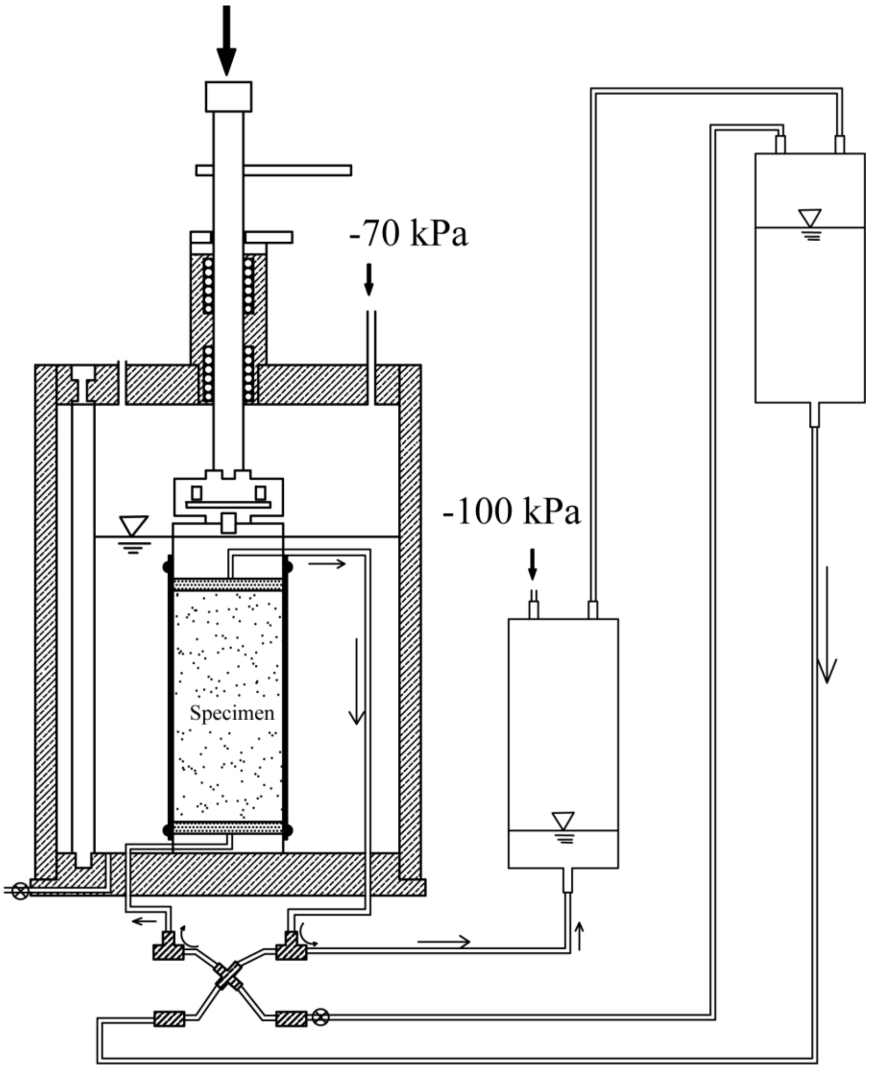

Fig. 2.20 Saturation process in triaxial liquefaction tests

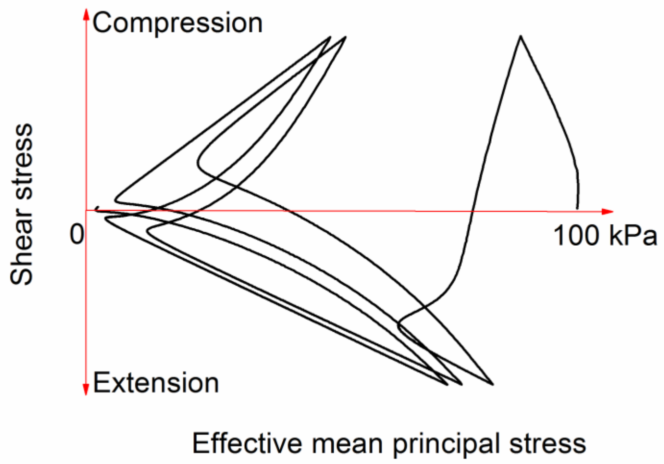

Fig. 2.21 Stress path applied in the triaxial liquefaction tests

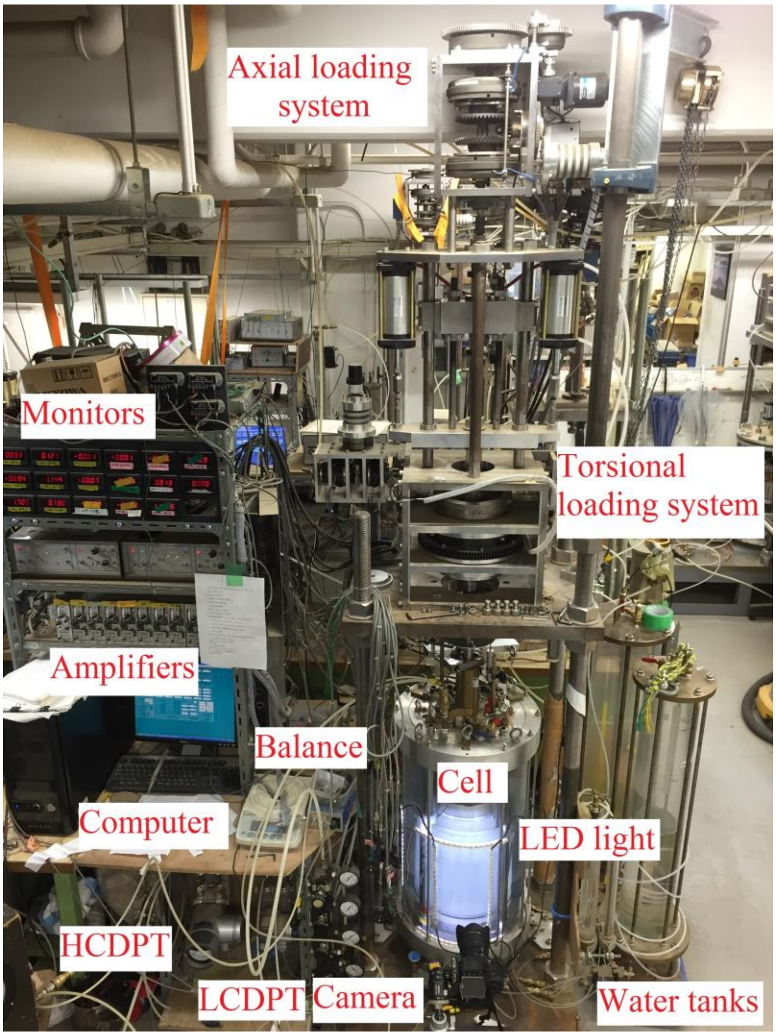

**Fig. 2.22 Torsional shear apparatus with camera applied in this study**

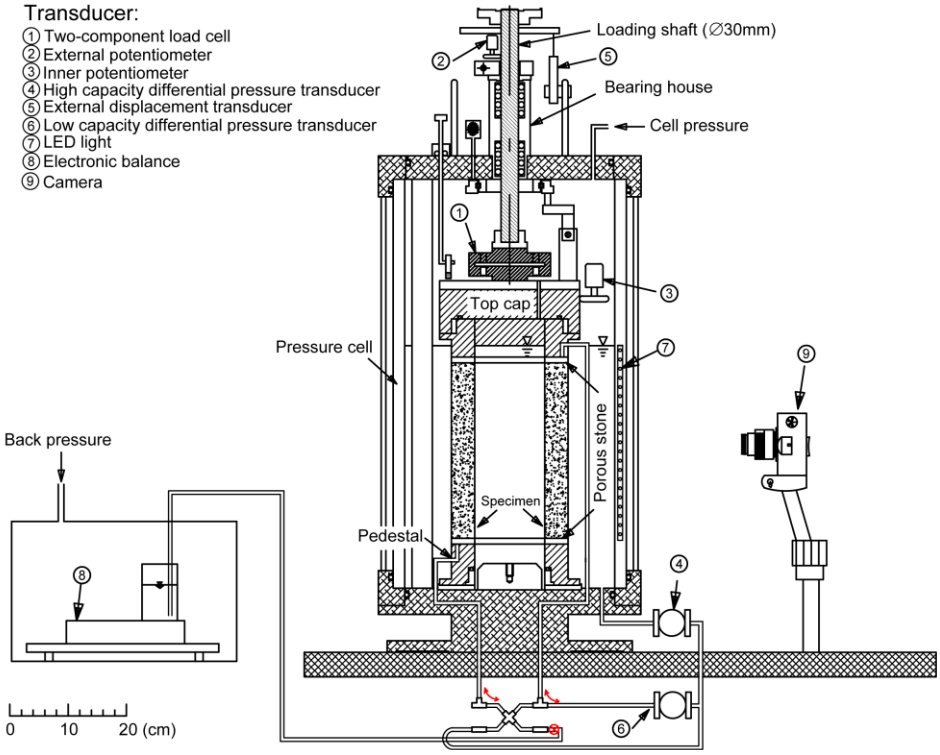

**Fig. 2.23 Schematic diagram of torsional shear apparatus and camera**

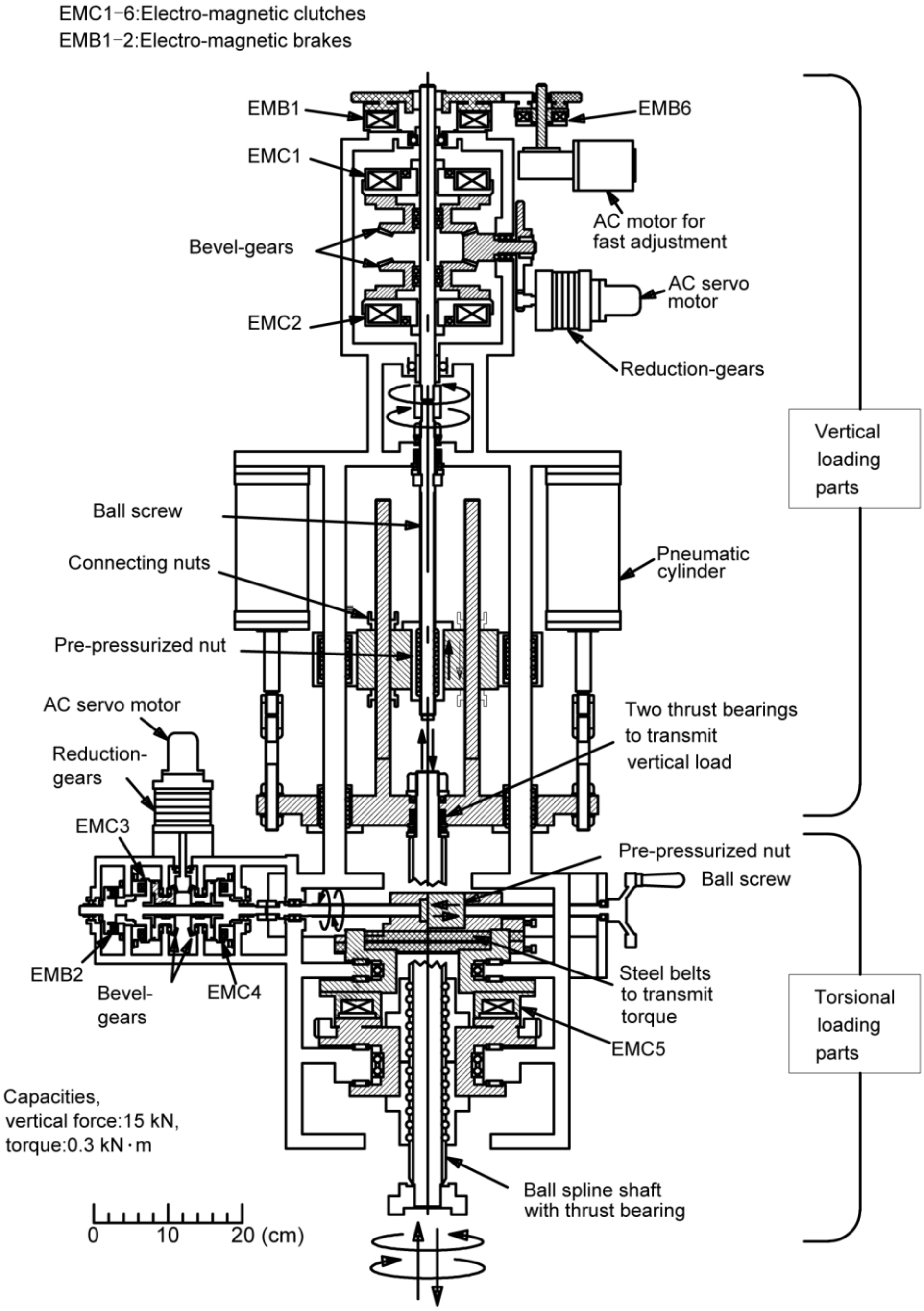

**Fig. 2.24 Schematic diagram of loading systems in torsional shear apparatus**

**Fig. 2.25 The setup of Load cell during undrained torsional shear tests**

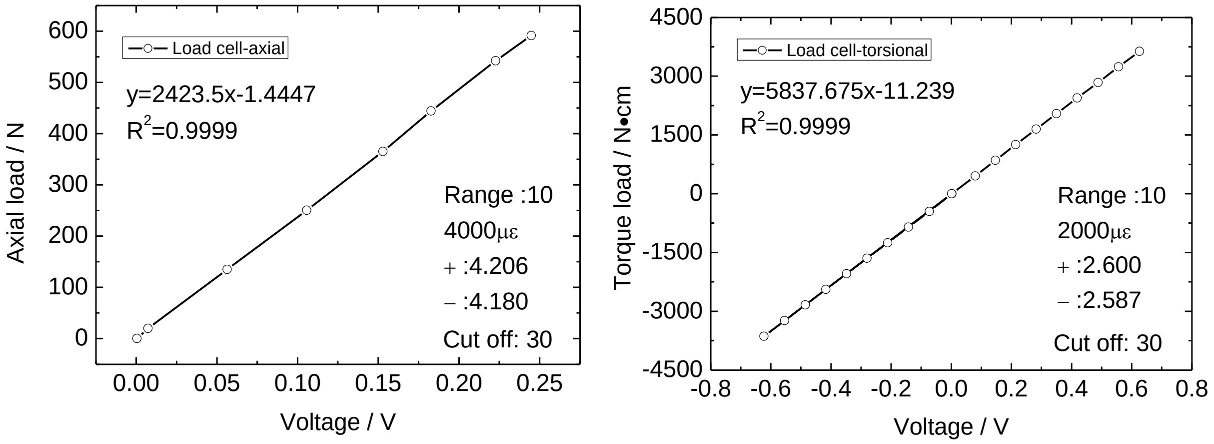

**Fig. 2.26 Calibration curves of load cell on axial and torsional shear directions**

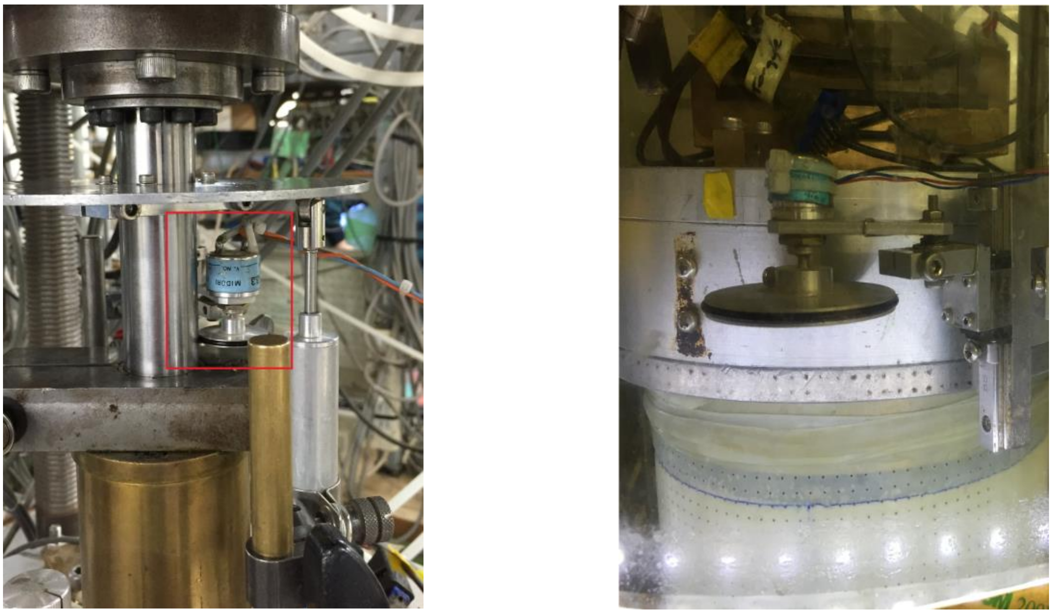

**Fig. 2.27 The setup of outer and inner potentio-meters in torsional shear apparatus**

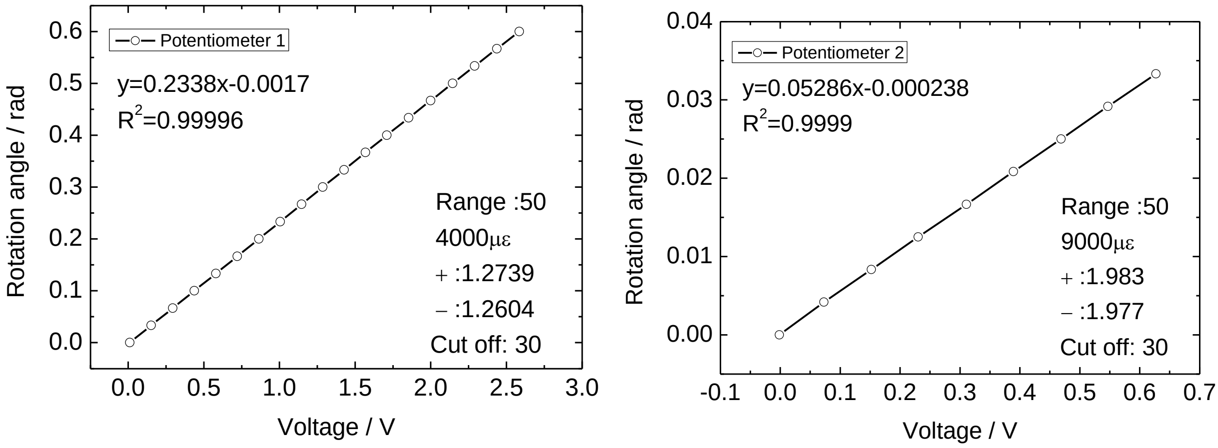

**Fig. 2.28 Calibration curves of potentio-meters**

**Fig. 2.29 The setup of EDT in torsional shear apparatus**

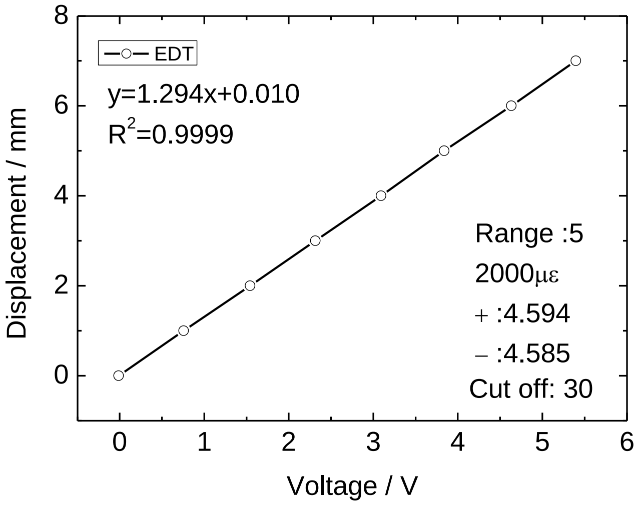

**Fig. 2.30 Calibration curve of EDT in torsional shear apparatus**

**Fig. 2.31 HCDPT in torsional shear apparatus**

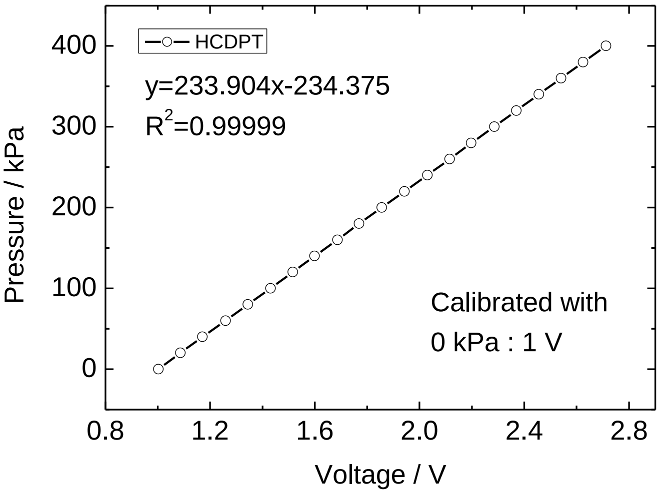

**Fig. 2.32 Calibration curve of HCDPT in torsional shear apparatus**

**Fig. 2.33 LCDPT in torsional shear apparatus**

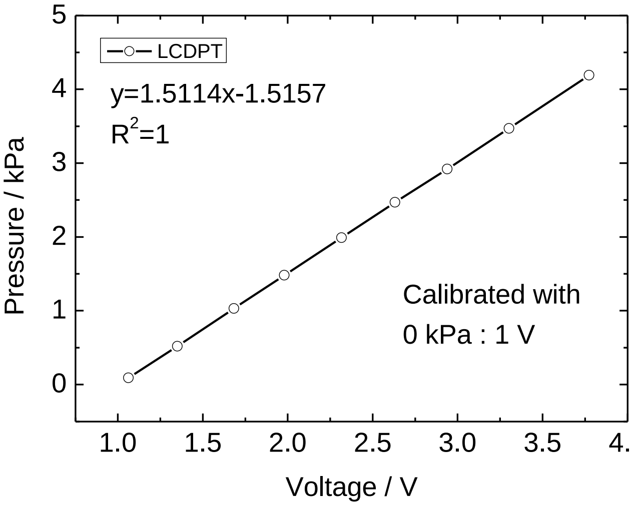

**Fig. 2.34 Calibration curve of LCDPT in torsional shear apparatus**

Fig. 2.35 Volume change measured by electronic balance

Fig. 2.36 Camera setup in torsional shear apparatus

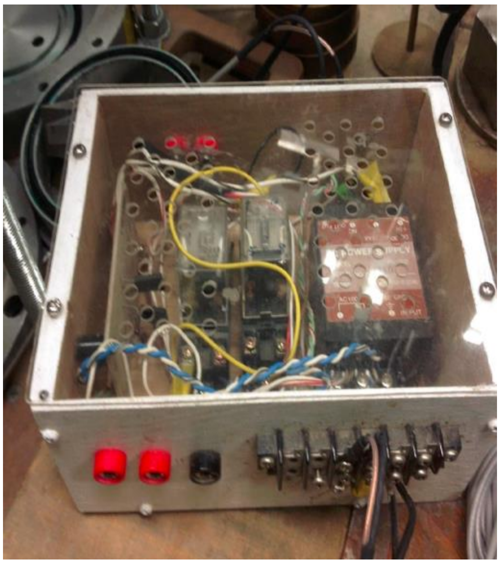

Fig. 2.37 Camera control unit in torsional shear apparatus

Fig. 2.38 Rubber O-ring used for inner membrane

Fig. 2.39 The setup of inner membrane in torsional shear apparatus

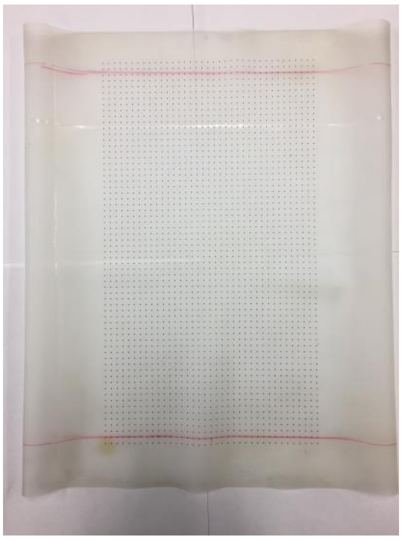

**Fig. 2.40 Transparent membrane used in torsional shear apparatus**

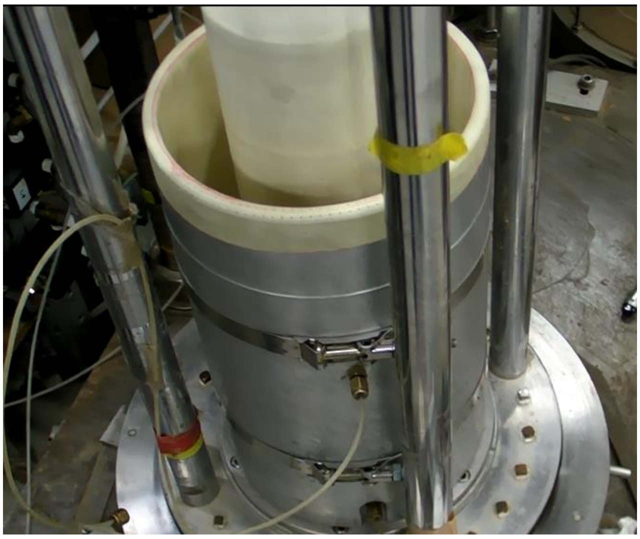

**Fig. 2.41 The setup of inner and outer membrane in undrained torsional shear tests**

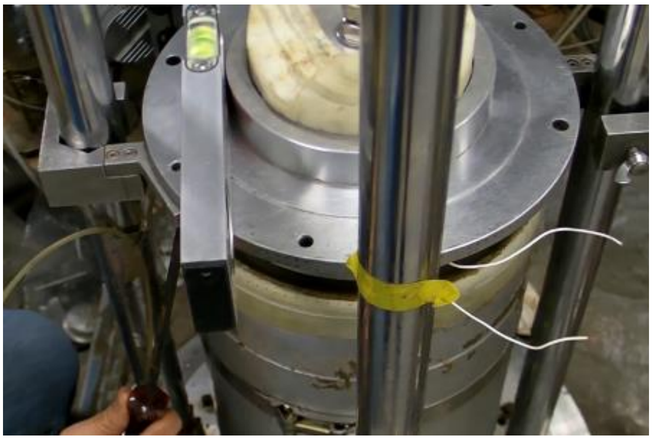

**Fig. 2.42 The setup of top cap in undrained torsional shear tests**

**Fig. 2.43 The hollow cylindrical specimen before saturation**

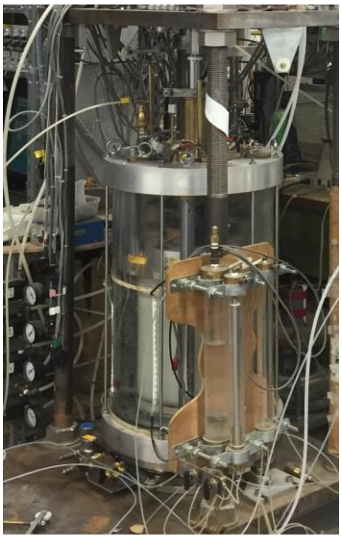

**Fig. 2.44 The photo of cell and specimen after filling water**

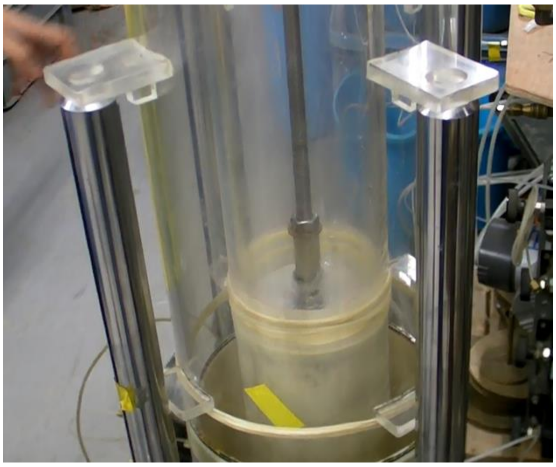

**Fig. 2.45 The setup of acrylic pipes for preparing segregated sand specimen**

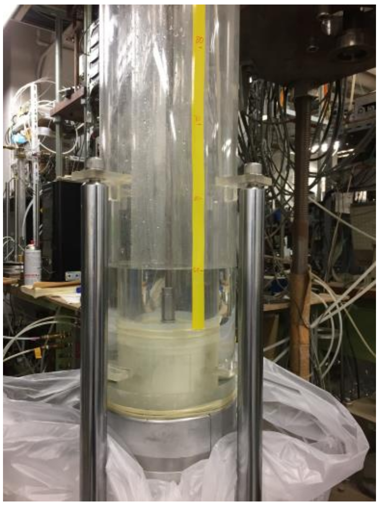

**Fig. 2.46 The photo before filling sand for segregated sand specimen**

**Fig. 2.47 The photo of water sediment method**

**Fig. 2.48 Fine layer at top after sedimentation**

**Fig. 2.49 Segregated sand specimen with fine layers**

**Fig. 2.50 The segregated specimen after filling water in the cell**

Fig. 2.51 Saturation process in undrained torsional shear tests

Fig. 2.52 The photo taken during undrained torsional shear test

# 3. FORMULATION OF STRESSES AND STRAINS

## 3.1 Introduction

In general, it may be said that there are two main problems confronting the soil engineers and researchers dealing with a situation where soil liquefaction may occur: (1) Determining the stress conditions required to trigger liquefaction; and (2) determining the consequences of liquefaction in terms of potential sliding and deformations (Seed, 1987). Stress and strain are seen as the two of the most important parameters to evaluation the liquefaction properties of soils.

Triaxial apparatus is widely used in laboratory tests because the cylindrical shape of specimen makes it easy to run tests on the samples of a good quality collected from in-situ (Towhata, 2008). As introduced in chapter 2, the cylindrical specimen covered by a rubber membrane is pressurized by an isotropic stress condition and subjected to additional vertical load. Nevertheless, in view of accuracy for simulating the stress condition in the field during earthquake, triaxial apparatus is not the best method to evaluation the mechanical properties of sand specimen(Ishihara and Li, 1972). One drawback of triaxial apparatus is that the directions of principal stresses are reoriented intermittently by ninety degrees. The intermediate principal stress is also intermittently changed during cyclic loading.

As for the stress applied by torsional shear apparatus, it is similar to the stress condition in field during earthquake. Moreover, the direction of principal stress is reoriented continuously and the intermediate principal stress is almost constant during shearing. The hollow cylindrical specimen is seen as infinite long on circumferential direction which eliminates the affection of boundary. However, the shear stress along the cross section is not uniform. It is always assumed that the distribution of stress along radial direction is linear when the shear strain is small enough, and the sand will act as a rigid plastic material after exceeding a large shear strain. In most of cases, the sand stays in the status between elastic and rigid plastic.

In this study, triaxial apparatus and torsional shear apparatus were employed to investigate the liquefaction properties of soil under undrained cyclic loading. Since the modes of applying stress on the soil element between triaxial and torsional shear apparatuses are quite different, the stresses and strains of them will be introduced separately in this chapter.

## 3.2 General soil mechanics

The soils are three-phase materials, consisting of solid, liquid and air constituents. Irregular shapes are the basic structure of sand particles, which will induce the formation of voids. In the natural condition, the voids will be occupied by water and air. In the soil mechanics, the proportions of solid, liquid and air constituents are characterized by five dimensionless quantities: void ratio (*e*), porosity (*n*), water content (*w*), degree of saturation ($S_r$) and relative density ($D_r$). A soil sample that consists of solid, water and air is shown in Fig. 3.1.

The void ratio is defined as,

$$e = \frac{V_V}{V_S} = \frac{V - V_S}{V_S} \qquad (3\text{-}1)$$

In which $V_V$ is the volume of voids in the soil sample, $V_S$ is the volume of solids and $V$ is the total volume of soil sample.

$$\Rightarrow \frac{V}{V_S} = 1 + e \quad (3\text{-}2)$$

Porosity is the ratio of the volume of voids to the total volume, which is expressed as;

$$n = \frac{V_V}{V} \quad (3\text{-}3)$$

In case of dry soil where there is no water, the total weight *M* is equal to the weight of solids $M_S$ without considering the weight of air. Then,

$$\Rightarrow \frac{V}{V_S} = 1 + e$$
$$\Rightarrow \frac{M}{V_S} \times \frac{V}{M} = 1 + e$$
$$\Rightarrow \frac{M_S}{V_S} \times \frac{V}{M} = 1 + e$$

By definition,

$\frac{M_S}{V_S} = G_S$ (Specific gravity of soil) and $\frac{M}{V} = \rho$ (dry density of soil)

$$\Rightarrow \frac{G_S}{\rho} = 1 + e \qquad \Rightarrow e = \frac{G_S}{\rho} - 1 \qquad (3\text{-}4)$$

The water content *w* is the ratio of the weight of water ($W_w$) to the weight of solids ($W_s$):

$$w = \frac{W_W}{W_S} \qquad (3\text{-}5)$$

Relative density ($D_r$) of soil is defined as,

$$D_{\mathrm{r}} = \frac{(e_{\max} - e)}{(e_{\max} - e_{\min})} \quad (3\text{-}6)$$

Where $e_{\max}$ and $e_{min}$ are the maximum and minimum void ratios of the soil sample.

In conducting the test, all the specimens will be prepared with a certain initial relative density, which requires to measure the specific gravity, maximum and minimum void ratios in advance.

The degree of saturation ($S_r$) is the ratio of the volume of water ($V_w$) to the volume of void ($V_v$):

$$S_r = \frac{V_w}{V_s} \times 100\%$$

$S_r$ ranges from 100% (fully saturated status) to 0% (perfectly dry status). Similar to the function of degree of saturation, Skempton's B value is more sensitive than $S_r$. For example, the relationship between the degree of saturation and B value of Toyoura sand at a relative density of 60% is shown in Fig. 3.2 (Yoshimi et al., 1989).

## 3.3 Triaxial tests

### 3.3.1 Definition and computation of stress

The following equations are used to calculate the stress and strains in triaxial tests.

The deviator stress $q$ could be measured directly from by the load cell during compression and extension of triaxial test. As shown in Fig. 3.3, the maximum principal stress changes its direction during cyclic loading. The axial stress under compression condition is calculated by the following equations.

$$\sigma_V = \sigma_1 = \sigma_3 + q = \sigma_r + q \quad (3\text{-}7)$$

$$\Rightarrow \sigma'_V = \sigma'_1 = \sigma'_3 + q = \sigma'_r + q \quad (3\text{-}8)$$

In which $\sigma_V$ and $\sigma'_V$ are the total and effective axial stresses. $\sigma_1$ and $\sigma_3$ are the maximum and minimum principal stresses, with the corresponding effective stresses of $\sigma'_1$ and $\sigma'_3$. $\sigma'_r$ is the effective confining stress measured by HCDPT. $\sigma_r$ is the total confining pressure which includes the back pressure of pore water supplied by positive regulater.

As for the stresses in extension stage, the calculation method is similar to those in the compression stage, it will not be repeated herein.

Mean effective stresses, $p'$:

$$p' = \frac{\sigma'_V + 2\sigma'_r}{3} \qquad (3\text{-}9)$$

### 3.3.2 Definition and computation of strain

Strain as a normalized deformation parameter has been widely used to represent the deformation behavior of soils. In the triaxial test, the height of specimen without deformation was measured and set as a reference height. During the cyclic loading, the displacement of specimen was measured by EDT and recorded by computer program. Then the axial strain is calculated by the following equation.

$$\varepsilon_v = \frac{\Delta H}{H} \quad (3\text{-}10)$$

Where $\varepsilon_v$ is the axial strain. $\Delta H$ is the displacement of specimen and $H$ is the original height of specimen.

Since the tests were conducted under undrained condition, the volume of specimen was kept constant during loading. Then the radial strain $\varepsilon_{\mathrm{r}}$ could be obtained by equation 3-11.

$$\varepsilon_{\mathrm{r}} = -\frac{\varepsilon_{\mathrm{v}}}{2} \quad (3\text{-}11)$$

# 3.4 Hollow cylindrical torsional shear tests

As shown in Fig. 3.4, there are four stress and strain components on the specimen element, respectively. These four stresses could be controlled independently by this hollow cylindrical torsional shear apparatus. In this study, the inner cell pressure ($p_i$) and outer cell pressure ($P_o$) are set equally to each other. This cell pressure was supplied by the E/P and remained during undrained cyclic loading. The vertical stress was controlled by the cell pressure and vertical loading motor while the shear stress was applied by torque ($T$) from torsional loading motor. These four stresses are named as radial stress ($\sigma_r$), circumferential stress ($\sigma_\theta$), axial stress ($\sigma_z$) and shear stress ($\tau_{z\theta}$) correspond with radial strain ($\varepsilon_r$), circumferential strain ($\varepsilon_\theta$), axial strain ($\varepsilon_z$) and shear strain ($\gamma_{z\theta}$), respectively.

## 3.4.1 Definition and computation of stress

### 3.4.1.1 Radial and circumferential stress

Timoshenko and Goodier (Timoshenko and Goodier, 1970) proposed a solution for hollow cylinder specimen as a uniform material subjected to uniform inner cell pressure ($P_i$) and outer cell pressure ($P_o$). The stress distribution is assumed to be symmetrical with respect to the vertical axis (z) of the hollow cylinder and the stress components do not depend on the radial angle ($\theta$) and are a function of radius ($r$) only. As a result, the shear stress ($\tau_{r\theta}$) should be equal to 0 kPa. The equation of equilibrium in the radial direction yields,

$$\frac{\partial \sigma_r}{\partial r} + \frac{\sigma_r - \sigma_\theta}{r} + \omega = 0 \qquad (3\text{-}12)$$

in which $\omega$ is the body force, when $\omega$ equals to 0, eq. (3-12) is satisfied by the following,

$$\sigma_r = \frac{B}{r^2} + 2C \qquad (3\text{-}13)$$

$$\sigma_\theta = -\frac{B}{r^2} + 2C \qquad (3\text{-}14)$$

where $B$ and $C$ are constants, which could be obtained by the following boundary conditions:

$$\sigma_r|_{r=R_i} = p_i \quad (3\text{-}15)$$

$$\sigma_r|_{r=R_o} = p_o \quad (3\text{-}16)$$

in which $R_o$ and $R_i$ donate the outer and inner radii of the hollow cylindrical specimen, respectively.

By substituting eq. (3-15) and (3-16) into eq. (3-13) and (3-14), the following results are obtained:

$$\sigma_r = \frac{p_o R_o^2 - p_i R_i^2}{R_o^2 - R_i^2} - \frac{R_i^2 R_o^2 (P_o - P_i)}{R_o^2 - R_i^2} \times \frac{1}{r^2} \quad \text{(3-17)}$$

$$\sigma_\theta = \frac{p_o R_o^2 - p_i R_i^2}{R_o^2 - R_i^2} + \frac{R_i^2 R_o^2 (P_o - P_i)}{R_o^2 - R_i^2} \times \frac{1}{r^2} \quad \text{(3-18)}$$

Average stress components are calculated without weighting and with weighting (Ampadu, 1991)as follows:

*Averaging without weight*

$$\overline{\sigma_r} = \frac{\int_{R_i}^{R_o} \sigma_r dr}{\int_{R_i}^{R_o} dr} \qquad \overline{\sigma_\theta} = \frac{\int_{R_i}^{R_o} \sigma_\theta dr}{\int_{R_i}^{R_o} dr} \quad \text{(3-19)}$$

By substituting eq. (3-17) and (3-18) into (3-19), we get,

$$\overline{\sigma_r} = \frac{P_o R_o + P_i R_i}{R_o + R_i} \quad \text{(3-20)}$$

$$\overline{\sigma_\theta} = \frac{P_o R_o - P_i R_i}{R_o - R_i} \quad \text{(3-21)}$$

These equations are commonly used by a number of researchers such as Hight et al. (Hight et al., 1983, 1985) and Saada (Saada, 1988).

*Averaging with weighting*

$$\int_{R_i}^{R_o} \sigma_r r dr = \int_{R_i}^{R_o} \overline{\sigma_r} r dr \quad \text{(3-22)}$$

$$\int_{R_i}^{R_o} \sigma_\theta r dr = \int_{R_i}^{R_o} \overline{\sigma_\theta} r dr \quad \text{(3-23)}$$

$$\overline{\sigma_r} = \frac{\int_{R_i}^{R_o} \sigma_r r dr}{\int_{R_i}^{R_o} r dr} \quad \text{(3-24)}$$

$$\overline{\sigma_\theta} = \frac{\int_{R_i}^{R_o} \sigma_\theta r dr}{\int_{R_i}^{R_o} r dr} \quad \text{(3-25)}$$

By substituting eq. (3-17) and eq. (3-18) into eq. (3-24) and eq. (3-25), we get,

$$\overline{\sigma_r} = \frac{p_o R_o^2 - p_i R_i^2}{R_o^2 - R_i^2} - \frac{2 R_i^2 R_o^2 (P_o - P_i)}{(R_o^2 - R_i^2)^2} \times \ln(\frac{R_o}{R_i}) \quad \text{(3-26)}$$

$$\overline{\sigma_\theta} = \frac{p_o R_o^2 - p_i R_i^2}{R_o^2 - R_i^2} + \frac{2 R_i^2 R_o^2 (P_o - P_i)}{(R_o^2 - R_i^2)^2} \times \ln(\frac{R_o}{R_i}) \quad \text{(3-27)}$$

In this study, the outer and inner cell pressures are kept equal to each other ($P_i = P_o$). Therefore, $\overline{\sigma_r} = \overline{\sigma_\theta} = P_o = P_i$ could be obtained from equations (3-26) and (3-27).

### 3.4.1.2 Vertical stress

The average of vertical stress could be calculated by the following equation:

$$\overline{\sigma_z} = \frac{LC}{A} + \sigma_h + \sigma_{cap} + \sigma_{mem} \quad \text{(3-28)}$$

where,

$LC$ : Deviator load measured by load cell

$A$ : Cross-section area of the specimen (considering volume change)

$\sigma_h$ : Horizontal stress, which is equal to the cell pressure.

$\sigma_{cap}$ : The stress affected by the weight of top cap .

$\sigma_{mem}$ : Correction stress induced by the membrane (Tatsuoka et al., 1986).

### 3.4.1.3 Shear stress

When the specimen is rotated by a unit angle $d\theta$, the rotation displacements of sand particles along the radial direction will be $rd\theta$.Therefore, the shear stress acting on the soil element is not uniform along the radial direction. The soil element may be subjected to the elastic stage under a small shear strain, followed by elastic-plastic stage and eventually the plastic stage. A proper calculation of $\tau_{z\theta}$ should satisfy the toque that is applied to the specimen,

$$T = \int_{R_i}^{R_o}\int_0^{2\pi} \tau_{z\theta} r^2 d\theta dr = 2\pi\int_{R_i}^{R_o} \tau_{z\theta} r^2 dr \quad (3\text{-}29)$$

If the material stays in a perfectly elastic stage, then,

$$\tau_{z\theta}^e = kr$$

$$T = \int_{R_i}^{R_o}\int_0^{2\pi} \tau_{z\theta}^e r^2 d\theta dr = 2\pi k\int_{R_i}^{R_o} r^3 dr = \frac{\pi}{2}(R_o^4 - R_i^4)k \quad (3\text{-}30)$$

Therefore, the average shear stress on radial direction will be:

$$\overline{\tau_{z\theta}^e} = k \times \frac{R_o + R_i}{2} = \frac{T}{\pi(R_o^2 + R_i^2)(R_o - R_i)} \quad (3\text{-}31)$$

$$k = \frac{2T}{\pi(R_o^4 - R_i^4)} \quad (3\text{-}32)$$

On the other hand, if the material stays in a perfectly plastic stage, then,

$$\tau_{z\theta}^p = const$$

$$T = \int_{R_i}^{R_o}\int_0^{2\pi} \tau_{z\theta}^p r^2 d\theta dr = 2\pi\tau_{z\theta}^p\int_{R_i}^{R_o} r^2 dr = \frac{2\pi}{3}(R_o^3 - R_i^3) \times \tau_{z\theta}^p \quad (3\text{-}33)$$

Then,

$$\tau_{z\theta}^p = \overline{\tau_{z\theta}^p} = \frac{3T}{2\pi(R_o^3 - R_i^3)} \quad (3\text{-}34)$$

In this study, the shear stress is averaged from equation (3-31) and equation (3-34) as shown below.

$$\overline{\tau_{z\theta}} = \frac{\overline{\tau_{z\theta}^e} + \overline{\tau_{z\theta}^p}}{2} = \frac{1}{2}\left[\frac{T}{\pi(R_o^2 + R_i^2)(R_o - R_i)} + \frac{3T}{2\pi(R_o^3 - R_i^3)}\right] \quad (3\text{-}35)$$

Since the membrane has a large affection on the torque, the torque is corrected by:

$$T = T_{LC} - T_{mem} \quad (3\text{-}36)$$

Where,

$T_{LC}$ : The torque detected by the load cell

$T_{mem}$: Membrane force (inner and outer membrane)

The membrane force is calculated by the following equations:

$$T_{mem} = \frac{2}{3}\pi \times t_m \times E_m \times \frac{\theta}{H} \times (R_o^3 + R_i^3) \quad (3\text{-}37)$$

in which, $t_m$ : the thickness of membrane.

$E_m$ : the elasticity modulus of membrane.

$\theta$: the rotation angle detected by potentiometer.

$H$ : the height of specimen.

### 3.4.1.4 Principal stresses

Based on the four stresses components of element A shown in Fig. 3.4, the principal stress of the corresponding element could be computed and plotted in the Mohr's circle in Fig .3.5.

$$\begin{Bmatrix}\sigma_1 \\ \sigma_3\end{Bmatrix} = \frac{\sigma_z + \sigma_\theta}{2} \pm \sqrt{(\frac{\sigma_z - \sigma_\theta}{2})^2 + \tau_{z\theta}^2} \quad (3\text{-}38)$$

$$\sigma_2 = \sigma_r \quad (3\text{-}39)$$

The angle $\alpha$, between the direction of maximum principal stress and vertical direction, could be calculated by:

$$\tan 2\alpha = \frac{2\tau_{z\theta}}{\sigma_z - \sigma_\theta} \quad (3\text{-}40)$$

Moreover, the coefficient of intermediate principal stress is defined as:

$$b = \frac{\sigma_2 - \sigma_3}{\sigma_1 - \sigma_3} = \frac{1}{2}\left[\frac{\sigma_r - \dfrac{\sigma_z + \sigma_\theta}{2}}{\sqrt{(\dfrac{\sigma_z - \sigma_\theta}{2})^2 + \tau_{z\theta}^2}} + 1\right] \quad (3\text{-}41)$$

## 3.4.2 Definition and computation of strain

Corresponding to the four stress components of element A, there are four strain components as shown in Fig. 3.4, named as axial strain ($\varepsilon_z$), radial strain ($\varepsilon_r$), circumferential strain ($\varepsilon_\theta$) and shear strain ($\gamma_{z\theta}$).

As shown in Fig. 3.6, the radial strain and circumferential strain are computed as follows:

$$\varepsilon_r = -\frac{u(r+dr) - u(r)}{dr} = -\frac{du}{dr} \quad (3\text{-}42)$$

$$\varepsilon_\theta = -\frac{(r+u)d\theta - rd\theta}{rd\theta} = -\frac{u}{r} \quad (3\text{-}43)$$

in which,

$u$ : the deformation of a soil element in radial direction

$r$ : the distance to center of hollow specimen

If there is a linear relationship between $u(r)$ amd $r$, we get:

$$\overline{\varepsilon_r} = -\frac{u_o - u_i}{R_o - R_i} \qquad (3\text{-}44)$$

$$\overline{\varepsilon_\theta} = -\frac{2\pi\left(\frac{(R_o+u_o)+(R_i+u_i)}{2} - \frac{R_o+R_i}{2}\right)}{2\pi\left(\frac{R_o+R_i}{2}\right)} = -\frac{u_o+u_i}{R_o+R_i} \qquad (3\text{-}45)$$

in which $u_o$ and $u_i$ are the increments of inner and outer radii, respectively.

In addition, the axial strain is defined above.

$$\varepsilon_z = \frac{dH}{H} \qquad \overline{\varepsilon_z} = \frac{\Delta H}{H_o} \qquad (3\text{-}46)$$

Where,

$\Delta H$ : the displacement of specimen measured by EDT.

$H_o$ : the original height of specimen before testing.

As for the shear strain, it is defined by the following equation,

$$\gamma = \frac{r\Delta\theta}{H} \qquad (3\text{-}47)$$

$$\overline{\gamma} = \frac{\int_{R_i}^{R_o}\int_0^{2\pi} r \times \frac{\Delta\theta}{H} r dr d\theta}{\int_{R_i}^{R_o}\int_0^{2\pi} r dr d\theta} = \frac{2\Delta\theta(R_o^3 - R_i^3)}{3H(R_o^2 - R_i^2)} \qquad (3\text{-}48)$$

where,

$H$ : the height of specimen

$\Delta\theta$ : the rotation angle detected by the potentiometer.

As for the volume strain, it is defined by:

$$\varepsilon_{vol} = \frac{\Delta V}{V_o} \qquad (3\text{-}49)$$

Where $\Delta V$ is the volume change during consolidation measured by electronic balance, and $V_o$ is the original volume of specimen. Since the measurement of inner cylinder is of difficulty and there may be non-uniform deformation along the height and boundary of specimen, some assumptions are made to compute the deformed inner and outer diameters by the following equations:

$$D_o = D_{oo} \times \sqrt{\frac{(1-\varepsilon_{vol})}{(1-\varepsilon_z)}} \qquad (3\text{-}50)$$

$$D_i = D_{io} \times \sqrt{\frac{(1-\varepsilon_{vol})}{(1-\varepsilon_z)}} \qquad (3\text{-}51)$$

where,

$D_o$ : the deformed outer diameter of specimen.

$D_i$ : the deformed inner diameter of specimen.

$D_{oo}$ : the original outer diameter of specimen.

$D_{io}$ : the original inner diameter of specimen.

## 3.5 Reference

1. Ampadu, S. (1991). *Undrained behaviour of kaolin in torsional simple shear*. 東京大学.
2. Hight, D., Gens, A. and Symes, M. (1983). The development of a new hollow cylinder apparatus for investigating the effects of principal stress rotation in soils. *Géotechnique, 33*(4), 355-383.
3. Hight, D., Gens, A. and Symes, M. (1985). Discussion: The development of a new hollow cylinder apparatus for investigating the effects of principal stress rotation in soils Undrained anisotropy and principal stress rotation in saturated sand. *Géotechnique, 35*(1), 78-85.
4. Ishihara, K. and Li, S.-I. (1972). Liquefaction of saturated sand in triaxial torsion shear test. *Soils and Foundations, 12*(2), 19-39.
5. Saada, A. S. (1988). State-of-the-art paper: Hollow cylinder torsional devices: Their advantages and limitations *Advanced triaxial testing of soil and rock*: ASTM International.
6. Seed, H. B. (1987). Design problems in soil liquefaction. *Journal of Geotechnical Engineering, 113*(8), 827-845.
7. Tatsuoka, F., Sonoda, S., Hara, K., Fukushima, S. and Pradhan, T. (1986). Failure and deformation of sand in torsional shear. *Soils and Foundations, 26*(4), 79-97.
8. Timoshenko, S. and Goodier, J. (1970). Theory of Elasticity. *Auckland, McGraw-Hill, New York*.
9. Towhata, I. (2008). *Geotechnical earthquake engineering*: Springer Science & Business Media.
10. Yoshimi, Y., Tanaka, K. and Tokimatsu, K. (1989). Liquefaction resistance of a partially saturated sand. *Soils and Foundations, 29*(3), 157-162.

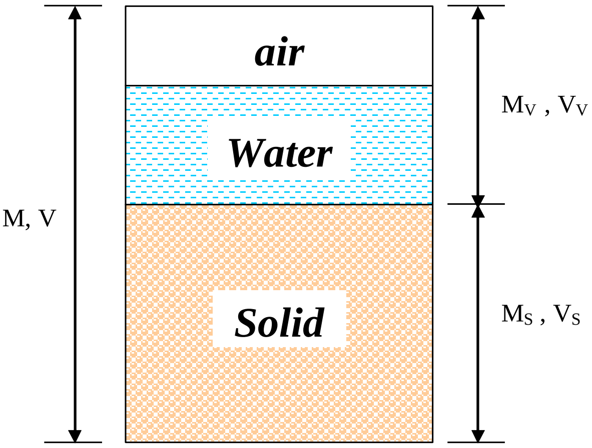

**Fig. 3.1 Phase diagram of soil sample**

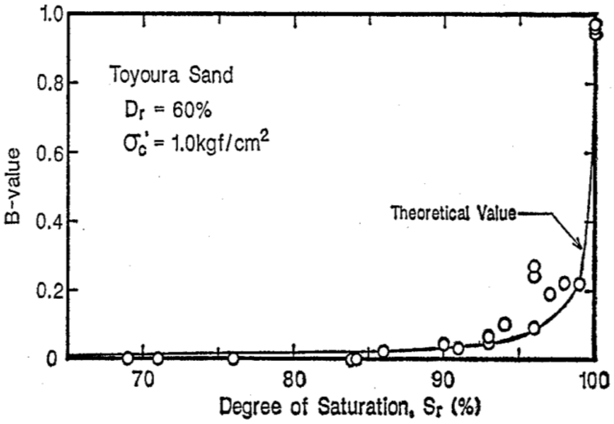

**Fig. 3.2 Relationship between degree of saturation and B value (Yoshimi et al., 1989)**

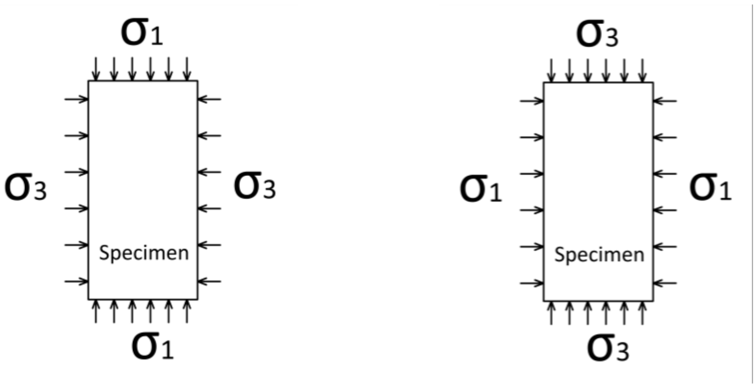

(a) Compression ( $\sigma_2 = \sigma_3 = \sigma_r$ ) (b) Extension ( $\sigma_1 = \sigma_2 = \sigma_r$ )

**Fig. 3.3 Stress conditions in triaxial test**

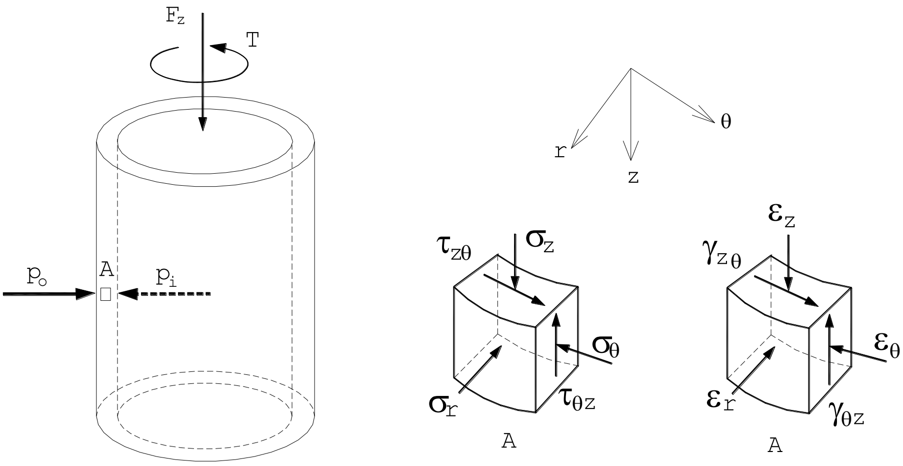

**Fig. 3.4 Stresses and strains in element A**

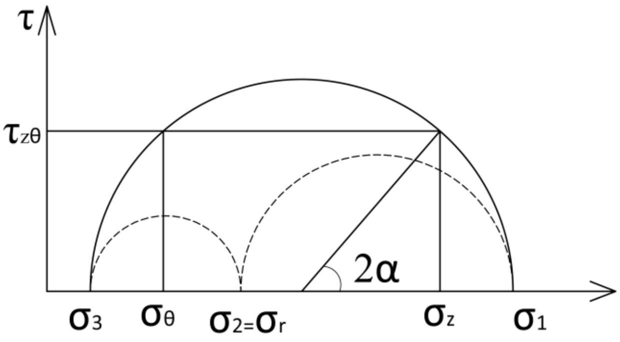

**Fig. 3.5 The stress statuses in hollow cylindrical torsional shear test**

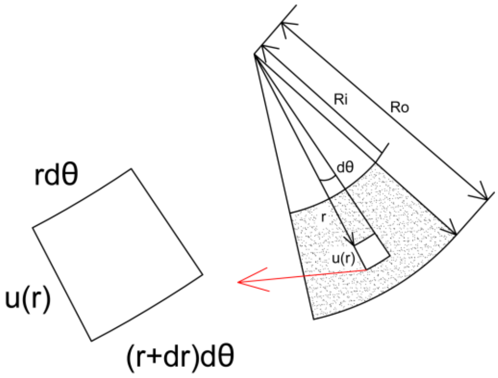

**Fig. 3.6 Radial and circumferential strains of a soil element**

# 4. IMAGE ANALYSIS TECHNIQUE

## 4.1 Introduction

The image analysis method employed in this study is based on the technique of Particle Image Velocimetry (PIV). It allows the displacements of an object to be measured through series digital images taken during moving. Occasionally, Particle Tracking Velocimetry and Particle Image Velocimetry are mixed by researchers when deal with image analysis process. By Raffel, et al. (2013), the situation, when the density of tracer particle is low, is referred to 'Particle Tracking Velocimetry'. As for the medium image density, it is impossible to identify the tracer particles by visual inspection. Then the standard statistical PIV method is required. In the case of high image density, this situation is named as 'Laser Speckle Velocimetry'. In the past decades, the development of Particle Image Velocimetry is characterized by the fact that the analog pictures have been replaced by digital images with the corresponding evaluation techniques. Recently, PIV is widely used in geotechnical element and model tests. The non-contact condition between sample and camera is the main advantage of PIV applied in laboratory tests without any disturbances.

Similar as seeded flow in fluid mechanics from which the PIV technique was originally developed, natural sand has its own texture structure in the form of different colored grains and their corresponding shadows formed between neighboring grains when illuminated (White et al., 2003). The displacement vectors of measured patches during the interval between different images are obtained by locating the peak of correlation function of each patch. This is the basic principle of image analysis used in this study. Previous image-based local deformation systems assumed that the image scale between the distance of two objects and the length in the image was constant across the field of view. This assumption was valid only when the camera was far away from object and could be seen as a pinhole model, and the object moved under an exactly plane condition which was perpendicular to the camera lens. However, these conditions could not be satisfied perfectly in the laboratory tests, especially when the sample was cylindrical. Therefore, some derived image-based deformation systems were developed.

In order to measure of volume change of sand specimen, Macari et al. (1997) proposed a coordinate correction method on cylindrical specimen in triaxial tests by considering the refractions between water, cell and atmosphere, respectively. The Snell's law was applied twice to calculate the real coordinates of measured points on the surface of specimen. However, the assumptions in the proposed method were never all valid in the real case. Lin and Penumadu (2006) used digital image analysis technique to evaluate strain localization in combined axial-torsional tests. A numerical interpolation method was employed to obtain a continuous deformation field. The coefficients of displacement function were computed, based on the displacement of nodes. However, coordinate correction was not applied to calculate the displacements of nodes. Bhandari et al. (2012) built three dimensional geometry relations of the ray tracing by using three digital cameras for evaluating the local strains of sand specimen in triaxial test. In the implementation, local strains on radial and circumferential directions were assumed to be same with each other when calculating local volume strains. In addition, all the strains calculated were based on the movement of membrane, which might be not valid when slippage occurred between membrane and sand specimen. Moreover, since the coordinate correction program by taking account of image distortion was complicated, it might be not so applicable in other laboratories. Zhang et al. (2015) used a photogrammetry-based method to evaluate the volume changes of unsaturated sand specimen in triaxial test. Compared with the existing methods for measuring the volume changes, a high accuracy was obtained by the photogrammetry method. Shao et al. (2016) developed a digital image technique to plot the deformation distributions cross the entire surface of specimen in triaixal test. In order to eliminate the affection by distortion, a quadratic polynomial was used to correct the coordinates of measured corner points.

In general, most of the image-based analysis in drained tests assumed that there were no deformations on the radial direction, or the deformation on radial direction was same as the one on circumferential direction. Because the displacement parallel to the perpendicular line of camera lens could not be detected exactly. In fact, becoming shorter and thicker of specimen after compression or higher and thinner after extension would decrease and increase the distance between fixed camera and specimen surface. These complicated geometry conditions in triaxial test would affect the magnification of specimen in the image, which would have a significant influence on the image analysis results.

In the University of Tokyo, Hoshino et al. (2015) developed an image analysis technique in the undrained triaxial tests to evaluate the local deformations of specimen directly and indirectly. Through the transparent membrane, the sand particle patterns were used for the direction evaluation of local deformations, dots on membrane for the indirect evaluation. Meanwhile, another image-based local deformation evaluation program was developed in the undrained torsional shear test (Fauzi, 2015; Fauzi and Koseki, 2014). The vertical displacement was not allowed during undrained cyclic loading. Further, the cross section of specimen along specimen height was constant during shearing. Therefore, the distance between camera and specimen surface was not changed. The apparent coordinate obtained from the digital image directly was corrected by a ninth order polynomial. As for the coefficients of this ninth order polynomial, they were obtained by establishing the relations between the apparent and real coordinates when there were no deformations. However, these coefficients were not valid for computing the real coordinates of measured points when shear displacement of tracked point exceeded the boundary for coefficient calculation. Moreover, the direct evaluation of local deformation from sand particle is also needed in the undrained torsional shear test. The fact is that the coordinate correction method for dots on membrane is not suitable for the sand particle patterns which are located in different positions. Therefore, a new coordinate correction method for the indirect and direct evaluations of local deformation is needed in the undrained torsional shear test. In this chapter, the newly proposed coordinate correction method as well as the corresponding calibration tests will be introduced, respectively. Subsequently, the local strain calculation method will be explained in detail.

## 4.2 Scale and origin setting

As for photochrome, it consists of three colors, namely R, G and B, at one pixel. Meanwhile, there is a gray level of a black-and-white photograph. In the image analysis, the gray level is a key parameter used to track the movement of target point. In this study, there are 4912*7360 pixels in one photograph, which means 36152320 pixels with their corresponding gray levels combine into the photograph. Therefore, pixel is seen as a unit which can be used to measure the distance (pixels) between two targets. All the images sorted by taken time are loaded into the software Move-Tr2D. Before starting analyzing the digital images, the origin and scale from pixel to real distance between two dots on membrane are set in the first image without deformation. The origin of coordinate, coordinate axis and scale setting are shown in Fig. 4.1 and Fig. 4.2. All the pixel information will be converted into coordinate by distance. The origin is fixed by the pixels of digital image and it is not related with the specimen in the image. Therefore, the position of origin is fixed without considering the deformed specimen during loading. After computing, the resolutions in triaxial and torsional shear tests are around 0.025 mm/pixel and 0.05 mm/pixel, respectively.

## 4.3 Dots tracking

On the surface of membrane, dots are pasted by the interval of 5 mm on horizontal and vertical directions. The details of pasting dots on membrane have been introduced in chapter 2. The digital image before deformation is shown in Fig. 4.3 in which some target dots have been marked by squares. All the marked dots are selected manually before analyzing.

There are two main methods to track the movements of dots which have been introduced by Wahyudi (2014), Fauzi (2015) and Hoshino (2015). The first method is that the dot could be tracked by the center of ‘gravity’. As shown in Fig. 4.4(a), large difference of gray between dot and its surrounding transparent membrane make the detection of dot possible by setting a suitable threshold of gray. After the setting, the dots will be marked by green color, as well as other positions which have the same gray level of the dots. As shown in Fig. 4.4(b), the coordinates of dots are designed by the evaluating the central positon of each dot. The central position of each dot is obtained by the assumption that the dot is seen as a kind of plane with density. Then the center of gravity could be computed, which will be converted into the coordinate later.

The other one used in this study is tracking the gray pattern of dot. The pattern of dot will be recorded and compared with the dot in the followed images. For example, there are two squares in Fig. 4.4(a) with red and yellow colors. These two squares are set in advance when there is no deformation. The pattern of gray inside of the red square is recorded and the similar or same pattern will be searched inside of the yellow square in the next image. Therefore, the suitable searching square and strain interval of images are of significance to guarantee the possibility of image analysis.

Since the specimen is rotated as well as the one inside of the image, the number of dots intended to search on horizontal direction is required to be appropriate. If the single amplitude of shear strain is quite large, some tracked dots will disappear at the boundaries. In general, 16 columns and 60 rows of dots, located in the green square of Fig. 4.3, are tracked during loading when the single amplitude of shear strain is less than 10%. During the preparation of marking these dots, the marking order of each row should be started from left and the starting dot of each row need to be in the same column.

The coordinates of each tracked dots in every image will be obtained and could be saved. The local stains will be calculated and analyzed, which will be introduced later.

## 4.4 Sand particle patterns tracking

Since a transparent membrane is employed in this study, the sand particles could be seen clearly through it as shown in Fig. 4.6. Similarly, the gray pattern of sand particles in the red square is tracked and searched in the yellow square of next image. For convenience, there is only one tracked sand particle pattern in the four dots grid. As shown in Fig. 4.5, 15 columns and 60 rows of sand particle patterns are tracked totally. The coordinates of each sand particle patterns will be obtained and saved for the calculation of local strains.

## 4.5 Coordinates correction

As is known, a photograph will record three dimensions information of an object by the two dimensions plane in which the information paralleling to perpendicular of the 2D plane will be lost. Due to the curvature of specimen, refraction of different materials (water, plastic cell and air) and other factors, a suitable coordinate correction method will decide the validity of derived results. The apparent coordinate without correction is shown in Fig. 4.7(a). In the figure, the cylindrical shape of specimen is distorted while the distances between adjacent dots are changing along the surface of specimen. It is confirmed that the real distance between adjacent dots is 5 mm. Therefore, the real coordinates of each dot are shown in Fig. 4.7(b). There should be a bridge to connect the apparent coordinates without correction and real coordinates. Moreover, the dots after deformation may be located in the grid of four dots. Sand particle patterns are also located in the grids of dots. An effective interpolation method in each element (including four dots) has been applied to the analysis.

### 4.5.1 Development of coordinate correction

The coordinate correction is the basis of image analysis, especially on the analysis of curvature object. Unlike the image analysis in plane strain compression test, the plane condition eliminates the affection of curvature distortion. In the triaxial test, the deformation of tracked points at the surface of specimen is limited. Large amount of displacement is on the vertical direction and the corresponding horizontal strain is relatively small. Under such circumstance, a lot of coordinate correction methods have been employed into the triaxial tests by previous researches (Lin and Penumadu, 2006; Macari et al., 1997; Shao et al., 2016; Zhang et al., 2015).

In the torsional shear test, the hollow cylindrical specimen is rotated as well as the one in the images. Being different from the condition in triaxial test, the curvature of specimen on horizontal direction will affect the results largely. This distortion in the image is more complicated than the status in triaxial test.

Recently, large amount of efforts has been made on the coordinate correction of torsional shear test in the University of Tokyo. Wahyudi et al. (2014) has proposed the coordinate method by introducing a parabola function (equation 4-1), by which the apparent coordinate without correction could be converted into real coordinates. In addition, Fauzi et al. (2015) also has developed a similar coordinate correction method by a ninth order polynomial (equation 4-2). There are some drawbacks in the two proposed method. Firstly, the coefficients of each equation are obtained by the substitution of the real coordinates and apparent coordinate before deformation. For Wahyudi's method, even though there is one equation for each row, the dots in the row would move to the other positions where the obtained coefficients will be not suitable anymore after deformation. For the method proposed by Usama, the coordinates of all the points (near 1000 tracked dots) are substituted into the ninth order polynomial which is not accurate enough. In addition, the real y coordinate of dot in each row is from the apparent y coordinate of central dot of each row, which is not reflecting the real y coordinate. Another drawback of these two method is that the results are not reliable after the tracked dots exceed the boundaries of the dots region, which is used to obtain the coefficients of the ninth order polynomial.

$$x_i' = a_{0i} + a_{1i}x_i + a_{2i}y_j + a_{3i}x_i^{2} + a_{4i}x_i y_j + a_{5i}y_j^{2}$$

$$y_j' = b_{0j} + b_{1j}x_i + b_{2j}y_j + b_{3j}x_i^{2} + b_{4j}x_i y_j + b_{5j}y_j^{2} \qquad (4\text{-}1)$$

in which,

$x_i, y_j$ are the apparent coordinates of target dot.

$x_i', y_j'$ are the real coordinates of garget dot.

$a_{0i}$ through $a_{5i}$ and $b_{0i}$ through $b_{5i}$ are the coefficients obtained by fitted parabola function of the dots before deformation.

$i$ and $j$ are the indices of column and row, respectively.

$$\begin{aligned} x_{i,j}' &= a_0 + a_1.x_{i,j} + a_2.y_{i,j} + a_3.x_{i,j}^{2} + a_4.x_{i,j}.y_{i,j} + a_5.y_{i,j}^{2} + a_6.x_{i,j}^{3} + a_7.x_{i,j}^{2}.y_{i,j} + a_8.x_{i,j}.y_{i,j}^{2} \\ &\quad + a_9.y_{i,j}^{3} ... + a_{45}.x_{i,j}^{9} + .... + a_{54}.y_{i,j}^{9} \end{aligned}$$

$$\begin{aligned} y_{i,j}' &= b_0 + b_1.x_{i,j} + b_2.y_{i,j} + b_3.x_{i,j}^{2} + b_4.x_{i,j}.y_{i,j} + b_5.y_{i,j}^{2} + b_6.x_{i,j}^{3} + b_7.x_{i,j}^{2}.y_{i,j} + b_8.x_{i,j}.y_{i,j}^{2} \\ &\quad + b_9.y_{i,j}^{3} ... + b_{45}.x_{i,j}^{9} + .... + b_{54}.y_{i,j}^{9} \end{aligned} \qquad (4\text{-}2)$$

Where,

$x_{i,j}'$ and $y_{i,j}'$ are the real coordinates of target dot.

$x_{i,j}$ and $y_{i,j}$ are the apparent coordinates of target dot.

$i$ and $j$ are the indices of column and row, respectively.

### 4.5.2 Correction of camera inclination

Since the position of camera could not be perfectly set in front of the cell. There may be little inclination of the specimen in the image. Additionally, the dots of each column also may not be vertical. Therefore, the inclination is corrected by the following equation:

$$\begin{bmatrix} x \\ y \end{bmatrix} = \begin{bmatrix} \cos\theta & -\sin\theta \\ \sin\theta & \cos\theta \end{bmatrix} \begin{bmatrix} x' \\ y' \end{bmatrix} \qquad (4\text{-}3)$$

where $x$, $y$ and $x'$, $y'$ are the apparent and real coordinates of target dot, respectively. $\theta$ is the gradient angle as shown in Fig. 4.8 for the inclination correction. As introduced in the above section, 16 columns are tracked during the shear loading. Then the central column is selected to obtain the inclination angle of the specimen in image.

### 4.5.3 Proposed coordinates correction

A new coordinate correction method has been developed by author without using fitting equations. As is known, all the dots are following a rigid grid with a standard interval of 5 mm before pasting on the membrane. It means that the apparent coordinates of dots after correction could be expanded into the plane condition. As shown in Fig. 4.9, all the coordinate of dots before deformation are satisfying the rigid grid with 5 mm interval after an appropriate coordinate correction.

Since the height of specimen is kept constant during the cyclic shearing after consolidation, it is assumed that the specimen is sheared by a constant cylindrical shape without radial deformation in undrained condition. Based on the comparison between apparent and real coordinates shown in Fig. 4.9, a sole relationship between the apparent and real coordinates of each grid is developed. There are around 2000 grids and corresponding relationships totally, which include almost all the dots seen in the image. The image before testing will be named as reference image, while the region marked by black rectangle in Fig. 4.9 is named by reference region. Since the specimen will be sheared in the test, the dots only in the red rectangle will be tracked to measure the local deformation of specimen. The tracked dots or sand particle patterns in this region could not move out of the reference region during consolidation and shearing when a proper single amplitude of shear strain is set.

The tracked dots and sand particle patterns will be sheared and move to other positions in the reference region. Since the shape of specimen is kept, the tracked target will be located in the other girds inside of the reference region. The real and apparent coordinates of four dots of each grid are already known. Therefore, the real coordinates of the tracked target could be obtained by the bi-linear interpolation method through the real and apparent coordinates of four nearest dots. The schematic diagrams are shown in Fig. 4.7. The red point is the tracked target, whose real coordinates could be obtained by its own apparent coordinates (from software directly) and the real and apparent coordinates of four nearest dots. The tracked targets could be the tracked dots and sand particle patterns in the red rectangle shown in Fig. 4.9. The procedure of computing the real coordinates of target dot/sand particle pattern is shown in Fig. 4.10. The bi-linear interpolation method for the real coordinates of target point is expressed by the following equations.

$$f_1(x) = \frac{(x_2 - x_0)\times x_1^r}{(x_2 - x_1)} + \frac{(x_0 - x_1)\times x_2^r}{(x_2 - x_1)} \quad (4\text{-}4)$$

$$f_2(x) = \frac{(x_3 - x_0)\times x_4^r}{(x_3 - x_4)} + \frac{(x_0 - x_4)\times x_3^r}{(x_3 - x_4)} \quad (4\text{-}5)$$

$$f_1(y) = \frac{(x_2 - x_0)\times y_1}{(x_2 - x_1)} + \frac{(x_0 - x_1)\times y_2}{(x_2 - x_1)} \quad (4\text{-}6)$$

$$f_2(y) = \frac{(x_3 - x_0)\times y_4}{(x_3 - x_4)} + \frac{(x_0 - x_4)\times y_3}{(x_3 - x_4)} \quad (4\text{-}7)$$

$$f_3(y) = \frac{(x_2 - x_0)\times y_1^r}{(x_2 - x_1)} + \frac{(x_0 - x_1)\times y_2^r}{(x_2 - x_1)} \quad (4\text{-}8)$$

$$f_4(y) = \frac{(x_3 - x_0) \times y_4^r}{(x_3 - x_4)} + \frac{(x_0 - x_4) \times y_3^r}{(x_3 - x_4)} \quad (4\text{-}9)$$

$$x_0^r = \frac{[f_2(y) - y_0] \times f_1(x)}{[f_2(y) - f_1(y)]} + \frac{[y_0 - f_1(y)] \times f_2(x)}{[f_2(y) - f_1(y)]} \quad (4\text{-}10)$$

$$y_0^r = \frac{[f_2(y) - y_0] \times f_3(y)}{[f_2(y) - f_1(y)]} + \frac{[y_0 - f_1(y)] \times f_4(y)}{[f_2(y) - f_1(y)]} \quad (4\text{-}11)$$

In which, $(x_0, y_0)$ and $(x_0^r, y_0^r)$ are the apparent and real coordinates of tracked dot or sand particle pattern, respectively. As shown in Fig. 4.7, $(x_1, y_1)$, $(x_2, y_2)$, $(x_3, y_3)$ and $(x_4, y_4)$ are the apparent coordinates of the four nearest dots in the reference image by anti-clockwise direction. Meanwhile, $(x_1^r, y_1^r)$, $(x_2^r, y_2^r)$, $(x_3^r, y_3^r)$ and $(x_4^r, y_4^r)$ are the corresponding real coordinates of these four nearest dots. Each tracked point will follow the above process in every image taken during the test.

Therefore, by comparing the data of tracked points between target image and reference image, the displacement components of each could be computed by the corrected real coordinates. Without fitting equations, the proposed coordinate correction method eliminates the drawbacks mentioned in the previous methods. In addition, this method is working well and its calibration test will be introduced in next section.

## 4.6 Calibration of correction method

### 4.6.1 Theoretical analysis of bi-linear interpolation method

Due to the complex spatial locations between specimen surface and camera, an effective coordinate correction algorithm is the foundation of local deformation analysis. By supposing that camera is modeled as a pinhole, Fig. 4.11 and 4.12 present two schematic diagrams of the specimen-camera setup, which include the geometrical perspectives of the pinhole camera and specimen from vertical and horizontal views.

During the test, the pinhole camera is placed perfectly passing through the center of specimen. Since the ray from specimen to camera lens is refracted twice through the two interfaces, only two planes have the properties that all the rays and its refracted rays could stay in the same plane. Plane (1) is the horizontal plane shown in Fig. 4.13 passing through the middle height of specimen and it has the same height with camera. Plane (2) is the mid-perpendicular plane of specimen from camera. As for the non-plane conditions of ray and its refraction, it is still a challenge to obtain the coordinate relations theoretically. These two special planes are selected to search for the possibility of applying proposed method.

Since the camera faces the central position of specimen, the distortion effect in the image should be symmetrical about the central horizontal line and mid-perpendicular line of specimen, respectively. In the equations from (4-12) to (4-16), the indices of refractions of light in the materials are assumed to be $n_1 = 1$ (air), $n_2 = 1.49$ (cell) and $n_3 = 1.33$ (water) (Jenkins and White, 1976). Based on Snell's law and the geometrical relations of angles shown in Fig. 4.11, there is a sole relationship between $\gamma$ ($0 \le \gamma \le 0.8rad$) and $\alpha$.

$$\angle OBA = \pi - \arcsin(\frac{L_o}{R_1}\sin\alpha) \quad (4\text{-}12)$$

$$\angle OBC = \arcsin(\frac{n_1}{n_2} \times \frac{L_o}{R_1}\sin\alpha) \quad (4\text{-}13)$$

$$\angle OCB = \pi - \arcsin(\frac{n_1}{n_2} \times \frac{L_o}{R_2}\sin\alpha) \quad (4\text{-}14)$$

$$\angle OCD = \arcsin(\frac{n_1}{n_3} \times \frac{L_o}{R_2} \times \sin\alpha) \quad (4\text{-}15)$$

$$\angle ODC = \pi - \arcsin(\frac{n_1}{n_3} \times \frac{L_o}{R_3}\sin\alpha) \quad (4\text{-}16)$$

$$\Delta OAB + \Delta OBC + \Delta OCD = 3\pi \quad (4\text{-}17)$$

Based on the above equations, the sole relationship between $\gamma$ ($0 \le \gamma \le 0.8rad$) and $\alpha$ is confirmed. However, it is a tough calculation to get the explicit formula of $\gamma$. Herein, around ninety points are selected by 0.1 rad of $\gamma$ increasing from 0 rad to 0.85 rad, which satisfies the real conditions of angle $\gamma$. A quadratic polynomial ($\alpha = -0.1283\gamma^2 + 0.4423\gamma - 0.0027$) is obtained with the R-square of 0.9999 and shown in Fig. 4.14.

In the Fig. 4.11, $\theta$ and $\beta$ ($\theta + \beta = 0.5rad$) are the angles between tracked points and its adjacent dots on horizontal direction in reference image when tracked point locates in one grid of reference image. After achieving the apparent coordinates of track point, the validity of proposed calculation method for real coordinates could be proved properly. Even though the rigid grid is twisted into a cylindrical shape, the ratio of arc *a* over arc *b* is equal to their corresponding length ratio in the grid. However, only the length ratio *c* over *d* could be obtained from the distorted image as shown in Fig. 4.15. The x coordinate of red tracked point could be computed by the following equations:

$$x^r = \frac{a}{a+b} \times x_B + \frac{b}{a+b} \times x_A \quad (4\text{-}18)$$

$$x_c^r = \frac{c}{c+d} \times x_B + \frac{d}{c+d} \times x_A \quad (4\text{-}19)$$

where,

$x^r$: the real x coordinate of tracked point.

$x_c^r$: the x coordinate of track point after correction.

$x_A$ and $x_A$ : the real x coordinates of neighboring dots.

$$x_c^r - x^r = (x_B - x_A)(\frac{c}{c+d} - \frac{a}{a+b}) \quad (4\text{-}20)$$

It should be noted that not only the dots at the top part but also those at the bottom are considered in the proposed calculation method by using bi-linear interpolation.

In the special horizontal plane, one assumption for applying bi-linear interpolation method is that the ratio of arc *a* over the total arc of *a* and *b* could be replaced by the ratio of the length of line segment *c* over the total length *c* and *d*, including the distortion of camera lens. Clearly, these two ratios could not be same with each other except for the locations when the tracked point overlaps one of the nearest four dots in reference image. Therefore, it is necessary to calculate the potential error induced by this difference. The calculated horizontal error induced by using the above replacement could be obtained by equation (4-21). Base on the geometrical relations in Fig. 4.11, the lengths of line segments *c* and *d* as well as the arc *a* and *b* could be replaced by $\gamma$, $\theta$ and $\beta$.

$$\varepsilon_{error}^{horizontal} = \frac{\frac{c}{c+d} - \frac{a}{a+b}}{\frac{a}{a+b}} \quad (4\text{-}21)$$

In Fig. 4.16, the errors from this replacement of local proportions on horizontal direction vary with the value of $\gamma$, $\theta$ and $\beta$. The maximum of this error is around 2.5% when $\gamma$ reaches 0.8 rad (the boundary area of specimen in the image).

The proportion replacement has been discussed above, which is just a coefficient during the local deformation calculation. The final target of this study is about the displacement and strain. The induced error of displacement could be computed by:

$$\eta_{error}^{horizontal} = \frac{x_c^r - x^r}{x^r} = (x_B - x_A)(\frac{\frac{c}{c+d} - \frac{a}{a+b}}{x^r}) = f(\theta, \gamma) \quad (4\text{-}22)$$

The result of displacement error is shown in Fig. 4.17. The maximum error for rotation displacement is around 0.6% when the tracked target is located at the center of the central grid in the reference image. It could be concluded that the accuracy calculated from plane (1) satisfies the requirement of current study.

Similarly, based on Snell's law, the relations among $\alpha_1$, $\alpha_2$ and $\alpha_3$ in Fig. 4.12 are expressed by equation (4-23). Around sixty points are selected for calculating the relation of y (0 <y<150 mm) and $\alpha_1$. As shown in Fig. 4.18, a linear equation, $\tan\alpha_1 = 3.7139y - 0.0019$, is obtained with the R-square of 1 by equation (4-24). Therefore, a sole relationship between *y* and $\alpha_1$ is built. In Fig. 4.19, the *y* coordinate of tracked point in the grid of four nearest dots could be computed by equations (4-25) and (4-26).

$$n_1 \sin \alpha_1 = n_2 \sin \alpha_2 = n_3 \sin \alpha_3 \quad (4\text{-}23)$$

$$y = (R_2 - R_3) \times \tan \alpha_3 + (R_1 - R_2) \times \tan \alpha_2 + (L_o - R_1) \times \tan \alpha_1 \quad (4\text{-}24)$$

$$y_r = \frac{e}{e+f} \times y_D + \frac{f}{e+f} \times y_B \quad (4\text{-}25)$$

$$y_c^r = \frac{g}{g+h} \times y_D + \frac{h}{g+h} \times y_B \quad (4\text{-}26)$$

$$y_c^r - y^r = (y_B - y_D)(\frac{h}{g+h} - \frac{f}{e+f}) \quad (4\text{-}27)$$

$$\varepsilon_{error}^{vertical} = \frac{\frac{h}{h+g} - \frac{f}{f+e}}{\frac{f}{f+e}} \quad (4\text{-}28)$$

During using bilinear interpolation method on vertical direction, the length ratio of line segments *f* over (*f*+*e*) need to be replaced by the ratio of line segments *h* over (*h*+*g*). Fortunately, these two ratios are always same as each other. The calculated vertical error by the replacement of local proportion is always zero by equation (4-28) at the mid-perpendicular plane of specimen.

Based on the results from above analysis, the errors of those replacements, affected by the refractions at two interfaces between atmosphere, cell and water, are less than 3% both on horizontal and vertical directions. Even these errors are obtained from the two special planes, they provide the possibility of proposed coordinate correction method by bi-linear interpolation. In order to obtain the errors at other positions on specimen surface, a verification test is conducted to confirm the validity of proposed method.

### 4.6.2 Calibration tests

Being different from the above theoretical analysis on two special planes, one model designed by a twisted plastic plate is employed in the verification test, which has the same size as the specimen used in the liquefaction tests. Besides, no sand is filled into the model and the model is suspended in the cell which will be filled with water during the calibration test. Similar to the ordinary torsional shear test, the model could be rotated freely without any local deformations. The cylindrical shape of the plastic model is kept constant during the test. In addition, the top cap beneath the load cell could hold the model stably during rotation. This condition is almost same as the one set in the liquefaction test, in which the vertical displacement is not allowed and the cylindrical shape is kept. As shown in Fig. 4.20, black dots are pasted on the surface of model for later tracking and reference. After filling water in the cell, the loading speed is controlled equally to the ordinary torsional shear test of sand specimen. If the model is rotated directly, the black dots would follow horizontal rotation only, which will have the same height as the dots in the reference image. In the real case of torsional shear, specimen would be subjected to consolidation before shearing. Furthermore, the sand particle patterns will be tracked in the liquefaction test, which are located in the grids of reference image. For satisfying these requirement and find the maximum potential errors of interpolation, the model, which moves downward firstly by 2-3 millimeter, would make the tracked dots locate at the center area of each grid.

In this study, two calibration tests were conducted and only one of them will be introduced in this section. Firstly, the model moved downward by 2.5 mm. then it started rotation while the vertical displacement of top cap was not allowed during the calibration test. In Fig. 4.21, the apparent coordinates of dots in the black rectangle were obtained before rotation and their real coordinates were computed. Meanwhile, the relationship between the real and apparent coordinates of each dot in the black rectangle was established. The dots in the red rectangle were tracked and their apparent coordinates at each image could be computed by Move-Tr2D.

### 4.6.3 Evaluation of the correction method

Three positions in Fig. 4.21 marked by solid black square, red circle and blue triangle were selected for the comparison of displacements, respectively. In Fig. 4.22 (a) and (b), the time histories of the displacements from three positions on y direction during moving down and rotation are shown before and after the coordinate correction. Different positions on the surface of specimen will be subjected to different distortion processes even under the same rotation. Therefore, these three position also have suffered different distortion processes, the apparent coordinates of them demonstrate large errors by the fact that these points should have the same displacement as measured by EDT.

The point which locates at the red circle region is subjected to the similar displacement on y direction as measured by EDT. The possible reason of this phenomenon is that the camera is set at the same height of this region. The distortion affect may be smaller than other positions. Moreover, after coordinate correction, the curves of displacement on y direction from these three points overlap the displacement curve measured by EDT as shown in Fig. 22(b). Importantly, these curves behave stably even under large rotation displacement.

In terms of x coordinates shown in Fig. 4.23 (a) before coordinate correction, the different displacements among the three points and the one measured by potentiometer are relatively small when the rotation displacement is less than 15 mm. on the other hand, large gaps between each of them are increasing with the rotation displacement. The maximum difference is larger than 7 mm. After the correction of the coordinate on x direction shown in

Fig. 23 (b), the curves of the three points are coincident perfectly. However, there is still a gap between the displacements measured by potentiometer and image. Since the potentiometer is attached on the load shaft which has a diameter of 4 cm, the displacement from potentiometer in Fig. 4.23 (b) is enlarged by the ratio of the diameter of specimen over the load shaft. Meanwhile, the errors on the rotation displacement from potentiometer will be enlarged by the same ratio (5 times). Therefore, the amount of this gap increases quantitatively with the rotation displacement, which may be affected by the accuracy of potentiometer and the diameter of plastic model. The overlap of these three curves proves that proposed coordinate correction method works well currently.

Except for the above calibration test, another verification of this proposed coordinate correction method is introduced. Fig. 4.24(a) shows the schematic diagram of reference setting and the region of dots which will be tracked. Correspondingly, the real photo of these setting is shown in Fig. 4.24(b). All the dots tracked during test are situated in the red square before rotation. The black square is the reference region where the tracked dots may move in during rotation. The intervals of dots are perfectly 5 mm when they are expanded into plane condition. Moreover, one target of this correction method is transforming the cylindrical shape of specimen surface into plane condition. Nine positions shown in Fig. 4.24 from A to I are selected to show the calculated intervals of the neighboring dots (5 mm), respectively. In order to describe the details of these nine selected positions with horizontal and vertical two neighboring dots clearly, the widths of reference region and the region for tracked dots in schematic diagram are expanded when compared with those in the real photo. All positions except for position E have the large potential to reach the boundary area of black rectangle (reference region) where is seriously distorted. Based on the results of Fig. 4.16, these distorted areas will increase the calculation errors of proposed method.

Taking position A as an example, the two neighboring dots on horizontal and vertical directions are represented by $AA_1$ and $AA_2$, respectively. Due to the refractions and geometric relationships between specimen and camera, $AA_1$, $AA_2$ and dots in other regions would be subjected to different distortion processes during rotation. The calculated intervals of two neighboring dots from these nine positions are presented in Fig. 4.25 on horizontal and vertical directions, respectively. In Fig. 4.25 (a) through (c), the intervals on horizontal direction after coordinate correction keep constant value of 5 mm with a limited fluctuation less than 0.2 mm, even though the tracked points approach the boundary of reference region with largest distortion. On the other hand, the vertical intervals of nine positions, as shown in Fig. 4.25 (d) through (f), remain 5 mm stably with a fluctuation which is less than 0.1 mm. In addition, the model is rotated and the dots on the surface move horizontally. The dots tracked on the same height may pass through the same grids in the reference image. Based on the curves in Fig. 4.25, the intervals of tracked dots at the same height have the same fluctuation trend when they pass through the same positions in the reference image during rotation.

For the detection of tracked dots in this calibration test, the coordinates of each dot are evaluated by the center of gravity which has been introduced in the dot tracking section. It should be noted that the diameter of dot is 1 mm accounting for 1/5 of the interval and the shape of circular dot could not keep constant during rotation at different positions as shown in Fig. 4.26. By recognizing this phenomenon, small fluctuation in Fig. 4.25 could be understood easily. Additionally, the sharp increasing and decreasing of fluctuation curves maybe affected by some other inevitable factors such as camera lens, software, brightness and so on.

During the downward displacement and rotation, 922 photos were taken totally, which means there were 922 points in each curve of measured interval shown in Fig. 4.25. In order to learn more about the measured interval, the normal distribution of each curve is plotted and analyzed. The normal distribution curve of the interval of the two vertical neighboring dots in position B is shown in Fig. 4.27. The one for two horizontal neighboring dots is plotted in Fig. 4.28. The parameters of the normal distributions of all the intervals at ninth positions are summarized in Table 4.1 and Table 4.2. The maximum error of mean value on vertical neighboring dots is less than 0.05 mm, while the maximum error for horizontal neighboring dots is less than 0.1 mm.

In Fig. 4.29, all the photos taken during test are separated by vertical displacement and different amplitudes of shear strains. Being similar as the analysis above, the normal distributions of intervals at different stages of displacement are analyzed and the parameters of these normal distributions are shown in Fig. 4.30. The results obtained from vertical direction are more accurate than those from horizontal direction.

It should be noticed that the above discussion focused on the calculated interval of two neighboring dots. The relative movement of two different dots, especially at a large interval, is another important parameter to verify the proposed method. For example, two points at positions D and F are selected to calculate the relative movement to the dot at position E, respectively. As expected, the results in Fig. 4.31 indicate that the maximum relative movements to the reference point in position E on x and y directions are less than 0.2 mmm even the rotation displacement is approaching to 100 mm. Based on this, the errors from these total displacement calculations of tracked dots are less than 0.2%. In addition, another two points at positions B and H are also selected to calculate the relative movement to the dot at position E, respectively. The results in Fig. 4.32 shows that the relative movements to the reference point 457 on horizontal direction are slightly larger than those on the vertical direction. The maximum relative movements are less than 0.4 mm, by which the calculation errors will be less than 0.4%.

In order to confirm the relative movements to point 457 at position E along the model surface, sixty points are selected at different heights of model. The maximum relative movement to point 457 on x direction is less than 0.4 mm. The results in Fig. 4.33 demonstrate that the proposed method is valid for the calculation on the displacement.

The proposed coordinate correction method separates the surface of specimen into around 2000 regions and builds the corresponding independent relationships. By utilizing the same apparent coordinates obtained in one torsional shear test, the comparison of the results between this new coordinate correction method and the one proposed by Usama is shown in Fig. 4.34. It solves the defects mentioned above and could be used for tracking the movement of sand particles directly through the transparent membrane.

## 4.7 Strain calculations

The basic mechanism of strain calculation is shown in Fig. 4.35, in which the displacements of each point on vertical and horizontal directions could be computed by their coordinates after correction. Based on this calculation, only the average strains (vertical, horizontal and shear) are obtained. If the size of element is large, the local strains inside the element maybe not homogeneous and the average strains could not represent the deformation behaviors of the element. The interpolation and shape functions are introduced to compute the strains inside of the element.

### 4.7.1 Interpolation functions

The actual quadrilateral element of neighboring four dots in the global Cartesian coordinate system is shown in Fig. 4.36(a), in which the displacements and order of each dot have been marked. In order to conduct the iso-parametric mapping, this element will be mapped into the element in the local natural coordinate system as shown in Fig. 4.36(b). The linear element is considered to obtain the shape functions for the mapping from (*x*, *y*) coordinate system to ($\xi$, $\eta$) coordinate (Ergatoudis et al., 1968; Huebner et al., 2008).

The shape function for linear element by Lagrange interpolation formula,

$$N_1 = \frac{1}{4}(1-\xi)(1-\eta) \quad (4\text{-}29)$$

$$N_2 = \frac{1}{4}(1+\xi)(1-\eta) \quad (4\text{-}30)$$

$$N_3 = \frac{1}{4}(1+\xi)(1+\eta) \quad (4\text{-}31)$$

$$N_4 = \frac{1}{4}(1-\xi)(1+\eta) \quad (4\text{-}32)$$

They can be expressed by,

$$N_i = \frac{1}{4}(1+\xi\xi_i)(1+\eta\eta_i) \qquad (4\text{-}33)$$

where, $\xi_i$ and $\eta_i$ take their nodal values in local natural coordinate system. Therefore, the point (x, y) in Fig. 3.36(a) can be computed by,

$$x = N_1x_1 + N_2x_2 + N_3x_3 + N_4x_4 = \sum_{i=1}^{4} N_i x_i \qquad (4\text{-}34)$$

$$y = N_1y_1 + N_2y_2 + N_3y_3 + N_4y_4 = \sum_{i=1}^{4} N_i y_i \qquad (4\text{-}35)$$

In quadrilateral element derivations, the Jacobian of two-dimensional transformations is needed to connect the differentials of (x, y) to those of ($\xi, \ \eta$) and vice-versa (Felippa, 2001). By the chain rule, we can get,

$$\begin{bmatrix} dx \\ dy \end{bmatrix} = \begin{bmatrix} \frac{\partial x}{\partial \xi} & \frac{\partial x}{\partial \eta} \\ \frac{\partial y}{\partial \xi} & \frac{\partial y}{\partial \eta} \end{bmatrix} \begin{bmatrix} d\xi \\ d\eta \end{bmatrix} = J^T \begin{bmatrix} d\xi \\ d\eta \end{bmatrix} \qquad (4\text{-}36)$$

$$\begin{bmatrix} d\xi \\ d\eta \end{bmatrix} = \begin{bmatrix} \frac{\partial \xi}{\partial x} & \frac{\partial \xi}{\partial y} \\ \frac{\partial \eta}{\partial x} & \frac{\partial \eta}{\partial y} \end{bmatrix} \begin{bmatrix} dx \\ dy \end{bmatrix} = J^{-T} \begin{bmatrix} dx \\ dy \end{bmatrix} \qquad (4\text{-}37)$$

Where $J$ denotes Jacobian matrix of (x, y) with respect to ($\xi, \ \eta$), whereas $J^{-1}$ is the Jacobian matrix of ($\xi, \ \eta$) with respect to (x, y):

$$J = \frac{\partial(x,y)}{\partial(\xi,\eta)} = \begin{bmatrix} \frac{\partial x}{\partial \xi} & \frac{\partial y}{\partial \xi} \\ \frac{\partial x}{\partial \eta} & \frac{\partial y}{\partial \eta} \end{bmatrix} = \begin{bmatrix} J_{11} & J_{12} \\ J_{21} & J_{22} \end{bmatrix} = \begin{bmatrix} \sum_{i=1}^{4} \frac{\partial N_i}{\partial \xi} x_i & \sum_{i=1}^{4} \frac{\partial N_i}{\partial \xi} y_i \\ \sum_{i=1}^{4} \frac{\partial N_i}{\partial \eta} x_i & \sum_{i=1}^{4} \frac{\partial N_i}{\partial \eta} y_i \end{bmatrix} \qquad (4\text{-}38)$$

$$J^{-1} = \frac{1}{|J|} \begin{bmatrix} J_{22} & -J_{12} \\ -J_{21} & J_{11} \end{bmatrix} \qquad (4\text{-}39)$$

In terms of natural coordinates ($\xi, \ \eta$), the derivatives of shape function with respect to x and y are given by chain rule:

$$\begin{bmatrix} \frac{\partial N_i}{\partial x} \\ \frac{\partial N_i}{\partial y} \end{bmatrix} = \begin{bmatrix} \frac{\partial \xi}{\partial x} & \frac{\partial \eta}{\partial x} \\ \frac{\partial \xi}{\partial y} & \frac{\partial \eta}{\partial y} \end{bmatrix} \begin{bmatrix} \frac{\partial N_i}{\partial \xi} \\ \frac{\partial N_i}{\partial \eta} \end{bmatrix} = J^{-1} \begin{bmatrix} \frac{\partial N_i}{\partial \xi} \\ \frac{\partial N_i}{\partial \eta} \end{bmatrix} \qquad (4\text{-}40)$$

Since the shape function of determining coordinates (x, y) is same with the one for the displacements (u, v), the field function $\phi(u,v)$ for displacement could be obtained by,

$$\phi(u,v) = \sum_{i=1}^{4} N_i(\xi,\eta)\phi_i \qquad (4\text{-}41)$$

where,

$\phi_i = (u_i, v_i)$ is independent of the coordinates (x, y).

$u_i$ and $v_i$ take the nodal values in global Cartesian coordinate system.

$$\frac{\partial \phi}{\partial x} = \sum_{i=1}^{4} \frac{\partial N_i}{\partial x} \phi_i \quad (4\text{-}42)$$

$$\frac{\partial \phi}{\partial y} = \sum_{i=1}^{4} \frac{\partial N_i}{\partial y} \phi_i \quad (4\text{-}43)$$

The equations (4-42) and (4-43) can be expressed as,

$$\begin{bmatrix} \frac{\partial \phi}{\partial x} \\ \frac{\partial \phi}{\partial y} \end{bmatrix} = \begin{bmatrix} \frac{\partial N_1}{\partial x} & \frac{\partial N_2}{\partial x} & \frac{\partial N_3}{\partial x} & \frac{\partial N_4}{\partial x} \\ \frac{\partial N_1}{\partial y} & \frac{\partial N_2}{\partial y} & \frac{\partial N_3}{\partial y} & \frac{\partial N_4}{\partial y} \end{bmatrix} \begin{bmatrix} \phi_1 \\ \phi_2 \\ \phi_3 \\ \phi_4 \end{bmatrix} (4\text{-}44)$$

By substituting equation (4-40) to equation (4-44), we can get,

$$\begin{bmatrix} \frac{\partial \phi}{\partial x} \\ \frac{\partial \phi}{\partial y} \end{bmatrix} = [J]^{-1} \begin{bmatrix} \frac{\partial N_1}{\partial \xi} & \frac{\partial N_2}{\partial \xi} & \frac{\partial N_3}{\partial \xi} & \frac{\partial N_4}{\partial \xi} \\ \frac{\partial N_1}{\partial \eta} & \frac{\partial N_2}{\partial \eta} & \frac{\partial N_3}{\partial \eta} & \frac{\partial N_4}{\partial \eta} \end{bmatrix} \begin{bmatrix} \phi_1 \\ \phi_2 \\ \phi_3 \\ \phi_4 \end{bmatrix} \quad (4\text{-}45)$$

### 4.7.2 Strain calculations

As mentioned above, the field function $\phi(u,v)$ for displacement is a combination of u(x, y) and v(x, y). The displacements of any point inside of the element could be computed by the shape functions. As for the horizontal and vertical displacements (u, v), each of them is a function of (x, y). Then,

$$\{\phi(u,v)\} = \begin{Bmatrix} u(x,y) \\ v(x,y) \end{Bmatrix} \quad (4\text{-}46)$$

The strains (horizontal, vertical and shear) could be computed by,

$$\varepsilon_x = -\frac{\partial u}{\partial x} \quad (4\text{-}47)$$

$$\varepsilon_y = -\frac{\partial v}{\partial y} \quad (4\text{-}48)$$

$$\gamma_{xy} = -(\frac{\partial u}{\partial y} + \frac{\partial v}{\partial x}) \quad (4\text{-}49)$$

or they can be expressed by matrix:

$$\begin{bmatrix} \varepsilon_x \\ \varepsilon_y \\ \gamma_{xy} \end{bmatrix} = -\begin{bmatrix} \frac{\partial}{\partial x} & 0 \\ 0 & \frac{\partial}{\partial y} \\ \frac{\partial}{\partial y} & \frac{\partial}{\partial x} \end{bmatrix} \begin{bmatrix} u \\ v \end{bmatrix} \quad (4\text{-}50)$$

The displacement functions u and v are also a kind of field function as $\phi(u,v)$. By combining equations (4-45) and (4-50), we can get:

$$\begin{bmatrix} \frac{\partial u}{\partial x} & \frac{\partial v}{\partial x} \\ \frac{\partial u}{\partial y} & \frac{\partial v}{\partial y} \end{bmatrix} = [J]^{-1} \begin{bmatrix} \frac{\partial N_1}{\partial \xi} & \frac{\partial N_2}{\partial \xi} & \frac{\partial N_3}{\partial \xi} & \frac{\partial N_4}{\partial \xi} \\ \frac{\partial N_1}{\partial \eta} & \frac{\partial N_2}{\partial \eta} & \frac{\partial N_3}{\partial \eta} & \frac{\partial N_4}{\partial \eta} \end{bmatrix} \begin{bmatrix} u_1 & v_1 \\ u_2 & v_2 \\ u_3 & v_3 \\ u_4 & v_4 \end{bmatrix} \quad (4\text{-}51)$$

Based on the image analysis which has been introduced, the coordinates of tracked dots or sand particle patterns could be corrected at each image. Therefore, their displacements referring to the first image (without deformation) could be computed. As explained above, the coordinates and strains of any point inside of the grid could be obtained easily. In addition, the linear element in local natural coordinate system is suitable for all grids during analysis. MATLAB has been employed to run this calculation method. It should be noted that the order of four dots/sand particle patterns starts from left bottom to the left upper by counterclockwise direction. For convenience, the strains of the center position of each grid are selected to represent the strains of the grid (element), which means that $(\xi,\eta)$ should be (0, 0) in the shape function.

As introduced at the beginning of this section, the average strains of each grid also can be computed by the coordinates and displacements of the four nodes (dots/sand particle pattern). The local strain distributions from dots of one test when the academic shear strain is around -3.7% are shown in Fig. 4.37 by these two methods. The results indicate that the strains are almost same with each other, which proves the validity of these two local strain calculation methods in turn.

At last, the principal strains ($\varepsilon_1$ and $\varepsilon_3$) and maximum shear strain in one grid (element) are computed by,

$$\begin{Bmatrix} \varepsilon_1 \\ \varepsilon_3 \end{Bmatrix} = \frac{1}{2}(\varepsilon_x + \varepsilon_y) \pm \sqrt{\frac{1}{4}(\varepsilon_x - \varepsilon_y)^2 + (\frac{\gamma_{xy}}{2})^2} \quad (4\text{-}52)$$

$$\gamma_{xy}^{\max} = \varepsilon_1 - \varepsilon_3 \quad (4\text{-}53)$$

## 4.8 Local strain distributions

For plotting the strain contour, four methods are commonly used in MATLAB such as plotting by absolute value, linear interpolation, cubic interpolation and nearest neighbor interpolation. As explained by Fauzi (2015), all interpolation methods are based on Delaunay triangulation. Finally, the linear interpolation method is employed to plot the strain contour.

Similar to the previous researches (Lin and Penumadu, 2006), the purpose of using a local strain distribution or a contour plot is not to focus on a certain individual point on the specimen surface, but to obtain an overall view of the local deformation at any prescribed time during test. As shown in Fig. 4.37, the deformation of specimen is localized at some regions which could be visualized by the local strain distributions.

As introduce above, the model is rotated freely in the cell without any local deformations. If the proposed coordinate correction method works well, the local strains in the local strain distributions should be always zero. Fig. 4.38 shows the local strain distributions of the model when rotation displacements reach 31 mm and -46 mm on x direction with their corresponding academic shear strains of 4% and -6%, respectively. The leftmost distribution represents local horizontal strains along the tracked region. The middle one illustrates local vertical strain distribution while the rightmost one shows local shear strain distribution. Fortunately, perfect results of the vertical and shear local strains are obtained. However, the local horizontal strain distribution shows the results with some errors by the reason that the traced points reach the boundaries of reference region, which also has been mentioned in Fig. 4.26.

Each grid (element) has three values of strains such as horizontal, vertical and shear strains. The normal distributions of all strains in one image have been analyzed respectively and shown in Fig. 4.39. The results indicate that the vertical and shear strains are computed accurately. However, the horizontal strains are worse than the vertical and shear strains due to the fact that the image is distorted seriously on horizontal direction. In order to solve this issue, a suitable width of the region for tracked dots is necessary to improve the accuracy of local horizontal strains.

The above analysis is focusing on the local strains at one image. In addition, as shown in Fig. 4.24, nine positions are selected to analysis the development of local strains under different strain stages. Each grid is a quadrate at the original photo without deformation. After the rotation of model, the deformed grid may like the one in Fig. 4.40, in which the horizontal and vertical angles are expressed by $\alpha$ and $\theta$. They could be computed by following equations:

$$\theta \approx \tan\theta = \frac{x_2 - x_1}{y_2 - y_1} \quad (4\text{-}54)$$

$$\alpha \approx \tan\alpha = \frac{y_3 - y_1}{x_3 - x_1} \quad (4\text{-}55)$$

Shear angle is the average value of horizontal and vertical angles. Taking the element in position B as an example, the parameters of normal distributions of these three angles at different stages of displacement are summarized in table 4.3. The results also prove the validity of local shear strains after applying the newly proposed coordinate correction method.

## 4.9 Summary

Based on the previous coordinate correction methods, a new one by dividing the surface of specimen into around 2000 grids has been developed and verified. Theoretical analysis and calibration tests were employed to confirm the possibility of applying this new method. Several conclusions are summarized as follows:

1. Through a transparent membrane, the movements of dots and sand particle patterns could be tracked by Move-Tr2D successfully.
2. Since the relationship of real and apparent coordinates of each element was established independently and directly, it could be deemed that the affection by camera lens, light, refraction and other factors have been taken into consideration.
3. For the triaxial test, a resolution of 0.025mm/pixel is obtained, while the one for torsional shear is 0.05 mm/pixel.
4. The theoretical analysis on two special planes indicate that less than 3% error occurs by the replacement of real arc ratio to the length ratio in image, which makes the application of bi-linear interpolation possible.
5. By applying calibration test, the errors of the interval between two neighboring dots are less than 0.2 mm on horizontal direction during vertical displacement and rotation. Additionally, the errors on vertical direction are almost less than 0.1 mm.
6. The maximum relative movements to reference point on horizontal and vertical directions are less than 0.4 mm even under the rotation displacement as large as 46 mm.
7. The errors on local strains are less than 2% during the rotation and the accuracies of local vertical strains and shear strains by proposed method are higher than the one of horizontal strains.
8. The overall view of local strains of specimen could be displayed visually and clearly by local strain distributions

# References

1. Bhandari, A., Powrie, W. and Harkness, R. (2012). A digital image-based deformation measurement system for triaxial tests. *Geotechnical Testing Journal, 35*(2), 1-18.
2. Ergatoudis, I., Irons, B. and Zienkiewicz, O. (1968). Curved, isoparametric,“quadrilateral” elements for finite element analysis. *International Journal of Solids and Structures, 4*(1), 31-42.
3. Fauzi, U. J. (2015). *Local Deformation and Repeated Liquefaction Properties of Segregated Sand Specimen in Hollow Cylindrical Torsional Shear Tests.* The University of Tokyo.
4. Fauzi, U. J. and Koseki, J. (2014). Local deformation properties of segregated sand specimen in hollow cylindrical torsional shear tests. *Bulletin of ERS*(47), 27-36.
5. Felippa, C. A. (2001). Introduction to finite element methods. *Department of Aerospace Engineering Sciences and Center for Aerospace Structures, University of Colorado Boulder*.
6. Hoshino, R., Miyashita, Y., Sato, T. and Koseki, J. (2015). Local deformation properties of sand specimens in triaxial liquefaction tests evaluated by direct and indirect observations. *Bulletin of ERS, 48,* 63-71.
7. Huebner, K. H., Dewhirst, D. L., Smith, D. E. and Byrom, T. G. (2008). *The finite element method for engineers*: John Wiley & Sons.
8. Jenkins, F. A. and White, H. E. (1976). Fundamentals of optics 4th edition. *Fundamentals of Optics 4th edition by Francis A. Jenkins, Harvey E. White New York, NY: McGraw-Hill Book Company, 1976*.
9. Lin, H. and Penumadu, D. (2006). Strain localization in combined axial-torsional testing on kaolin clay. *Journal of engineering mechanics, 132*(5), 555-564.
10. Macari, E. J., Parker, J. K. and Costes, N. C. (1997). Measurement of volume changes in triaxial tests using digital imaging techniques. *Geotechnical Testing Journal, 20*(1), 103-109.
11. Raffel, M., Willert, C. E., Wereley, S. and Kompenhans, J. (2013). *Particle image velocimetry: a practical guide*: Springer.
12. Shao, L. T., Liu, G., Zeng, F. T. and Guo, X. X. (2016). Recognition of the Stress-Strain Curve Based on the Local Deformation Measurement of Soil Specimens in the Triaxial Test. *Geotechnical Testing Journal, 39*(4), 20140273. doi: 10.1520/gtj20140273
13. Wahyudi, S., Koseki, J. and Sato, T. (2014). Characteristics of re-liquefied behavior of sand by means of image analysis in stacked-rings shear apparatus. *Bull Earthq Resist Struct Res Cent, 47*, 15-26.

14. White, D., Take, W. and Bolton, M. (2003). Soil deformation measurement using particle image velocimetry (PIV) and photogrammetry. *Géotechnique, 53*(7), 619-631.

15. Zhang, X., Li, L., Chen, G. and Lytton, R. (2015). A photogrammetry-based method to measure total and local volume changes of unsaturated soils during triaxial testing. *Acta Geotechnica*, *10*(1), 55.

**Table 4. 1 Parameters of normal distributions of intervals (vertical neighboring dots)**

| N. D. | Positions (Vertical neighboring dots) | | | | | | | | |
|---|---|---|---|---|---|---|---|---|---|
| | A | B | C | D | E | F | G | H | I |
| Mean. | 5.003 | 4.994 | 5.020 | 5.000 | 4.989 | 5.000 | 5.018 | 5.043 | 5.071 |
| S. D. | 0.032 | 0.025 | 0.030 | 0.021 | 0.017 | 0.024 | 0.034 | 0.028 | 0.036 |
| Coef. /% | 0.65 | 0.51 | 0.60 | 0.43 | 0.34 | 0.49 | 0.69 | 0.56 | 0.72 |

**Table 4. 2 Parameters of normal distributions of intervals (horizontal neighboring dots)**

| N. D. | Positions (Horizontal neighboring dots) | | | | | | | | |
|---|---|---|---|---|---|---|---|---|---|
| | A | B | C | D | E | F | G | H | I |
| Mean. | 5.037 | 5.044 | 4.986 | 5.028 | 5.097 | 4.977 | 5.028 | 5.097 | 4.977 |
| S. D. | 0.045 | 0.044 | 0.064 | 0.029 | 0.032 | 0.042 | 0.110 | 0.060 | 0.048 |
| Coef. /% | 0.90 | 0.88 | 1.28 | 0.58 | 0.63 | 0.84 | 2.20 | 1.18 | 0.96 |

**Table 4. 3 Parameters of normal distributions of the three angles at position B**

| position B | Directions | Mean/rad | SD | Coef. /% |
|---|---|---|---|---|
| vertical displacement | vertical $\theta$ | 0.00562 | 0.00424 | 0.754448 |
| | Horizontal $\alpha$ | -0.00612 | 0.00647 | -1.05719 |
| | shear angle $\gamma/2$ | -0.00025 | 0.00311 | -12.49 |
| 1% shear strain | vertical $\theta$ | -0.00058 | 0.00294 | -5.06024 |
| | horizontal $\alpha$ | 0.00475 | 0.00413 | 0.869474 |
| | shear angle $\gamma/2$ | 0.00208 | 0.00265 | 1.274038 |
| 2% shear strain | vertical $\theta$ | 0.000486 | 0.00413 | 8.497942 |
| | horizontal $\alpha$ | 0.00698 | 0.0043 | 0.616046 |
| | shear angle $\gamma/2$ | 0.00373 | 0.00298 | 0.798928 |
| 5% shear strain | vertical $\theta$ | 0.000417 | 0.0047 | 11.27098 |
| | horizontal $\alpha$ | 0.00429 | 0.00449 | 1.04662 |
| | shear angle $\gamma/2$ | 0.00236 | 0.00324 | 1.372881 |
| 10% shear strain | vertical $\theta$ | 0.000878 | 0.00612 | 6.970387 |
| | horizontal $\alpha$ | 0.002 | 0.00518 | 2.59 |
| | shear angle $\gamma/2$ | 0.00144 | 0.00391 | 2.715278 |

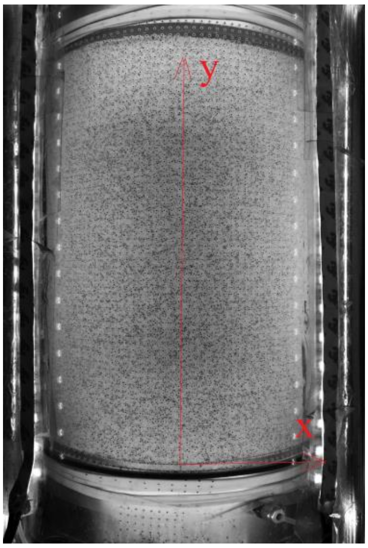

**Fig. 4.1 Origin of coordinate axis**

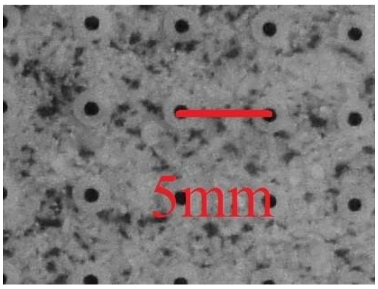

**Fig. 4.2 Scale from pixel to distance**

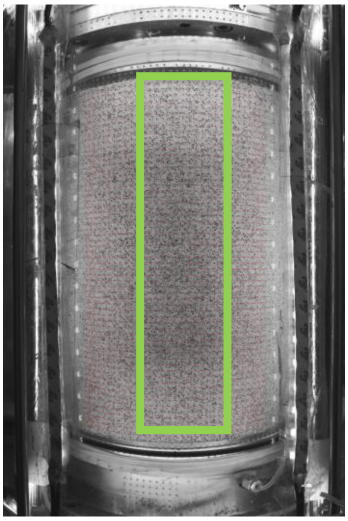

**Fig. 4. 3 Marked dots as reference before deformation**

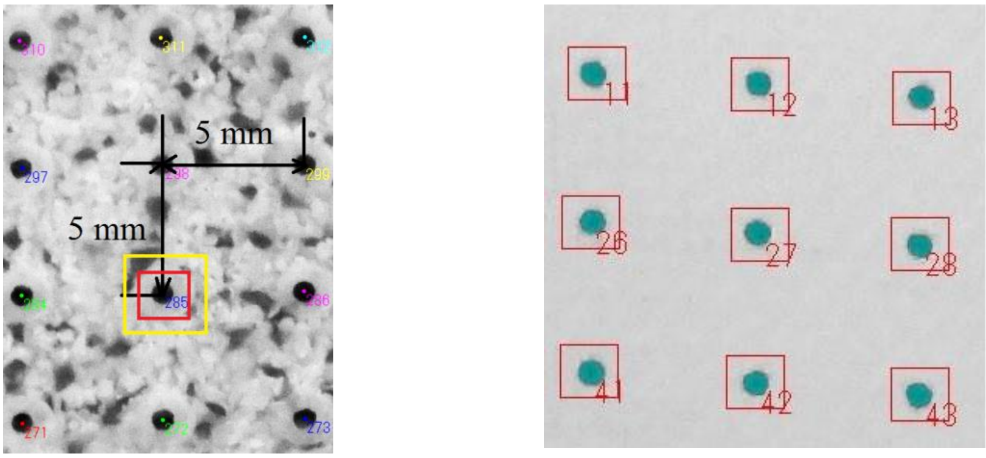

(a) Recorded and searching squares of dots

(b) Schematic of the center of ‘gravity’ for dot analysis

**Fig. 4.4 Two methods to track the movements of dots**

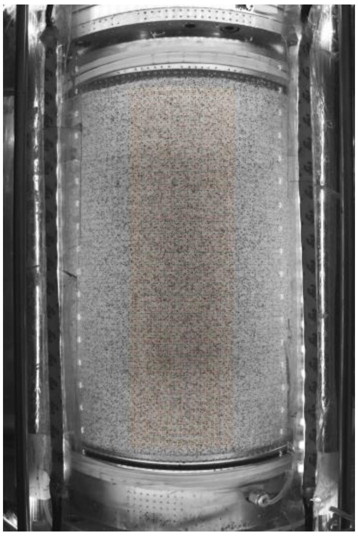

**Fig. 4.5 Marked sand particle patterns before deformation**

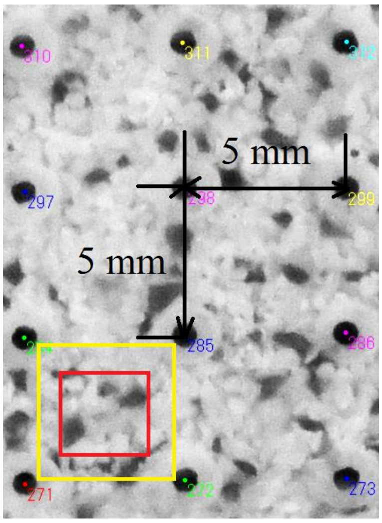

**Fig. 4.6 Recorded and searching squares of sand particle pattern**

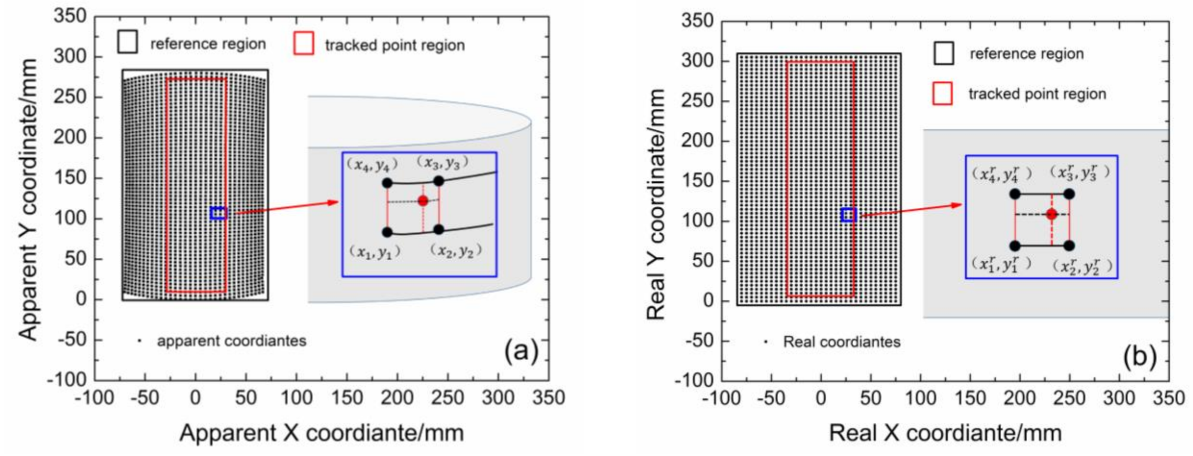

Fig. 4.7 Apparent coordinate and real coordinate of dots without deformation

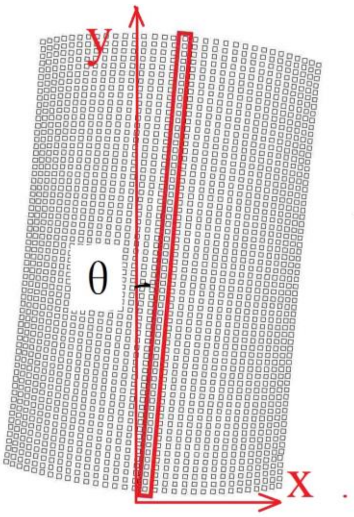

Fig. 4.8 Schematic diagram of inclination correction

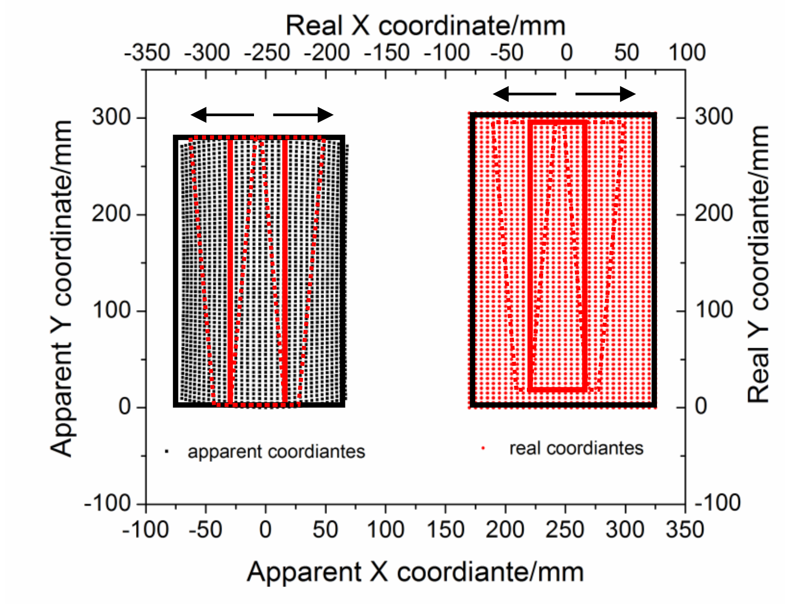

Fig. 4.9 Schematic diagram of coordinate correction method

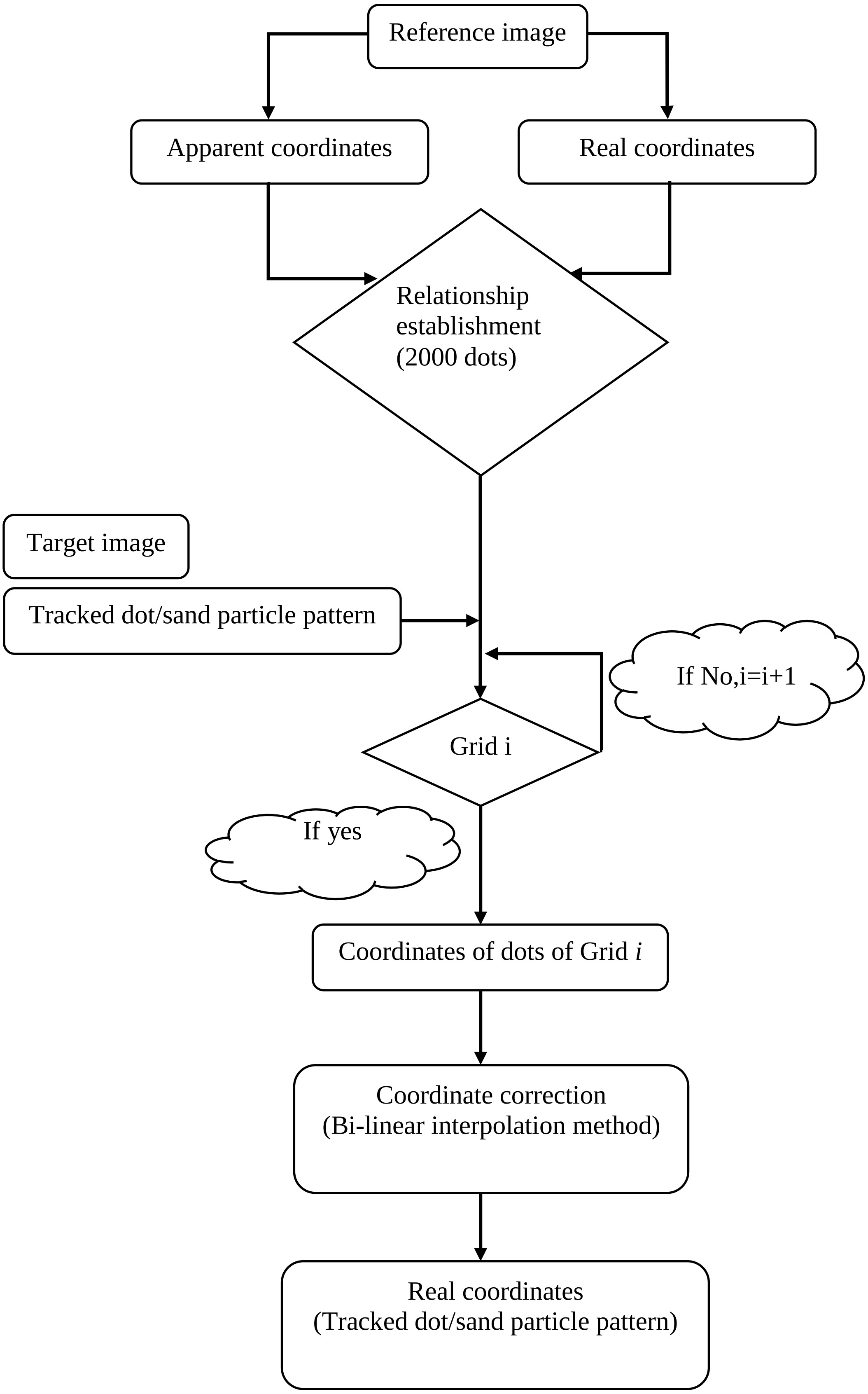

**Fig. 4.10 The flow diagram of proposed coordinate correction method**

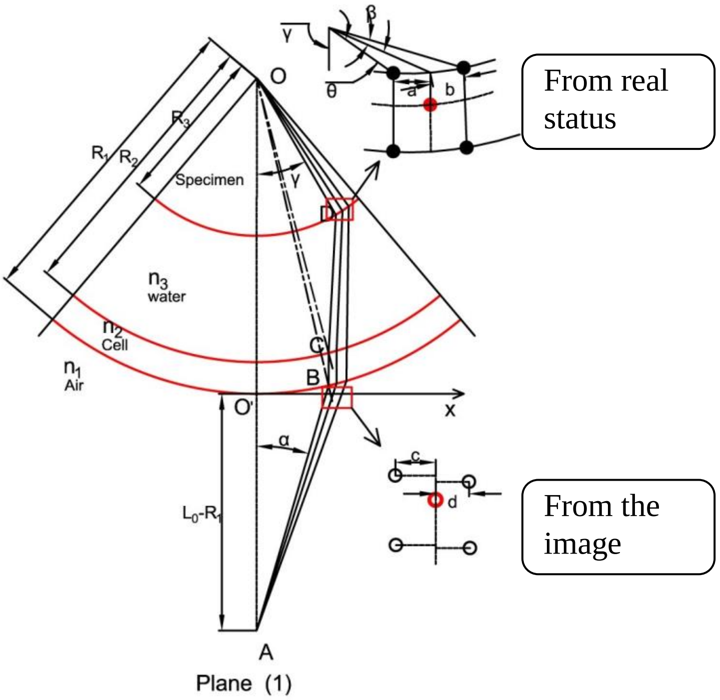

Fig. 4.11 Schematic diagram of specimen-camera from vertical view

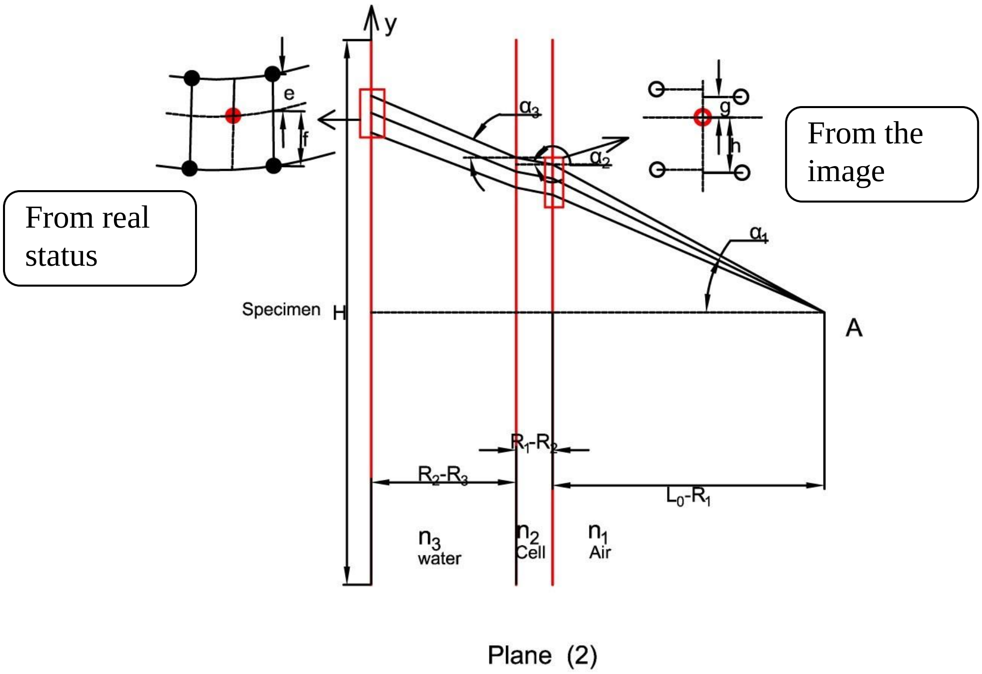

Fig. 4.12 Schematic diagram of specimen-camera from horizontal view

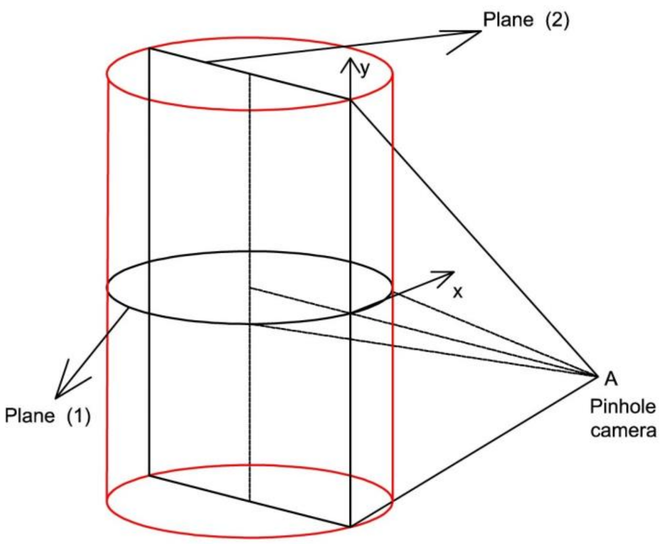

**Fig. 4.13 Schematic diagram of the two special planes**

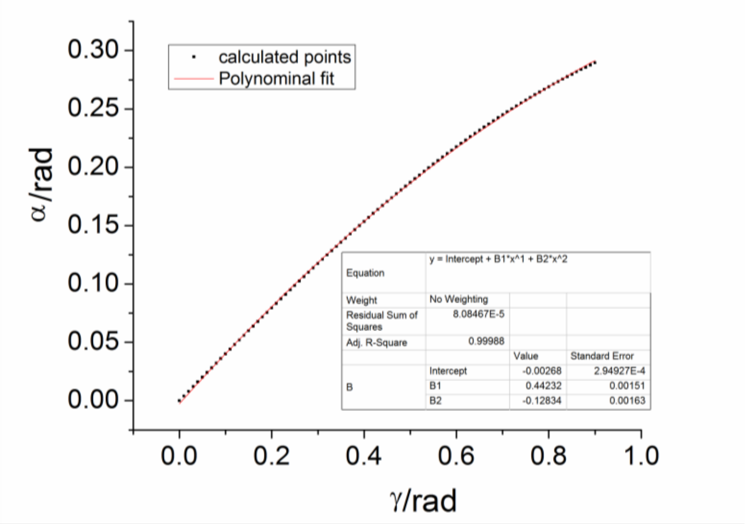

| | | | |
|---|---|---|---|
| Equation | y = Intercept + B1*x^1 + B2*x^2 | | |
| Weight | No Weighting | | |
| Residual Sum of Squares | 8.08467E-5 | | |
| Adj. R-Square | 0.99988 | | |
| | | Value | Standard Error |
| B | Intercept | -0.00268 | 2.94927E-4 |
| | B1 | 0.44232 | 0.00151 |
| | B2 | -0.12834 | 0.00163 |

**Fig. 4.14 The fitting curve of the relationship between $\gamma$ and $\alpha$**

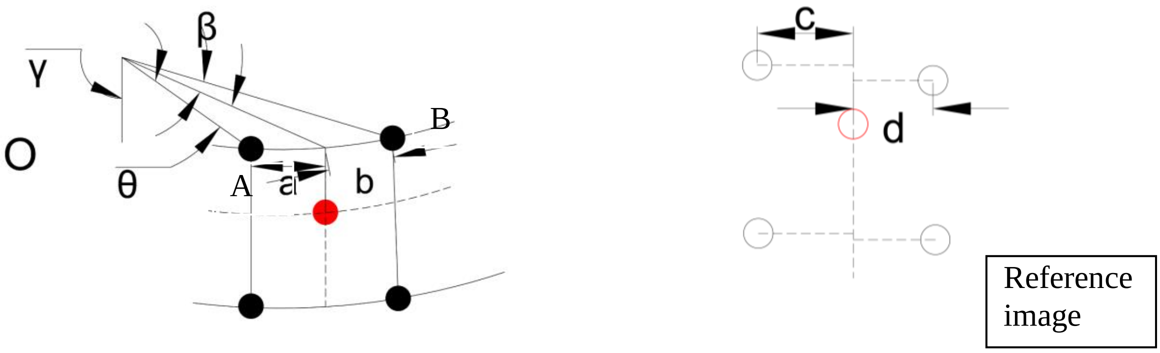

**Fig. 4.15 The real and apparent relationships of tracked point with its four nearest dots in the reference image**

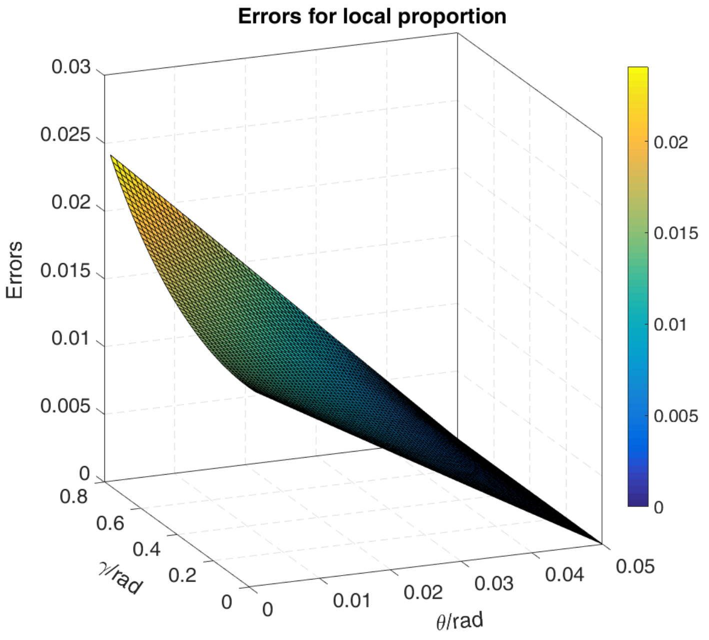

**Fig. 4.16 The calculated errors by basic assumptions of bi-liner interpolation method at horizontal plane**

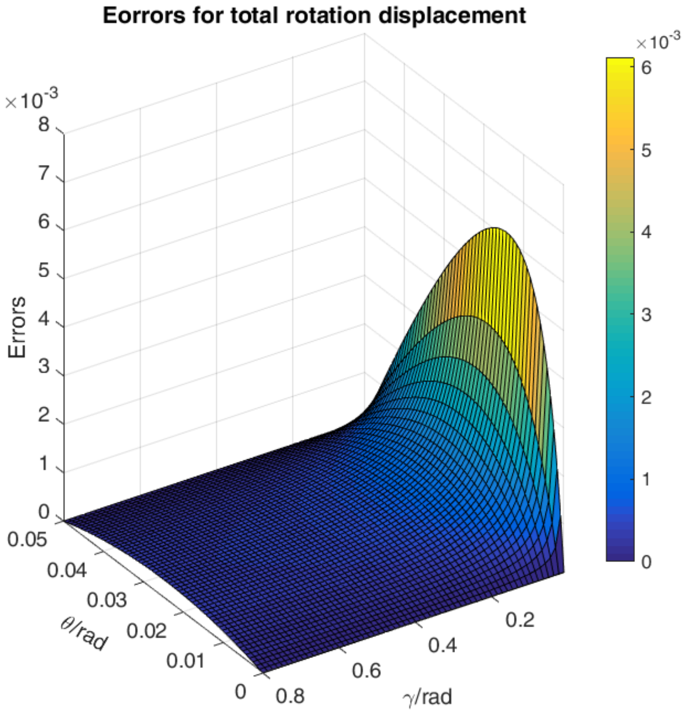

**Fig. 4.17 Displacement errors of proposed method on plane (1)**

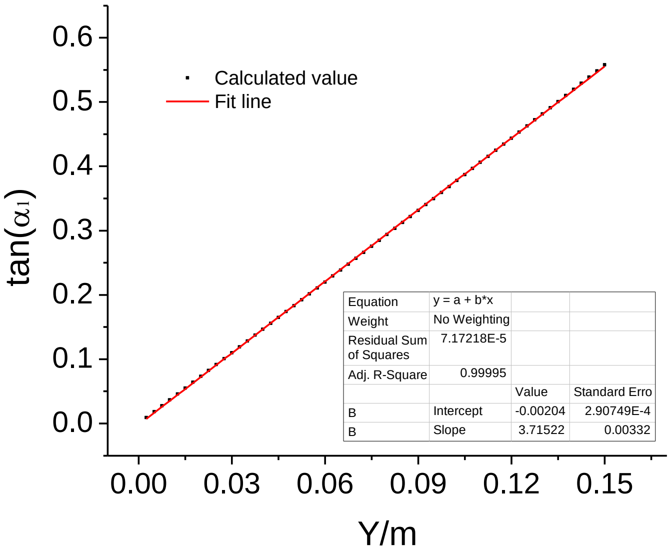

**Fig. 4.18 The fitting curve of the relationship between $\tan\alpha_1$ and y**

**Fig. 4.19 The real and apparent relationships of tracked point with its four nearest dots on vertical direction**

**Fig. 4.20 The plastic model pasted with black dots in the calibration test**

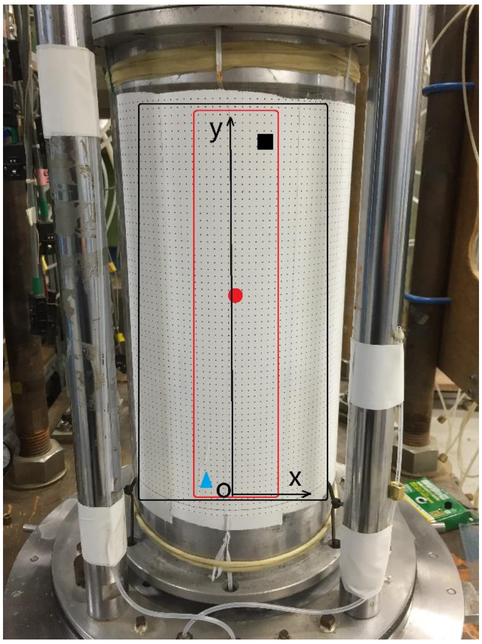

**Fig. 4.21 The reference dots and tracked**

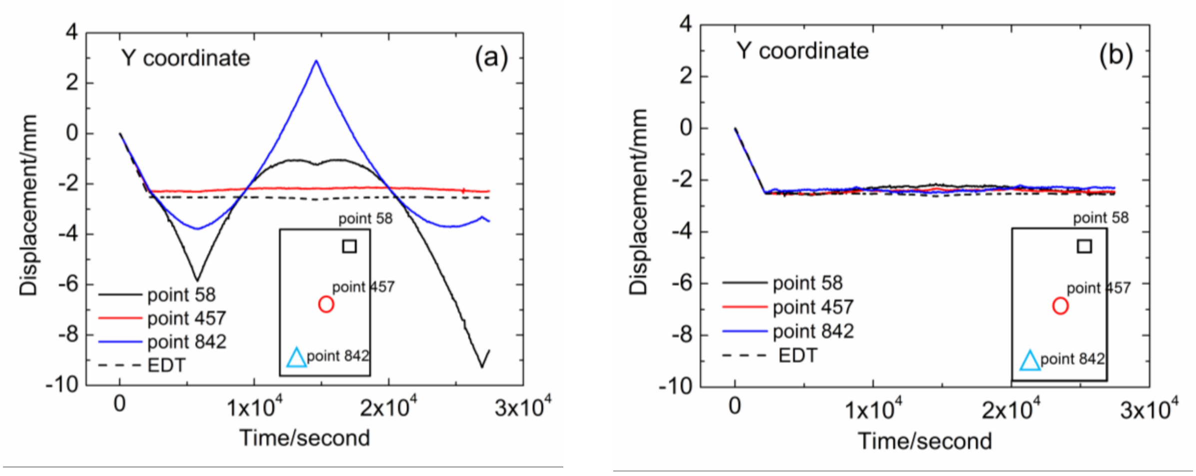

**Fig. 4.22 Time histories of the displacements on y direction from three positions before and after coordinate correction**

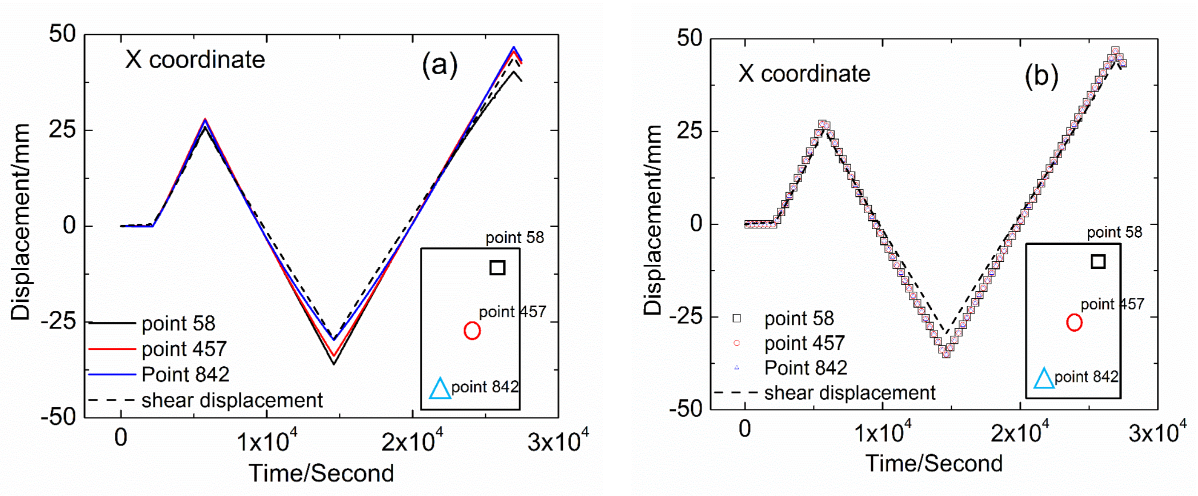

**Fig. 4.23 Time histories of the displacement on x direction form three positions before and after coordinate correction**

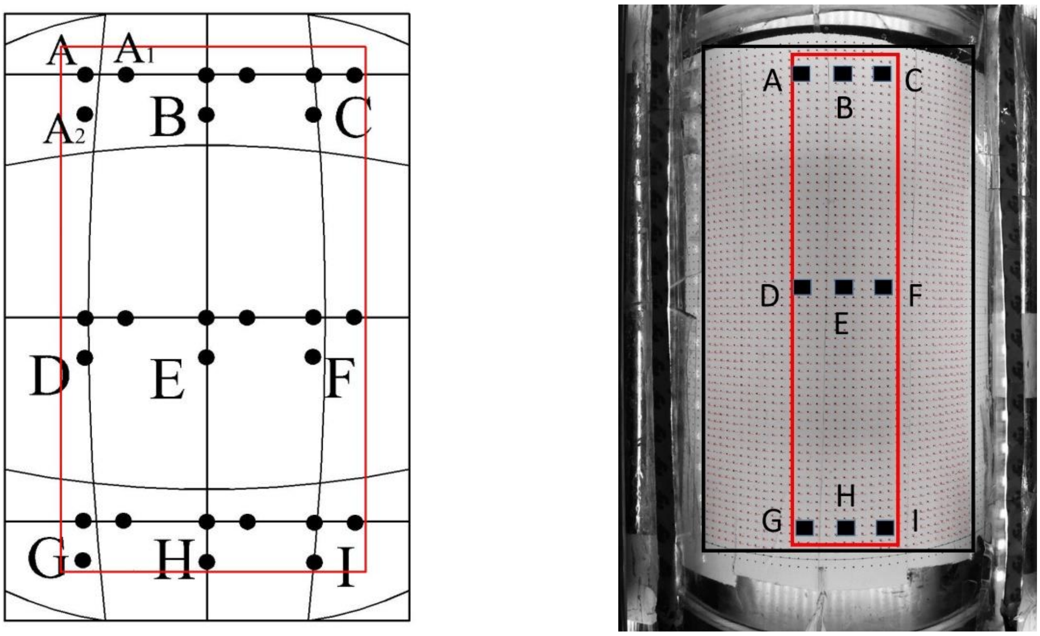

**Fig. 4.24 The setting of reference and the region for tracked dots in calibration test**

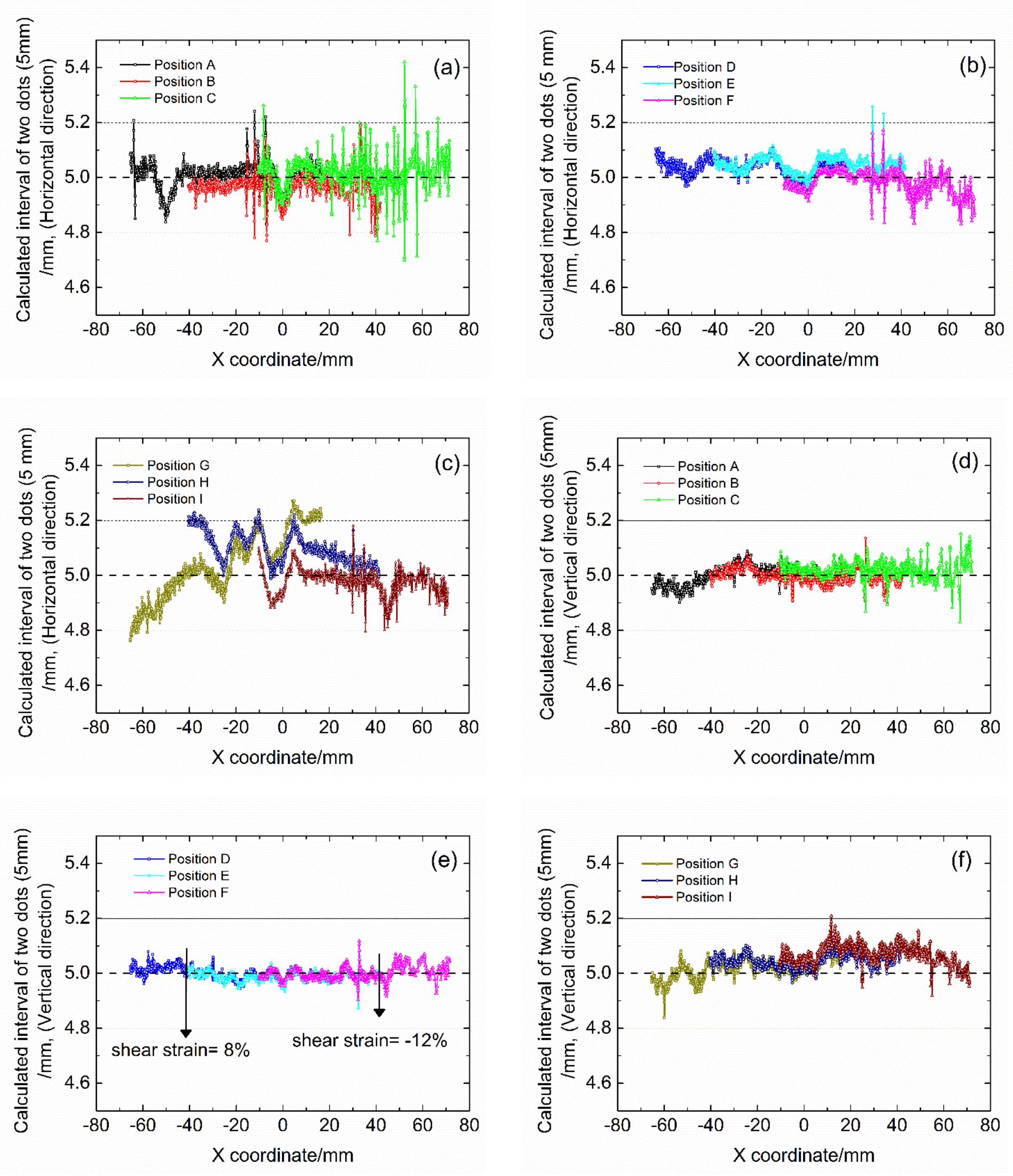

**Fig. 4.25 The calculated interval of two nearest dots on horizontal and vertical directions**

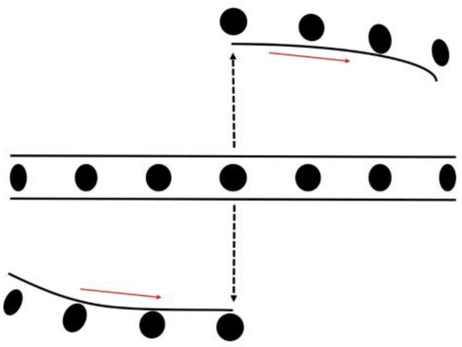

Fig. 4.26 Shape changing of circular dots at different positions during rotation

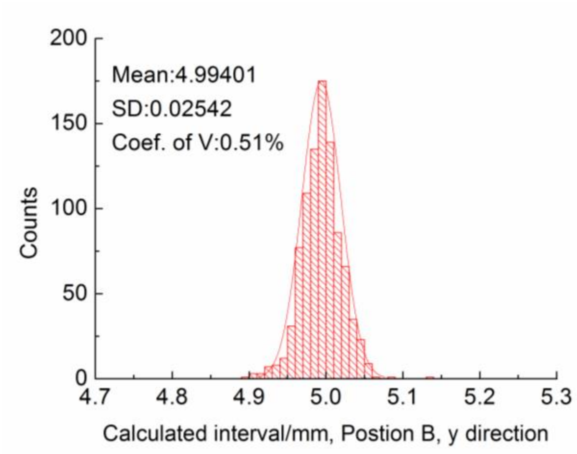

Fig. 4.27 Normal distribution of the interval of two neighboring vertical dots

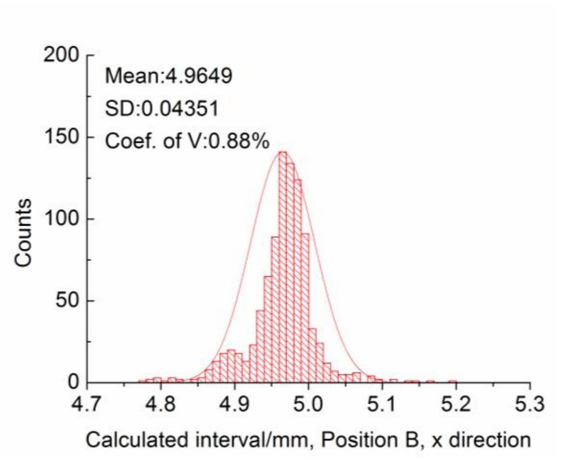

Fig. 4.28 Normal distribution of the interval of two neighboring horizontal dots

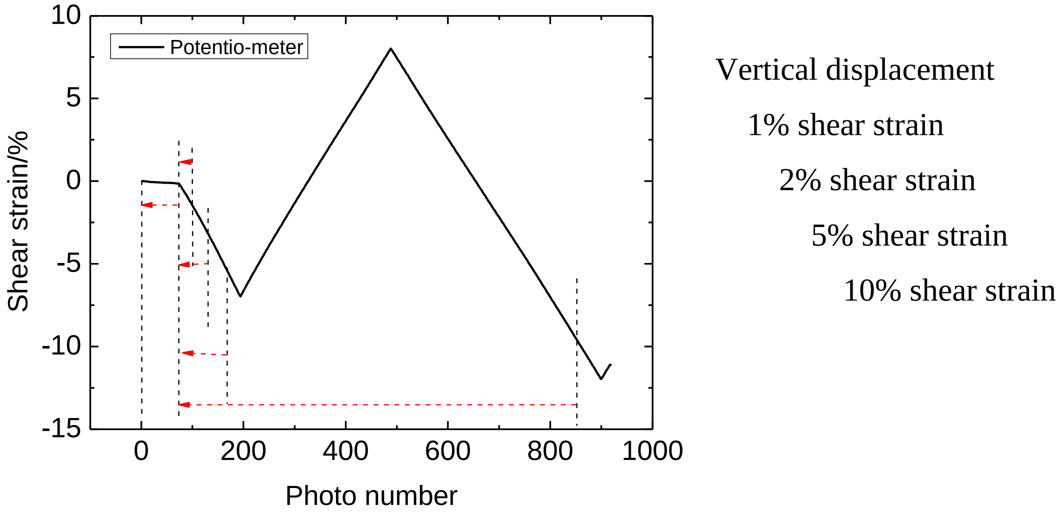

Fig. 4.29 The separation of shear strain by different amplitudes

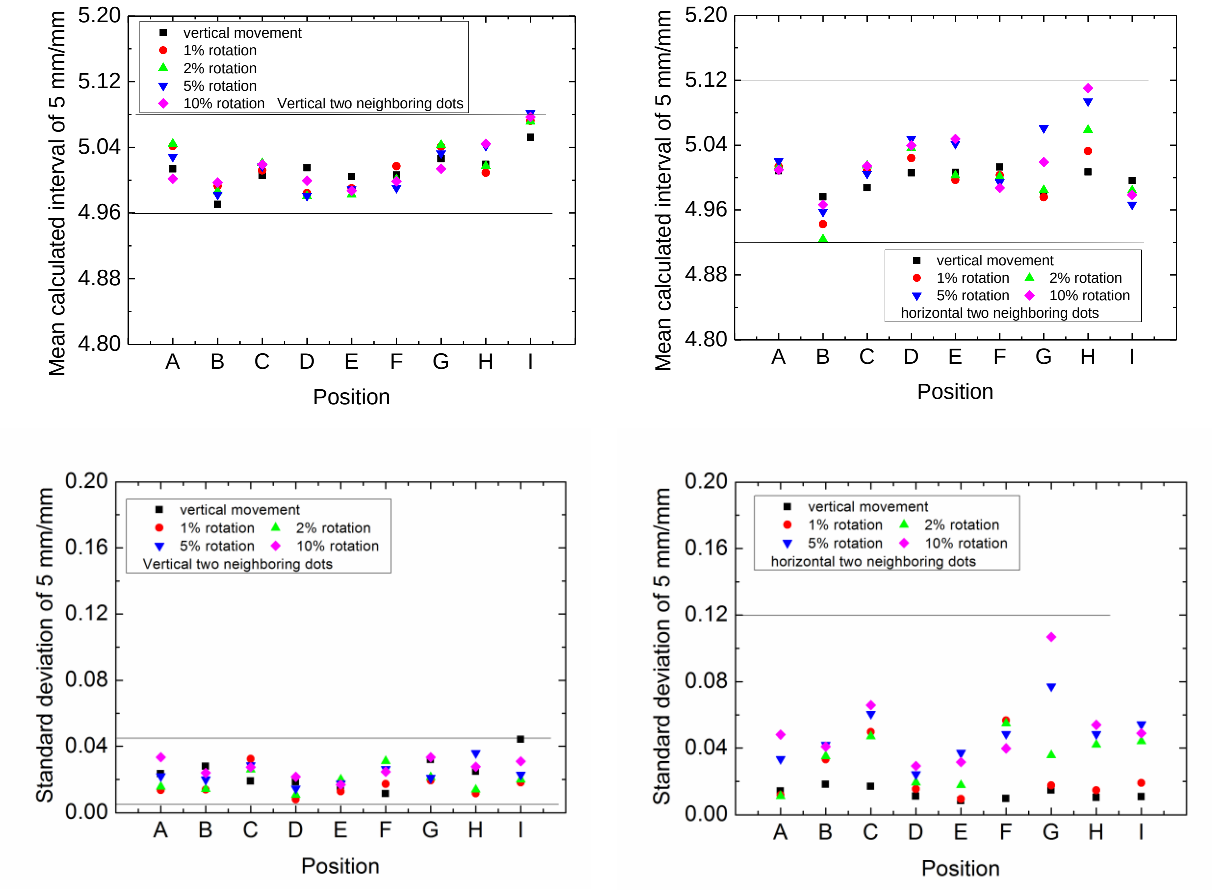

**Fig. 4.30 Mean value and S. D. of the normal distributions at different displacements**

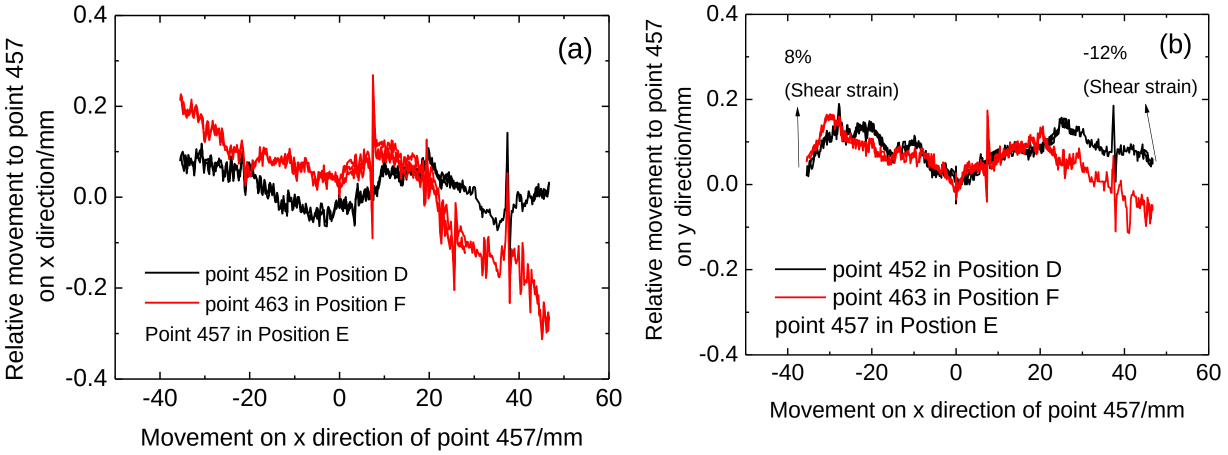

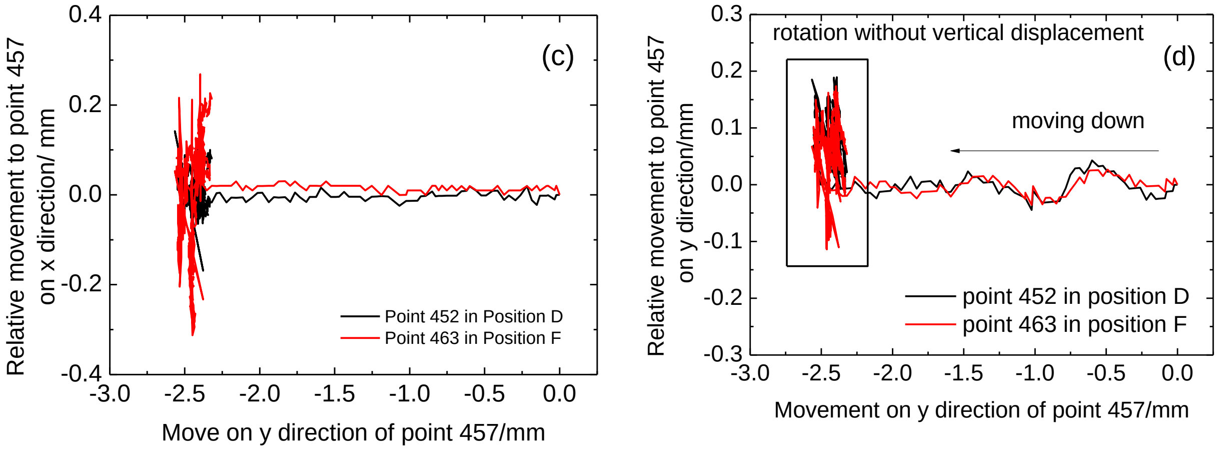

Fig. 4.31 Horizontal and vertical relative movements to reference point at horizontal plane

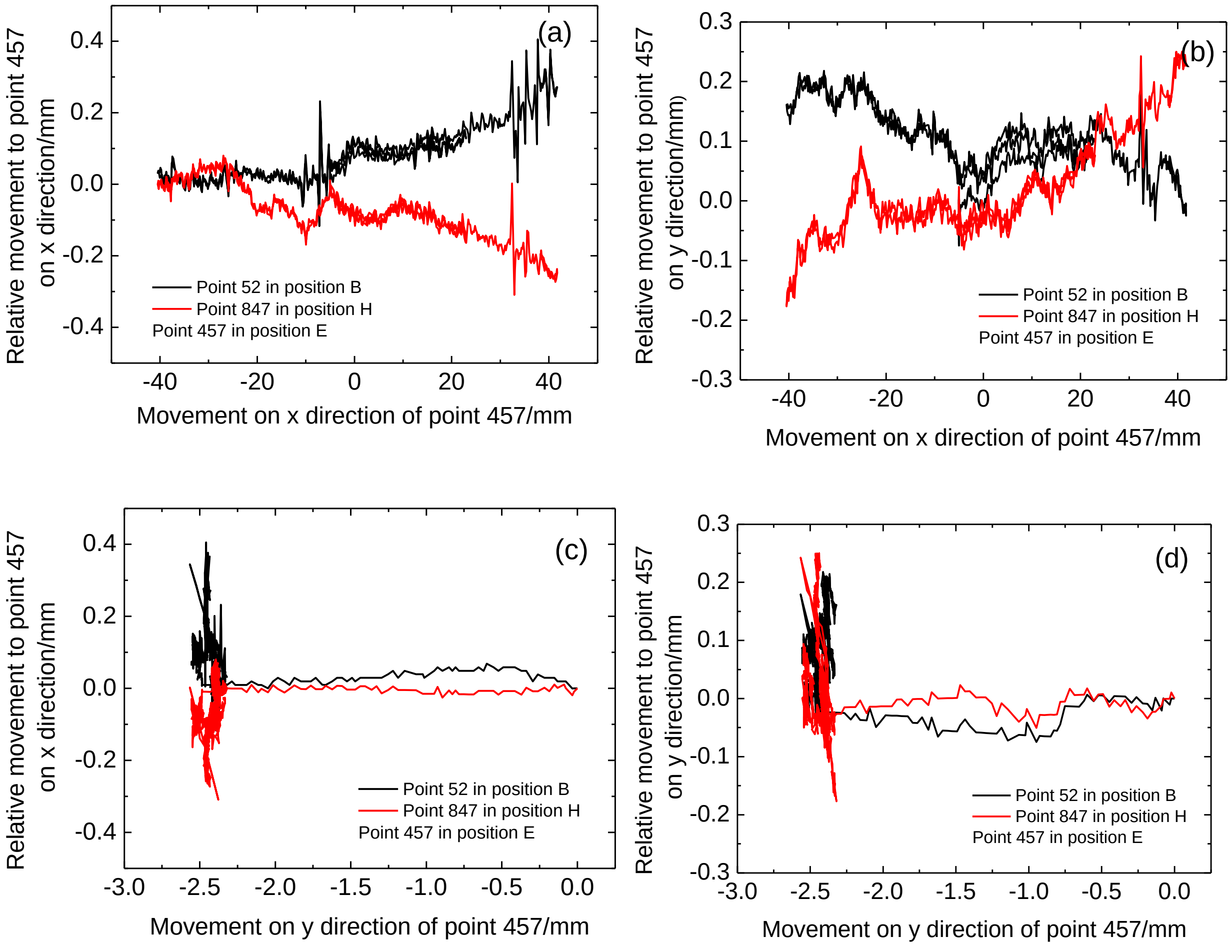

Fig. 4.32 Horizontal and vertical relative movements to reference point at vertical plane

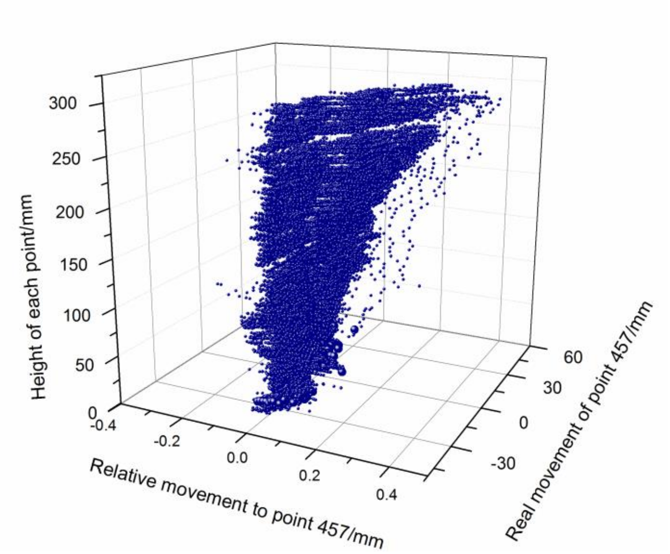

Fig. 4.33 Relative movements to reference point 457 on x direction along the model surface

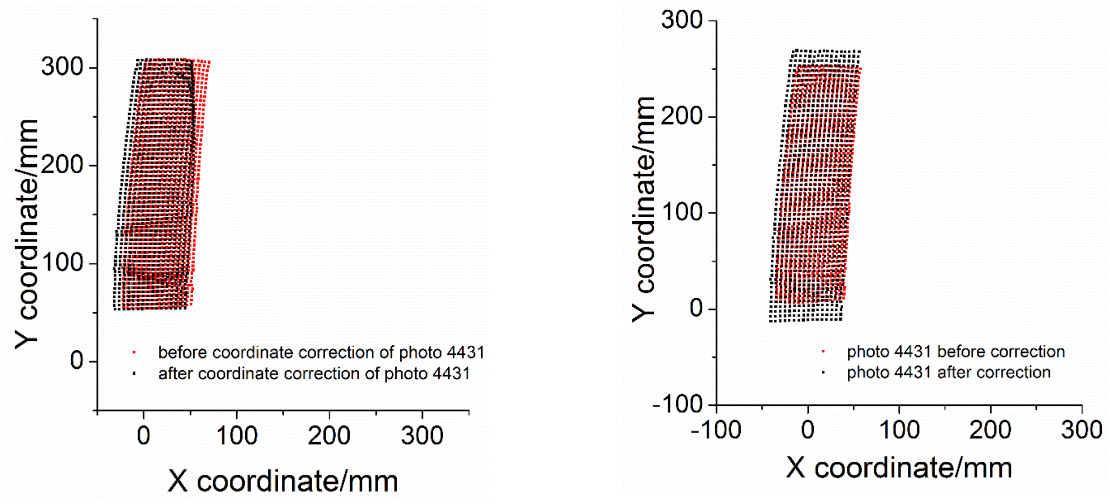

Fig. 4.34 Comparison of the two coordinate correction methods with the same apparent coordinates

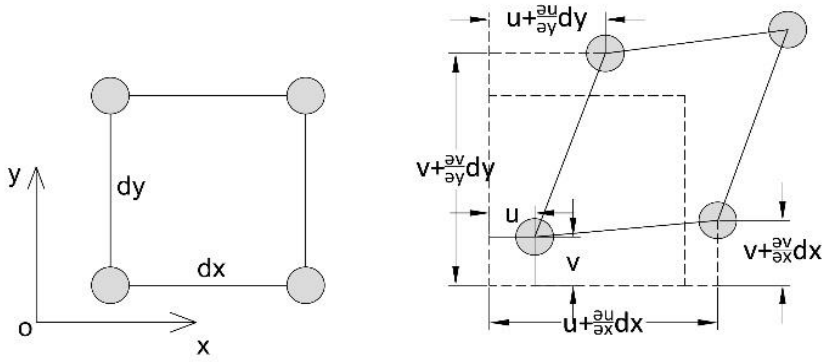

Fig. 4.35 Schematic diagram of strain calculation in one element

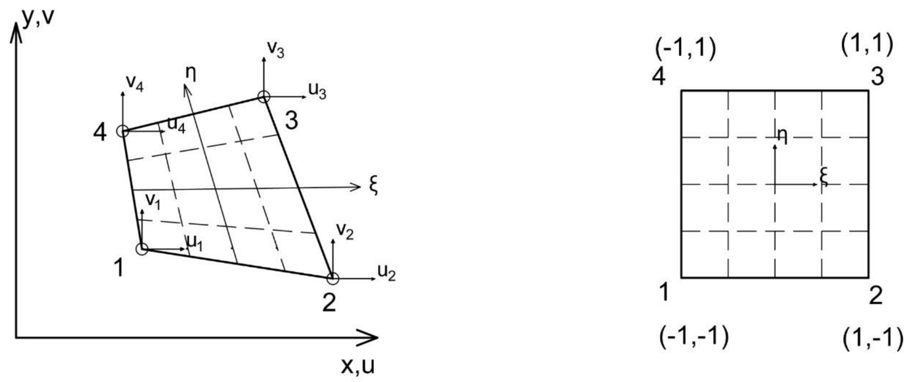

**Fig. 4.36 Global Cartesian coordinates and local natural coordinates of one element**

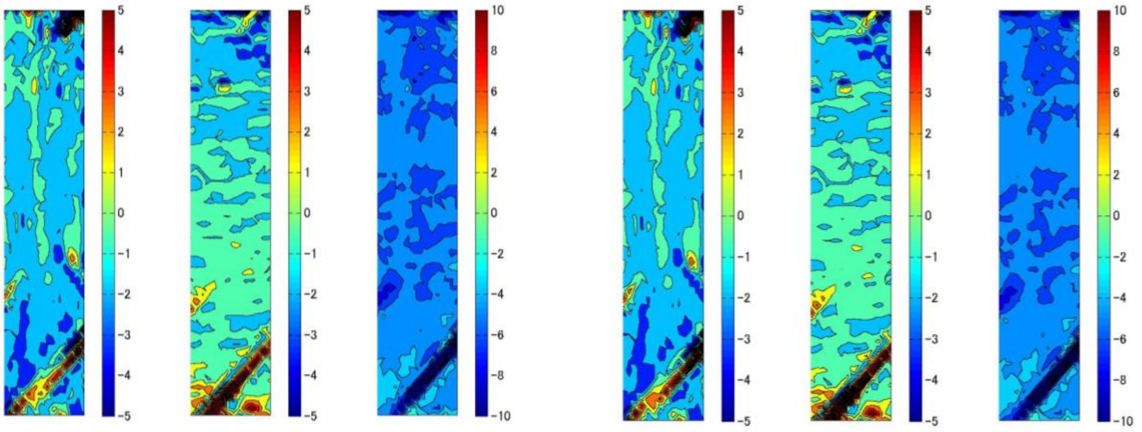

horizontal vertical shear horizontal Vertical shear

Average by four nodes Interpolation method by shape function

**Fig. 4.37 Local strain distributions of one test with the academic shear strain of -3.7%**

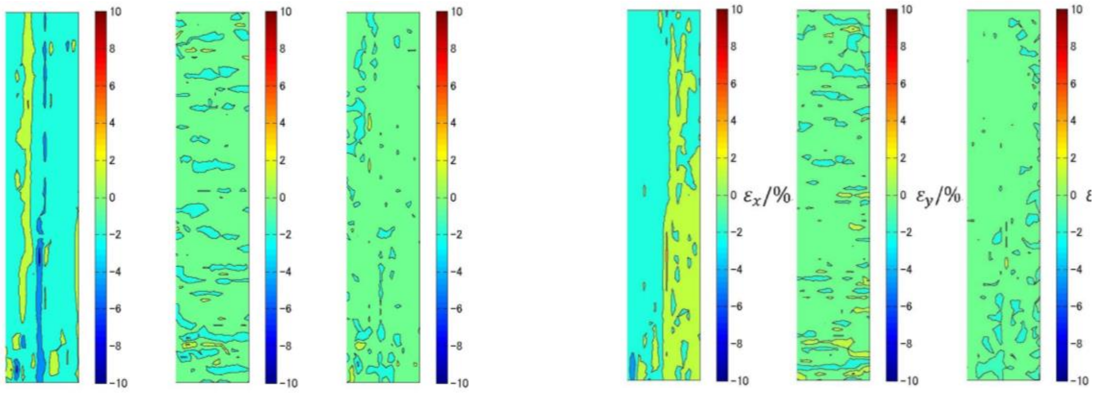

horizontal vertical shear horizontal Vertical shear

Similar to the 4% of academic shear strain Similar to the -6% of academic shear strain

**Fig. 4.38 Local strain distributions of the model at different rotation displacements**

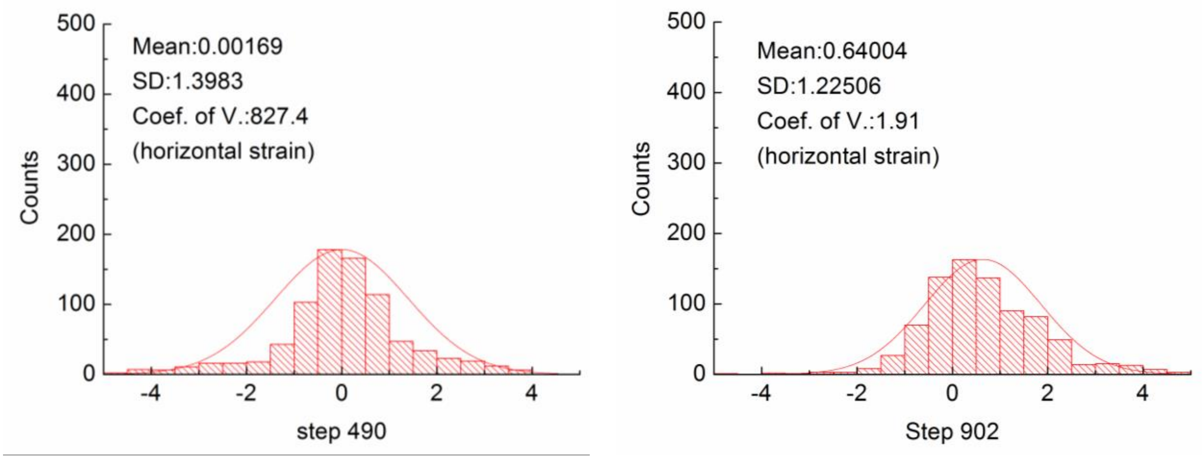

Horizontal strain

Horizontal strain

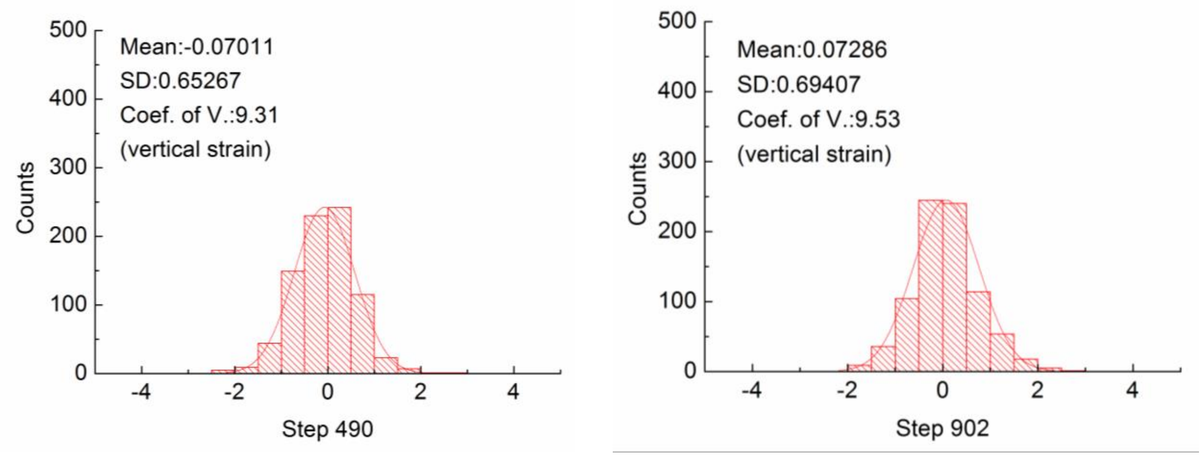

Vertical strain

Vertical strain

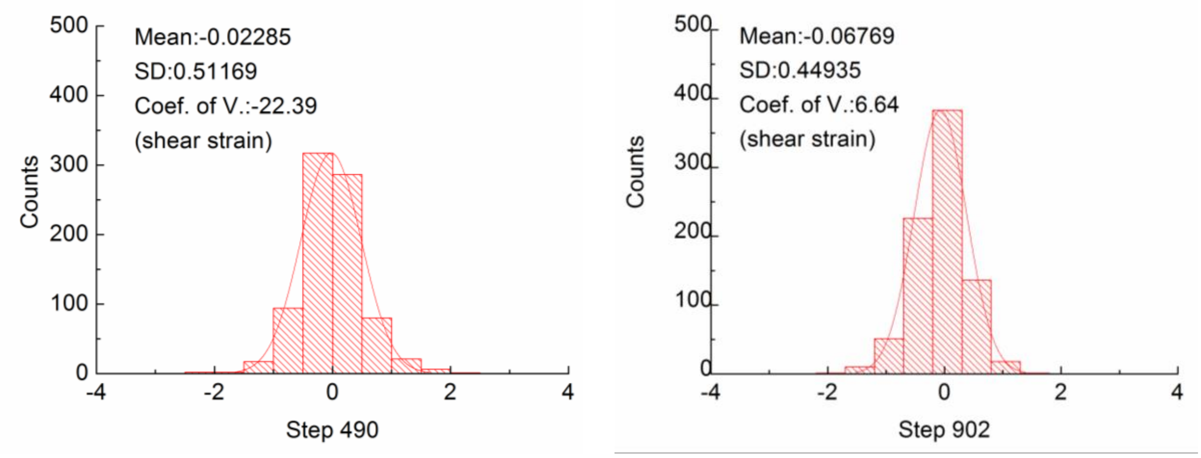

Academic shear strain

Academic shear strain

**Fig. 4.39 Normal distributions of strain at two shear strain conditions**

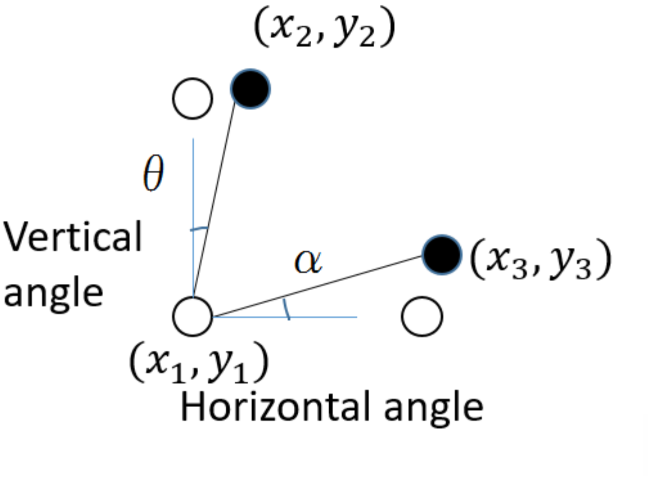

**Fig. 4.40 Horizontal and vertical angles in one element**

# 5. LOCAL DEFORMATION OBSERVATIONS IN TRIAXIAL LIQUEFACTION TESTS

## 5.1 Introduction

Conventional triaxial apparatus is widely used by researcher and engineers to evaluate the soil behavior under different stress conditions. As for the deformation properties of soil specimen, axial strain is deemed as a representative parameter by the assumption that the response of soil specimen is homogeneous even under complicated stress condition. Recently, accompanied with the development of continuously updated techniques, interests in strain localization have rapidly increased. In the laboratory tests, soil failure is always affected by strain localization, which may result in the formation of shear band in drained condition. Yoshida et al. (1995; 1997) used analog pictures taken from the outside of transparent cell to measure the local deformation of sand sample in plain strain compression tests. Harris et al. (1995) also conducted plain strain compression test to investigate the formation of shearing band in sand by stereo-photogrammetry method. In order to describe the mesoscale instabilities in localized granular shear, Rechenmacher et al. (2011) applied digital image correlation method into the plain strain test. Similarly, void ratio evaluation inside of shear band was investigated by applying computed tomography in triaxial tests (Desrues et al., 1996). Additionally, image-based techniques have been applied in the drained element tests on sand specimen by researchers diffusely (Mokni and Desrues, 1999; Rechenmacher and Finno, 2003; Sadrekarimi and Olson, 2010; White et al., 2003). In the above researches, the local deformation properties of sand specimen in drained tests have been detected and described both qualitatively and quantitatively.

However, little attention has been paid on the strain localization in undrained element tests. The fact is that homogeneous deformation is always assumed when dealing with the local deformation of uniform sand specimen. Han and Vardoulakis (1991) presented that there was no strain localization of loose sand specimen in undrained compression test. However, undrained plane strain compression test was conducted by Mokni and Desrues (1999) for the strain localization, the results indicated that shear banding also occurred in the test. It was also found that the onset of localization was delayed when compared with the drained test. In addition, Kiyota et al. (2008) and Chiaro et al. (2013) claimed that the deformation of specimen became non-uniform after exceeding a certain level of overall shear strain, which was named as strain localization in undrained torsional shear test. It was found that the initiation of strain localization was related to the sudden decrease of deviator stress when the vertical displacement was prohibited in undrained torsional shear test. Moreover, strain softening was observed from the evolution curves of modified stress ratio versus shear strain.

Based on image analysis technique, direct and indirect evaluation methods of local deformation were proposed by Hoshino et al. (2015) with a transparent membrane in undrained triaxial cyclic loading test. The results indicated that the local deformations of dense sand specimen evaluated by indirect observation were almost same with those from direct evaluation up to a double amplitude axial strain of 5%.

In this chapter, air pluviation and moist tamping methods are employed to prepare the cylindrical sand specimen. The direct and indirect observations of local deformations in undrained triaxial tests are presented and compared.

## 5.2 Local deformations of Toyoura sand specimen in undrained triaxial tests

Toyoura sand with a mean diameter of 0.2 mm is used as the test materials, which is seen as a standard sand material in Japan for research and exhibits yellowish color as shown in Fig. 5.1 (a). In order to conduct the direct evaluation of local deformation, the Toyoura sand was speckled by a blue-colored Silica sand with a mean diameter of 0.5 mm. Fig. 5.1 (b) shows the blue-colored Silica sand before mixed with Toyoura sand. The Toyoura sand and blue-colored Silica sand are mixed at a mass ratio of 100 to 15. As shown in Fig. 5.1 (c), the transparent was painted by red dots with an interval of 5 mm both on horizontal and vertical directions.

As introduced in chapter 3, the Toyoura sand specimen used in triaxial test was prepared by moist tamping method in a mold where the mixed test materials with a water content of 15% were compacted by a cylindrical tamper. The specimen was separated into five layers totally and the sand in each layer was compacted into the target thickness to achieve relatively uniform specimen. Thus, the relative density of specimen could be adjusted by changing the weight of sand at each layer. After frozen in a freezer for 24 hours, the specimen was de-molded and vacuumed by a 30 kPa confining pressure. The red dots were sprayed by red paint with an interval of 5 mm as shown in Fig. 5.1c.

As summarized in Fig. 5.2, the digital images taken by camera were saved in RAW format and then converted into TIFF format for later process. Since a transparent membrane was employed, the dots on membrane and sand particles were tracked, respectively. In order to evaluate the deformations of dots and sand particles separately, two sets of image analysis procedures were designed. One was the indirect evaluation of local deformation, where the dots were tracked only by setting the filtering process with $(R'_{ij}, G'_{ij}, B'_{ij}) = (255, G_{ij}, 255)$. Another one was for the direct evaluations of local deformation by setting $(R'_{ij}, G'_{ij}, B'_{ij}) = (R_{ij}, 255, 255)$. $(R'_{ij}, G'_{ij}, B'_{ij})$ and $(R_{ij}, G_{ij}, B_{ij})$ were the intensity scale of red, green and blue components before and after the filtering process, respectively. After the filtering process, the images for indirect and direct evaluations of local deformations are shown in Fig. 5.3, respectively. Subsequently, the images were converted into gray scale and enhanced by their dynamic ranges as shown in

Fig .5.4.

PIV (particle Image Velocimetry) is used to track the movements of patterns of red dot and blue-colored sand group, which are named as indirect and direct evaluations of local deformations. As for the direct evaluations, two different patterns are conducted, which are excluding the surrounded dots and including these dots as shown in Fig. 5.5 (b) and (c), respectively. Moreover, the red dots on membrane as shown in Fig. 5.5 (a) are for the indirect evaluation. Based on the digital images taken during the test, these three types evaluations were conducted separately. After analyzing, the coordinates of the tracked points could be obtained. Subsequently, the local stains and deformations along the specimen were calculated. However, in order to compare the indirect and direct evaluations of local deformation in a simplified manner, no coordinate correction was applied to the apparent coordinates. The apparent coordinate in this study is the one obtained directly from the distorted image. At last, based on the local strains at each image, the corresponding local strain distribution could be plotted visually. The resolution of image analysis in this undrained triaxial test is around 0.025 mm/pixel.

In Fig. 5.6 through 5.8, the relationships between cyclic stress ratio and cyclic number to induce 2%, 5% and 10% DA of axial strains for Toyoura sand are compared with those experimental data from the paper of Prof. Tatsuoka (1986). Fig. 5.9 shows the relationships between cyclic stress ratio and cyclic number to induce 10% DA axial strain of Toyoura sand by moist tamping method with different relative densities.

Observed behavior of test 7 where sand specimen was consolidated to an initial effective stress of 200 kPa and subjected to undrained cyclic loading with a cyclic stress ratio of 0.25 is shown in Fig. 5.10 (a) through (e). In order to illustrate the evolution of local deformations measured and computed by image analysis method, some statuses were selected to plot their corresponding local strain distributions. As shown in Fig. 5.11, the statuses when the maximum values of axial strain during compression and extension were reached. Additionally, the statuses when excess pore water pressure reached its temporary peak at each cycle were selected.

The corresponding local strain distributions of these selected statuses are shown in Fig. 5.12. Based on the results, the local strain distributions from three kinds of evaluation methods are almost same with each other when the double amplitude of axial strain is less than 7.5%. Since the shape of specimen under relative large axial strain was seriously deformed, some sand particles patterns were not traced accurately, resulting in some missing regions in the local strain distributions. Moreover, the local strains along the specimen surface are not uniform. For example, local strain distribution is stratified at step 385 when the axial strain reaches its temporary maximum strain at -1.6% during extension. Five layers with four interfaces could be recognized by the local strain distributions clearly. Due to the weakness of the interface between each two layers, necking phenomenon is found near the interfaces during extension when the local strain distributions and original photo are compared. These stratification of local strain distributions imply that strain localization occurs very early even under small axial strains. Additionally, moist tamping method induces these non-uniform deformations.

Without considering the missed local strains along the specimen, the distribution of local strains from indirect evaluation are almost coincident with those from direct evaluations, which means the local deformations from indirect evaluation could represent the behavior of sand specimen in undrained triaxial test to some extent. Due to the fact that sand particle pattern could not follow the serious deformation of specimen occasionally, the results near the missing regions maybe not valid enough to show the local deformations of these regions.

It should be noted that local strain distribution is used to show an overview of the local deformations at any prescribed time, rather than focusing on a certain individual point. In order to get the evolutions of local strains during the whole test, nine positions were selected to show the step histories of local strains by direct and indirect evaluations. As shown in Fig. 5.13 (a) through (i), these local strains follow the change rule of axial strain measured by EDT when double amplitude of axial strain is less than 5%. Theoretically, the local strains along the specimen should be equal to each other in the triaxial test. However, the absolute displacement of sand at top part is relatively larger than the bottom part. This phenomenon will induce non-uniformity of specimen during deformation. The sand at upper part may become looser than the bottom part gradually. It also can be observed in Fig. 5.13 that the local strains at top part are relatively larger than the axial strain measured by EDT. Moreover, the local strains at middle positions of specimen are almost same as the global axial strain. The local strains at bottom of specimen are relatively smaller than the global axial strain. The evaluations of local strains are not valid when wrinkles and extremely large deformations occur, especially at the top of specimen.

Strains, defined as a percentage of relative deformations, could not reflect the different movement between dots on membrane and the sand particles of specimen. Instead of stains, displacements of dots and sand particles patterns are compared at the same positions for checking the potential slippages between each other. Similarly, three positons are selected to compare the displacements of dots and sand particles patterns which are located at the same positions. Based on the results in Fig. 5.14, it can be obtained that the displacements of traced dots and sand particles patterns are almost same with each other. However, there is a downward shifting of the curves in Fig. 5.14 (a) and (b) at the top and middle parts of specimen. The intercepts at x axis and y axis have different physical meanings. For example, the intercept at x axis means the residual displacement of dot when the displacement of sand particle pattern returns back to 0 mm. On the other hand, the intercept at y axis gives the residual displacement of sand particle pattern when the displacement of dot returns back to 0 mm. Fig. 5.15 shows the relationships of relative movement between dot and sand particle pattern versus cyclic number and excess pore water pressure ratio at top, middle and bottom of specimen. The relative movements start increasing after the initial liquefaction. This relative movement between dot and sand particle pattern is a kind of slippage which is relative larger at the top part of specimen than those from bottom parts. These slippages maybe affected by the gravity of sand particles when liquefaction occurs. In addition, this relative movement is accumulated during the following cycles.

## 5.3 Local deformations of Silica sand specimen in undrained triaxial tests

Fig. 5.16 shows the relationship between cyclic stress ratio and number of cycles required to cause 5% double amplitude of axial strain for Silica sand in undrained triaxial test when compared with the liquefaction resistance curves of Silica sand in undrained torsional shear tests. The results indicate that the liquefaction resistances of Silica sand in triaxial and torsional shear liquefaction tests are coincident with each other under the same experimental conditions. Moreover, specimens prepared by moist tamping method have a larger liquefaction resistance than those by air pluviation method at the same relative density.

### 5.3.1 Moist tamping method

The indirect and direct evaluation methods of local deformations have been introduced in chapter 4. Fig. 5.17 shows the observed behavior in test 10 where Silica sand specimen was consolidated to an initial effective confining stress of 104 kPa and subjected to undrained cyclic stress with a cyclic stress ratio of 0.288. Being similar with the analysis in section 5.2, several statuses during experiment were selected to plot the local strain distributions, such as the statuses when the maximum absolute value of axial strain was reached during extension and compression stages and when maximum excess pore water pressure ratio was reached in each cycle. These selected statuses are marked by blue circles and red triangles as shown in Fig. 5.18.

In Fig. 5.19 (a) through (c), the local strain distributions from direct and indirect evaluations are almost same with each other, which have the same trend as test 7. Since the moist tamping method induces stratification during specimen preparation, strain localization also occurred very early even when the axial strain was less than 2%. Based on the photos, these strain strips were affected by the necking phenomenon. As for the direct evaluations by excluding and including dots, the local strain distributions are almost same with each other, which mean the dots on the membrane have negligible affection on the direct evaluation. Under large axial strain conditions, the local strains from direct evaluations are relatively larger than those from indirect evaluations, especially when the excess pore water pressure ratio reaches 1.0.

As shown in Fig. 5.20, the local strain distribution at step 5200 is compared with its corresponding photo. The numbers marked at the local strain distribution present the order of elements. One element consists of four dots. Based on the comparison between local strain distribution and original photo, necking phenomenon is always accompanied with wrinkles when the loading direction is changed. Fig. 5.20 (b) shows the reason for the strain strip in Fig. 5.20 (a). The curvature of the membrane will affect the interval of the nearby dots in the digital image which is used for the calculation of local strain. On the other hand, these strain strips are significant character of strain localization.

In Fig. 5.21, axial strain and local strains from direct and indirect evaluations are compared at the same positions along the sand specimen. It can be observed that the local strains are following the same change trend as the axial strain measured by EDT. Since wrinkles, necking phenomenon and sand flowing near the pedestal occurred during testing, the local strains, especially from direct evaluation, were larger than the axial strain measured by EDT. Even without coordinate correction in triaxial tests, the local strains on vertical direction worked well and could represent the local deformation of specimen. There was a fact that wrinkles took place frequently when double amplitude of axial strain was larger than 5%. If the wrinkles occurred, accompanied with the local drainage in the wrinkles, considerable movement of sand particles near wrinkles would be found.

In Fig. 5.22, several photos are selected to show the relative movement between sand particles and the nearest dots. Based on these photos, a new black sand particle which was covered by white particles at beginning of test came out at step 222. In addition, the relative locations of black particles were always changing during testing. As for the local strains, dots and sand particles patterns were computed separately. Even the local strains at one position from direct and indirect evaluations are same with each other, it does not indicate there is no relative movement between dots and sand particles. As shown in Fig. 5.23, the displacements of sand particles are not zero when the dots return to their original positions during testing. Same as the results on Toyoura sand, the settlement of sand particles at top part of specimen is larger than the settlement at the bottom and middle positions. Since sand flowed out to the gap between membrane and pedestal during liquefaction, the selected sand particle pattern at bottom of specimen had a relatively larger settlement than the sand particles at middle position.

Based on the results in Fig. 5.22 and 5.23, it can be concluded that there are relative movements between dots and sand particles during undrained triaxial liquefaction test. This relative movement indicates that slippage between membrane and sand specimen occurs. Generally, sand particles are suspended in the liquid during liquefaction as a common sense. However, sand particles migration in liquefaction test is still unclear even before the initial liquefaction. Moreover, an assumption of deformation of sand specimen in liquefaction test is that it is uniform throughout the test. Strain localization will not occur in liquefaction test. In the test results, evidence has proved that settlement of sand particles took place to some extent. Even though it is a common sense, it is worthy of investigating sand particle migration in liquefaction tests.

*Slippage*

Being different from local strain, slippage is another important parameter in this study to present the liquefaction characteristics of sand specimen. In order to eliminate the location affection, the investigation of slippage is started at selecting the positions of sand particles and dots. As shown in Fig. 5.24, sand particles are selected at the positions adjacent to the dots. Same as the tracing of dot, single sand particle was tracked to evaluate its displacement. After obtaining the coordinates of each, their corresponding displacements and slippage could be computed by the following equations:

$$D_{dot,ydisp,i} = Y_{dot,coord,i} - Y_{dot,coord,original} \qquad (5\text{-}1)$$

$$D_{sand,ydisp,i} = Y_{sand,coord,i} - Y_{sand,coord,original} \qquad (5\text{-}2)$$

$$Slippage = D_{dot,ydisp,i} - D_{sand,ydisp,i} \qquad (5\text{-}3)$$

Where *i* is the photo number and original is the first photo without deformation. The physical meaning of positive slippage is that the dot moves upward relatively to the sand particle. In other words, positive slippage also means that sand particle moves downward relatively to the adjacent dot. As plotted in Fig. 5.25, there are four statuses with potential positive slippages.

The relationships between vertical slippage and axial strain at selected points are shown in Fig. 5.26. The results indicate that vertical slippage is accumulated during the cyclic loading. However, the quantity of vertical slippage is largely affected by the positions of selected points. It can be seen in the figure that slippage keeps constant at first and increases to large value suddenly. In order to find the reasons for the leap of slippage, Fig. 5.27 shows the relationships between excess pore water pressure ratio, deviator stress and slippage of the data in Fig. 5.26. The leap of vertical slippage occurs only when the excess pore water pressure reaches almost 1.0. Moreover, little slippage may take place when there is effective stress. Since coordinate correction is not applied in the triaxial test, the little vertical slippage maybe affected by the accuracy of image analysis. Additionally, these slippages are evaluated by the movements of selected dots and adjacent sand particles. In the study of slippage, the movement of sand particle pattern used for calculating local strains is also compared with the movement of adjacent dot.

Fig. 5.28 shows the relationships between vertical slippage and axial strain at different positions along the specimen. The vertical slippage is computed by the relative movement between sand particle pattern and adjacent dot. Since the top part of specimen was subjected to the maximum absolute displacement referring to the pedestal, the slippages at top part were relatively larger than the slippages at the bottom. A slight inclination of vertical slippage was also found during the cyclic loading. In compression stage, the downward movement of sand particle pattern is relative larger than the dot. On the other hand, in extension stage, the upward movement of sand particle pattern is also larger than the dot. This phenomenon satisfies the mechanism of sand specimen in triaxial test. The deformation of membrane is following the deformation of sand. Regardless of extension and compression, the vertical stress was always positive. Therefore, the radial stress induces the upward movement of sand particles during extension. After the reversion of loading direction to downward, the temporary maximum of excess pore water pressure would be reached subsequently. If the corresponding maximum value was almost equal to the initial effective stress, the liquefied condition of specimen may induce the leap of slippage as shown in Fig. 28 (c). Under such circumstance, the loose status of top part of specimen increases the potential of triggering vertical slippage.

Fig. 5.29 gives the relationships between vertical slippage and excess pore water pressure ratio at top part of specimen. Significant leap of vertical slippage occurs when excess pore water pressure ratio reaches almost 1.0. As for the liquefaction status defined by excess pore water pressure ratio, the specimen is assumed to liquefy when it is larger than 0.95. 1.0 is also widely used to express the fully liquefied status. Before the initial liquefaction, vertical slippage remains constant when there is effective stress. After the initial liquefaction, vertical slippage may increase to a higher value or keep constant to some extent. As a common sense, vertical slippage could be triggered when the loose specimen is liquefied. Based on the results, this common sense was proved. Another phenomenon is that the vertical slippage may happen during cyclic mobility to some content. It should be noticed that there may be no vertical slippage even when the excess pore water pressure ratio is 1.0.

In order to find the quantity of accumulated slippage during cyclic mobility, the vertical slippage was selected when excess pore water pressure reached its maximum value in each cycle. As shown in Fig. 5.30, in each cycle, the excess pore water pressure ratio would reach its temporary maximum value twice at extension and compression stages, respectively. From the curves, it can be seen that the recovery of slippage appears at each cycle. This means the movements of sand particles are always larger than the dots, regardless of loading direction. Therefore, the decreasing of slippage indicates that the large movement of sand particles after the reversion of loading direction at the half cycle offsets the accumulated slippage. The global change trend of accumulated slippage is increasing with the cyclic number.

Based on the above analysis, almost all the vertical slippages are triggered when the excess pore water pressure ratio is 1.0. Therefore, Fig. 5.31 shows the relationship between accumulated vertical slippage and excess pore water pressure ratio when excess pore water pressure ratio reaches the maximum at each half cycle. The results indicate that there is no slippage before excess pore water pressure ratio reaching 0.96. The slippage will be accumulated during cyclic mobility, especially at the top part of specimen which is subjected to serious deformation. Fig. 5.32 gives the relationship between amplitude of vertical slippage and double amplitude of axial strain at each cycle. The trend indicates that the vertical slippage increases with the double amplitude of axial strain. Fig. 5.33 shows the relationships between vertical slippage and cyclic number when the axial strain returns to 0. It can be seen that the accumulated vertical slippage increases with the cyclic number.

### 5.3.2 Air pluviation method

Fig. 5.34 gives the observed behavior in test 14 where specimen was prepared by air pluviation method and subjected to undrained cyclic loading with a cyclic stress ratio of 0.4. Since the relative density of specimen was 70%, number of cycles was needed to achieve the cease condition of test by the double amplitude axial strain of 20%. Due to limitation of memory card, only 10000 photos were taken during this test. As shown in Fig. 5.34 (b) and (f), the statuses when axial strain as well as excess pore water pressure ratio reached its temporary maximum at each cycle were selected to plot the local strain distributions.

Fig. 5.35 shows the local strain distributions at selected statuses in test 14. The local strain distributions by direct and indirect evaluations are same as each other, which indicate that the deformations of dots on membrane are coincident with those of sand particle patterns. Compared with the local strain distributions of specimen prepared by moist tamping method, necking phenomenon is not observed on the specimen prepared by air pluviation method in test 14. The local deformations along the specimen are uniform. For the evaluation of local strains, Fig. 5.36 gives the time histories of local strain at one selected position along the specimen, compared with the axial strain by EDT. These three curves are overlapped with each other, which support the same evaluations of local deformations from direct and indirect measurements. Another evidence is shown in Fig. 5.37, the slippage on vertical direction is less than 0.1 mm even under the axial strain of 8%. Based on the relationship between vertical slippage and excess pore water pressure ratio shown in Fig. 5.38, it can be deemed that slippage did not occur in the test. Since the mean diameter of colored Silica sand is around 0.5 mm, the center of tracked pattern may be affected by its movement and the rotation of sand particles. In addition, the shape of dot could not remain during compression and extension. Therefore, the coordinate of tracked point may be influenced by these tracing conditions. Compared with the local strain distributions in test 10, sand specimen prepared by air pluviation method has a more uniform local strain distribution than the specimen prepared by moist tamping method.

The specimen in test 14 was prepared by air pluviation method with a relative density of 65%. In order to compare the results under the same relative density by different specimen preparation methods, the specimen in test 16 was prepared by air pluviation method at a relative density of 53%. Observed behavior in test 16, where specimen was consolidated to 104 kPa and subjected to undrained cyclic stress at a cyclic stress ratio of 0.288 subsequently, is shown in Fig. 5.39.

Being similar as test 10, statuses when the absolute value of axial strain and excess pore water pressure ratio reach their corresponding maximums at each half cycle are selected and marked in Fig. 5.39 (b) and (e). The local strain distributions of these selected statuses by direct and indirect evaluations are shown in Fig. 5.40, respectively. Based on these comparisons between direct and indirect evaluations, the dots have the same local strain distributions with the sand particles patterns to some extent. Since the cell was not so clear, some dots were not tracked perfectly. As shown in the local strain distribution of step 2831 from indirect evaluation, local strains with large difference occurred at the bottom part of specimen. It was affected by the missing dots which would be subjected to large and incorrect displacements. In addition, the neighboring dots were tracked accurately and their displacements precisely represented the local behaviors of specimen. Therefore, the error regions of local strain distributions were always combined by large negative and positive local strains. As for the direct evaluations at step 2402, large local strain occurred at the left bottom of specimen. From the original photo at step 2402, wrinkle appeared vertically in which sand was flowing to the gap between membrane and porous stone. Accompanied with sand flowing, the sand particle rotation and re-mixing would affect the accuracy of the traced sand particle pattern. On the other hand, there was no affection on the indirect evaluations. Strange local strains were not found on the positions of membrane where sand flowing happened. These strange local strains expanded to the top part of specimen when the axial strain reached a large value. Based on the above analysis, the direct evaluations of local deformations have the advantages of measuring the real local behaviors of sand specimen in liquefaction tests. When wrinkles occur during the test, the local deformations near wrinkle from both indirect and direct evaluations are not valid. The dots on winkle could not present the movement of sand particles inside. In addition, the movement of sand particles inside of wrinkle could not be traced accurately. However, the strange or invalid local strains point out that serious strain localization takes place near the wrinkle. Compared with the local strain distributions in test 10 where the sand specimen was prepared by moist tamping method, the local strain distributions of sand specimen prepared by air pluviation method in tests 14 and 16 are more uniform.

In Fig. 5.41, the local stains of one selected position at top part of specimen are compared with global axial strain. They have the same change trend and overlap with each other when the double amplitude of axial strain is less than 15%. After that, the local strains were relatively larger than the global axial strain. Fig. 5.42 shows the relationships between vertical slippage and excess pore water pressure ratio at two selected positions at the top of specimen. The vertical slippages keep 0 mm until the initial liquefaction. Significant slippage occurs when excess pore water pressure ratio reaches 1.0 during cyclic mobility. Slippage will keep constant when there is effective stress of specimen. Moreover, the relationships between vertical slippage and axial strain at the same selected positions are plotted in Fig. 5.43. The slippages keep 0 mm under small axial strains during which the excess pore water pressure ratio is less than 1.0. Following that, leaps of vertical slippage only occur at negative axial strains when the loading direction is changed from extension to compression. As is known, the excess pore water pressure will achieve its temporary maximum after the reversion of loading direction. After the reversion of loading direction, the specimen has the largest potential to liquefy. Due to the gravity of sand particles, vertical slippage will be triggered in the followed compression stage. Beyond that, the curves of slippage vs axial strain start tilting under larger axial strain in the extension stage, which indicates the slippage may occur even there is effective stress. Serious strain localization induces the extreme loose local part of specimen. This vertical slippage may be affected by the non-uniform deformations and local densities at measured positions.

## 5.4 Summary

Particle Image Velocimetry was employed in the triaxial liquefaction tests with a transparent membrane to study the local deformations of sand specimen indirectly and directly. The results are summarized as follows:

1. Image analysis could be used for measuring the local deformations directly and indirectly with a high resolution of 0.025mm/pixel. Local strains could be displayed visually and clearly by local strain distributions.
2. Based on the indirect and direct evaluations of local deformations on Toyoura sand and Silica sand in undrained cyclic triaxial tests, the local strains from dots on membrane are almost same as those from sand particles patterns, except for the positions near wrinkle.
3. Compared with the local strain distributions of Silica sand specimen prepared by moist tamping method, air pluviation method induces relatively uniform local strain distributions. This also indicates that specimen prepared by air pluviation method is more uniform than the specimen prepared by moist tamping method. Since the sand specimen was prepared by moist tamping method with five layers and four interfaces, necking phenomenon was observed at the interfaces during extension stage even under a small axial strain. In addition, non-uniform local strains were formed along the specimen even when the axial strain was less than 2%.
4. The relative displacement between dot on membrane and adjacent sand particle named as slippage will not be zero and could not remain constant along cyclic loading. When global axial strain returns to zero, vertical slippage is accumulated and increases with the cyclic number.
5. Leap of slippage is triggered under non-effective stress condition during cyclic mobility. Non-slippage before initial liquefaction proves the validity of previous researches which used the deformations of membrane to represent the sand behavior in drained tests.
6. Comparing the quantities of slippage in the tests with different relative densities, loose specimen has a larger potential to induce vertical slippage than dense specimen.

# Reference

1. Chiaro, G., Kiyota, T. and Koseki, J. (2013). Strain localization characteristics of loose saturated Toyoura sand in undrained cyclic torsional shear tests with initial static shear. *Soils and Foundations, 53*(1), 23-34.
2. Desrues, J., Chambon, R., Mokni, M. and Mazerolle, F. (1996). Void ratio evolution inside shear bands in triaxial sand specimens studied by computed tomography. *Géotechnique, 46*(3), 529-546.
3. Han, C. and Vardoulakis, I. (1991). Plane-strain compression experiments on water-saturated fine-grained sand. *Géotechnique, 41*(1), 49-78.
4. Harris, W. W., Viggiani, G., Mooney, M. A. and Finno, R. J. (1995). Use of stereophotogrammetry to analyze the development of shear bands in sand. *Geotechnical Testing Journal, 18*(4), 405-420.
5. Hoshino, R., Miyashita, Y., Sato, T. and Koseki, J. (2015). Local deformation properties of sand specimens in triaxial liquefaction tests evaluated by direct and indirect observations. *Bulletin of ERS, 48,* 63-71.
6. Kiyota, T., Sato, T., Koseki, J. and Abadimarand, M. (2008). Behavior of liquefied sands under extremely large strain levels in cyclic torsional shear tests. *Soils and Foundations, 48*(5), 727-739.
7. Mokni, M. and Desrues, J. (1999). Strain localization measurements in undrained plane-strain biaxial tests on Hostun RF sand. *Mechanics of Cohesive ‐ frictional Materials, 4*(4), 419-441.
8. Rechenmacher, A. L., Abedi, S., Chupin, O. and Orlando, A. D. (2011). Characterization of mesoscale instabilities in localized granular shear using digital image correlation. *Acta Geotechnica, 6*(4), 205-217.
9. Rechenmacher, A. L. and Finno, R. J. (2003). Digital image correlation to evaluate shear banding in dilative sands. *Geotechnical Testing Journal, 27*(1), 13-22.
10. Sadrekarimi, A. and Olson, S. M. (2010). Particle damage observed in ring shear tests on sands. *Canadian Geotechnical Journal, 47*(5), 497-515.
11. Tatsuoka, F., Ochi, K., Fujii, S. and Okamoto, M. (1986). Cyclic undrained triaxial and torsional shear strength of sands for different sample preparation methods. *Soils and Foundations, 26*(3), 23-41.
12. White, D., Take, W. and Bolton, M. (2003). Soil deformation measurement using particle image velocimetry (PIV) and photogrammetry. *Géotechnique, 53*(7), 619-631.
13. Yoshida, T. (1995). Shear banding in sands observed in plane strain compression. *Localization and bifurcation theory for soils and rocks*, 165-179.

14. Yoshida, T. and Tatsuoka, F. (1997). Deformation property of shear band in sand subjected to plane strain compression and its relation to particle characteristics. *Proc. 14^<th> ICSMFE, Hamburg, 1997, 1*, 237-240.

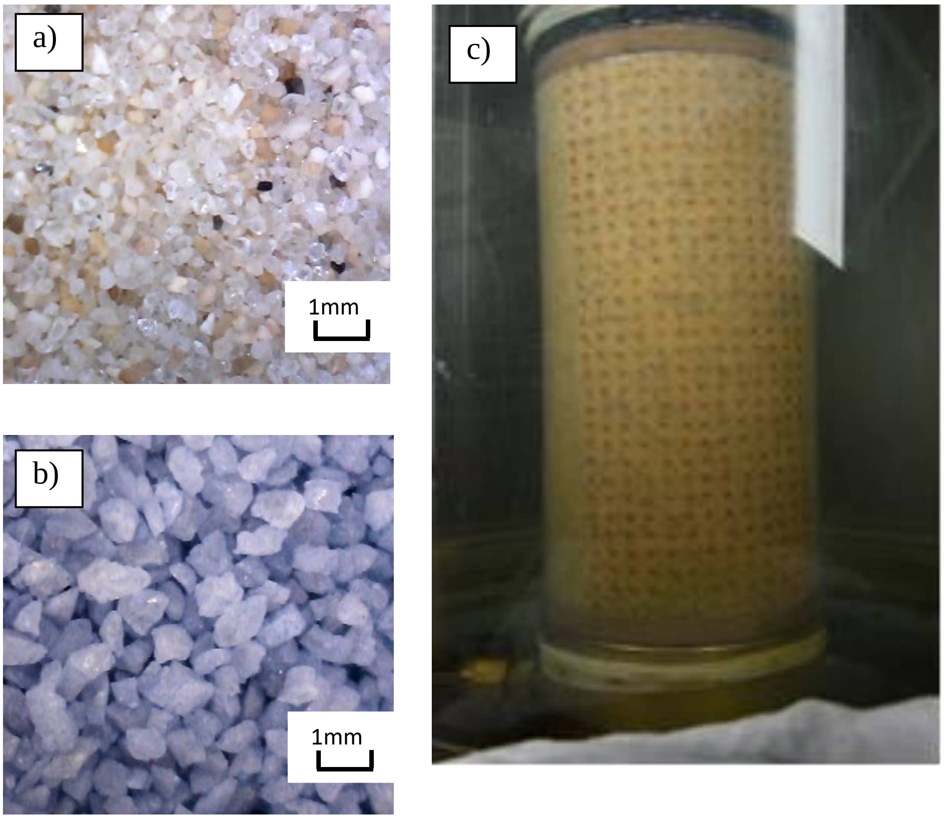

a) Toyoura sand, b)blue-colored sand, c)side view of specimen using transparent membrane and red dots

**Fig. 5.1 Photos of Toyoura sand, colored Silica sand and side view of specimen (Hoshino et al., 2015)**

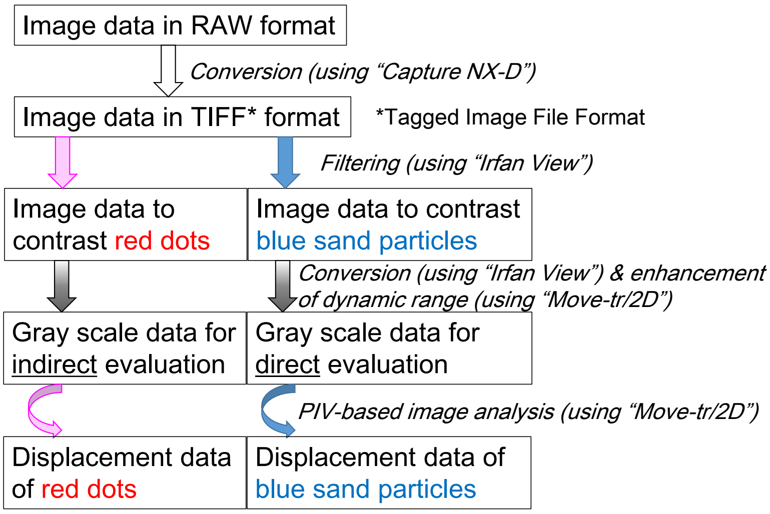

**Fig. 5.2 Flow chart of image data process (Hoshino et al., 2015)**

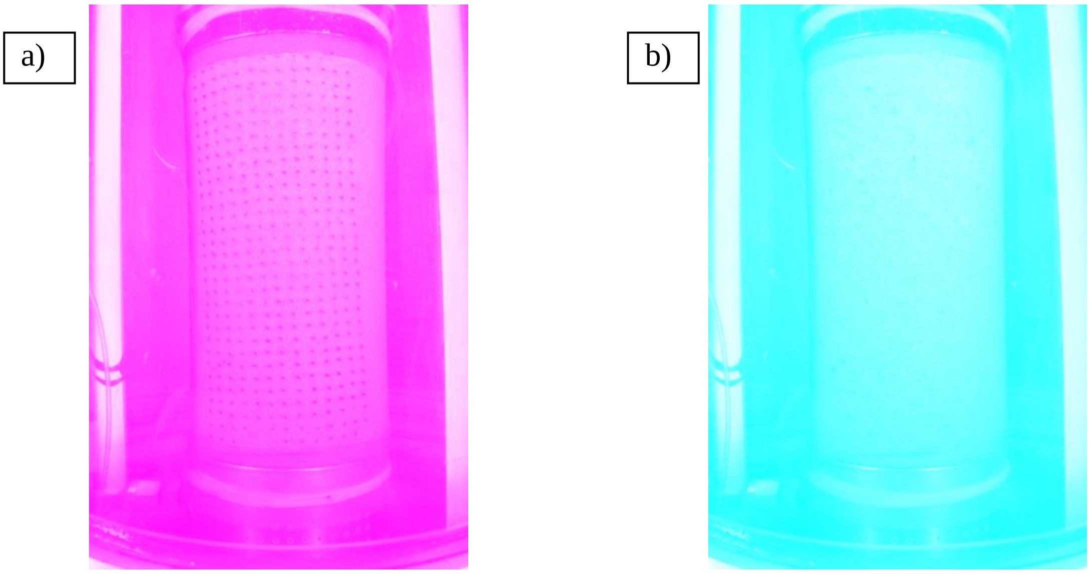

a) indirect and b) direct evaluations

**Fig. 5.3 Typical images after filtering process (Hoshino et al., 2015)**

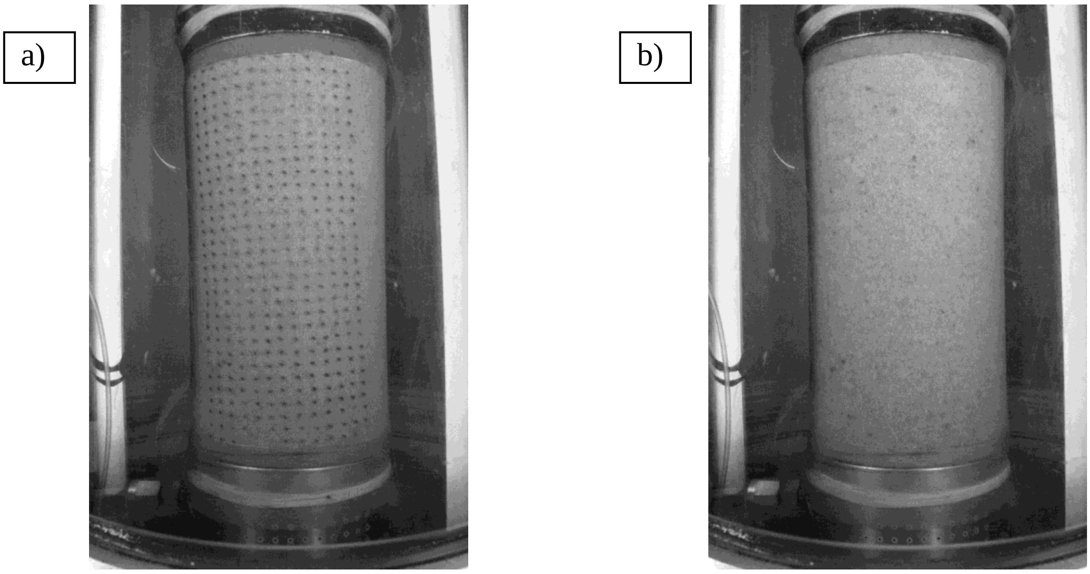

a) indirect and b) direct evaluations

**Fig. 5.4 Typical images after converting (Hoshino et al., 2015)**

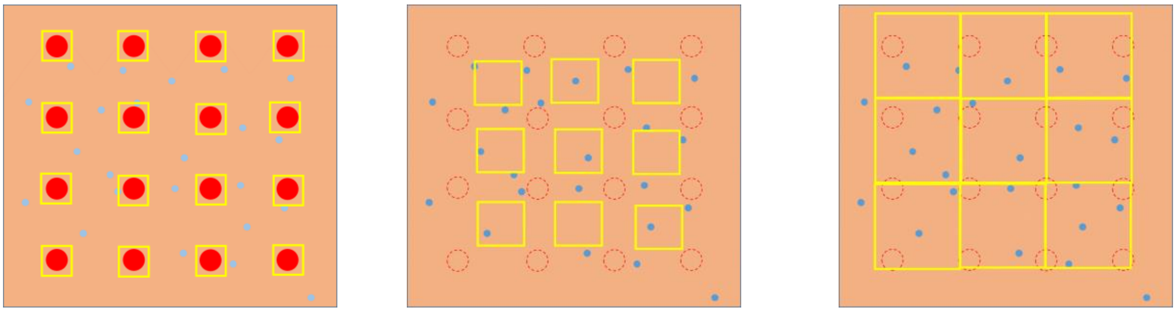

a)Dot analysis b)Sand analysis excluding dots c. Sand analysis including dots

**Fig. 5.5 Tracked regions of direct and indirect evaluations of local deformations (Hoshino et al., 2015)**

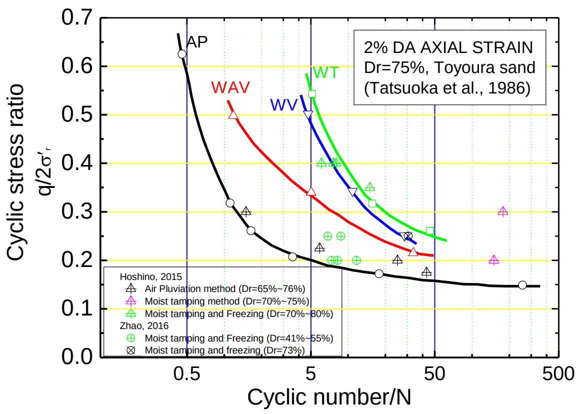

**Fig. 5.6 Stress ratio versus cyclic number to 2% DA axial strains by triaxial tests on Toyoura sand (Tatsuoka et al., 1986)**

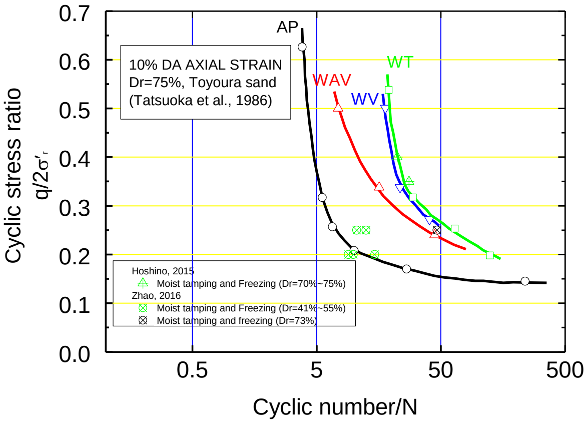

**Fig. 5.8 Stress ratio versus cyclic number to 10% DA axial strains by triaxial tests on Toyoura sand (Tatsuoka et al., 1986)**

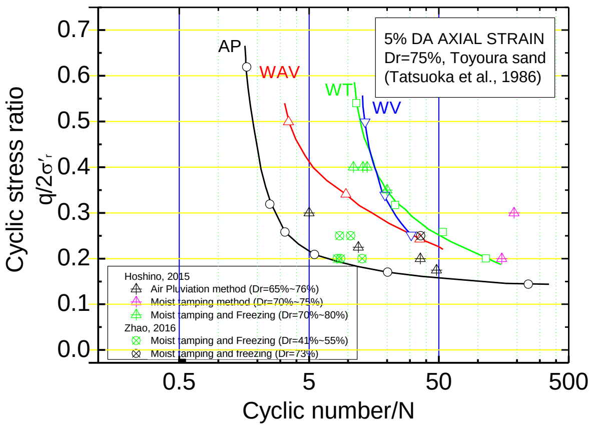

**Fig. 5.7 Stress ratio versus cyclic number to 5% DA axial strains by triaxial tests on Toyoura sand (Tatsuoka et al., 1986)**

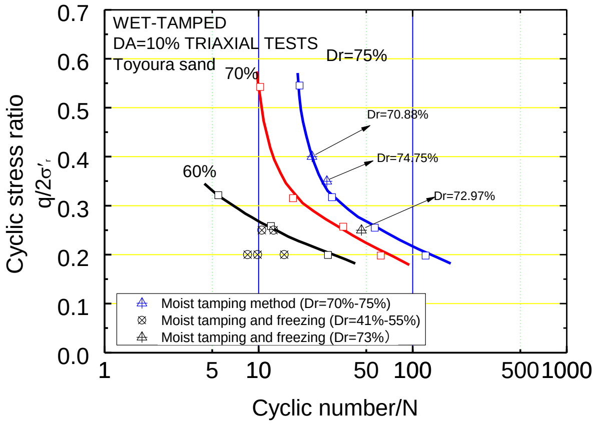

**Fig. 5.9 Stress ratio versus cyclic number to 10% DA axial strain by tiaxial tests on Toyoura sand with different relative densities (Tatsuoka et al., 1986)**

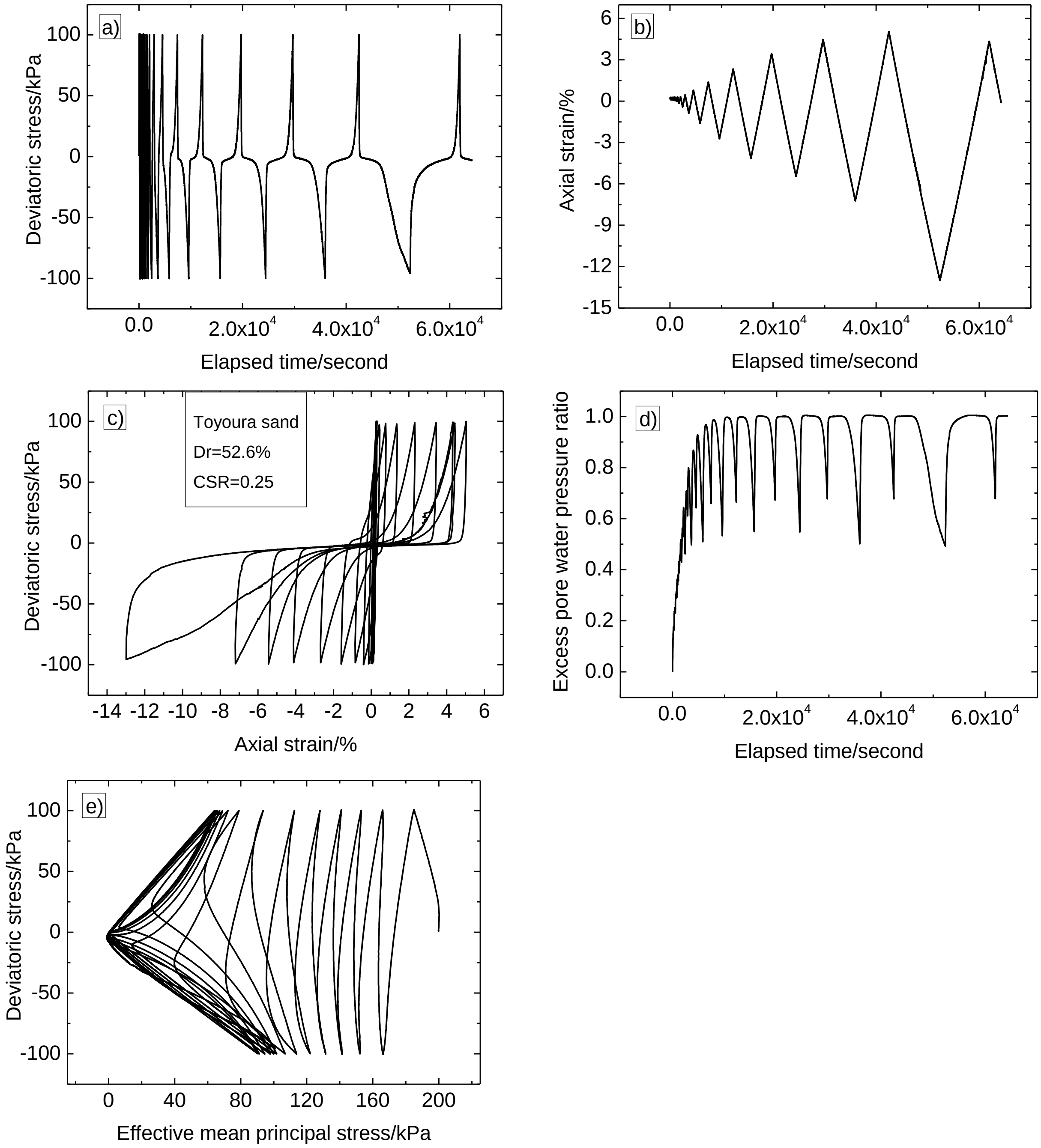

**Fig. 5.10 Results from test 7 on Toyoura sand**

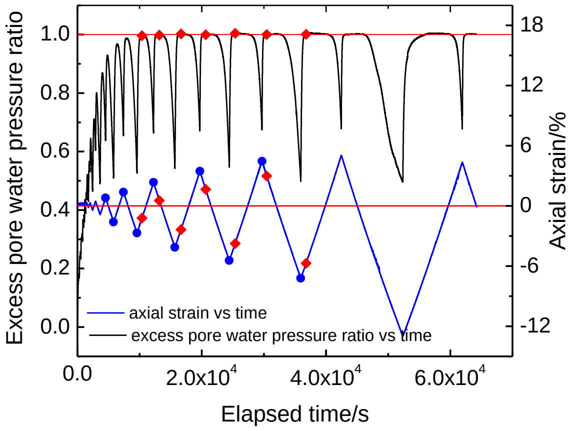

**Fig. 5.11 Selected statuses to plot the local strain distributions in test 7**

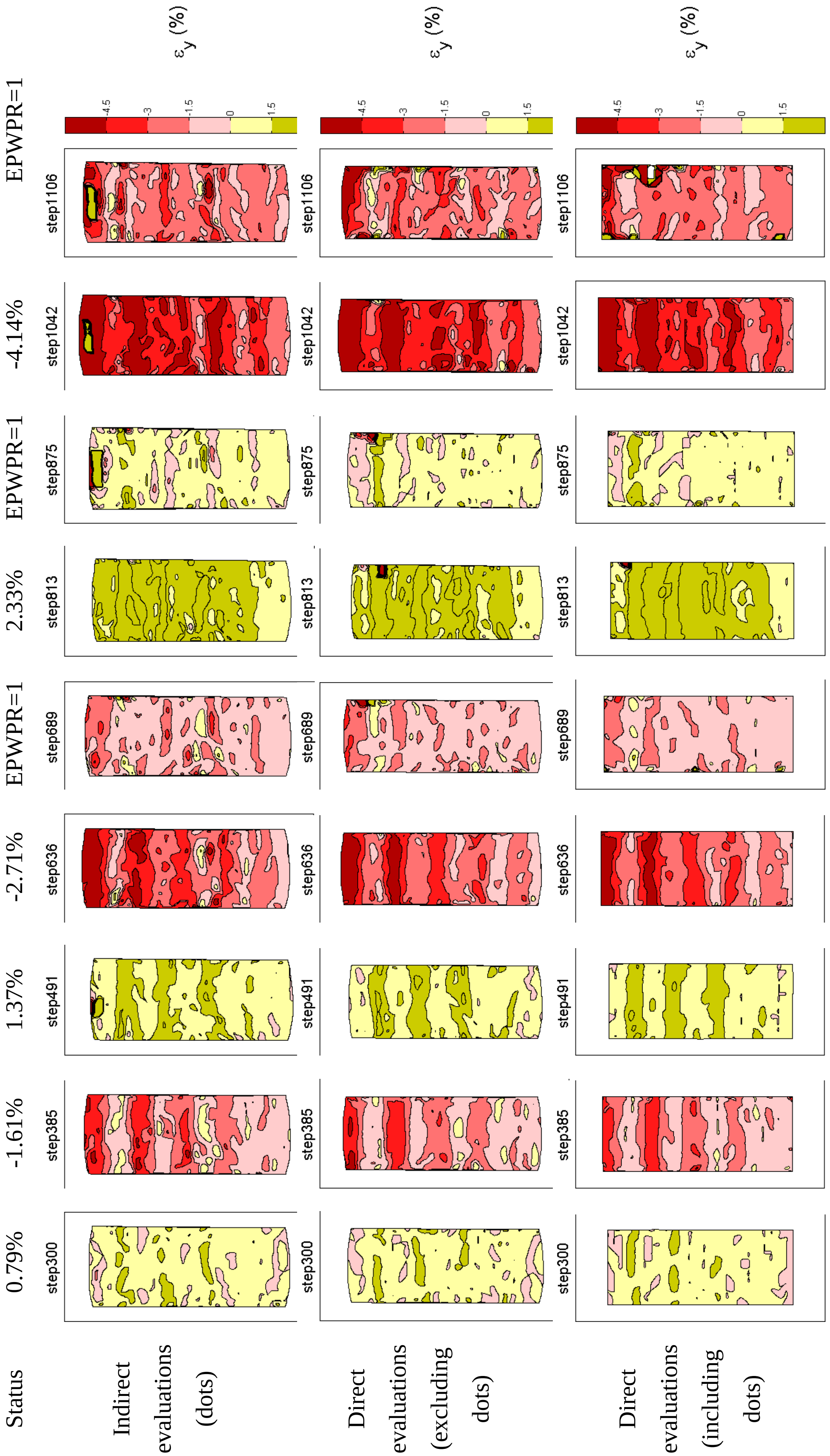

Fig. 5.12a, Local strain distributions of test 7 at selected statuses

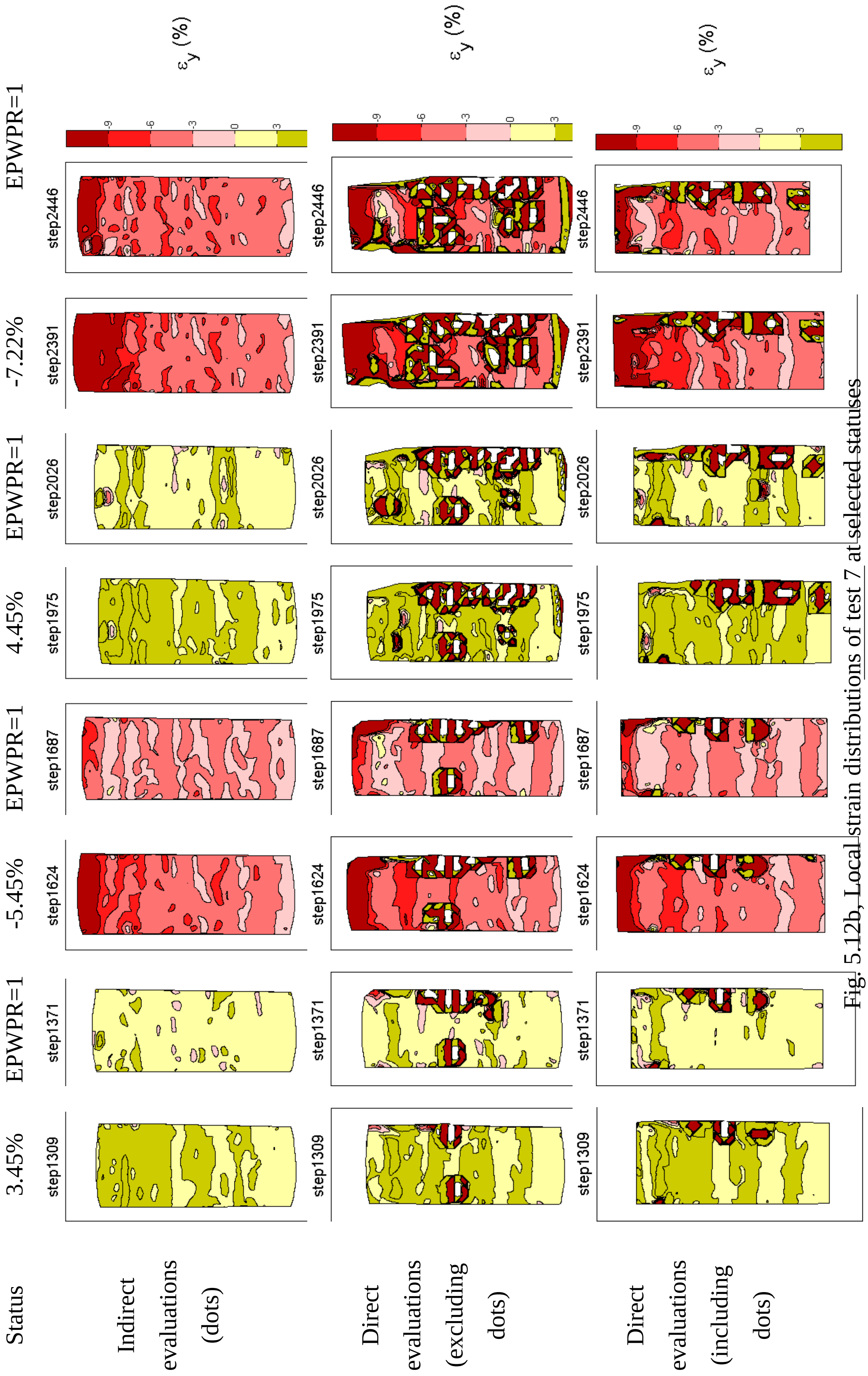

Fig. 5.12b, Local strain distributions of test 7 at selected statuses

**Fig. 5.12 Local strain distributions of test 7 at selected statuses**

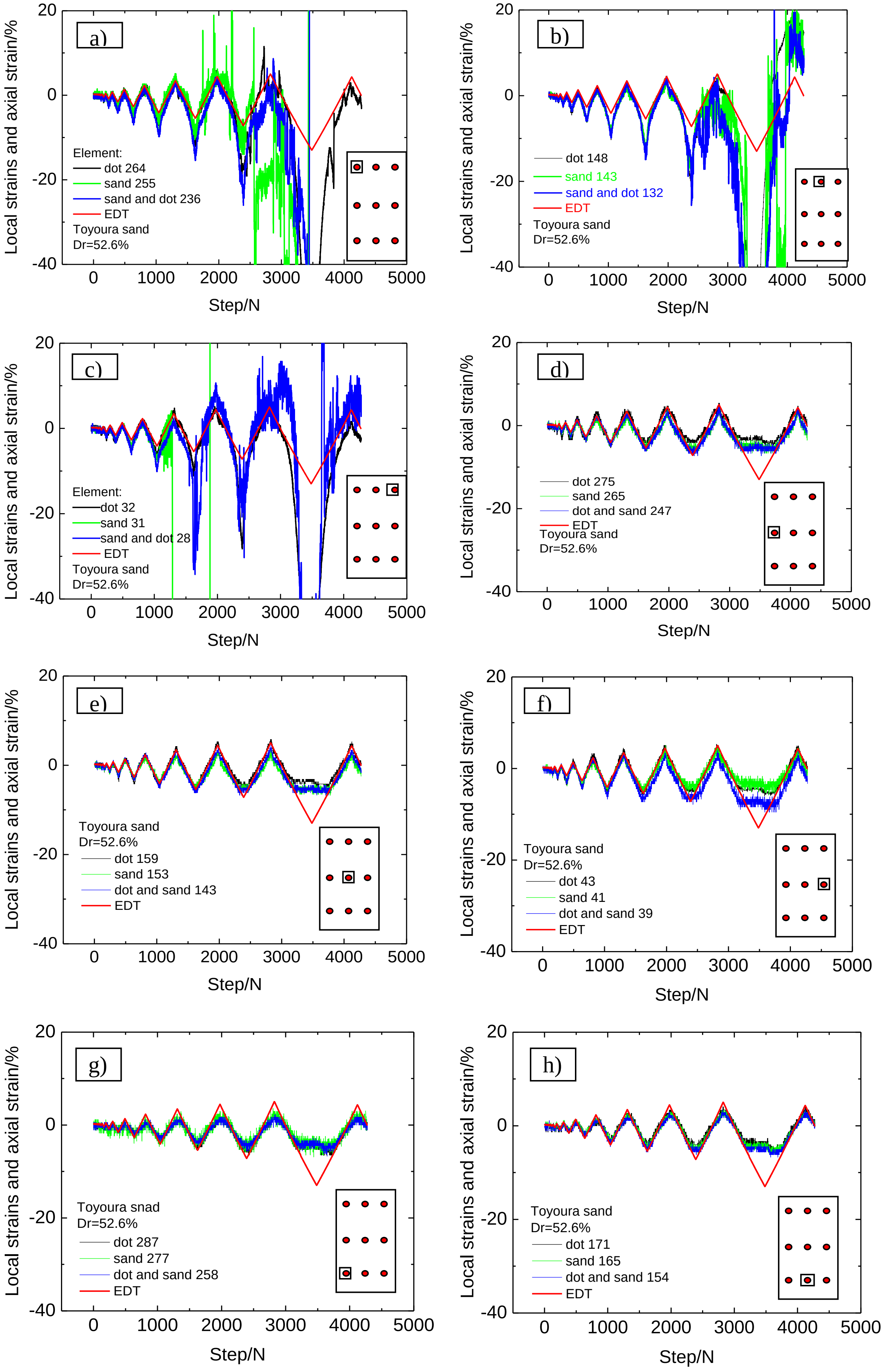
a)
Local strains and axial strain/%
20
0
-20
-40
0
1000
2000
3000
4000
5000
Step/N
Element:
dot 264
sand 255
sand and dot 236
EDT
Toyoura sand
Dr=52.6%
b)
dot 148
sand 143
sand and dot 132
EDT
Toyoura sand
Dr=52.6%
c)
Element:
dot 32
sand 31
sand and dot 28
EDT
Toyoura sand
Dr=52.6%
d)
dot 275
sand 265
dot and sand 247
EDT
Toyoura sand
Dr=52.6%
e)
Toyoura sand
Dr=52.6%
dot 159
sand 153
dot and sand 143
EDT
f)
Toyoura sand
Dr=52.6%
dot 43
sand 41
dot and sand 39
EDT
g)
Toyoura snad
Dr=52.6%
dot 287
sand 277
dot and sand 258
EDT
h)
Toyoura sand
Dr=52.6%
dot 171
sand 165
dot and sand 154
EDT

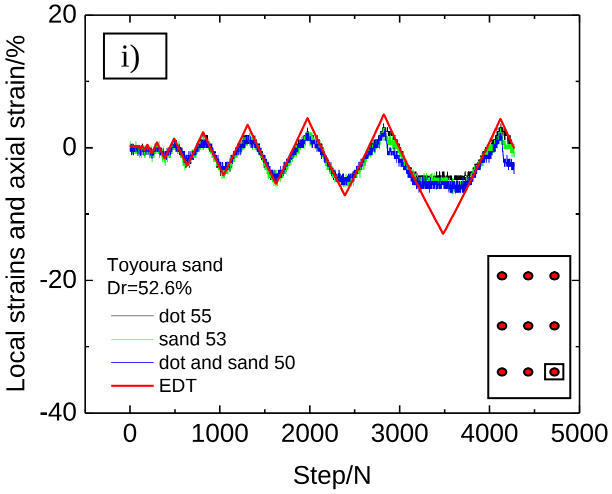

Fig. 5.13 Comparison of local strains and axial strain at different positions

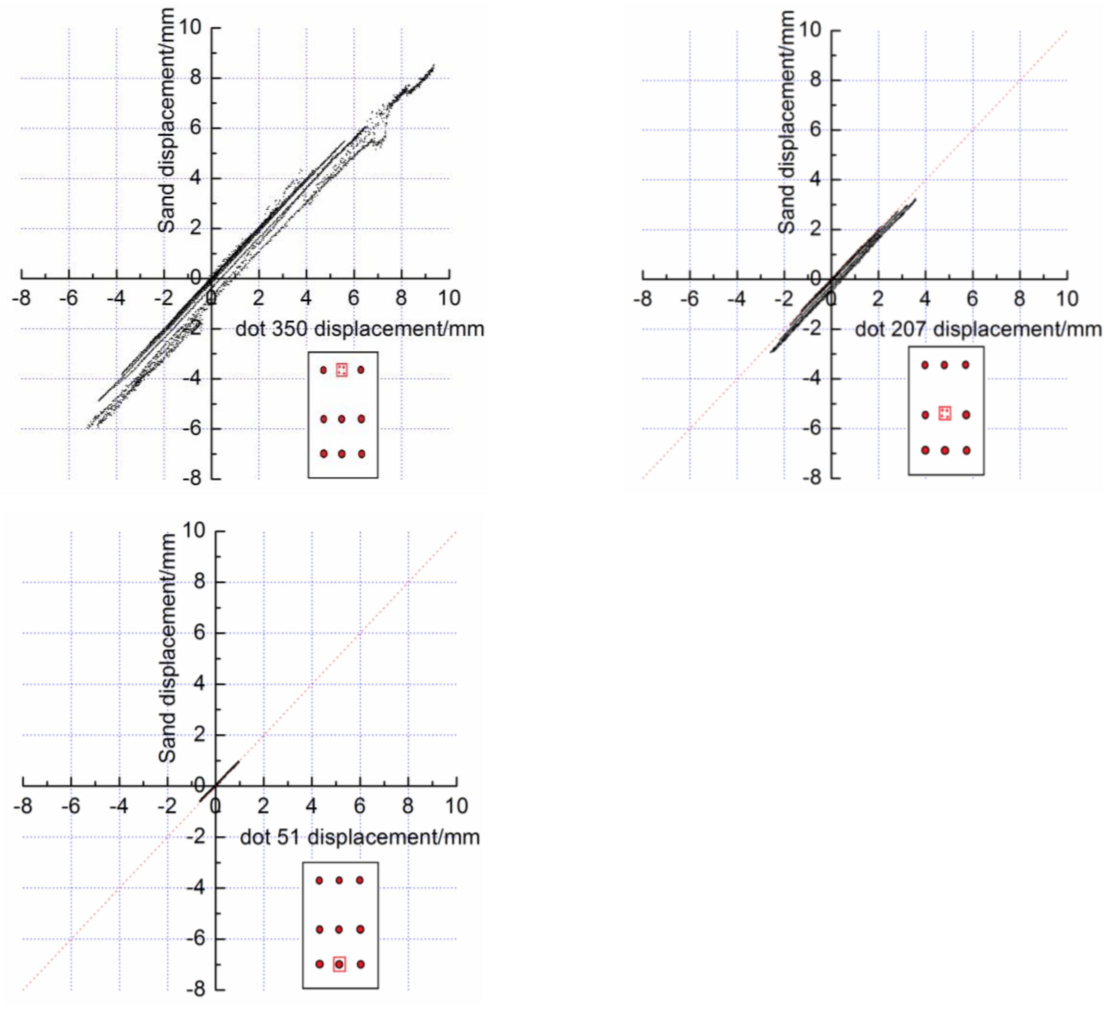

Fig. 5.14 Comparison between the displacements of dots and sand particle patterns at different positions

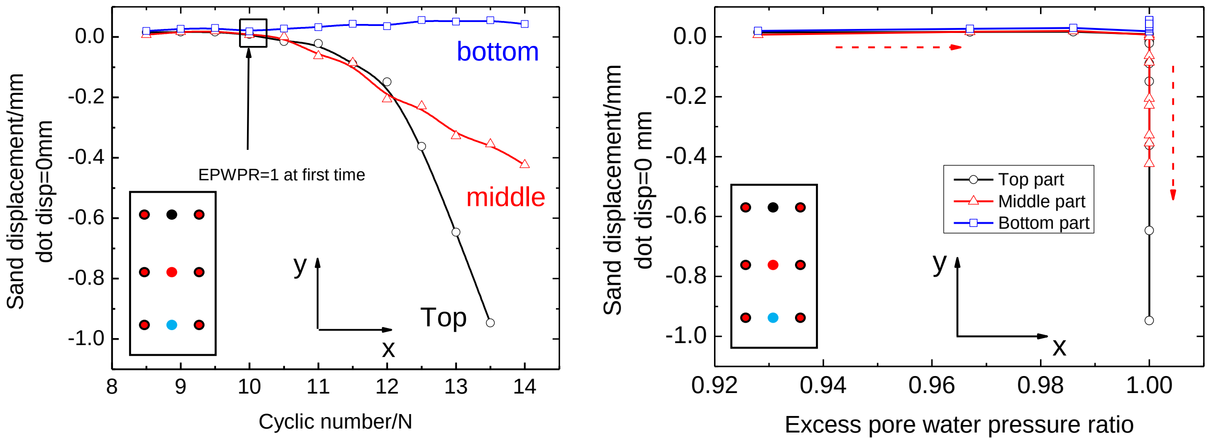

**Fig. 5.15 Sand displacements at different positions when dot displacement returned back to 0 mm at each cycle**

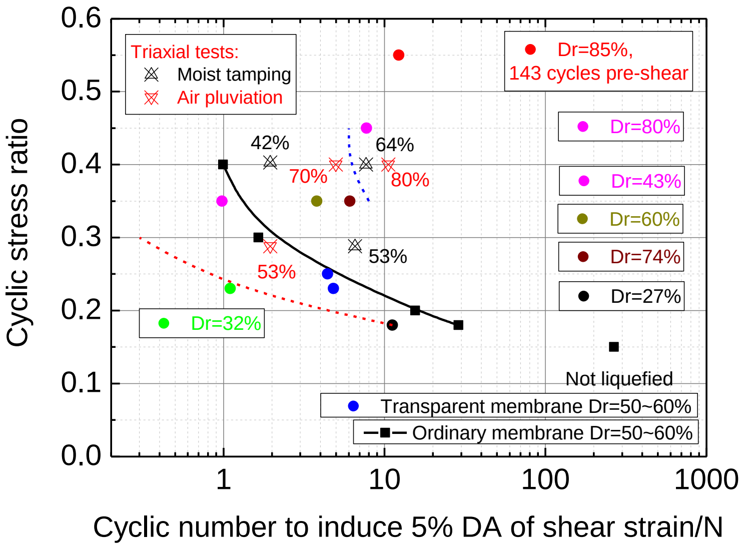

**Fig. 5.16 Liquefaction resistance curves of Silica sand to cause 5% DA of strains in triaxial and torsional shear liquefaction tests**

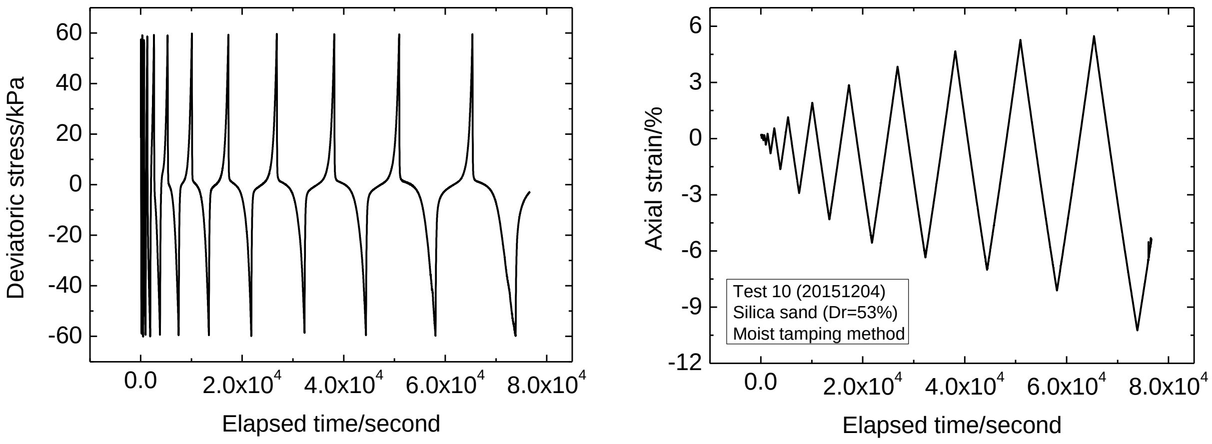

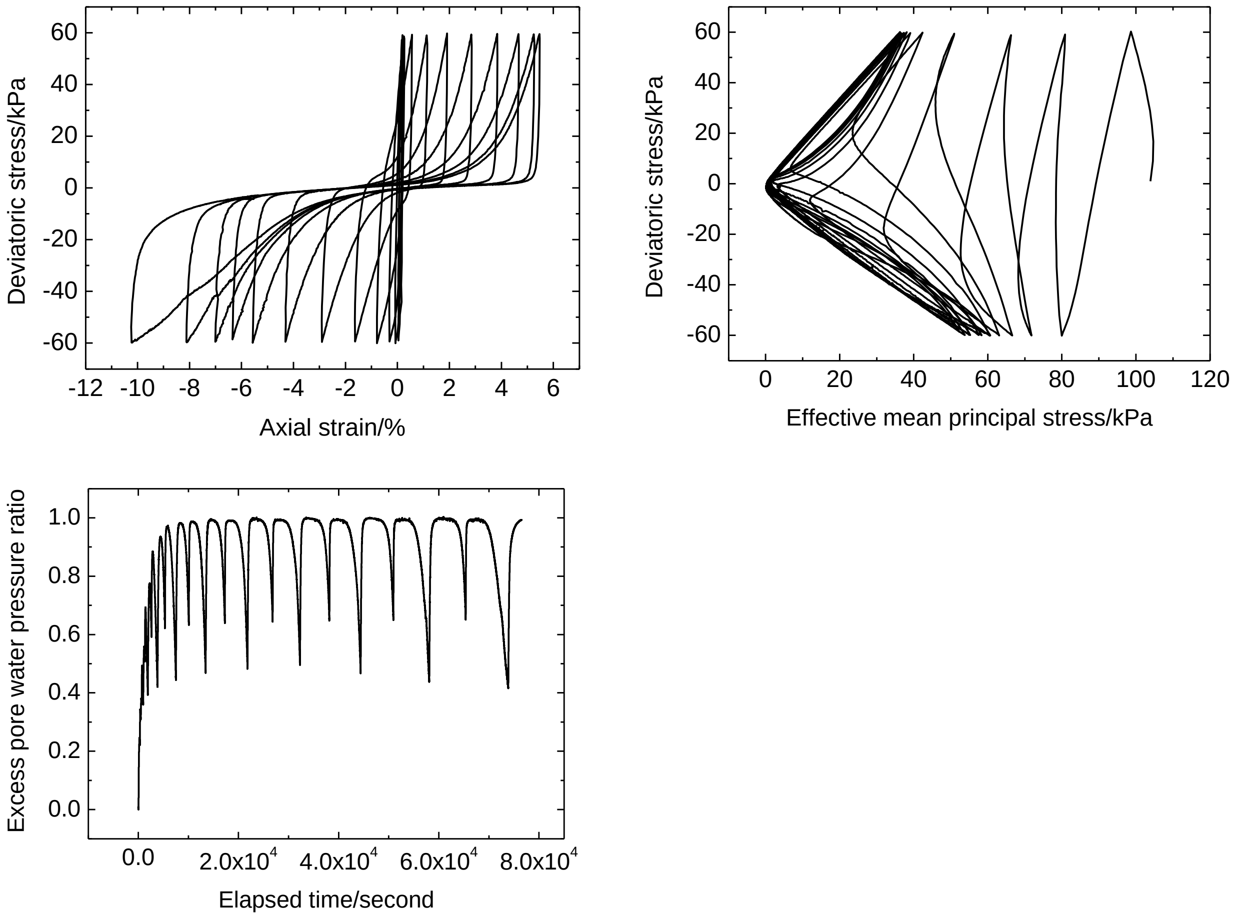

Fig. 5.17 Results from test 10 (Silica sand prepared by moist tamping method)

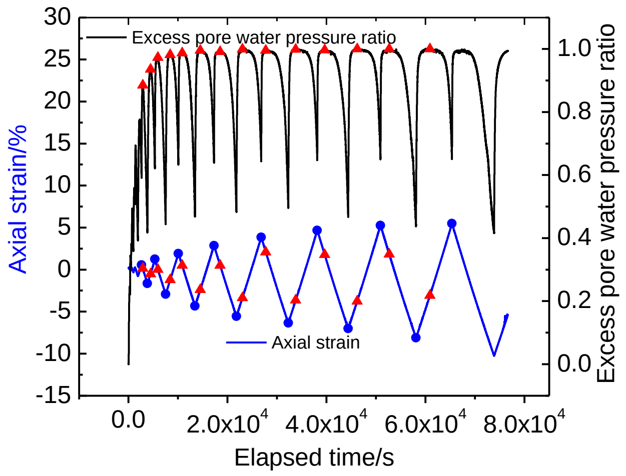

Fig. 5.18 Selected statuses in the time histories of axial strain and excess pore water pressure ratio

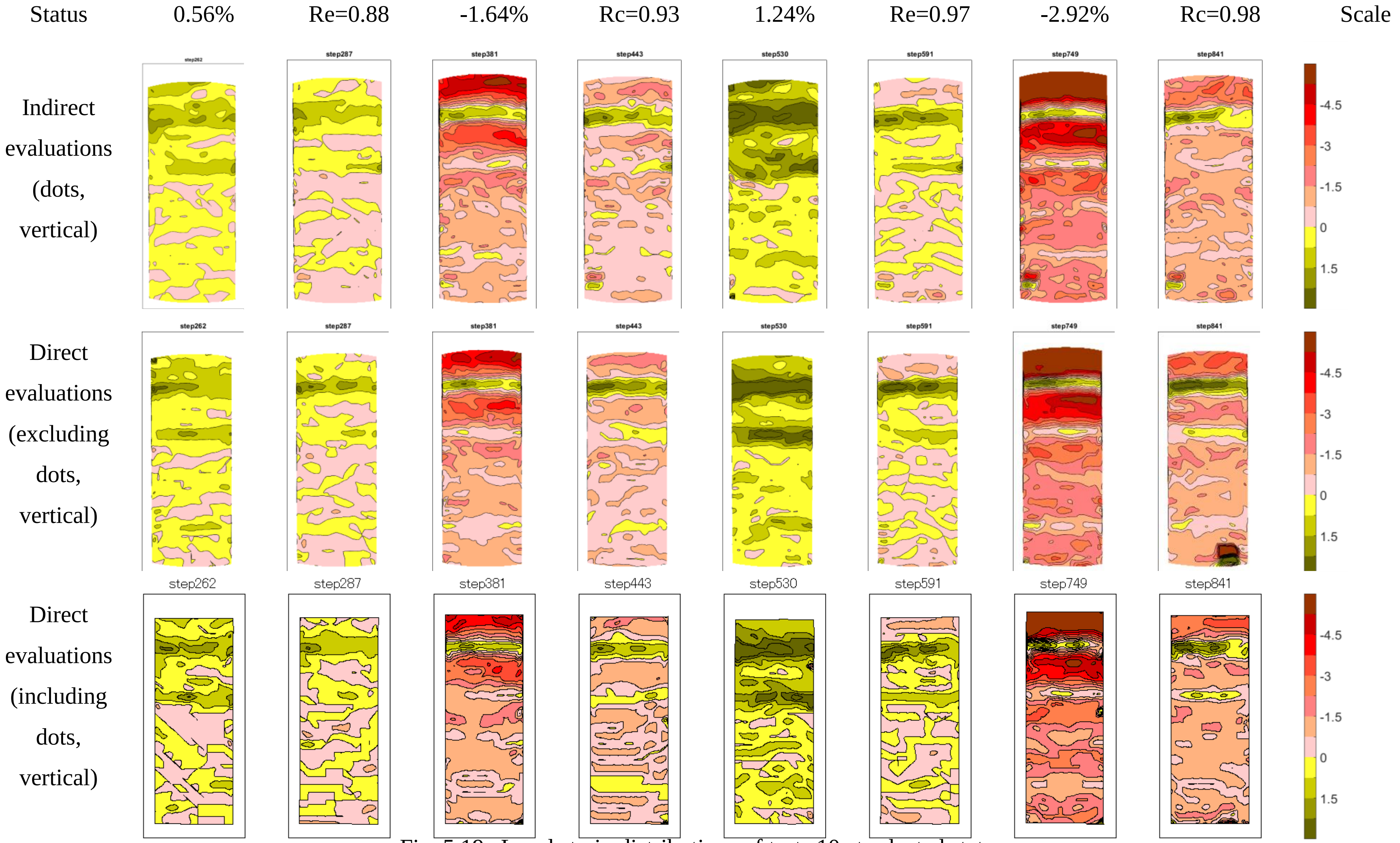

Fig. 5.19a Local strain distributions of tests 10 at selected statuses

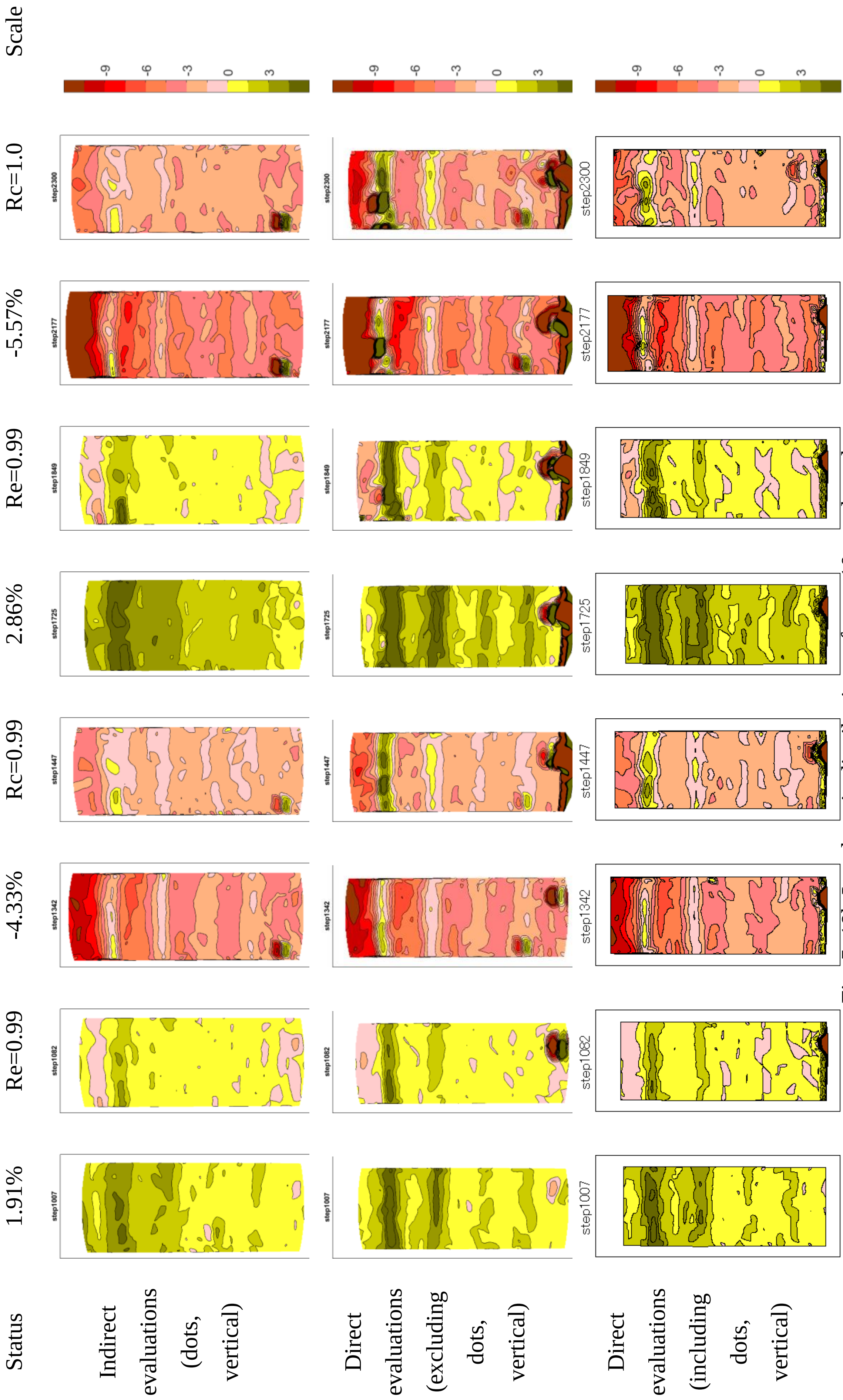

Fig. 5. 19b Local strain distributions of tests 10 at selected statuses

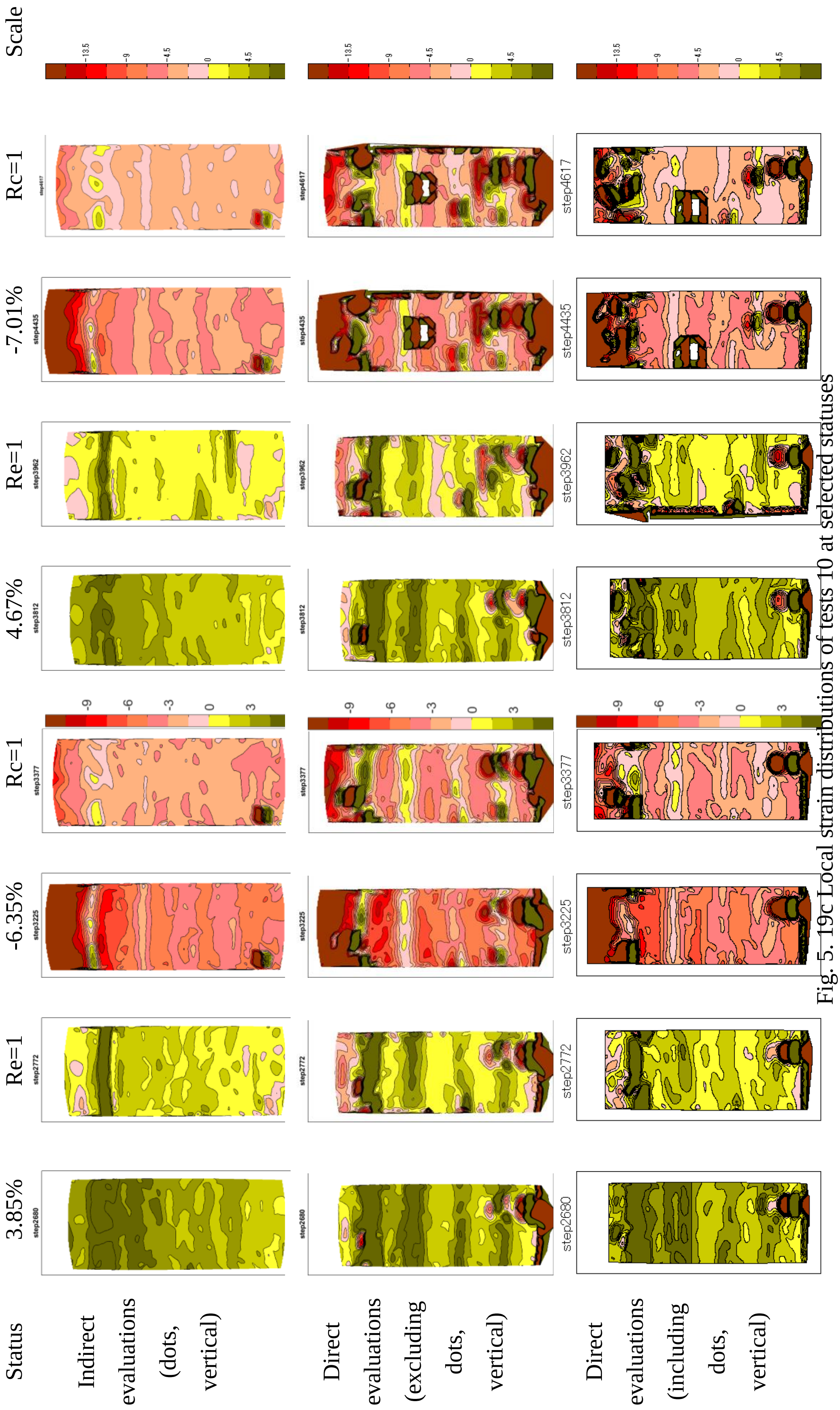

Fig. 5. 19c Local strain distributions of tests 10 at selected statuses

**Fig. 5.19 Local strain distributions of tests 10 at selected statuses**

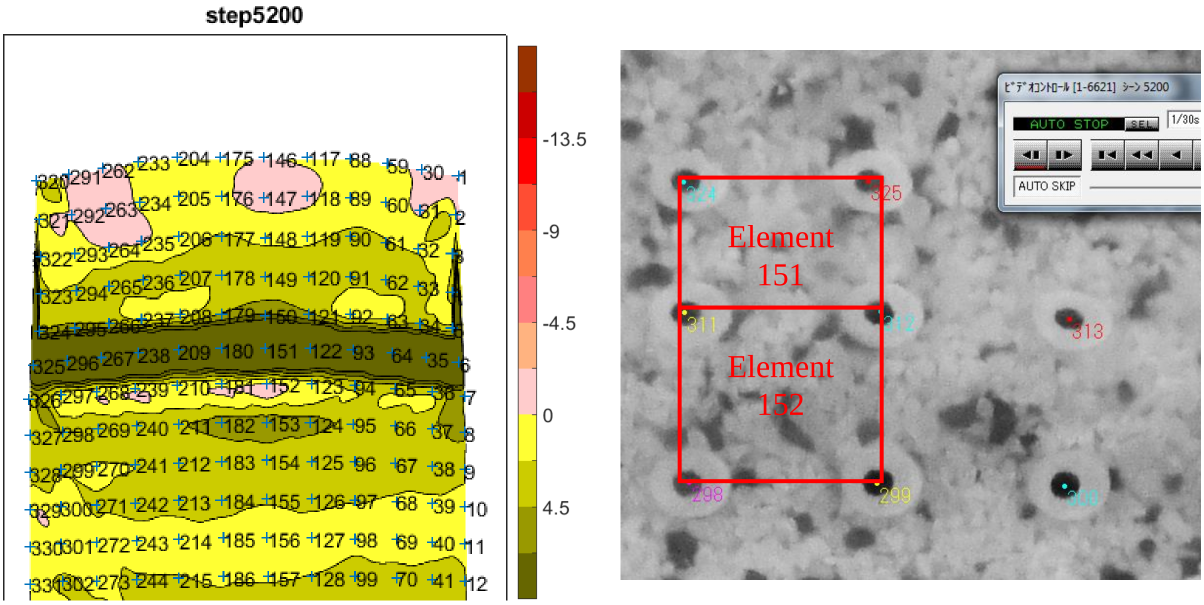

a) Local strain distributions

b) Corresponding photo

**Fig. 5.20 local strain distribution and corresponding photo at step 5200**

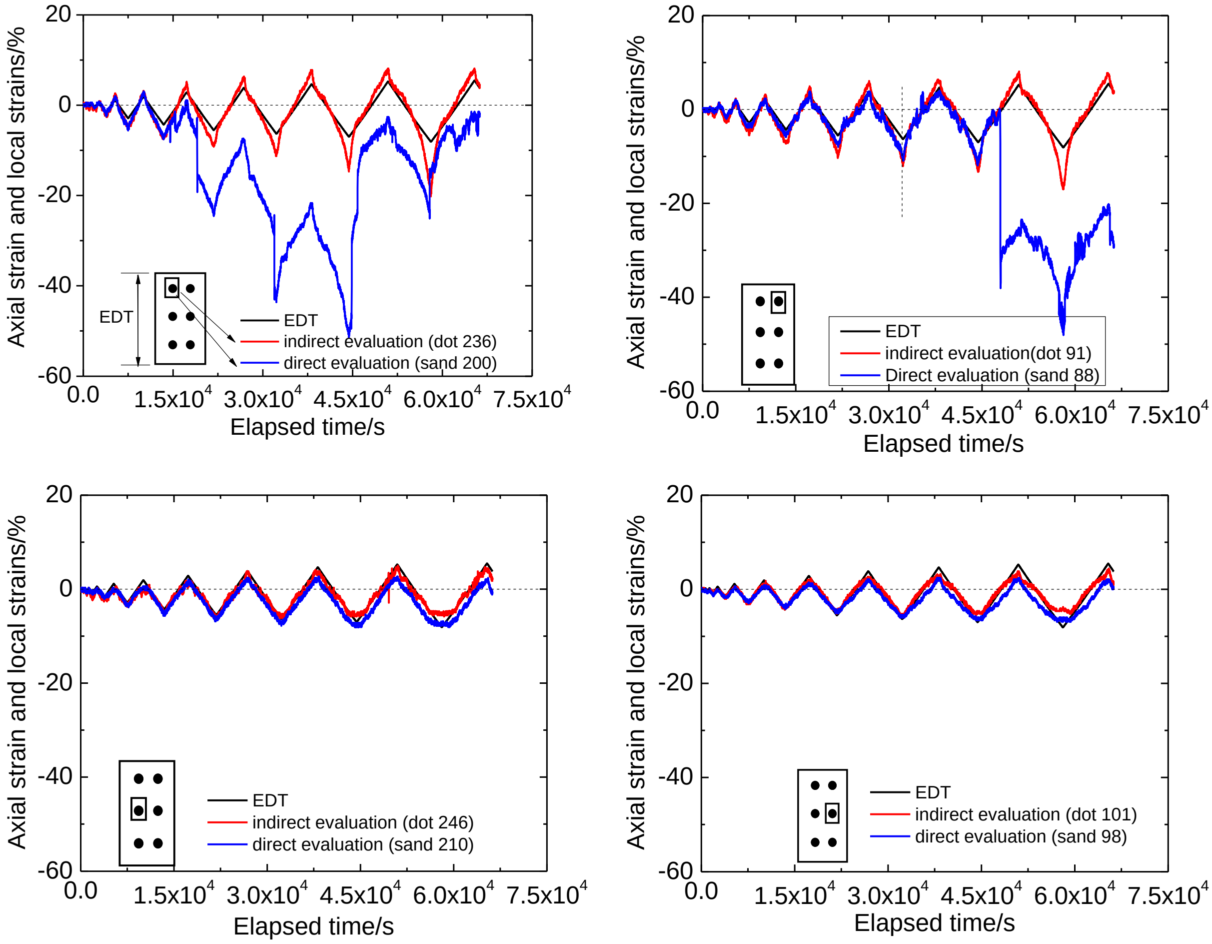

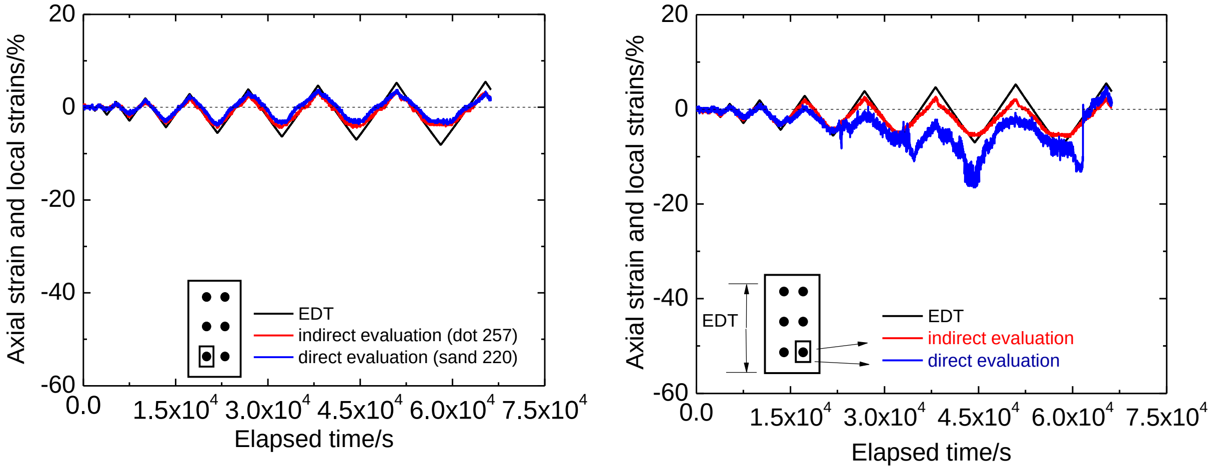

**Fig. 5.21 Time histories of axial strain and local strains of Silica sand specimen in test 10**

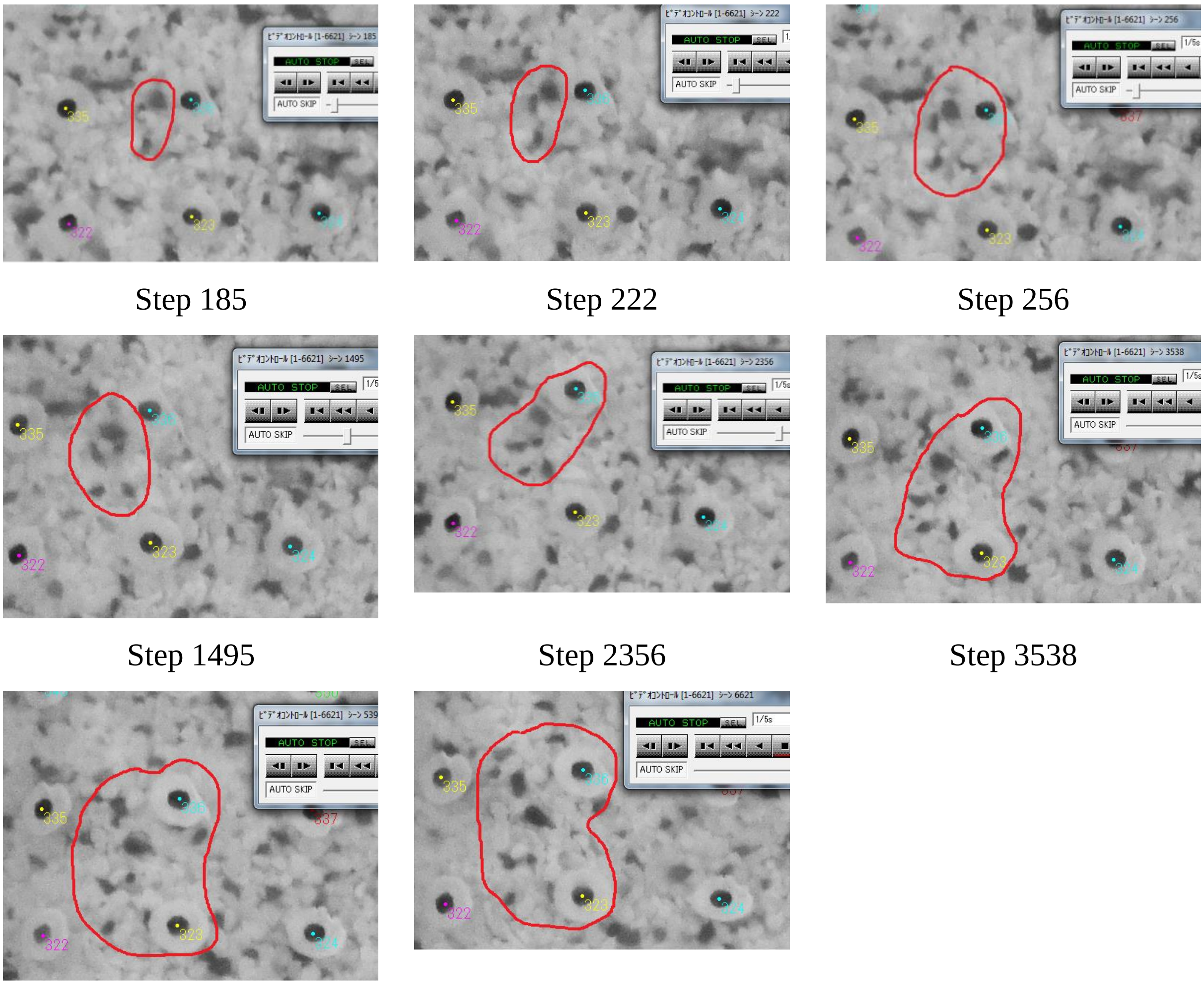

Step 185

Step 222

Step 256

Step 1495

Step 2356

Step 3538

Step 5395

Step 6621

**Fig. 5.22 Relative movement of sand particles during test**

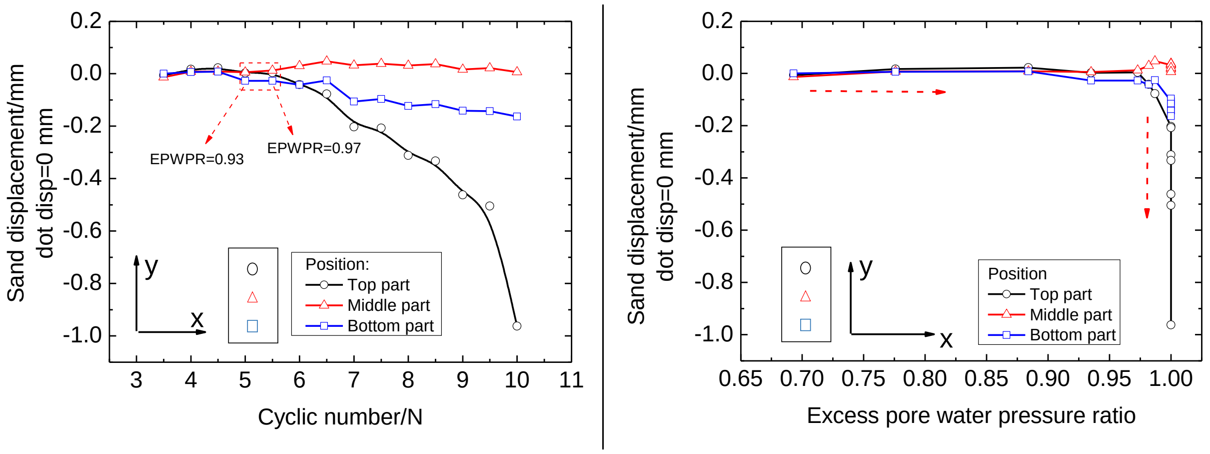

**Fig. 5.23 Sand displacements at different positions when dot displacement returned back to 0 mm in test 10**

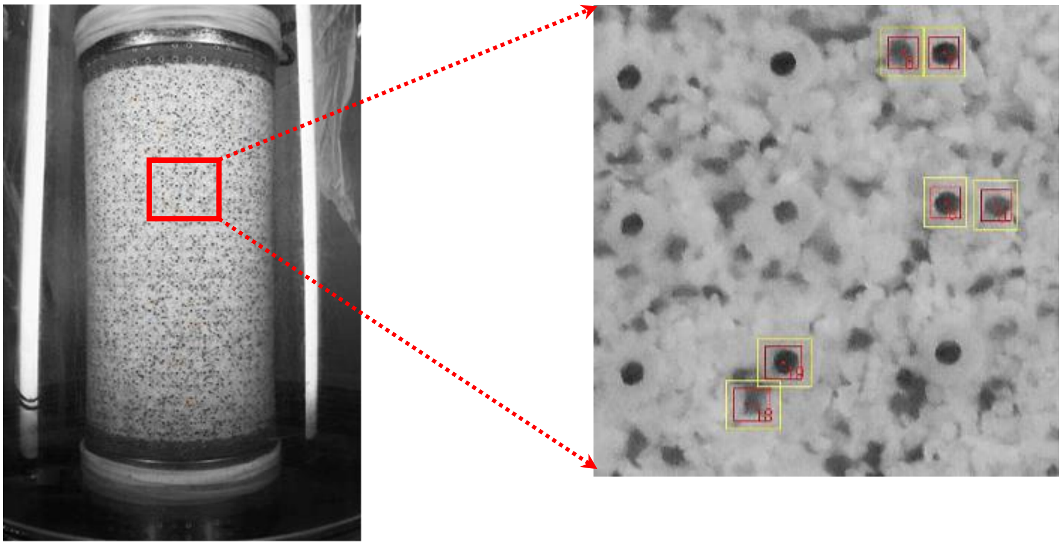

**Fig. 5.24 dots and sand particles setting for slippage analysis**

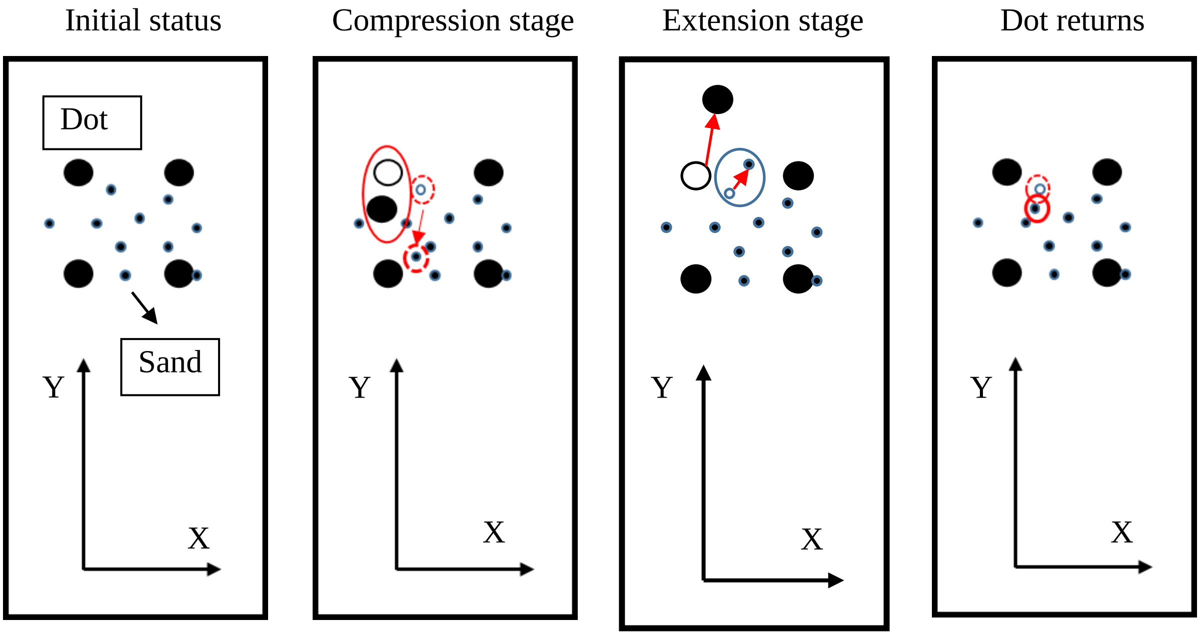

No slippage

Positive slippage

Positive slippage

Positive slippage

**Fig. 5.25 The physical meanings of positive slippage at different statuses**

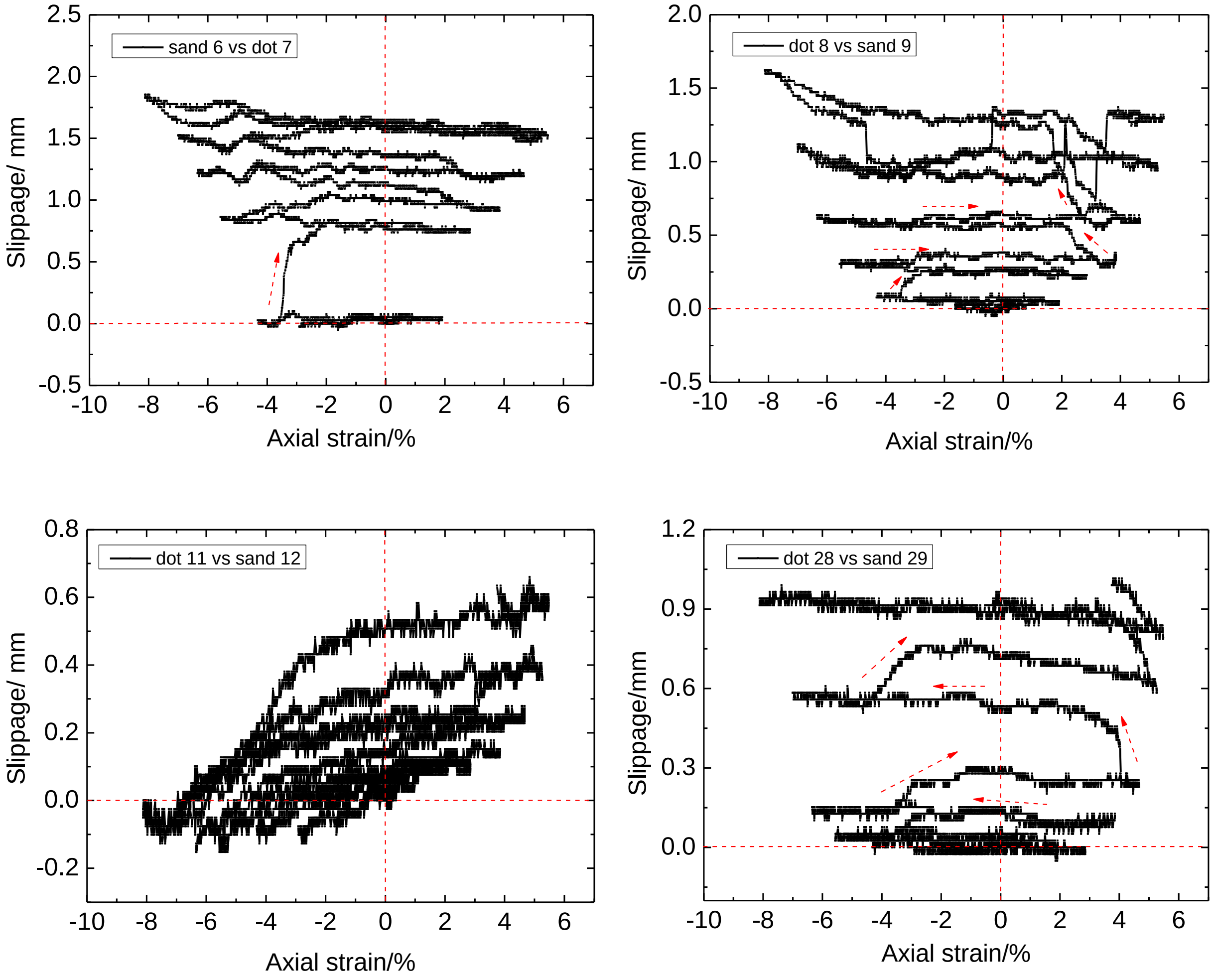

**Fig. 5.26 Relationship between vertical slippage and axial stain at selected points in test 10**

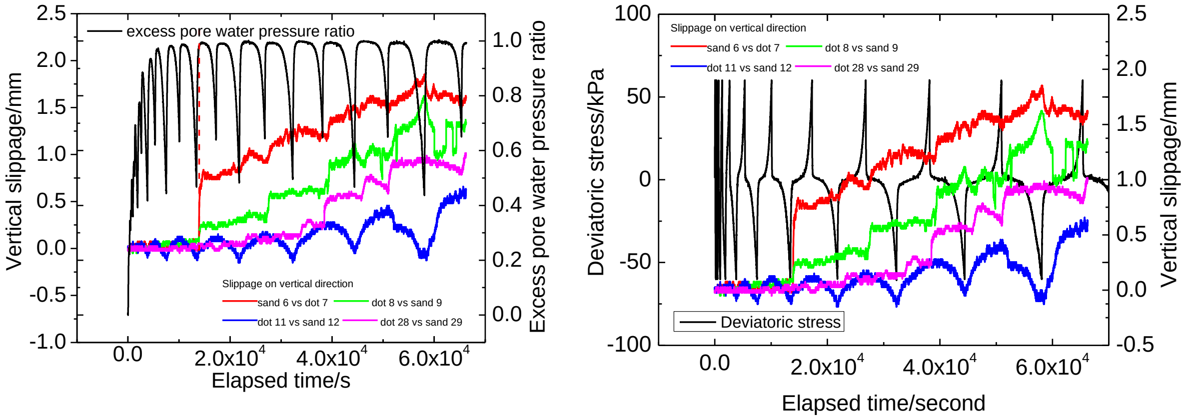

**Fig. 5.27 Time histories of vertical slippage, excess pore water pressure ratio and deviator stress**

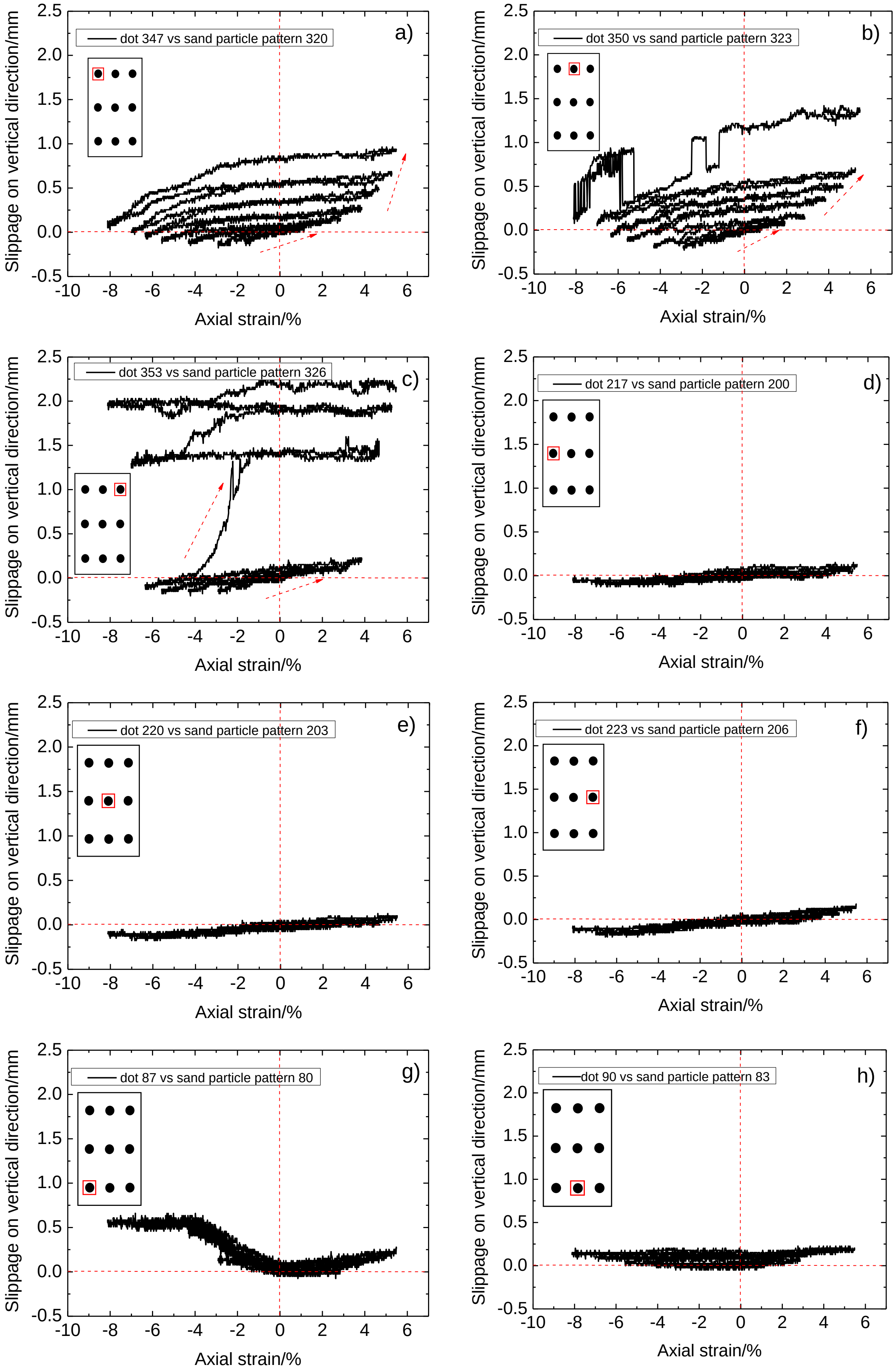
a)
dot 347 vs sand particle pattern 320
b)
dot 350 vs sand particle pattern 323
c)
dot 353 vs sand particle pattern 326
d)
dot 217 vs sand particle pattern 200
e)
dot 220 vs sand particle pattern 203
f)
dot 223 vs sand particle pattern 206
g)
dot 87 vs sand particle pattern 80
h)
dot 90 vs sand particle pattern 83
Slippage on vertical direction/mm
Axial strain/%
2.5
2.0
1.5
1.0
0.5
0.0
-0.5
-10
-8
-6
-4
-2
0
2
4
6

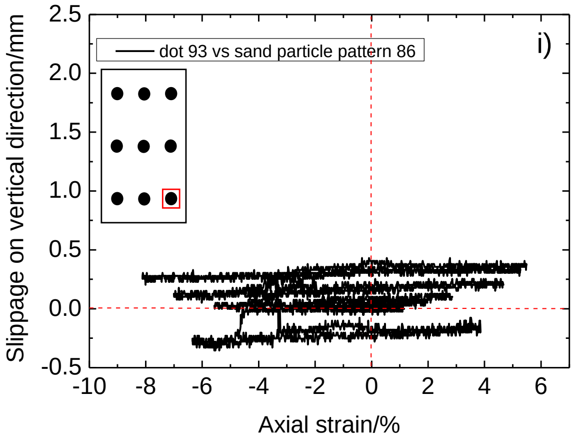

**Fig. 5.28 Relations between vertical slippage and axial strain at different positions in test 10**

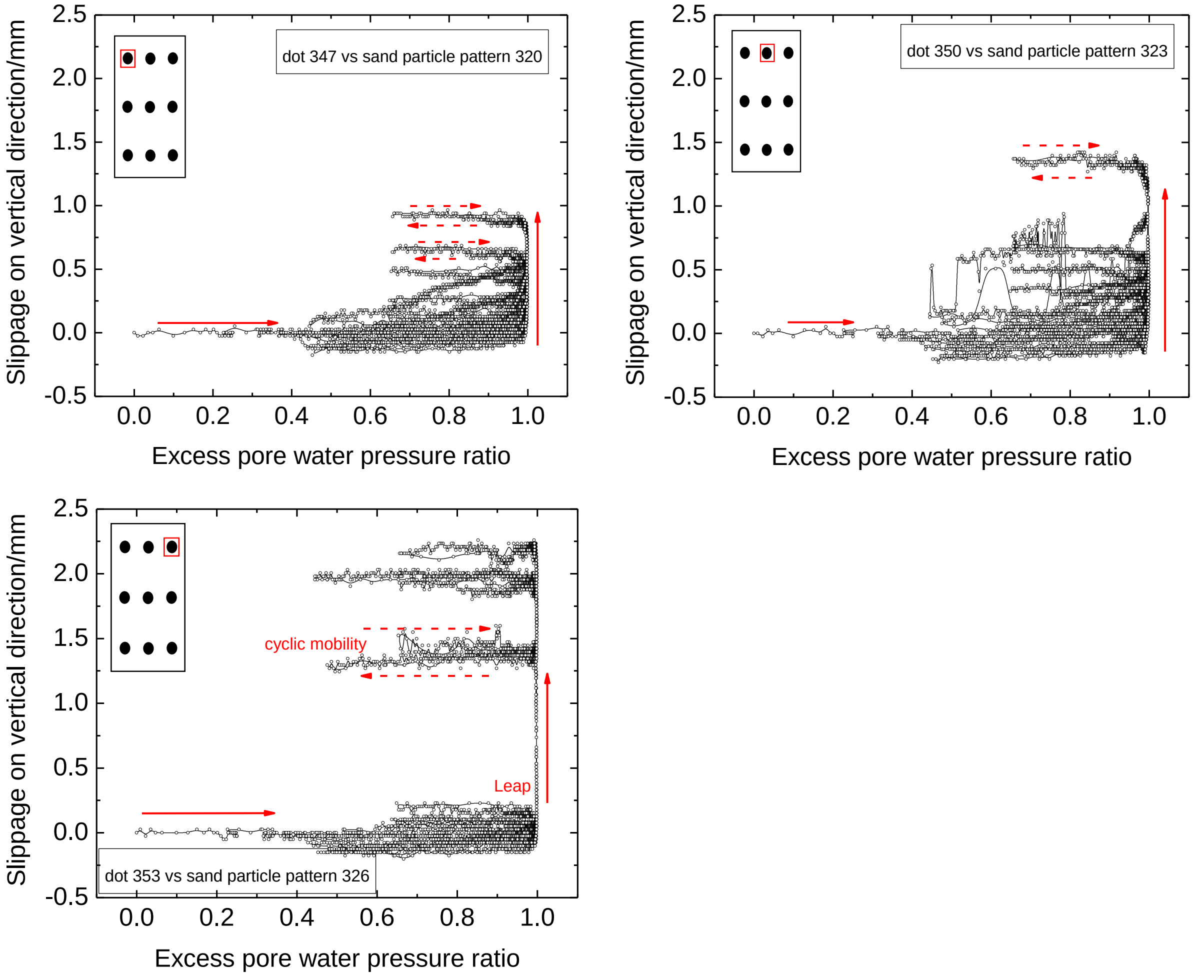

**Fig. 5.29 Relationship between vertical slippage and excess pore water pressure ratio at top part of specimen in test 10**

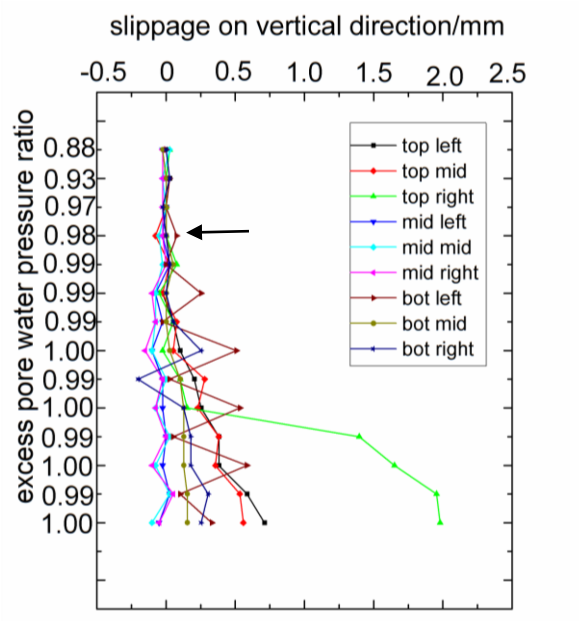

Fig. 5.30 Vertical slippage vs excess pore water pressure ratio at test 10

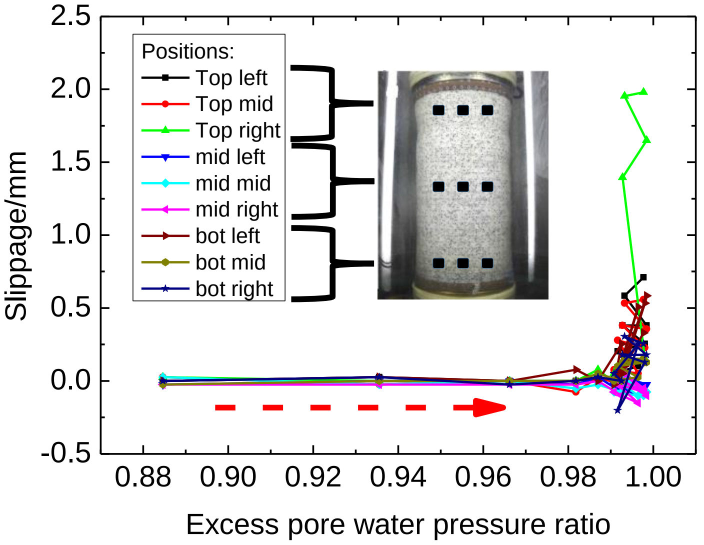

Fig. 5.31 Relationship between vertical slippage and excess pore water pressure ratio of test 10

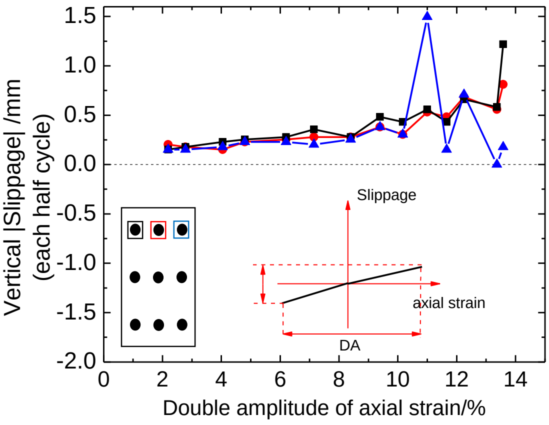

Fig. 5.32 Relationship between amplitude of vertical slippage and double amplitude of axial strain at each half cycle

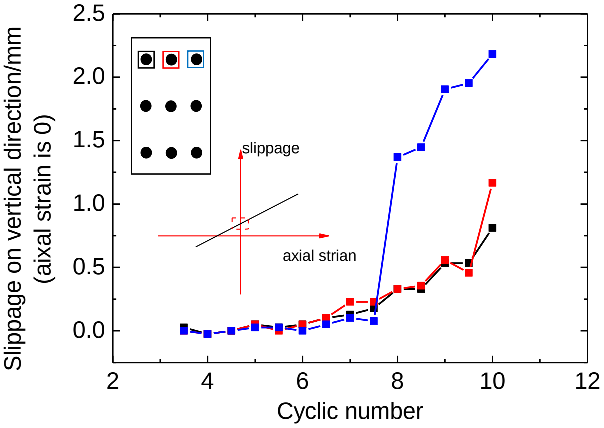

Fig. 5.33 Relationship between vertical slippage and cyclic number when the axial strain returns to 0

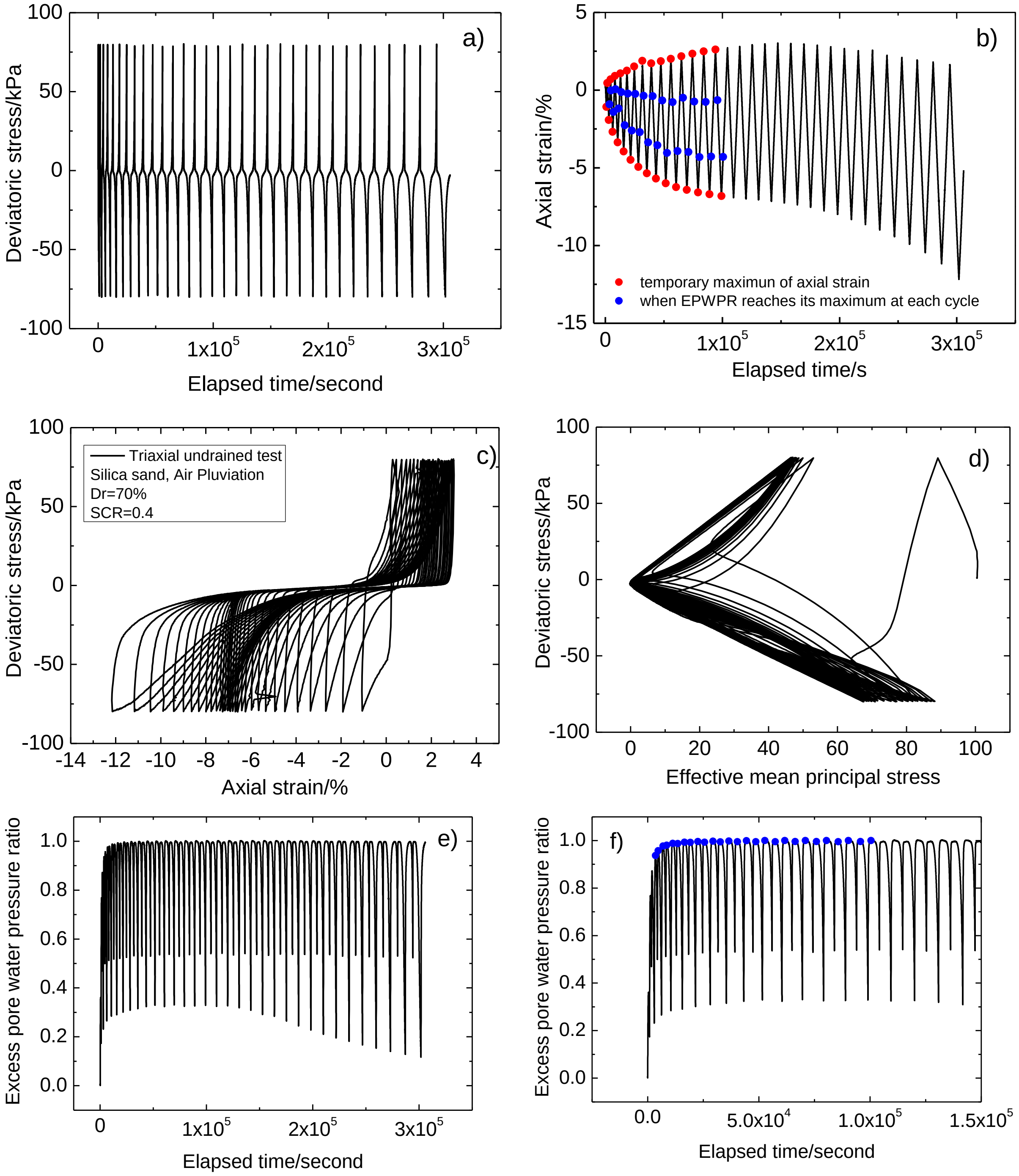

**Fig. 5.34 Results from test 14 (Silica sand specimen prepared by air pluviation method)**

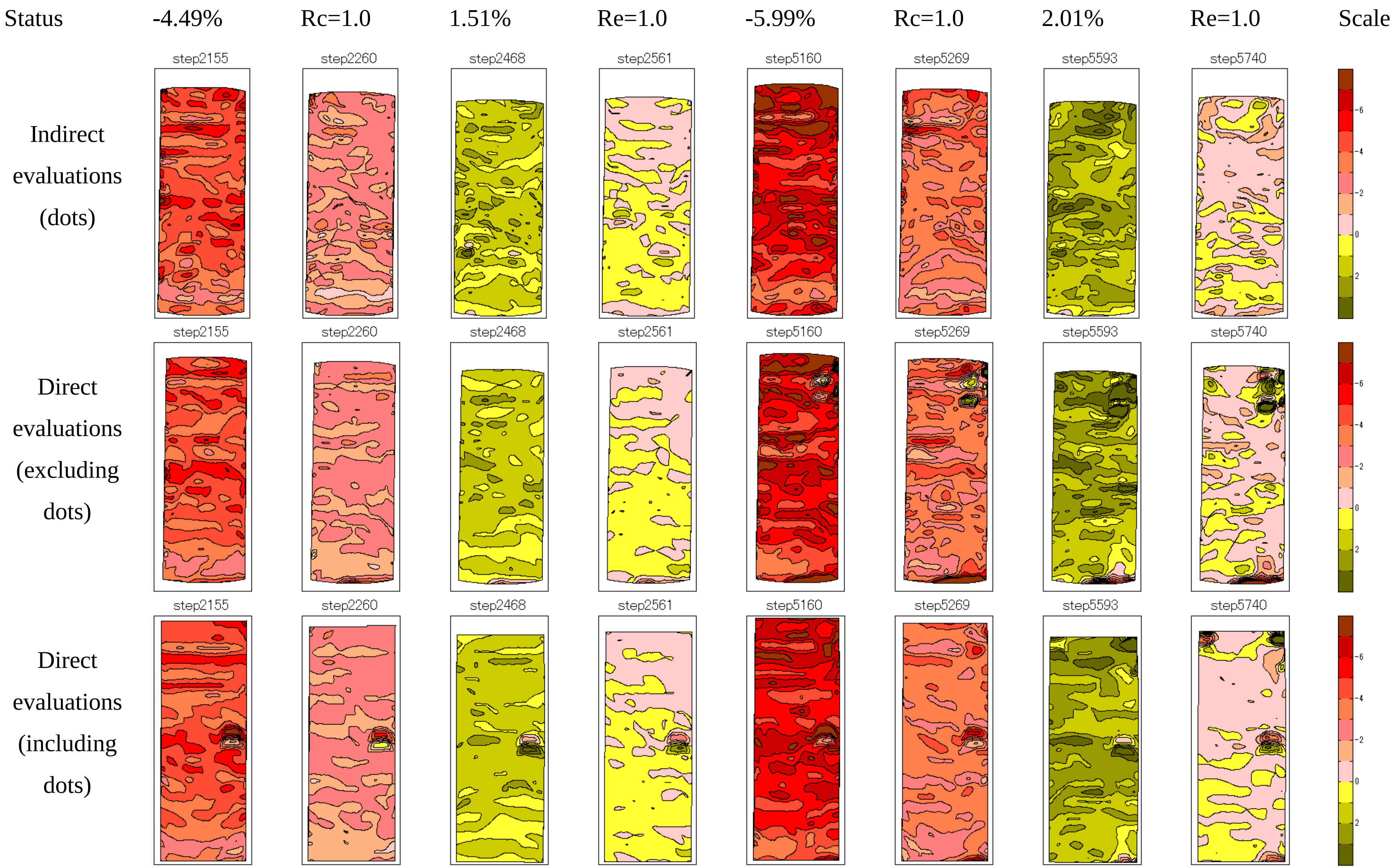

Fig. 5.35 Local strain distributions of test 14 at selected statuses ( vertical strain)

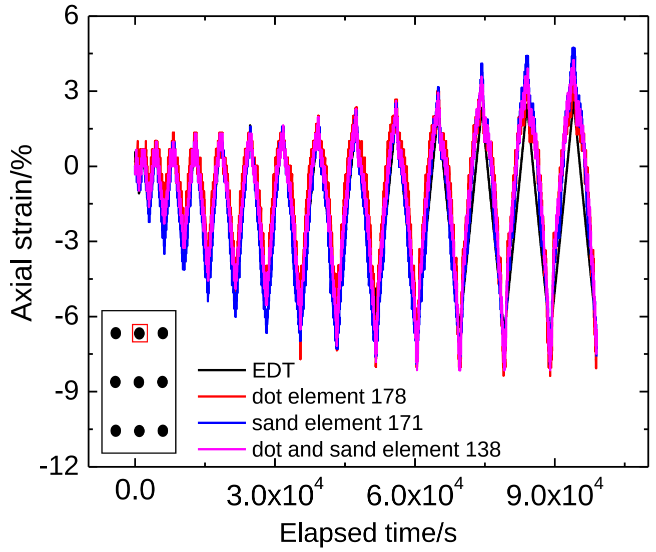

**Fig. 5.36 Time histories of axial strain and local stains at top part of specimen in test 14**

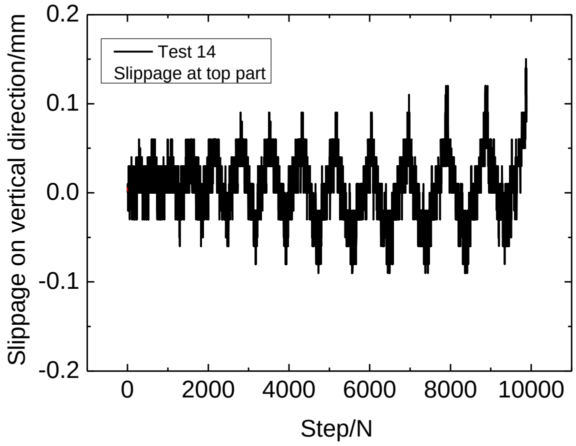

**Fig. 5.37 Step history of vertical slippage at top part of specimen in test 14**

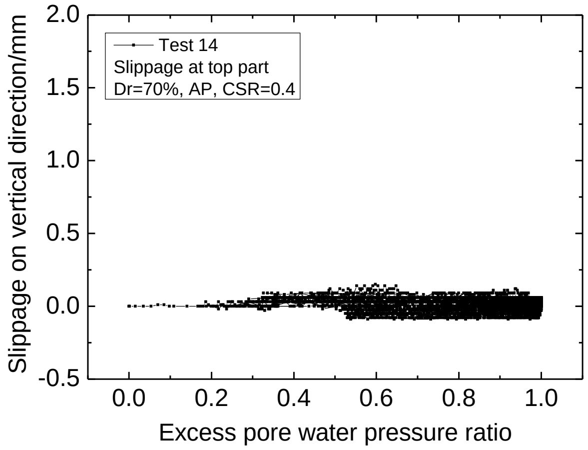

**Fig. 5.38 Relationship between vertical slippage and excess pore water pressure**

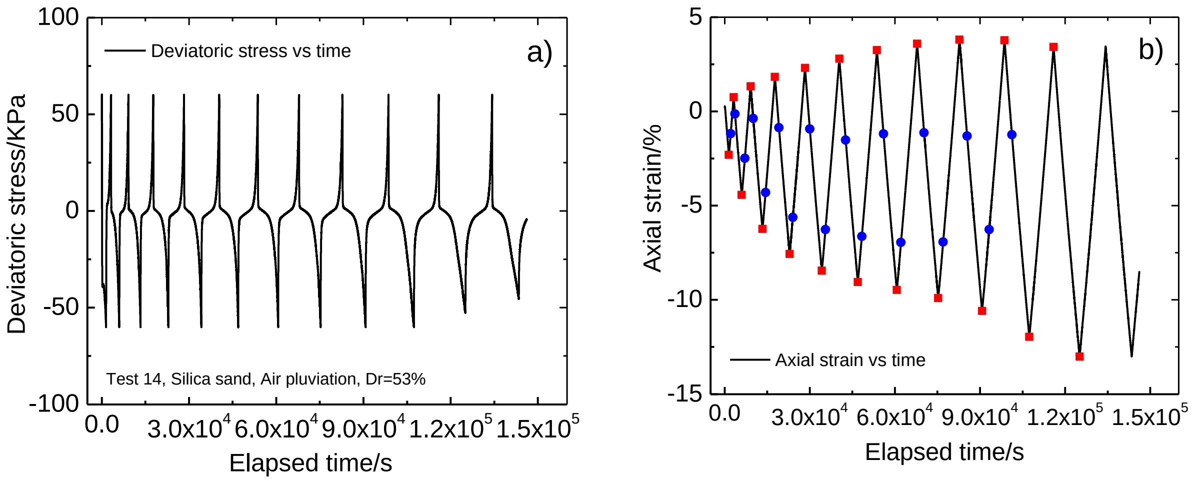

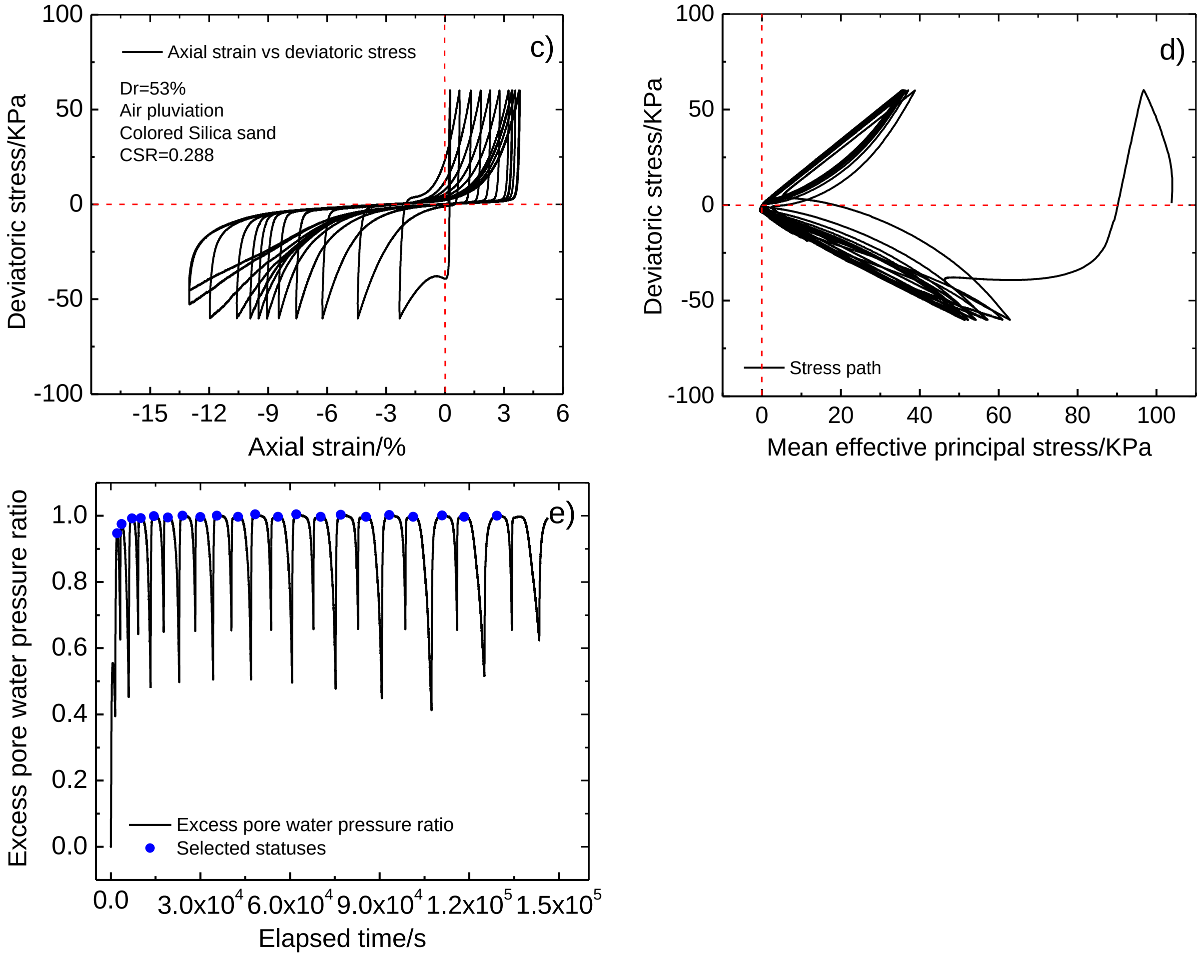

**Fig. 5.39 Results from test 16 ( Silica sand specimen prepared by air pluviation method)**

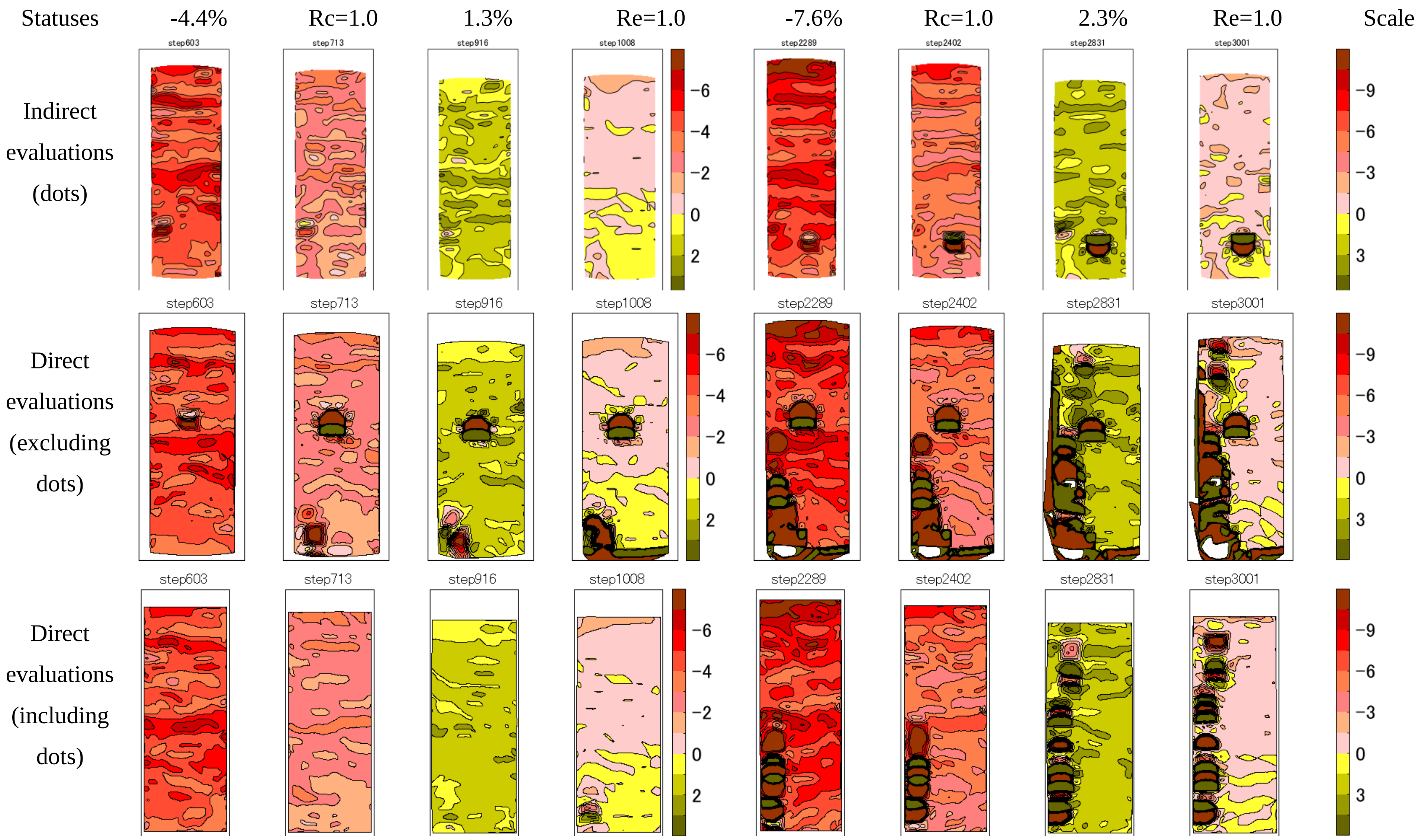

Fig. 5.40a Local strain distributions at selected statuses in test 16 ( vertical local strain)

Statuses -9.1% Rc=1.0 3.2% Re=1.0 Original photo of step 2402

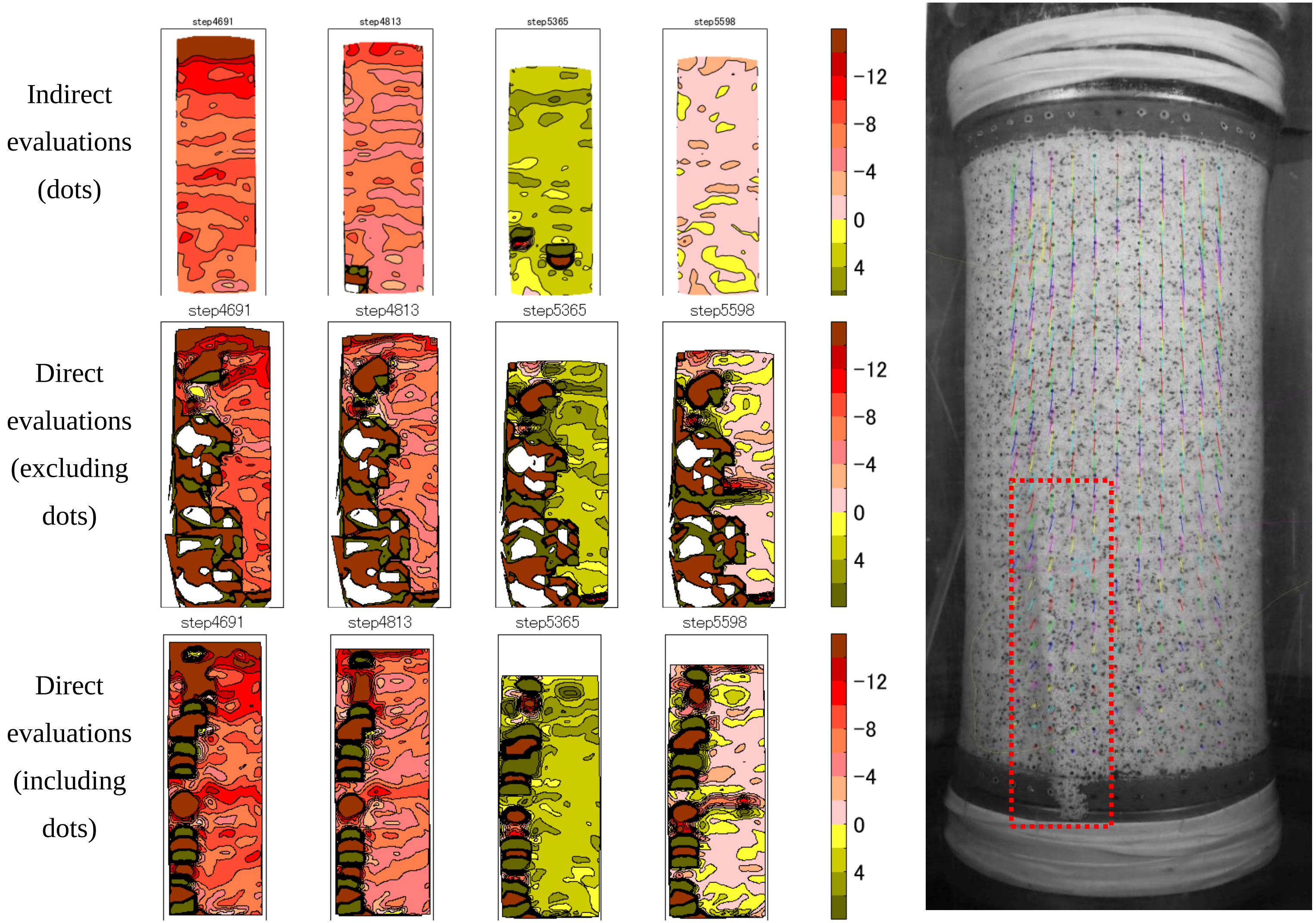

Fig. 5.40b Local strain distributions at selected statuses in test 16 ( vertical local strain)

**Fig. 5.40 Local strain distributions at selected statuses in test 16 ( vertical local strain)**

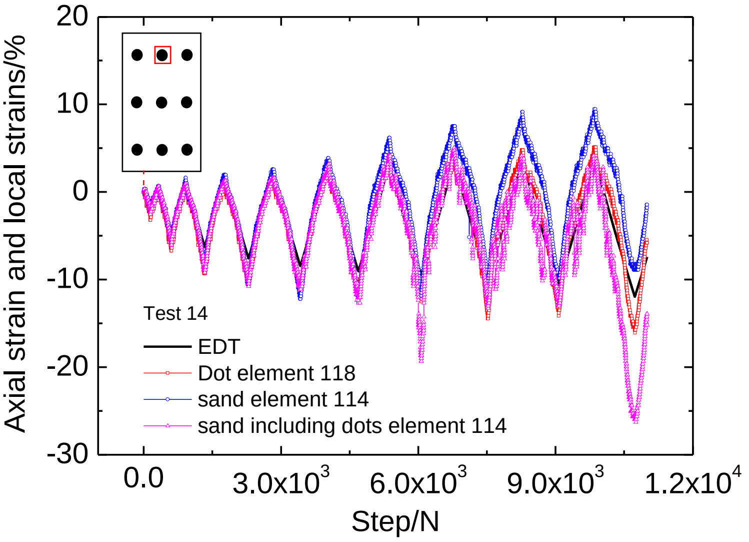

Fig. 5.41 Step histories of axial strain and local strains at top part of specimen in test 16

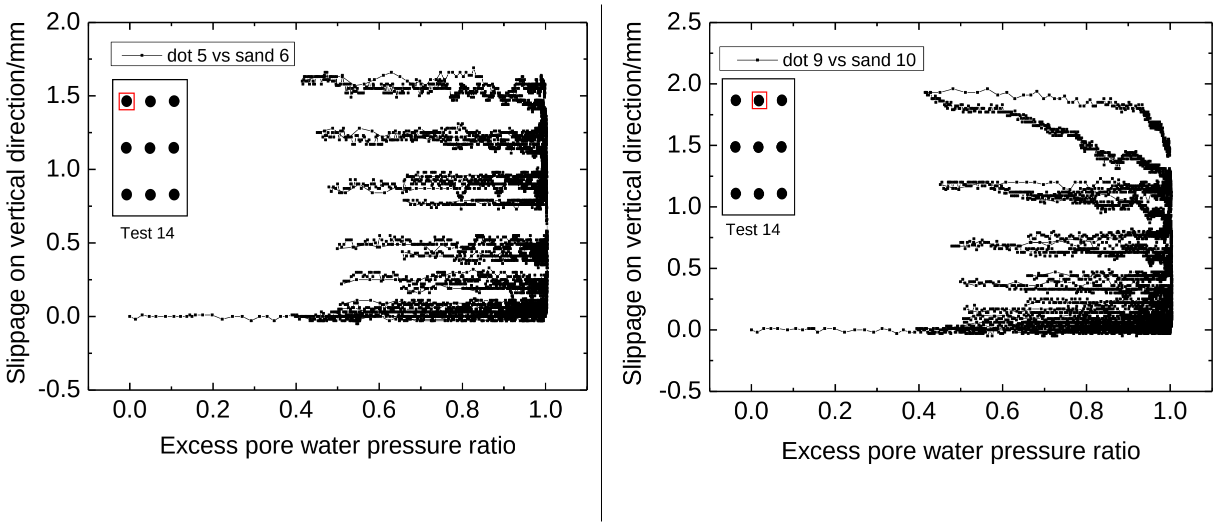

Fig. 5.42 Relationship between vertical slippage and EPWPR at selected points in test 16

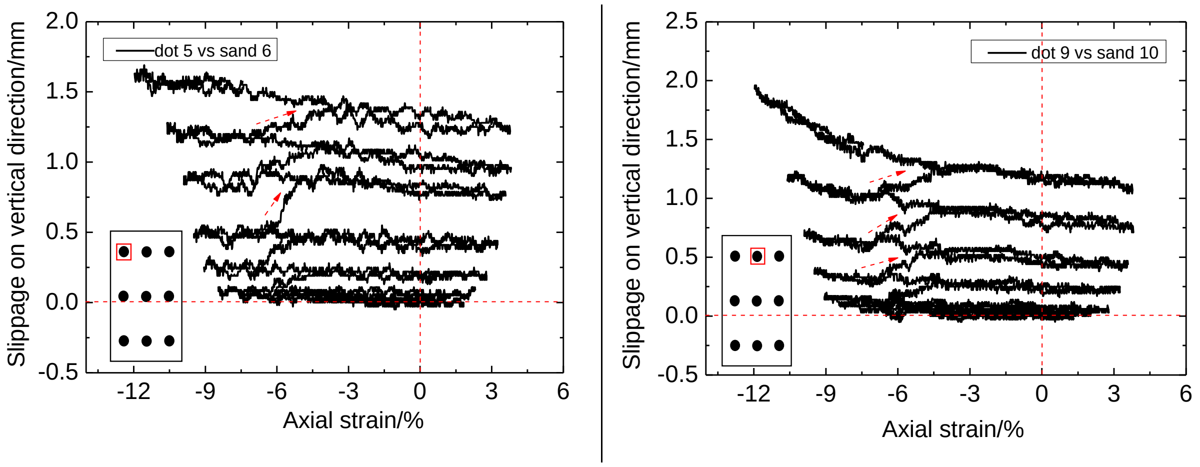

Fig. 5.43 Relationship between vertical slippage and axial strain at selected points in test 16

# 6. LOCAL DEFORMATIONS IN UNDRAINED TORSIONAL SHEAR TESTS

## 6.1 Introduction

As introduced in chapter 3, in view of the accuracy for simulating the stress condition of foundation in field during earthquake, torsional shear apparatus has more advantages than the triaxial apparatus. Moreover, the coordinate correction method has been developed to evaluate the local deformation of sand specimen in torsional shear test. Therefore, based on the motivation for conducting this study introduced in chapter 5, torsional shear apparatus is employed in this study to investigate the evolutions of local deformation of sand specimen directly and indirectly.

It has been recognized by researchers and civil engineers that sands tend to settle and densify when they suffer from earthquake shaking. Based on the site investigations after earthquake, small settlements of ground significantly affected the performance of structures (Tokimatsu and Seed, 1987). Silver and Seed (1971) had shown that the shear strain, which deformed specimen allowing particles to move into a denser packing, might be a fundamental parameter in determining the volume change of cohesionless soil under seismic events. Moreover, the settlement of dry sands due to cyclic loading was a function of relative density, magnitude of shear strain and number of cycles applied to the soil. In addition, Tatsuoka et al. (1984) investigated the volumetric strain after initial liquefaction in simple shearing test. The results indicated that the amount of settlement was significantly affected by the maximum shear strain developed in the test as well as the relative density of specimen. Therefore, the maximum shear strain might be an important parameter influencing the probable settlement.

Ueng et al. (2010) conducted shaking table test on saturated clean sand to investigate the probable settlement. It was observed that the settlement of sand deposit was generally small before the initial liquefaction. Subsequently, significant volume change calculated by corresponding settlement occurred only when the sand deposit was liquefied. Although some evaluation methods of earthquake-induced settlement have been proposed by researchers (Lee and Albaisa, 1974; Seed and Silver, 1972), there seems to be little works on the prediction of settlement, especially in the element tests. Based on the results obtained in chapter 5, settlement of sands in undrained triaxial test is always accompanied with strain localization. The reasons for triggering settlement are still poorly understood. In an attempt to study the local deformations and probable settlement of uniform sand specimen, the mixed colored Silica sand and transparent membrane will be used in the undrained torsional shear test.

In general, sand specimen is separated into three categories by its relative density, namely, loose, medium dense and dense (Ishihara, 1988). In this chapter, the local deformations of specimens will be introduced in order by the density state. The conditions for triggering slippage are investigated by comparing the direct and indirect evaluations of local deformations. Subsequently, the quantity of slippage is analyzed.

| Range of density | Status |
|---|---|
| $0 \le D_r < 40\%$ | Loose |
| $40 \le D_r < 65\%$ | Medium dense |
| $65 \le D_r \le 100\%$ | Dense |

As shown in Fig. 6.1, all the tests are divided into three regions by their relative densities. Dense specimens employed in the tests are marked by blue rectangle, while loose specimens by red rectangle. Other tests located outside of these two rectangles used medium dense specimens to evaluate the local deformations directly and indirectly.

## 6.2 Local deformations of loose sand specimen

Observed behavior in test SAUC11 is shown in Fig. 6.2 (a) through (f). The colored Silica sand (No. 5) specimen was consolidated to an initial effective confining stress of 100 kPa and subjected to undrained cyclic loading with a cyclic stress ratio of 0.18. The relative density of specimen was 27%. Six statuses were selected and marked by red rectangles in Fig. 6.2 to plot their corresponding local strain distributions. Based on the results in Fig. 6.3, the local strains from indirect evaluations had the same trend with those from direct evaluations when the absolute shear strain was less than 8.5% during the cyclic loading. After that, wrinkles occurred at step 1551, large differences of local strains between direct and indirect evaluations were triggered around the wrinkles. In order to study the evaluation of local strains, there positions at top, middle and bottom parts of specimen were selected as shown in Fig. 6.4. From Fig. 6.4 (a) through (c), the horizontal strain curves of dot element and sand particles pattern element overlapped with each other throughout the testing, even when the wrinkle occurred near the measured position after step 1551. As for the vertical strains, the displacements of measured elements at top part of specimen were largest than those from middle and bottom positions of specimen. Therefore, different local strain between membrane and sand occurred with large potential during liquefaction. As plotted in (d), different local strain appeared at step 690 when the first time of phase transformation was reached. It meant strain was localized at the status of phase transformation. Differently, the local vertical strains from middle and bottom parts of specimen were not affected by the phase transformation. However, the vertical local strain was influenced by the occurrence of wrinkles after step 1551. After the reversion of loading direction from the maximum shear strain of 12.0%, many wrinkles came out and affected the local strains seriously at step 2264. There was no affection on the vertical local strain at the bottom of specimen. As for the comparison of local shear strains and global shear strain measured by potentio-meter in (g) through (i), they were following the same change trend regardless of their positions. In addition, the local shear strains were slightly larger than the shear strain measured by potentio-meter. These slight differences indicated that the shear strain measured by potentio-meter underestimated the real shear strains, especially after the phase transformation. At status s-6, large amount of wrinkles occurred and affected the validity of local strains to some extent. The photos of first occurrence of wrinkle and serious wrinkles are shown in Fig. 6.5.

Based on the slippage calculation method introduced in chapter 5, Fig. 6.6 gives the step histories of excess pore water pressure ratio and vertical slippages at top, middle and bottom parts of specimen. Before status-1 (phase transformation), there was no slippages on vertical direction regardless the positions. After that, slight slippage was accumulated due to the large increment of excess pore water pressure in half cycle. As same as the results of local strains, slippage started increasing at status 4 when the wrinkles occurred at the first time. After the reversion of loading direction at s-4, liquefaction status was reached subsequently. Therefore, relative large slippage was accumulated before status-5. Between statuses 5 and 6, slippage remained to some extent when there was effective stress. The shear strain was 12% at status 6. After the reversion of loading direction at status 6, serious wrinkles occurred suddenly and remarkable slippage was accompanied at the top part of specimen. Since the repeatable recovery of effective stress made the sand particle settle during cyclic mobility, the top part of specimen became looser than the bottom parts. Under such circumstance, large settlement of sand particles at top part of specimen might be triggered during liquefaction which could be proved by the curve of slippage after status 6.

In order to confirm the condition when large slippage occurred, Fig. 6.7 plots the relationships between excess pore water pressure ratio and vertical slippage at selected positions. It could be verified that there was no vertical slippage before excess pore water reached 1.0. In addition, there was almost no vertical slippage when the effective stress was recovered during cyclic mobility. In other words, the vertical slippage was induced by the none-effective stress condition. This none-effective stress status might be necessary but not a sufficient condition for the leap of vertical slippage. Because slippage was not triggered sometimes when there was no effective stress.

As for the horizontal slippage, it can be computed by the following equations:

$$D_{dot,xdisp,i} = X_{dot,coord,i} - X_{dot,coord,original} \qquad (6\text{-}1)$$

$$D_{sand,xdisp,i} = X_{sand,coord,i} - X_{sand,coord,original} \qquad (6\text{-}2)$$

$$slippage = D_{dot,xdisp,i} - D_{sand,xdisp,i} \qquad (6\text{-}3)$$

in which *i* is the photo number and original is the photo without deformation. Positive value of displacement means the dot/sand particle pattern moves to the direction of positive axis, and vice versa. The positive value of horizontal slippage means that the relative movement of dot to sand particle pattern is toward the positive direction of axis. Fig. 6.8 gives the two situations of positive horizontal slippage at clockwise and anti-clockwise rotations, respectively.

Fig. 6.9 shows the step histories of excess pore water pressure ratio and horizontal slippages in test SAUC11. The horizontal slippage was likely not affected by the excess pore water pressure. As shown in Fig. 6.10, being different from vertical slippage, horizontal slippage did not remain constant when there was effective stress. Since the shear strain was small before the initial liquefaction, there was no horizontal slippage. In order to find the factors which affected the horizontal slippages. Fig. 6.11 shows the relationships between slippage and corresponding rotation displacement on horizontal and vertical directions. It was a common sense that the dot at the top part of specimen had a larger absolute rotation displacement than the one from bottom part even they had a similar local shear strains. The results in Fig. 6.11 (a) indicated that the horizontal slippage increased with the increasing rotation displacement. It meant the dot on membrane had a larger movement than the sand particles inside regardless of the positions. Remarkable horizontal slippage occurred under the circumstance of large rotation displacement. As shown in Fig. 6.11 (b), the vertical slippage kept constant even under large rotation displacement, which meant the horizontal rotation did not induce the vertical slippages directly. However, largest horizontal slippage occurred at the position which had the largest rotation displacement. It might be influenced by the local density and excess pore water pressure conditions. It also could be understood by the fact that large rotation created the conditions for sand particles re-arrangement.

Since the direction of vertical slippage was perpendicular to the shear direction and slippage occurred not only once, another parameter, accumulated displacement was introduced to study the triggering reasons for slippages.

$$D_{accumulated} = \sum_{i=1}^{n} \left| \Delta D_{disp,i} \right| \qquad (6\text{-}4)$$

where $\Delta D_{disp,i}$ is the displacement of measured points in one interval.

In Fig. 6.12 (a), the traces of tracked points are plotted. Compared with the results obtained in Fig. 6.12 (b), almost all the large vertical slippages occurred at the top of specimen, except for the positions affected by the wrinkles. The bottom part of specimen, which was suffered from small rotation, had little potential to induce vertical slippages. During the cyclic loading, the bottom part of specimen would become denser and upper part became looser under the undrained condition. Under such circumstance, upper part had larger potential than bottom part to trigger vertical slippage.

In Fig. 6.13, it can be seen that the horizontal slippage recovered during cyclic loading. The positive and negative values of horizontal slippage appeared alternatively. It meant the rotations of dot were always larger than the sand particles both on clockwise and anti-clockwise directions. Compared with the results in Fig. 6.11 (a), the maximum horizontal slippage was dominated by the corresponding maximum ration displacement. As introduced in Fig. 6.4, the local shear strains were almost same as the global shear strain measured by potentio-meter, regardless of the remarkable differences of accumulated movements. However, in Fig. 6.13, there was almost no slippage when the accumulated movement was small even under the same shear strain condition as the one from top part of specimen.

Fig. 6.14 gives the observed behavior in test SAUC9 where specimen was consolidated to 100 kPa isotropically and subjected to undrained cyclic shearing at a cyclic stress ratio of 0.23. Since the relative density of specimen was 32%, there was only 1.5 cycles before reaching the 15% double amplitude of shear strain. Three statuses marked by red rectangles in Fig. 6.14 were selected to show the local strain distributions. As plotted in Fig. 6.15, the local strain distributions by direct and indirect evaluations at these three statuses are same with each other. In addition, due to the little number of cycles, there were no remarkable wrinkles during test.

Fig. 6.16 shows the step histories of horizontal, vertical and shear local strains at the top of specimen in test SAUC9. These curves also indicated the same results obtained from the local strain distributions. The local strains evaluated indirectly were same as those from direct evaluations. On the other hand, the local shear strains from image analysis were relatively larger than the global shear strains, especially under the larger shear strain conditions. In other words, the global shear strain underestimated the real shear strain in this undrained torsional shear test.

Similarly, slippage was also analyzed in test SAUC9. The relationships between excess pore water pressure ratios and slippages are shown in Fig. 6.17. In figure (a), there were no vertical slippages at the top, middle and bottom parts of specimen before status-2. After that, the vertical slippage at bottom part increased suddenly after the recovery of liquefaction state during cyclic mobility. At status-3, vertical slippages at top and bottom parts increased after the reversion of loading direction. It might be due to the fact that quick liquefaction decreased the potential of settlement of sand particles. Moreover, as shown in figure (b), the status of excess pore water pressure ratio did not affect the horizontal slippages. Another fact was that the rotation displacements of dots were almost larger than the displacements of sand particle patterns. As introduced in the above section, the maximum value of horizontal slippage was influenced by the corresponding ration displacement of measured point.

## 6.3 Local deformations of medium dense specimen

As introduced in the first section of this chapter, the specimen with a relative density range from 40%~65% is defined as a medium dense sample. In this study, four tests with the relative densities of 43%, 53%, 55% and 60% were conducted to investigate the local deformations by direct and indirect evaluation methods. Observed behavior in test SAUC8 where the specimen was consolidated to an initial confining stress of 100 kPa and subjected to undrained cyclic loading with a cyclic stress ratio of 0.23 is shown in Fig. 6.18 (a) through (f). Three statuses were selected to show the local strain distributions. S-1 was the status when the first time of phrase transformation was reached. S-2 was the status when excess pore water pressure ratio reached 1.0 at the first time. S-3 was the status when the shear strain was 7.3%. These statuses were marked by red rectangles in Fig. 6.18 (a) through (f). The corresponding local strain distributions of these three statuses are shown in Fig. 6.19. Before step 576, the local strains from indirect and direct evaluation are same with each other. At step 2685, large differences of local strains between indirect and direct evaluations occurred. From the direct evaluations, remarkable strain strips appeared, which was affected by the wrinkles occurred before. Compared with the local strains by the indirect evaluation, there were no wrinkles at step 2685. It indicated that the strain localization in the wrinkles was irreversible for the direct evaluation. Nothing observed from the indirect evaluation proved the advantages of direct evaluations. Another fact was that wrinkles took place easily when the shearing direction was just reversed at large shear strains. In the wrinkles, water was concentrated and this phenomenon was named as local drainage by some researchers. Meanwhile, sand particles were flowing along the wrinkles. This phenomenon accelerated the strain localizations. Sand flowed into the gap between membrane and pedestal when nearby wrinkles appeared. Therefore, the local strains near pedestal were extremely large which might not reliable.

Fig. 6.20 gives the local strain comparison by indirect and direct evaluations at the top part of specimen. Based on the overall trends of these curves, both direct and indirect evaluations could represent the deformation behavior effectively. As explained at step 2685 (s-3), the local strains might be affected by the nearby wrinkles. In figure (b), the vertical local strains at the selected point were affected seriously after step 3000. However, it was still acceptable because direct evaluation was influenced by the sand flowing near wrinkles. In figures (a) and (c), no affections on horizontal and shear strains was found. One fact was that the local shear stains at top part of specimen measured by image analysis were 30%~50% larger than the shear strain from potentio-meter. It also indicated that the global shear strain might underestimate the shear strain of sand specimen. In figure (d), the local shear strains from the top, middle and bottom parts of specimen were compared with the global shear strain. Even though the change trends of these curves were same, there were still differences between each other. It indicated that non-uniform local deformations were induced during the undrained torsional shear test.

As stated earlier, the same value of strains from indirect and direct evaluations does not mean that the displacements of dots and sand particles are coincident with each other. Fig. 6.21 gives the relationships between excess pore water pressure ratio and vertical slippage during the test. No vertical slippage was found before the excess pore water pressure ratio reached 1.0. In addition, there were leaps of vertical slippage when the excess pore water pressure ratio recovered to 1.0 during cyclic mobility. This phenomenon also confirmed the reason for large increment of vertical slippage in liquefaction tests. In Fig. 6.21 (b), the trend of leap of vertical slippage was very distinct. The vertical slippage remained when there was a certain amount of effective stress. The jump was triggered only when the excess pore water pressure ratio was around 1.0. Actually, it was inevitable that wrinkles would affect the vertical slippage to some extent if there were wrinkles nearby.

The relationships between excess pore water pressure ratio and horizontal slippage are shown in Fig. 6.22. In can be obtained that horizontal slippage was not dominated by the excess pore water pressure ratio. It seemed affected by the shear stress or shear strains. Fig. 6.23 gives the relationships between horizontal displacement and horizontal slippage at measured point. The horizontal displacement meant the rotation displacement on horizontal direction at measured point. It had a linear relation with the global shear strain. Therefore, it was also a useful factor as shear strain to present the local deformation of sand specimen. As explained before, the maximum rotation displacement controlled the quantity of horizontal slippage. Moreover, since the image analysis method was very sensitive to measure the local displacement, the horizontal slippage was also affected by the nearby wrinkles.

Based on the above analysis, vertical slippage was always accumulated during the undrained torsional shear test. The positive value of vertical slippage indicated that sand particle sunk during liquefaction. As for the horizontal slippage, the movement of dot was always larger than the movement of sand particle during rotation. Fig. 6.24 shows the top and bottom parts of specimen at the last photo taken after finishing the test. Since the settlement of sand particles at the top part was accumulated and largest than those at the beneath positions, around 5 mm of water film was formed under the top cap. The re-arrangement of void induced a loose status at the top of specimen and dense status at bottom, resulting in the extended horizontal strain as shown in Fig. 6.19 at step 2685. The dark blue colored part at the bottom of horizontal local strain distribution indicated a distinct extended horizontal strains. This phenomenon also proved the settlement of sand particles during liquefaction. Since the membrane was suspended by the top cap, it did make sense that downward slippage of sand particles to the dots was found. In Fig. 6.24 (b), sand flowed away to the gap between membrane and pedestal during several cycles. Meanwhile, wrinkles would affect the movement of sand particles nearby, which resulted in significant strain localization in turn.

Another two tests where specimens were prepared at the relative densities of 43% and 60% will be introduced, respectively. The observed behavior of these two tests where specimens were consolidated to an initial effective confining stress of 100kPa and subjected to the undrained cyclic loading with a cyclic stress ratio of 0.35 is shown in Fig. 6.25 and Fig. 6.26, respectively.

As for test SAUC14, the specimen with a relative density of 43% reached 5% double amplitude of shear strain in one cycle. The test was terminated in three cycles when the double amplitude of shear strain reached 15%. The local strain distributions in test SAUC14 by indirect and direct evaluations were almost same with each other. Likewise, the indirect and direct local strains were coincident with each other along the specimen except for the positions near wrinkles. Interestingly, there was little wrinkle in test SAUC14. Compared with horizontal displacement of measured point at top of specimen, the step histories of vertical and horizontal slippages are plotted in Fig. 6.27. Very limited vertical slippages were found, as well as the horizontal slippages.

Similar results were obtained in Test SAUC13, for example, coincident local strains and local strain distributions by indirect and direct evaluations. Even though there were many cycles to induce the 15% double amplitude of shear strain, significant vertical slippages were not found. The relationship between step and vertical slippage is shown in Fig. 6.28 (a). While the step histories of horizontal slippage and horizontal displacement of measured point are shown in Fig. 6.28 (b). Being different from the slippage results in test SAUC8, the quantity of vertical slippage in test SAUC13 was negligible. The horizontal slippage was also not as large as the slippage in test SAUC8. It might be due to the fact that the test was stopped when the double amplitude of shear strain was 12.7%. However, there were no serious wrinkles throughout the test. It is a common sense that specimen with a large relative density will have little potential of sand particle settlement during liquefaction. Therefore, there might be a threshold of relative density for the significant settlement of sand particles during liquefaction. Another fact was that there were no distinct water films beneath the top cap in tests SAUC14 and SAUC13.

## 6.4 Local deformations of dense specimen

In this section, the local deformations of dense specimens from direct and indirect evaluations will be introduced and compared in sequence. Observed behavior in test SAUC12, where specimen was prepared by air pluviation method and had a relative density of 80%, is shown in Fig. 6.29 (a) through (f). It was consolidated to an initial effective confining stress of 100 kPa and subjected to undrained cyclic loading at a shear stress ratio of 0.45. Three statuses marked by red rectangles were selected to show their corresponding local strain distributions. S-1 was the status when the first time of phase transformation was reached. S-2 was the one when the excess pore water pressure ratio was 0.99. The last one was the status when a temporary maximum of shear strain was obtained. Since the relative density of specimen was very high, the experiment was stopped before the double amplitude of shear strain reached 15%. Another phenomenon of dense specimen was that the recovery of effective stress was very significant.

In Fig. 6.30, the local strain distributions at selected statuses were compared by direct and indirect evaluations. It can be seen that there was no strain localization before the first time of phase transformation (s-1). In addition, strain localization was found at s-2 from the local strain distributions. However, local strain distributions from indirect and direct evaluations were almost same with each other. Wrinkle did not appear through the test. At s-3, there was no large difference between indirect and direct evaluations of local strains. In Fig. 6.31 (a) through (c), the local strains at one selected positon are compared by indirect and direct evaluations. The coincident variation trend also proved that indirect evaluation of local deformations was valid to represent the local behaviors of dense specimen. Compared with the shear strain measured by potentio-meter, the local shear strains measured by image analysis was remarkably larger than the global shear strain. In Fig. 6.31 (d), the local shear strains at top, middle and bottom parts of specimen were compared with the global shear strain. The results indicated that only bottom part had the similar value of shear strains with the global one. The local strains from top and middle parts of specimen were larger than the one from bottom position. It also could be recognized by the local strain distributions. This phenomenon described the non-uniform deformations of dense specimen in undrained torsional shear tests.

The vertical and horizontal slippages at top part of specimen are plotted in Fig. 6.32, respectively. It can be seen that there was no vertical slippage throughout the test. It also satisfied the common sense that the settlement potential of dense sand was little and negligible even during no effective stress condition. It indicated that the movement of sand particles and dots were same other. As for the horizontal direction, the slippage was not distinct. It might be due to the fact that the maximum single amplitude of shear strain was less than 4%.

Fig. 6.33 shows the observed behavior in test SAUC10 where the relative density of specimen was 85%. In this test, the specimen was consolidated to an initial effective stress of 100 kPa. Subsequently, a single amplitude of shear stress at 23kPa was applied on the specimen. However, the results indicated that it could not liquefy. Therefore, the single amplitude of shear stress was increased from 23kPa to 40kPa. It can be seen as a pre-shearing liquefaction test. In figure (d), the absolute value of maximum shear strain was less than 6% both on clockwise and anti-clockwise directions. Due to the limitation of memory card, the camera stopped working when the shear strain reached 3.4%. However, all the images were analyzed to obtain the local strain distributions. Three statuses were selected and marked to plot the local strain distributions. S-1 is the status when the first time of phase transformation was reached. S-2 is the one when excess pore water pressure ratio was 0.99. The last one s-3 is the status when the shear strain was 3.4%. The corresponding local strain distributions are shown in Fig. 6.34. No strain localization can be seen in local strain distributions at step 70. However, strain localization was found at step 1961 when the double amplitude of shear strain was 4.5%. This strain localization was formed only on the shear strain distribution. From the shear strain distribution at step 5615, shear strains along the specimen were significantly non-uniform. The local shear strains at top part of specimen were remarkably larger than the local strains from bottom part. This situation was same as the local stain distributions at step 4522 in test SAUC12. Based on the local strain comparison, the local shear strains from the top part of specimen were larger than the shear strains at bottom part. As for the horizontal strains and vertical strains, since the vertical displacement was prohibited, no significant affection was found.

As shown in Fig. 6.35, the step histories of excess pore water pressure ratio and vertical slippage are compared at the top and bottom parts of specimen. There was no vertical slippage throughout the test. The results were same as test SAUC12. As for the horizontal slippage shown in Fig. 6.36, since the horizontal displacement of measured point was limited, the horizontal slippage followed the same trend as horizontal displacement. It meant that the rotation displacement of dot was slightly larger than the displacement of sand particle pattern. Even though the specimen had been subjected to several times of cyclic loading, there was no water film underneath the top cap.

The observed behavior in test SAUC15, where specimen was consolidated to an initial effective confining stress of 100 kPa and subjected to undrained cyclic stress by a loading rate of 0.8 %/min, is shown in Fig. 6.37 (a) and (b). Being different from the other tests introduced above, the loading rate in test SAUC15 was around 30 times faster than the formers. Fig. 6.37 (a) gives the relationship between stress and strain which is not fully plotted. Actually, the test stopped when the double amplitude of shear strain was 15%. Fig. 6.37 (b) shows the corresponding stress path. Based on the comparison of local strains between indirect and direct evaluations, there was no difference along the specimen. In addition, Fig. 6.38 gives the step histories of vertical and horizontal slippages at the top part of specimen. There was no slippage on the vertical direction either as same as the other tests on dense specimen. As for the horizontal slippage, it was always increasing with the rotation displacement.

## 6.5 Quantity of slippage

As discussed in the above sections, the leap of vertical slippage was affected by the status of excess pore water pressure ratio. Excess pore water pressure ratio reaching 1.0 was the sufficient but not necessary condition for the vertical slippage. In other words, the occurrence of vertical slippage of each point was unpredictable during each cycle. The non-effective stress condition satisfied the common sense that sand particle would sink during liquefaction. However, the quantity of vertical slippage was a comprehensive result of liquefied specimen. As for the horizontal slippage, the results indicated that the displacement of dot was always larger than the sand particles both on clock-wise and anti-clockwise directions. However, the quantity of horizontal slippage was very small and affected by the horizontal displacement of measured point. Based on the evolution of horizontal slippage, it continued increasing even there was effective stress. The difference of material characters between sand and membrane might induce the increment of horizontal slippage.

Based on the slippage analysis on loose, medium dense and dense specimens, the vertical slippage was affected by the relative densities. However, it was not dominated by the relative density only. For example, the specimen in test SAUC9 had a relative density of 32%, this specimen had a large potential to trigger sand particle settlement during liquefaction. Since the cyclic stress ratio was relative large, the 15% double amplitude of shear strain was reached in 1.5 cycles. Actually, there were little vertical slippages in test SAUC9. Similarly, the specimen in test SAUC11 had a relative density of 27%. Nonetheless, significant vertical slippage occurred at a low cyclic stress ratio of 0.18. Many cycles were underwent before reaching 15% double amplitude of shear strain. As introduced in the above, accumulated movement could be used to combine the affections by relative density and cyclic stress ratio. In addition, each cycle had different displacement or shear strains at different tests. It was impossible to compare two statuses which were in the same conditions in two different tests (Different shear strain, EPWPR, strain history and so on). Therefore, the slippages at different tests were incomparable. Under such circumstance, accumulated movement was a comprehensive parameter which was affected by relative density, cyclic stress ratio and so on. It was a deformation status reflecting the current situation of specimen with the consideration of displacement histories.

As shown in Fig. 6.12, the accumulated movements along the specimen were decreasing from the top to the bottom. Moreover, the vertical slippage was also decreasing with the decreasing accumulated movement. Fig. 6.39 summaries the relationships between vertical slippages and the corresponding accumulated movements at top part of specimens in different tests. Even though there were many cycles to induce the 15% double amplitude of shear strain, vertical slippage was not found when the specimen was dense. Moreover, the largest accumulated movement was obtained in test SAUC15, there were no vertical slippage both at top and bottom parts of specimen. It can be seen in Fig. 6.39 and 6.40, distinct vertical slippages were found in four tests where the relative densities of specimen were smaller than 55%. This condition satisfied the common sense that there was large potential to trigger vertical slippage when the specimen was loose. However, there was also no slippage in test SAUC14 in which the relative density of specimen was only 43%. In addition, slight vertical slippage was observed in test SAUC 9 where the relative density of specimen was 32%. As introduced above, the slippage was also affected by the rotation histories. Compared with the accumulated movements of measured points in test SAUC11, SAUC8 and SAUC7, the accumulated movements in test SAUC14 and SAUC9 were relatively smaller. Not only the vertical slippages of dense specimens but also the vertical slippage in test SAUC13, where the relative density of specimen was 60%, was negligible. Likewise, the same rule was obtained from the results of the points at the bottom parts of specimens. The negative value of vertical slippages at bottom of specimen in test SAUC7 might be affected by the nearby wrinkles.

As shown in Fig. 6.11 (a), the horizontal slippages were dominated by the horizontal displacements at each cycle. The double amplitudes of horizontal slippage and horizontal rotation were defined similarly as the double amplitude of shear strain. Therefore, the relationships between double amplitudes of horizontal slippages and horizontal rotations at top and bottom parts of specimen in different tests are shown in Fig. 6.41 and Fig. 6.42, respectively. A distinct trend could be observed in Fig. 6.41 that the double amplitude of horizontal slippage increased with the double amplitude of rotations. Similarly, the increasing trend also was recognized in Fig. 6.42. It should be noted that the double amplitude of horizontal slippage was very small, which resulted in the sensitivity and fluctuation of its curve.

Based on the vertical slippage analysis, it was irreversible during the test. The vertical slippage was accumulated at each cycle. Therefore, the value of vertical slippage at the end of each cycle was selected to show the evolution of vertical slippage throughout the test. As shown in Fig. 6.43, the selected statuses for vertical slippage analysis were marked by red solid circles in the time history curve of shear strain. Fig. 6.44 gives the relationships between vertical slippages and cyclic number after initial liquefaction. The initial liquefaction was the status when the excess pore water pressure ratio reached 1.0 at the first time. Based on the results, it can be concluded that vertical slippage occurred only after the initial liquefaction. Being same as the vertical slippage at top parts of specimens, the occurrence of vertical slippage at bottom parts shown in Fig. 6.45 was also after the initial liquefaction.

Actually, settlement of sand particle during and after liquefaction is the final result of vertical slippage. Since the vertical displacement of top cap is not allowed in undrained torsional shear test, the downward slippage of sand particle to the dot is also settlement. Therefore, the results obtained in this study can be linked to the investigation on deposit settlement during earthquake. Based on the observation of settlement in saturated sand during Tokachi-oki earthquake in 1968, Ohsaki (1970) tried to calculate the settlement by proposed method. Maximum settlement was observed in the extremely loose deposit, while relatively small settlement in medium dense sand. As stated early in this chapter, Silver and seed (1971) had shown that the settlement of dry sands induced by cyclic loading could be seen as a function of relative density, magnitude of shear strain and number of cycles. It was found that, for a given relative density and number of cycle, settlement only depended on the shear strain amplitude of soil. In addition, Tatsuoka et al. (1984) had concluded that the settlement was affected by the values of density and the maximum shear strain induced in the undrained simple shear test. It was also found that settlement of specimen decreased considerably with the increase in density for the same cyclic loading. Fortunately, the results of vertical slippage obtained in this study also agree with the conclusions of previous researches. It is hoped that this study could supplement useful data on the researches of deposit settlement during earthquake.

## 6.6 Summary

Based on the indirect and direct evaluations of local deformations on uniform sand specimen, the results from a series of undrained cyclic torsional shear tests could be summarized as follows:

*Local deformations of loose specimen*

1. The local strains from indirect evaluations had the same change trends as those from direct evaluations except for the positions where wrinkles occurred nearby. Moreover, almost same values of local strains at the same positions from direct and indirect evaluations were observed before the excess pore water pressure ratio reached 1.0. In general, both direct

and indirect evaluations of local deformations were valid to some extent to represent the local behavior of sand specimen in undrained torsional shear tests. Another advantage of direct and indirect evaluations of local strains was that they eliminated the underestimation of shear strains measured by potentio-meter. Distinct vertical slippage occurred only when the excess pore water pressure ratio reached around 1.0.

*Local deformations of medium dense specimen*

2. During non-liquefaction status, the local strains along the specimen were relatively uniform. On the other hand, strain localization was observed after the initial liquefaction. After the reversion of loading direction during cyclic mobility, wrinkles appeared and affected the deformations of neighboring sand particles. Sand particle flowing was observed near the wrinkle and pedestal of specimen. Since the sand particles sunk during liquefaction, water film was formed underneath the top cap at the end of test. Based on the local strain distributions, the settlement of sand particles was also recognized by the extended horizontal local strains at bottom part of specimen.

*Local deformations of dense specimen*

3. Regardless of high speed loading and pre-shearing, there was no significant vertical slippage in the tests where the specimens were dense. Based on the local strain distributions, strain localization took place after the initial liquefaction even when the shear strain was small. Several cycles after the onset of strain localization, the local shear strains at top and middle parts of specimen were significantly larger than the those at the bottom.

*Quantity analysis of slippage*

4. Liquefaction status was not sufficient but necessary condition for the leap of vertical slippage. Significant vertical slippage was observed only in those tests where the specimen was relatively loose and the accumulated rotation of measured point was large. Based on the results obtained, there was no remarkable vertical slippage when the relative density of specimen was larger than 60%. Meanwhile, slight vertical slippage was observed in test where the relative density of specimen was 55%. Therefore, relative density of 60% would be used as a threshold value for the significant vertical slippage. Beyond that there was no slippage either when the relative density of specimen was 43%. It was due to the fact that the test stopped quickly with limited rotation displacement. At present, there is no threshold of accumulated movement for the significant vertical slippage. However, the large accumulated movement is only considered as a factor which will increase the potential to trigger remarkable vertical slippage.

5. As for the horizontal slippage, it was dominated by the double amplitude of rotation displacement. Regardless of the relative density of specimen, the movements of dots on membrane were always larger than the movements of neighboring sand particles both on clockwise and anti-clockwise directions.

# Reference

1. Ishihara, K. (1988). Soil mechanics. *Maruzen, 297p.*
2. Lee, K. L. and Albaisa, A. (1974). Earthquake Induced Settlements in Saturated Sands. *Journal of the Geotechnical Engineering Division, 100*(4), 387-406.
3. Ohsaki, Y. (1970). Effects of sand compaction on liquefaction during the Tokachioki earthquake. *Soils and Foundations, 10*(2), 112-128.
4. Seed, H. B. and Silver, M. L. (1972). Settlement of dry sands during earthquakes. *Journal of Soil Mechanics & Foundations Div, 98*(sm4), 381-397.
5. Silver, M. L. and Seed, H. B. (1971). Volume changes in sands during cyclic loading. *Journal of Soil Mechanics & Foundations Div, SM 9*, 1171-1182.
6. Tatuoka, F., Sasaki, T. and Yamada, S. (1984). Settlement in Saturated Sand Induced by Cyclic Undrained Simple Shear, 8th World Conf. on Earthquake Eng. *Vo1, 3*, 95-102.
7. Tokimatsu, K. and Seed, H. B. (1987). Evaluation of settlements in sands due to earthquake shaking. *Journal of Geotechnical Engineering, 113*(8), 861-878.
8. Ueng, T., Wu, C., Cheng, H. and Chen, C. (2010). Settlements of saturated clean sand deposits in shaking table tests. *Soil Dynamics and Earthquake Engineering, 30*(1), 50-60.

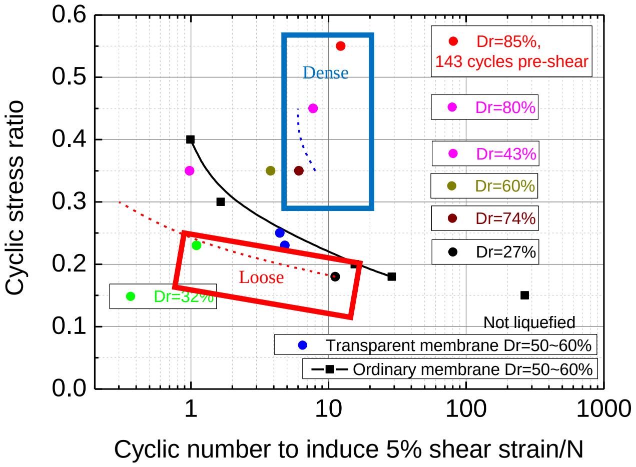

**Fig. 6.1 Shear stress ratios required to cause 5 % of double amplitude shear strain for colored Silica sand**

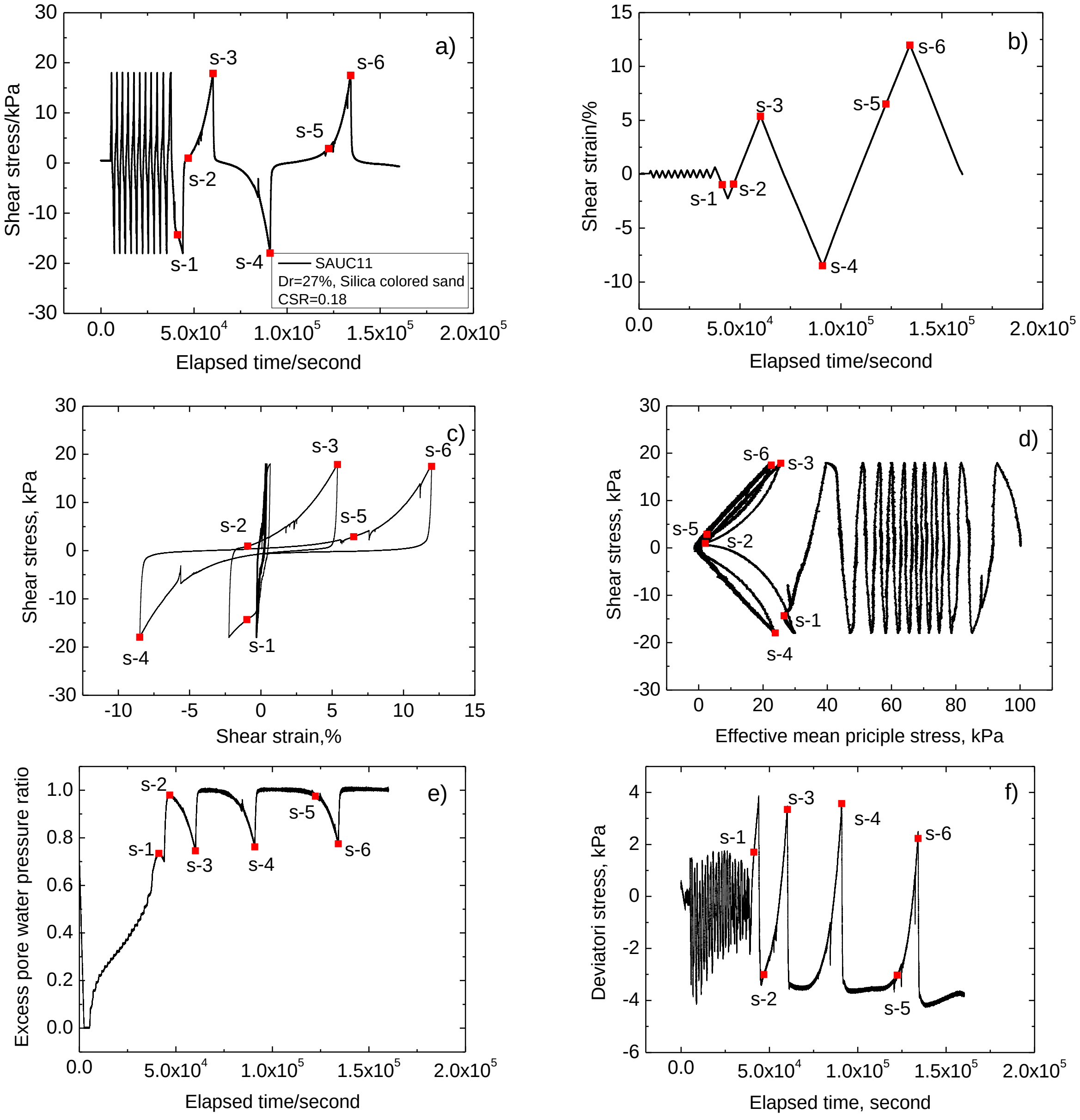

**Fig. 6.2 Results from test SAUC11**

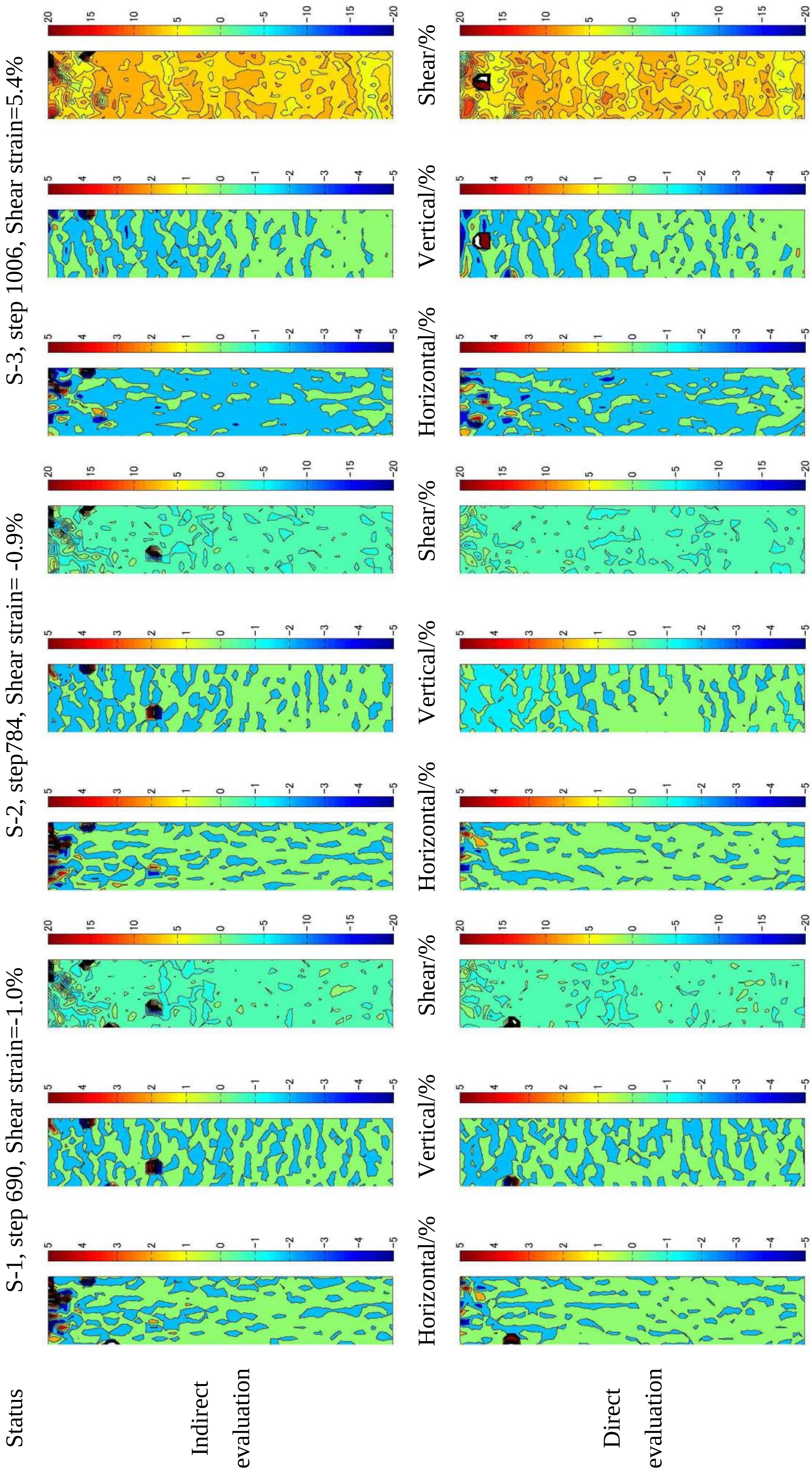

Fig. 6.3a Local strain distributions at selected statuses in test SAUC11

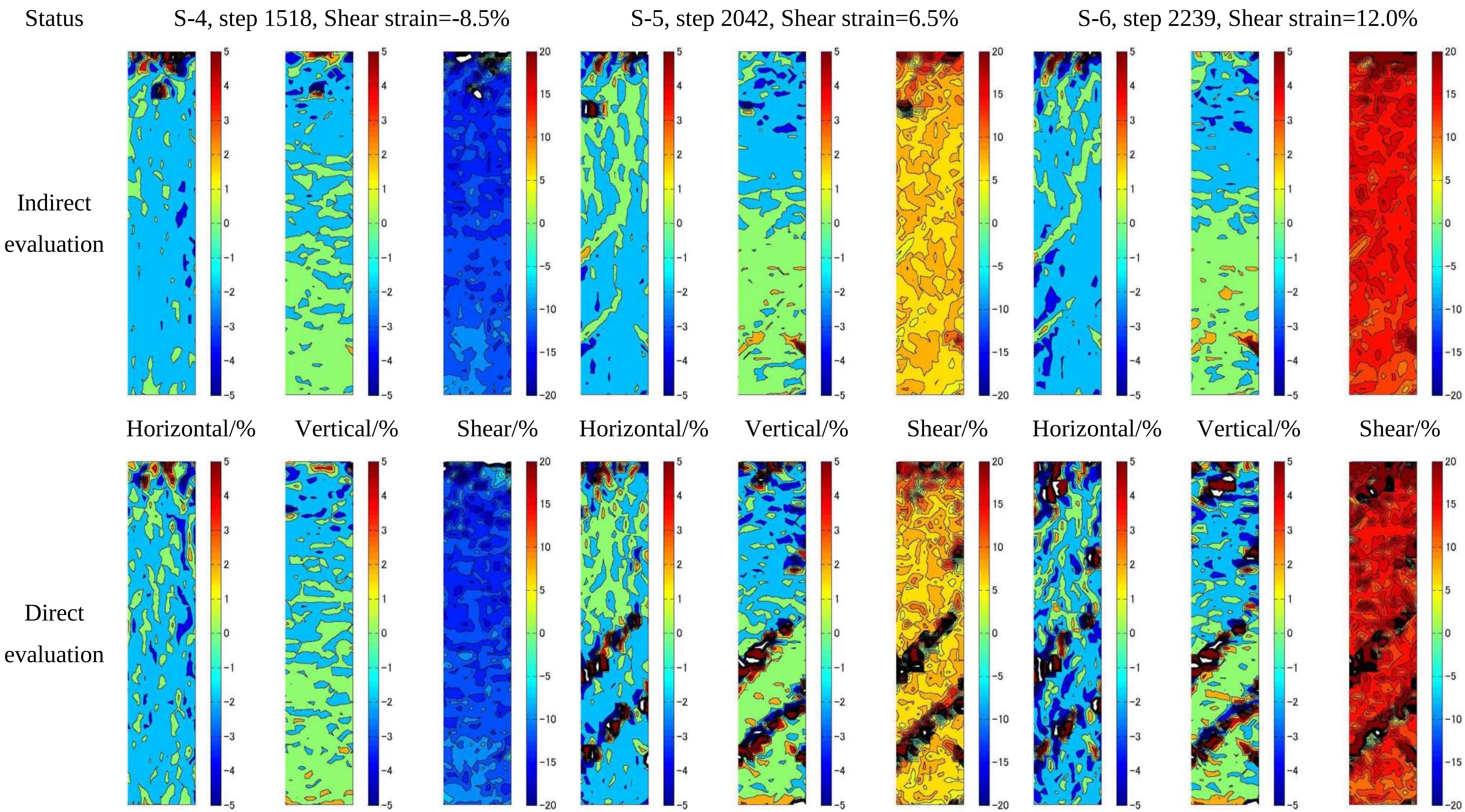

Fig. 6.3b Local strain distributions at selected statuses in test SAUC11

**Fig. 6.3 Local strain distributions at selected statuses in test SAUC11**

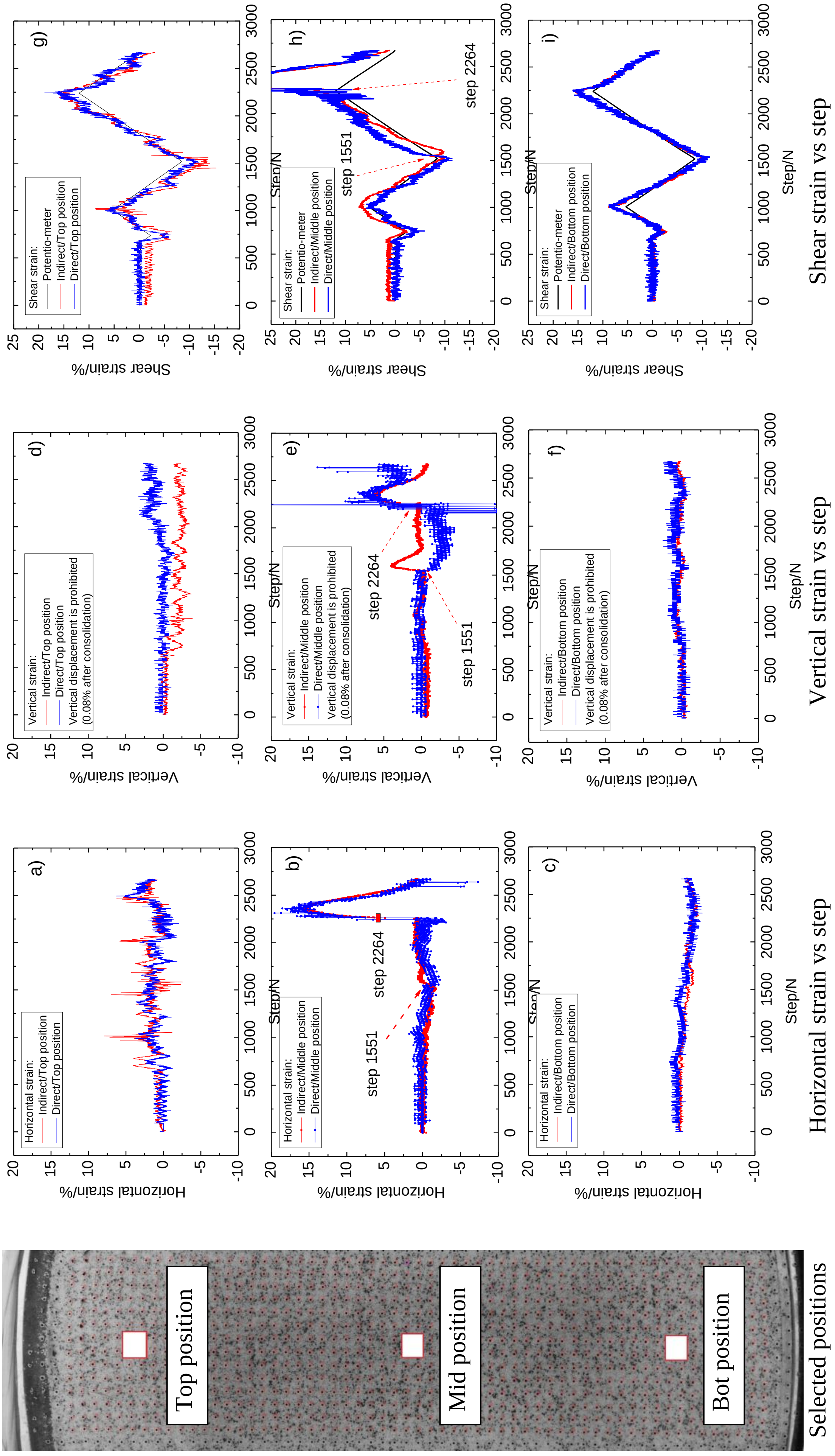

**Fig. 6.4 Step histories of horizontal, vertical and shear strains at selected positions along the specimen**

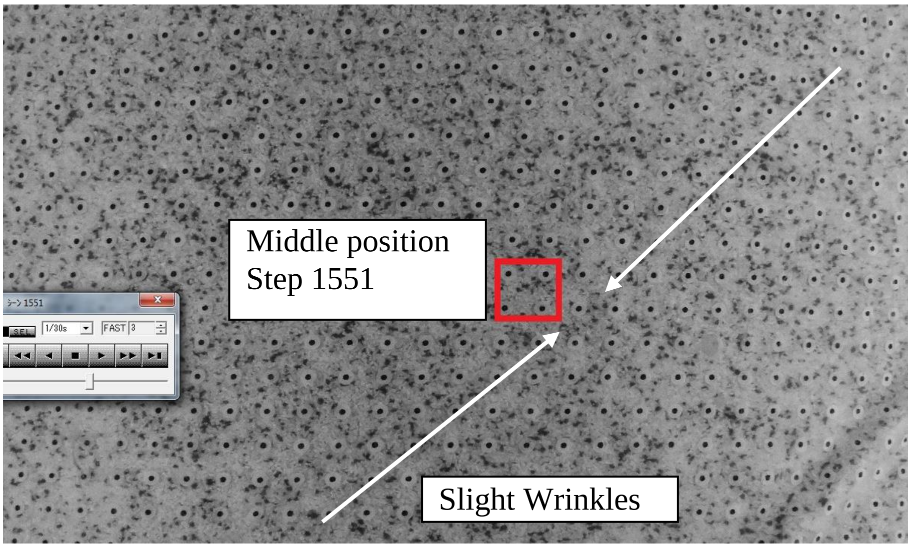

First occurrence of wrinkles

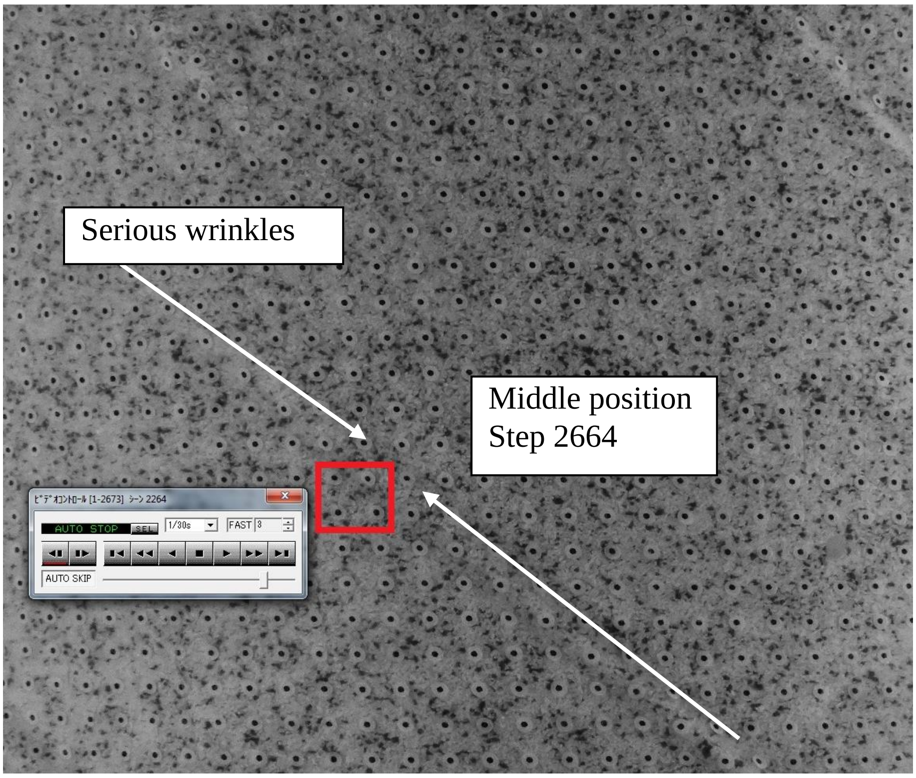

Serious wrinkles after reversion of loading direction

**Fig. 6.5 Wrinkles in test SAUC11**

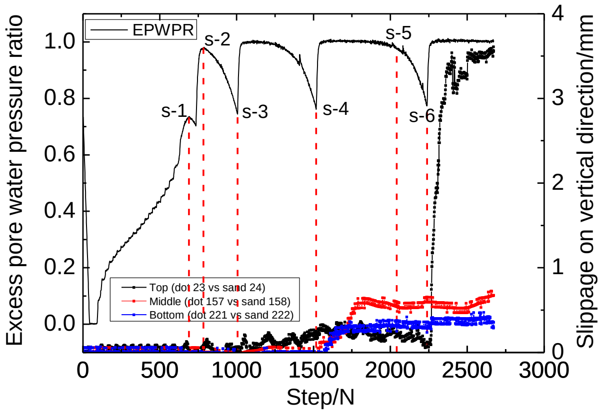

**Fig. 6.6 Steps histories of excess pore water pressure ratio and vertical slippages in test SAUC11**

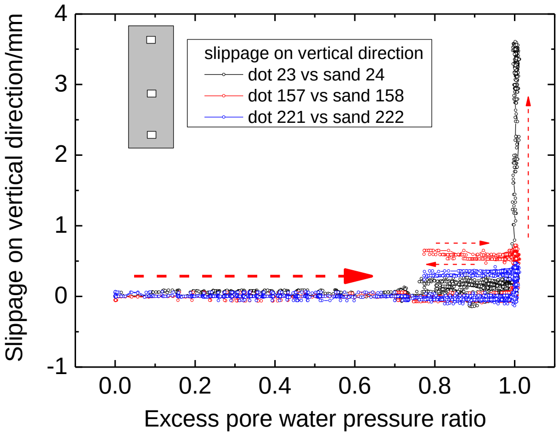

**Fig. 6.7 Relationships between excess pore water pressure ratio and vertical slippage in test SAUC11**

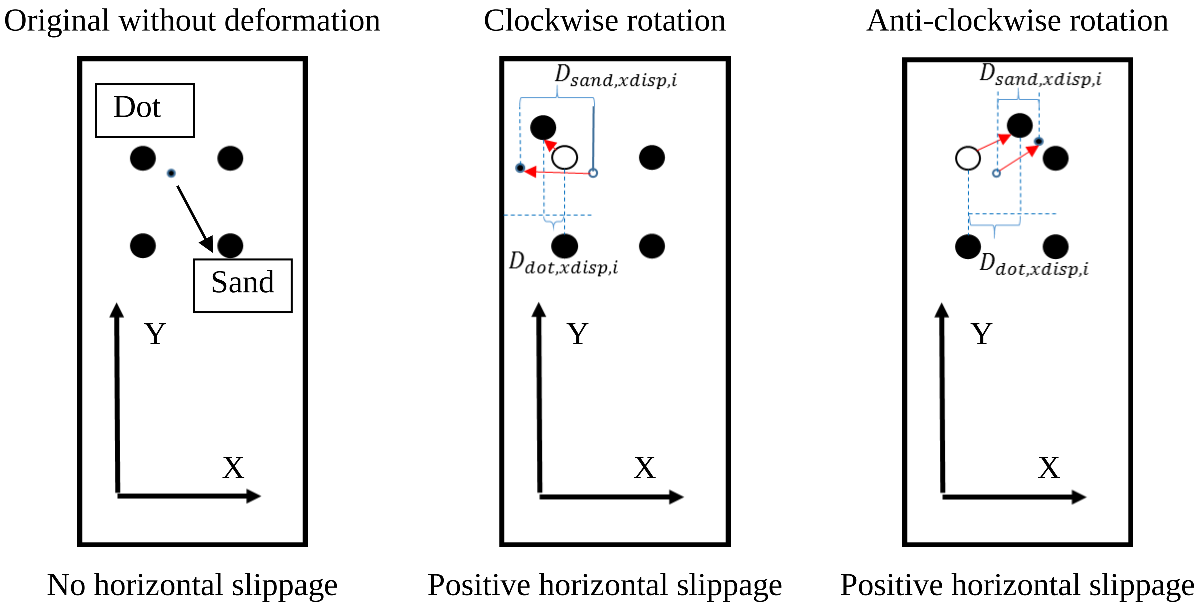
Original without deformation

Clockwise rotation

Anti-clockwise rotation

No horizontal slippage

Positive horizontal slippage

Positive horizontal slippage

**Fig. 6.8 Schematic diagrams of positive horizontal slippage in torsional shear tests**

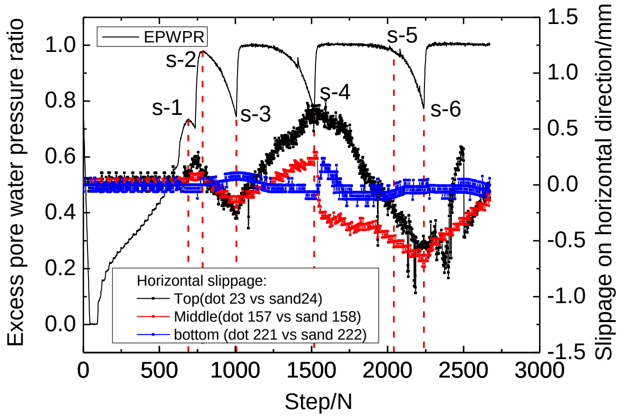

**Fig. 6.9 Steps histories of excess pore water pressure ratio and horizontal slippages in test SAUC11**

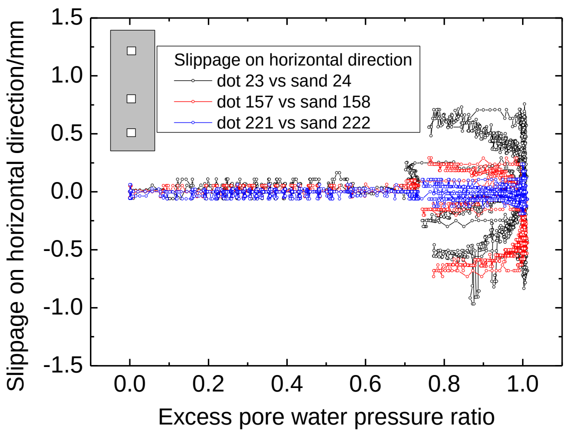

**Fig. 6.10 Relationships between excess pore water pressure ratio and horizontal slippage in test SAUC11**

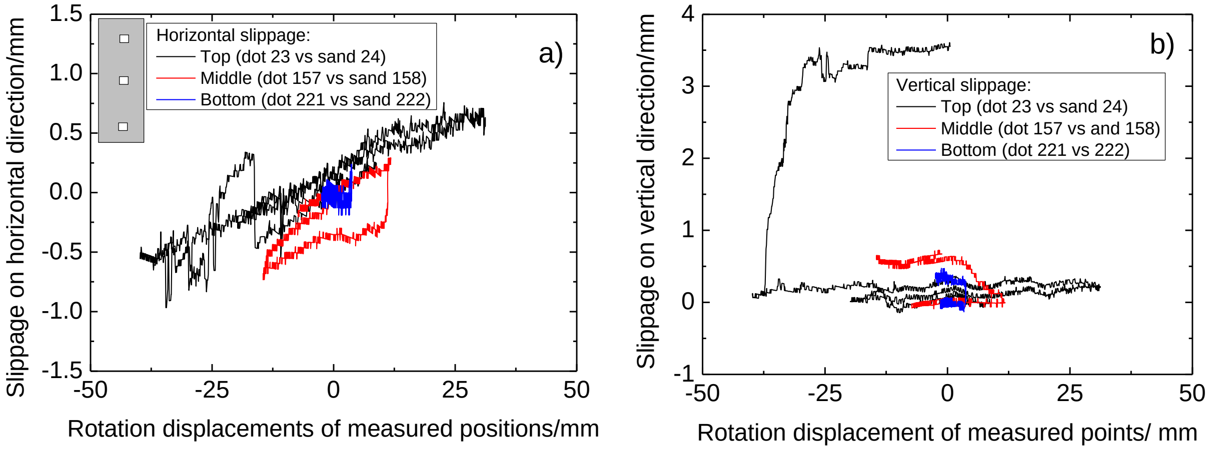

**Fig. 6.11 Relationships between slippage and corresponding rotation displacement on horizontal and vertical directions**

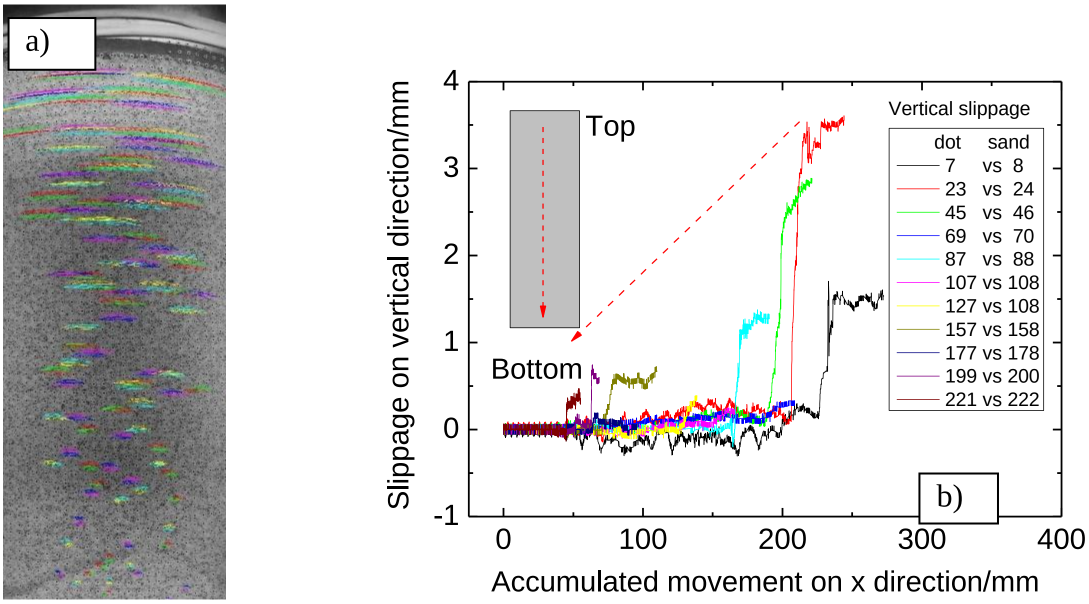

**Fig. 6.12 Schematic diagram of accumulated movement and the relationship between vertical slippage and accumulated movement**

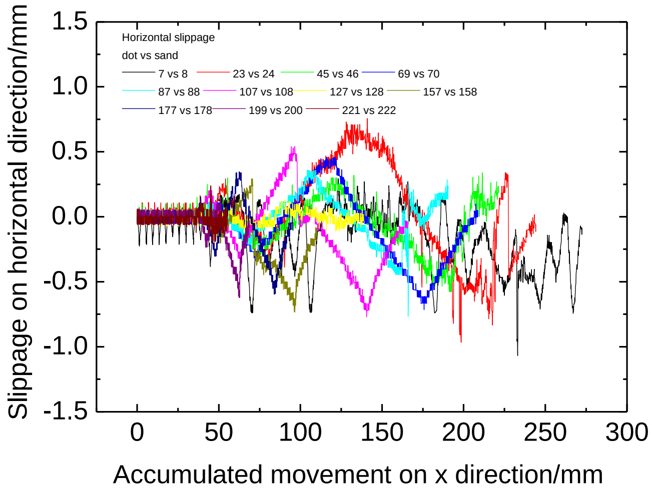

**Fig. 6.13 Relationships between horizontal slippages and accumulated movement**

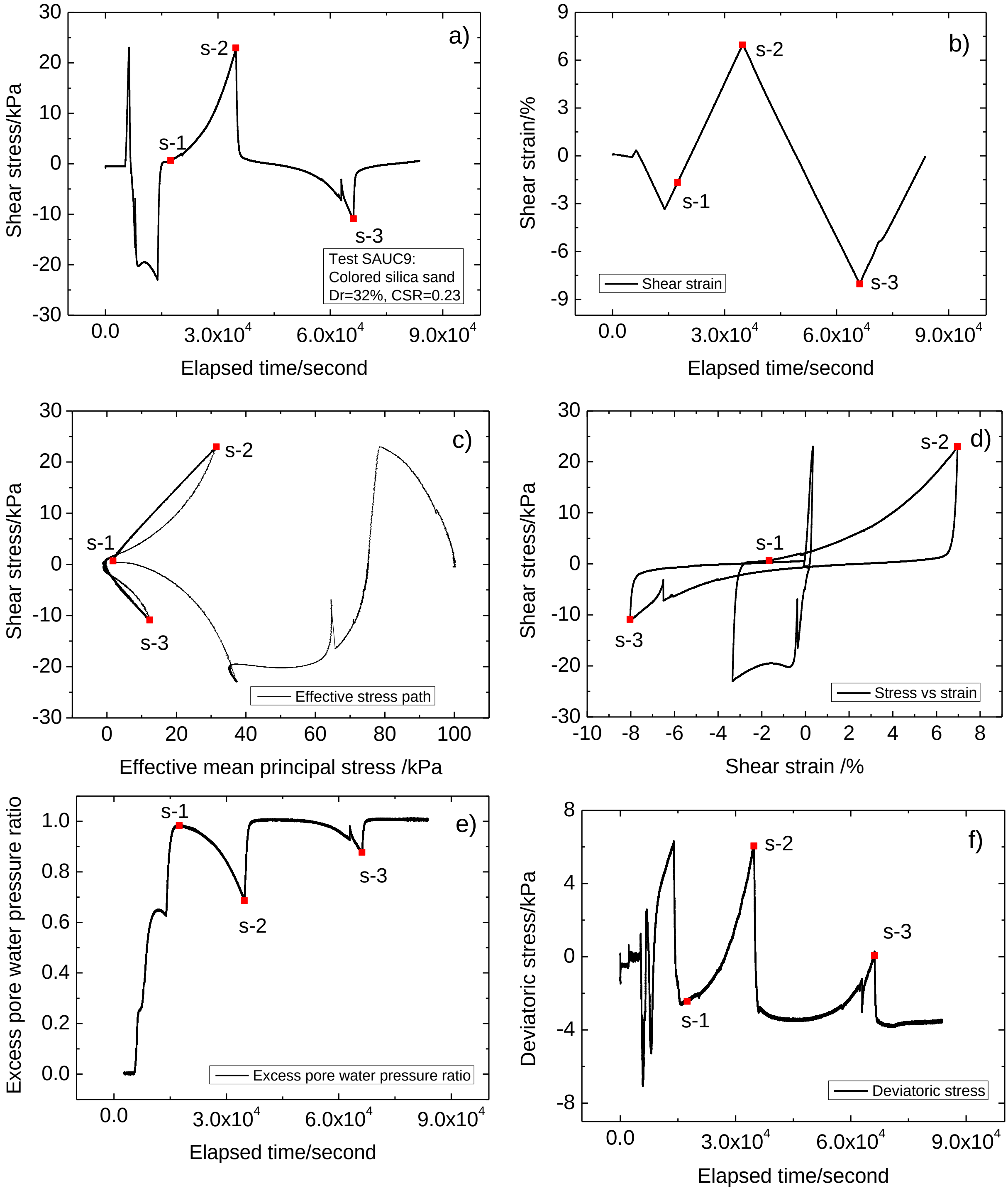

**Fig. 6.14 Results from test SAUC9**

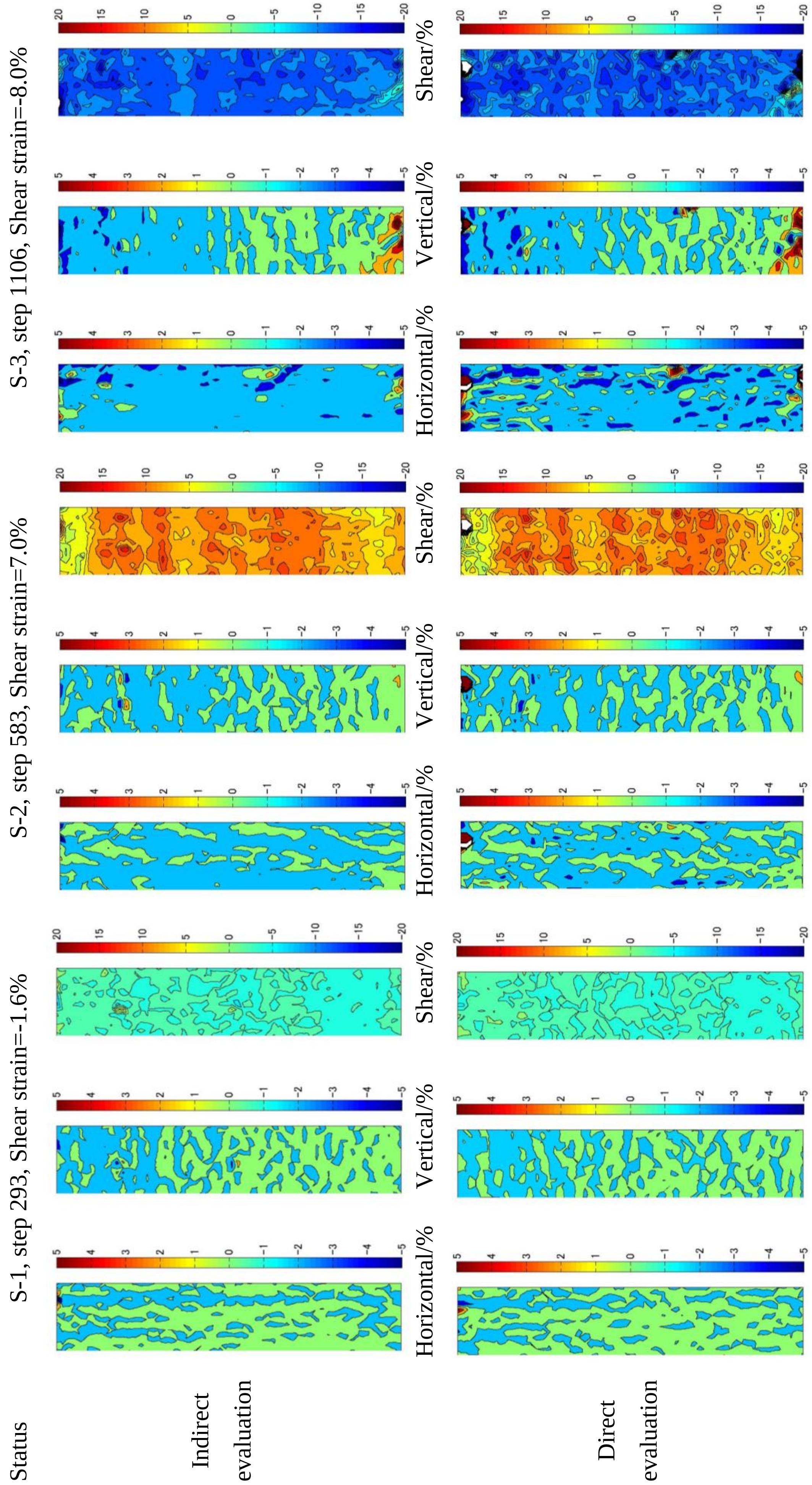

**Fig. 6.15 Local strain distributions of selected statues in test SAUC9**

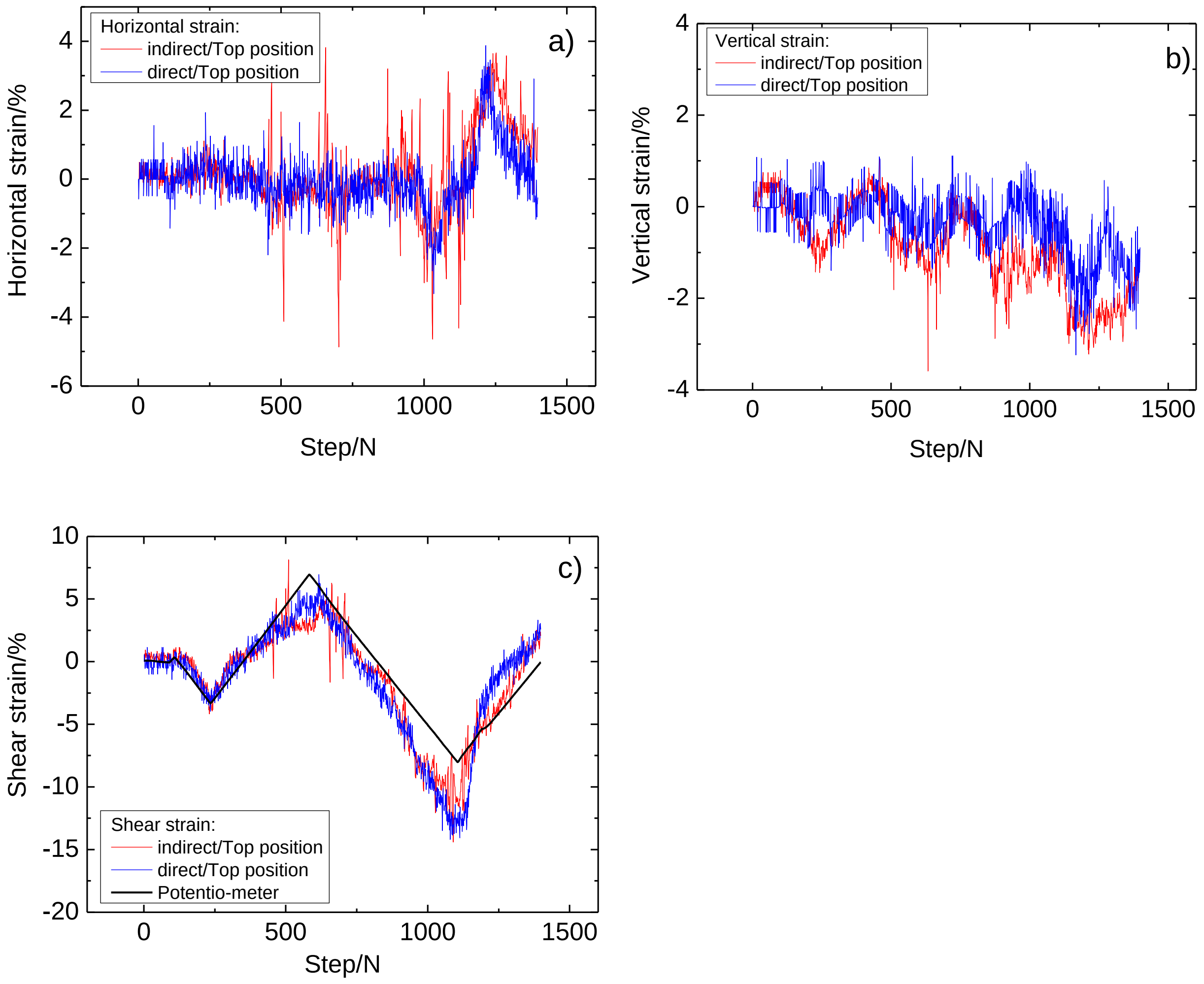

Fig. 6.16 Step histories of horizontal, vertical and shear strains at the top of specimen in test SAUC9

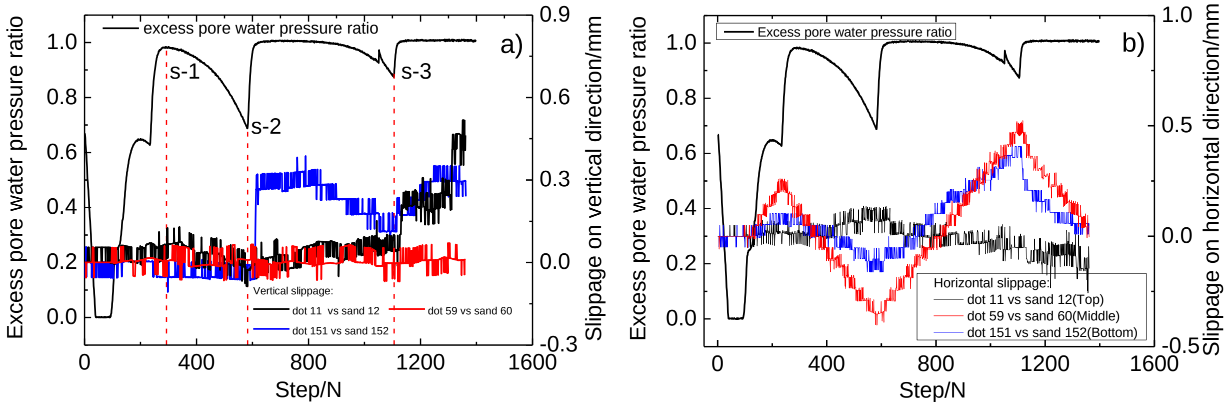

Fig. 6.17 Step histories of excess pore water pressure and slippages in test SAUC9

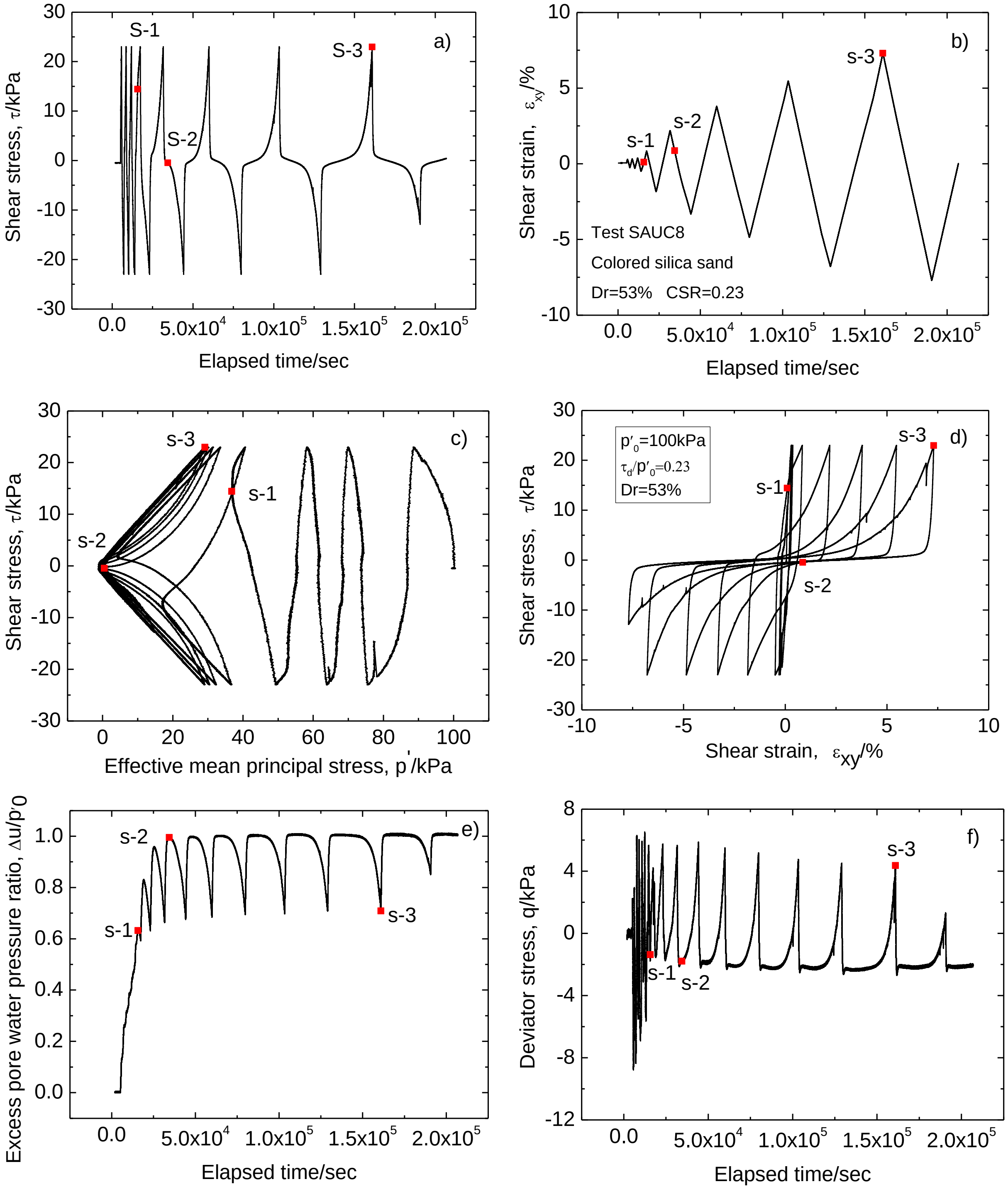

**Fig. 6.18 Results from test SAUC8**

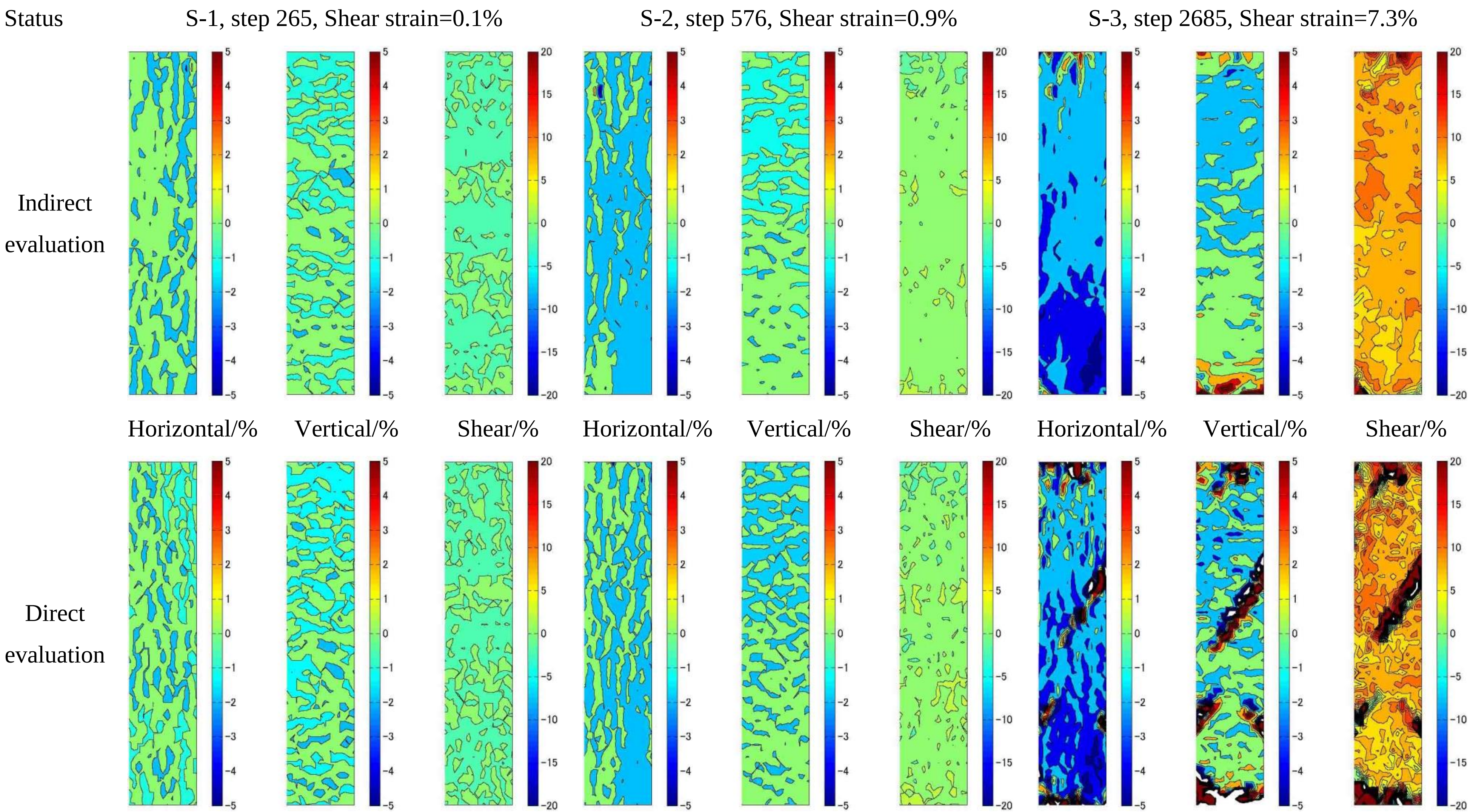

**Fig. 6.19 local strain distributions of selected statuses in test SAUC8**

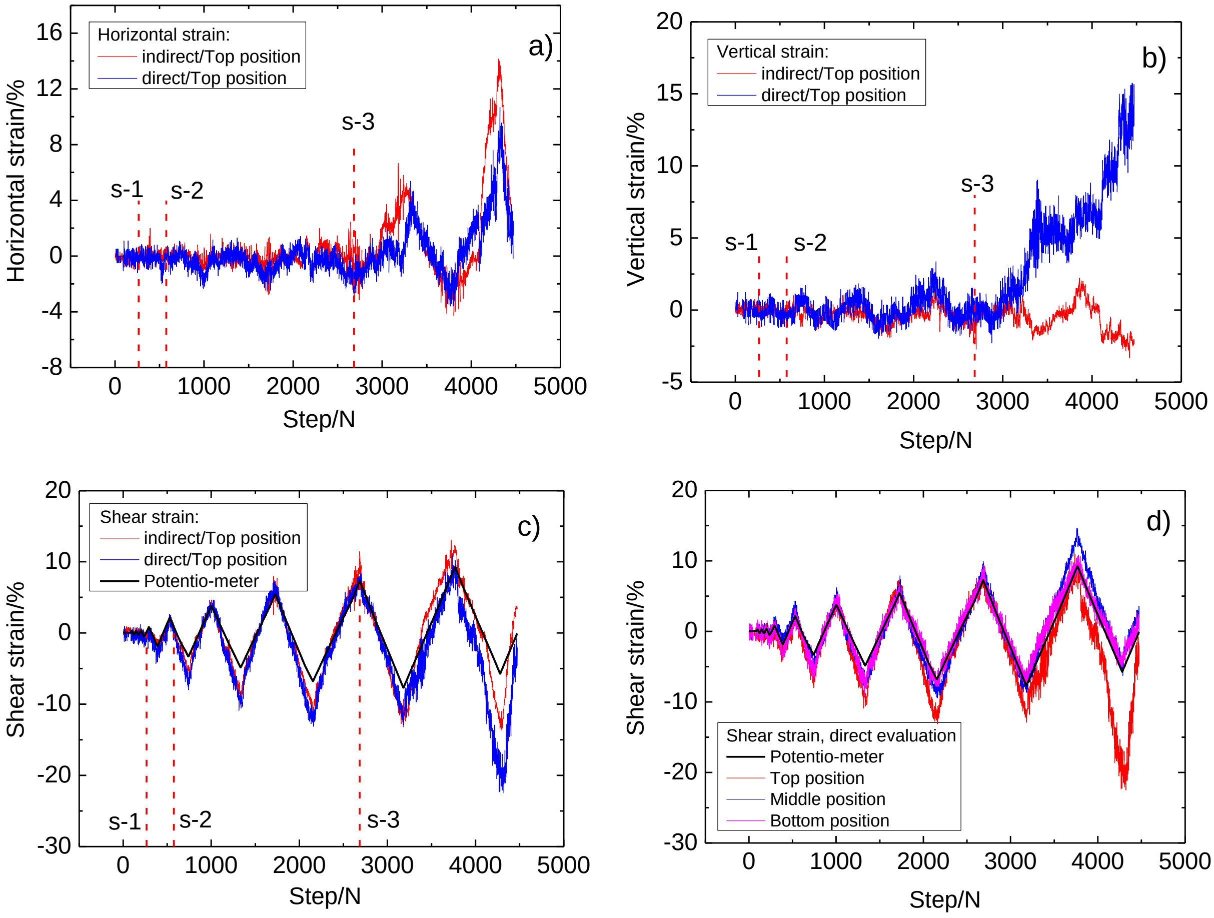

**Fig. 6.20 Local strain comparison at the top part of specimen in test SAUC8**

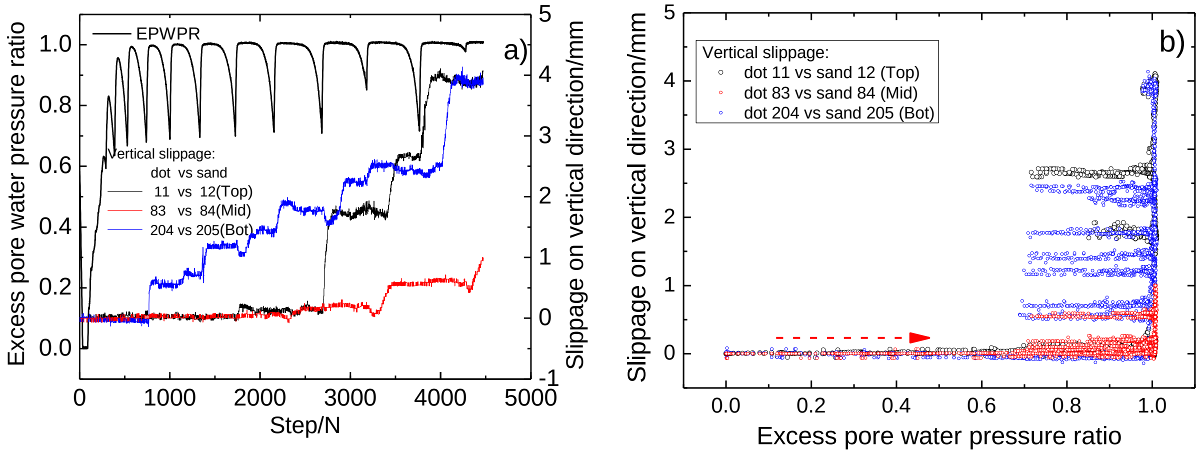

**Fig. 6.21 Relationships between excess pore water pressure ratio and vertical slippage**

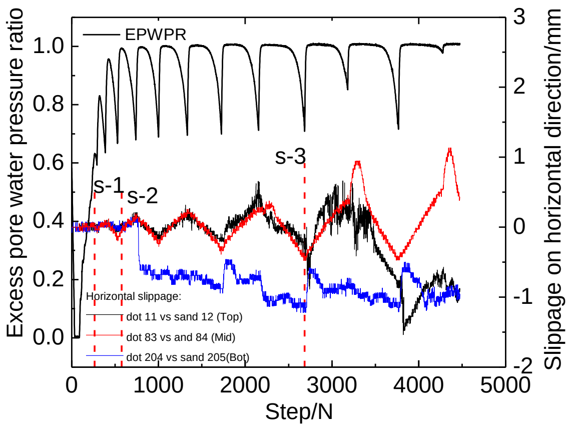

**Fig. 6.22 Step histories of excess pore water pressure ratio and horizontal slippage**

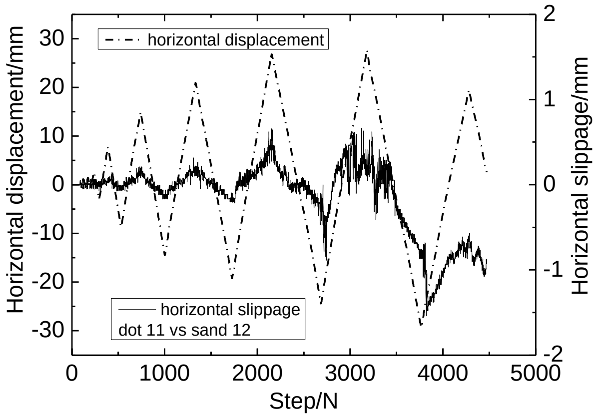

**Fig. 6.23 Step histories of horizontal slippage and horizontal displacement of measured point**

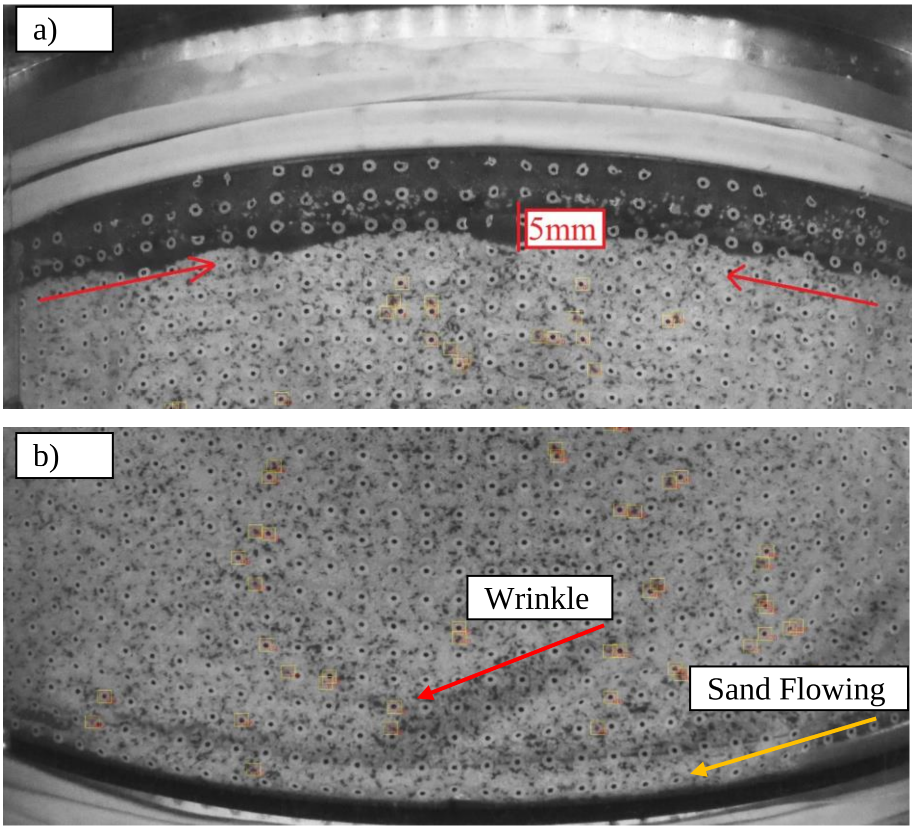

**Fig. 6.24 Top and bottom parts of specimen at the last photo in test SAUC8**

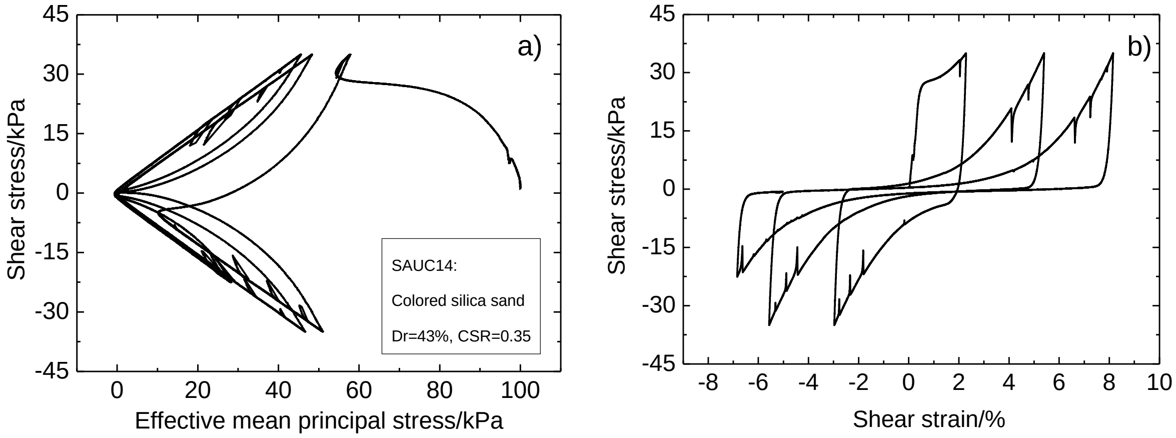

**Fig. 6.25 Stress path and stress vs strain in test SAUC14**

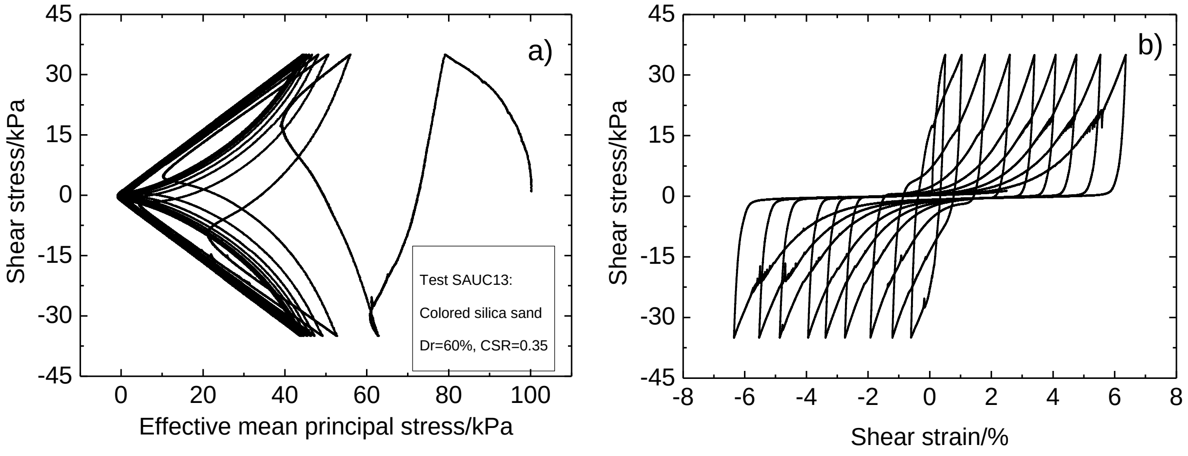

**Fig. 6.26 Stress path and stress vs strain in test SAUC13**

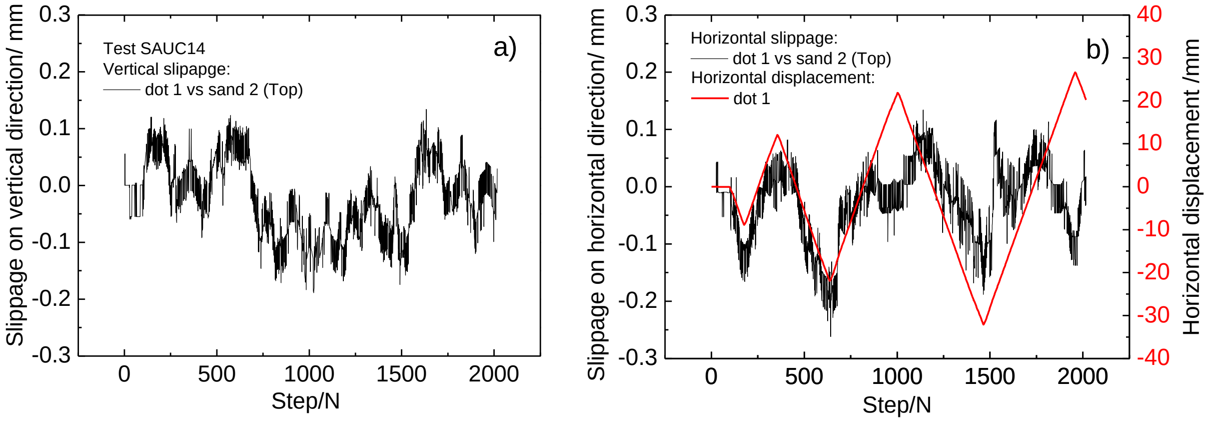

**Fig. 6.27 Step histories of vertical and horizontal slippages in test SAUC 14**

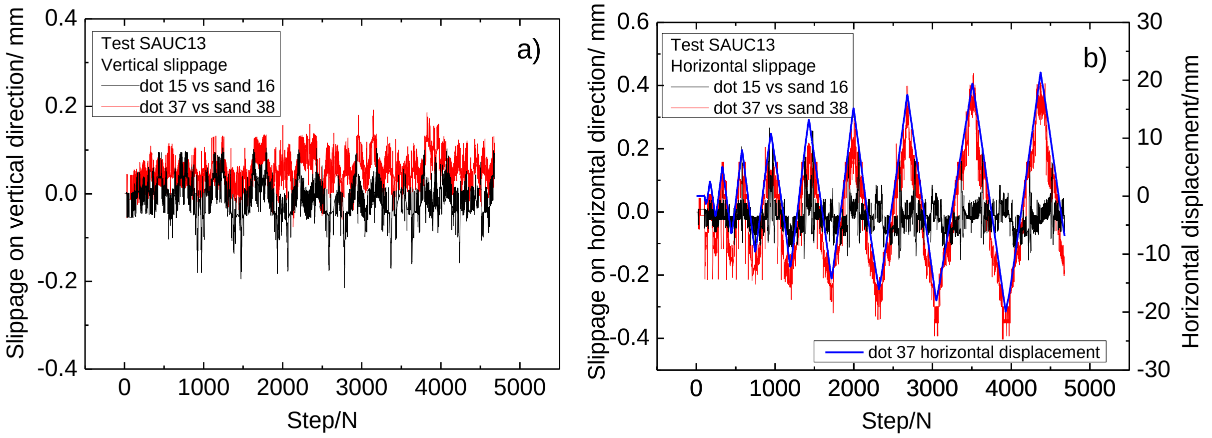

**Fig. 6.28 Step histories of vertical and horizontal slippages in test SAUC13**

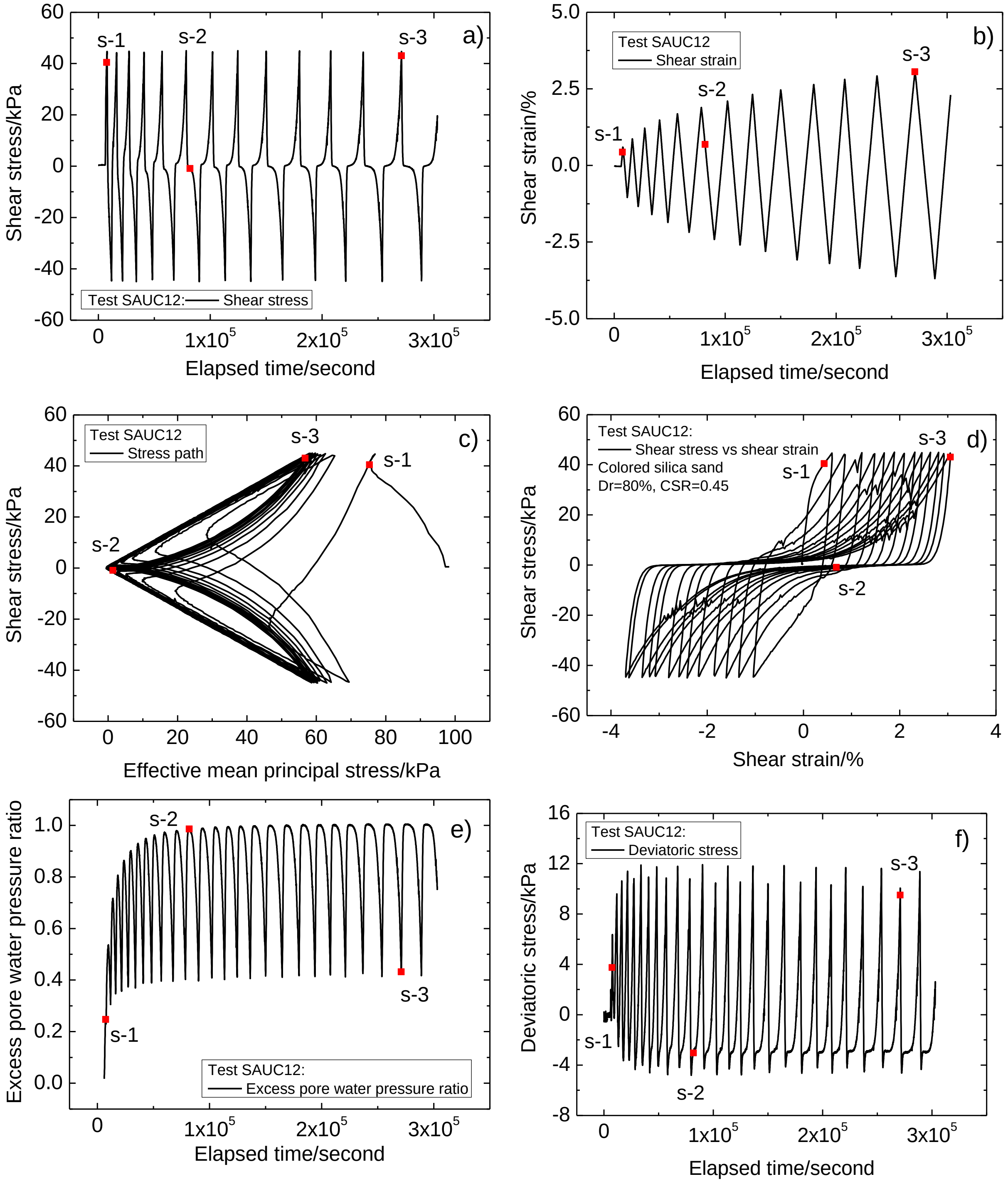

**Fig. 6.29 Results from test SAUC12**

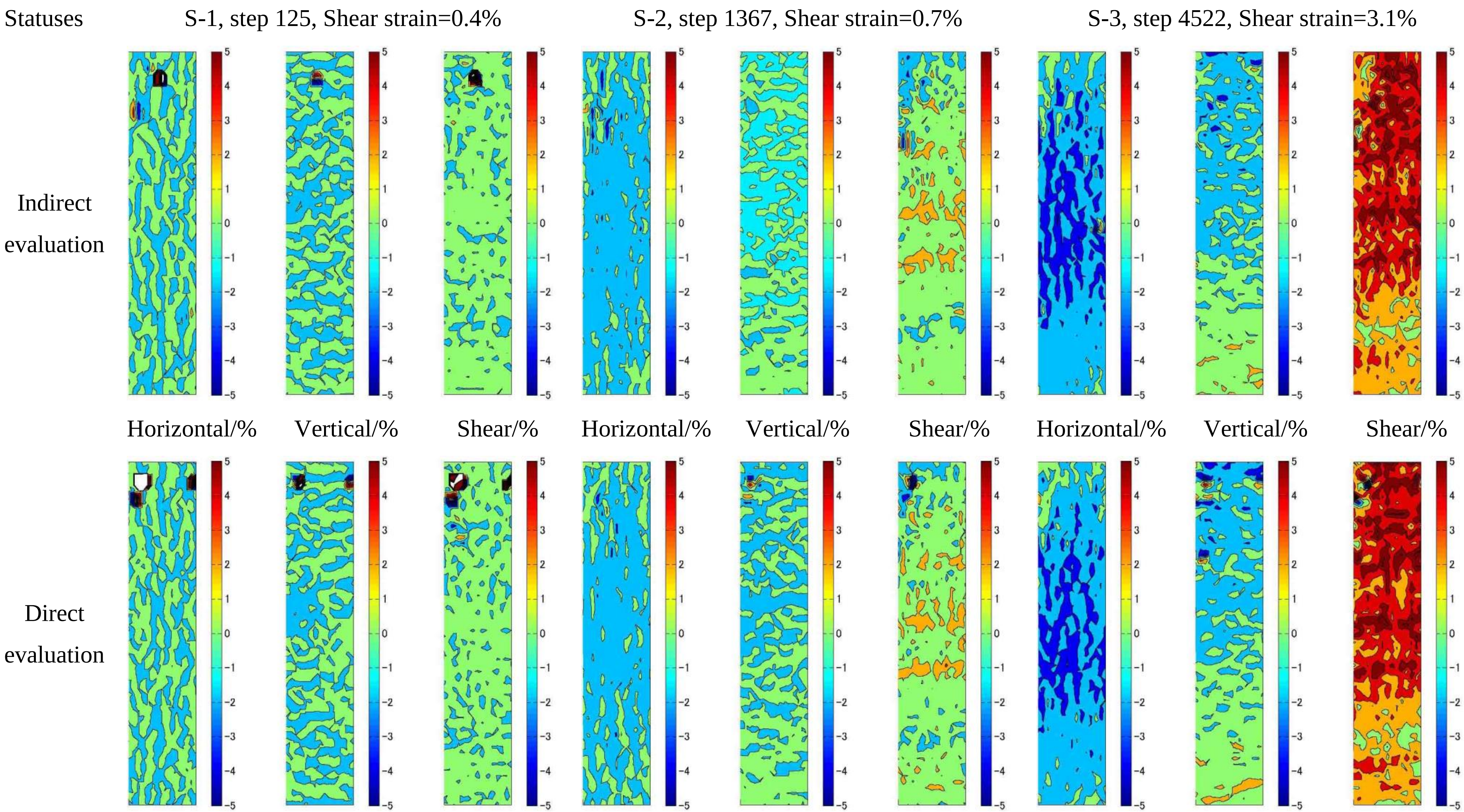

Fig. 6.30 Local strain distributions of selected statuses in Test SAUC12

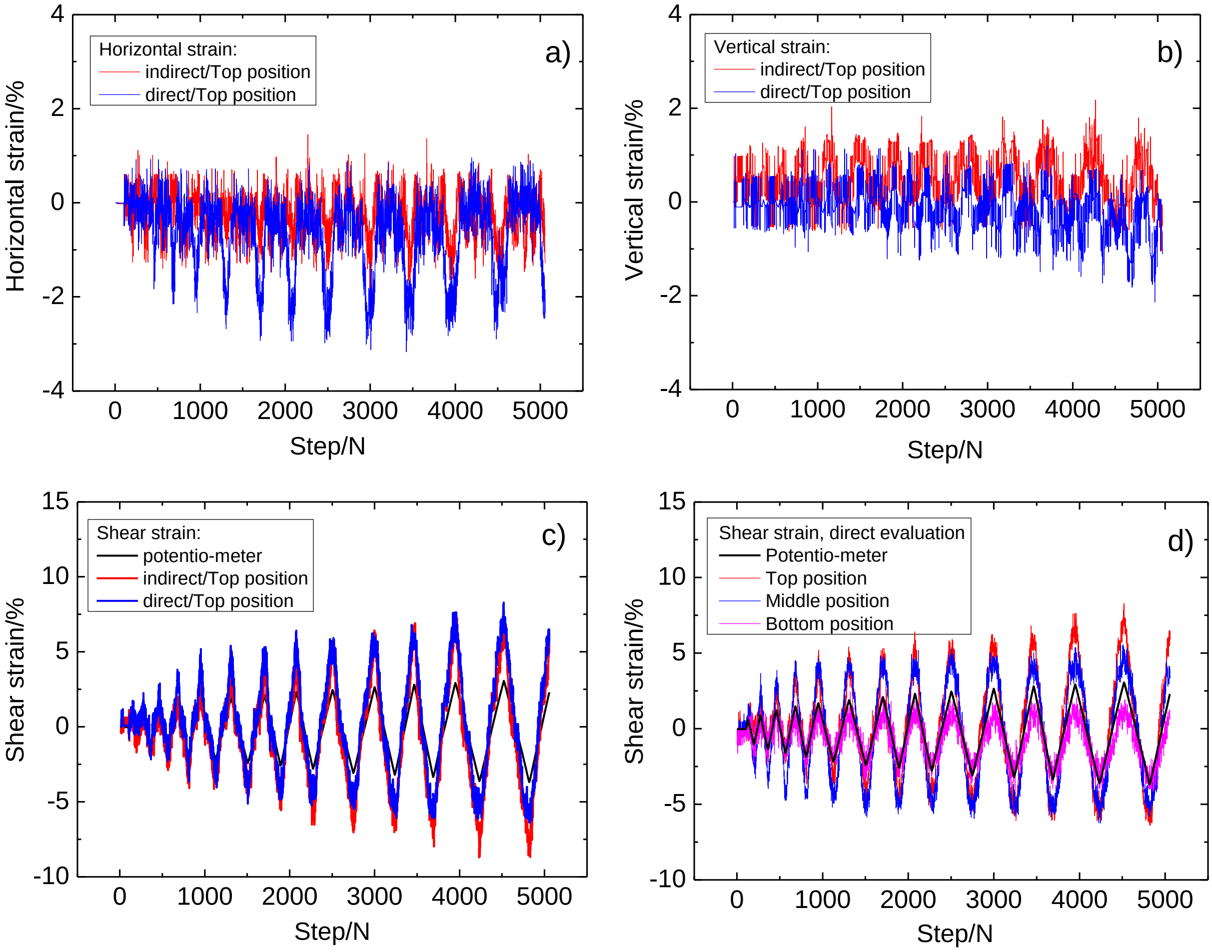

**Fig. 6.31 Local strain comparison between direct and indirect evaluations at top part of specimen**

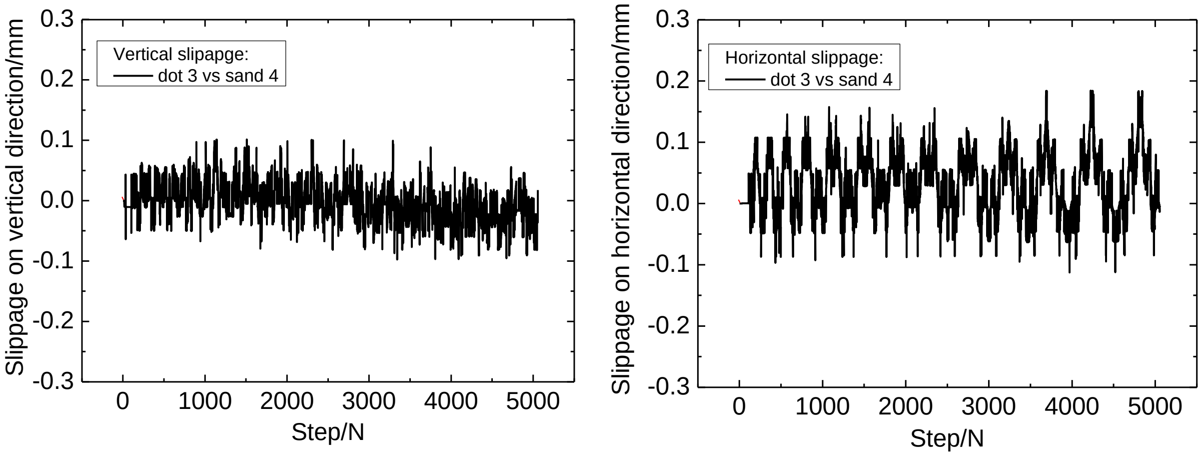

**Fig. 6.32 Step histories of vertical and horizontal slippages at top part of specimen in test SAUC12**

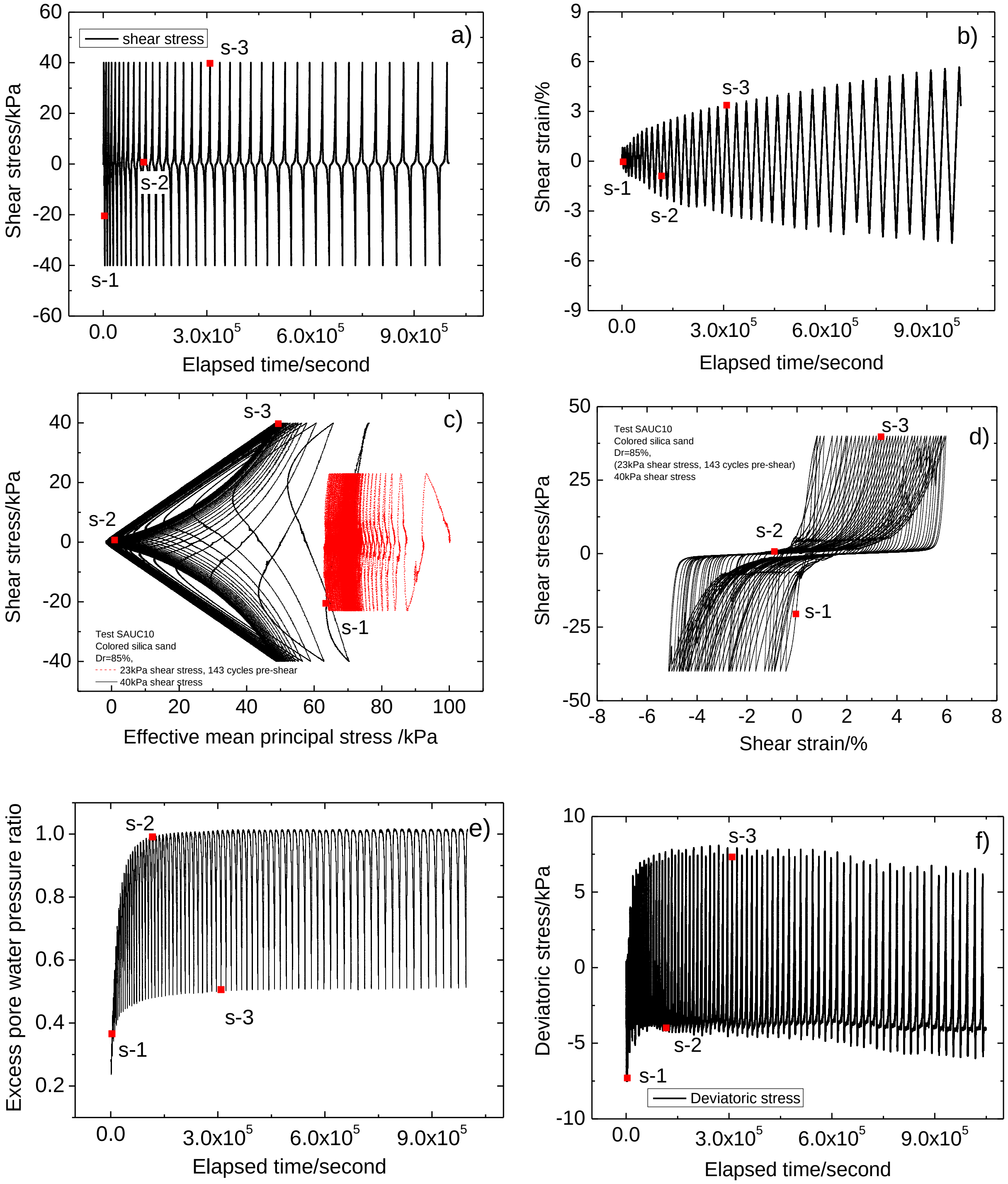

**Fig. 6.33 Results from test SAUC10**

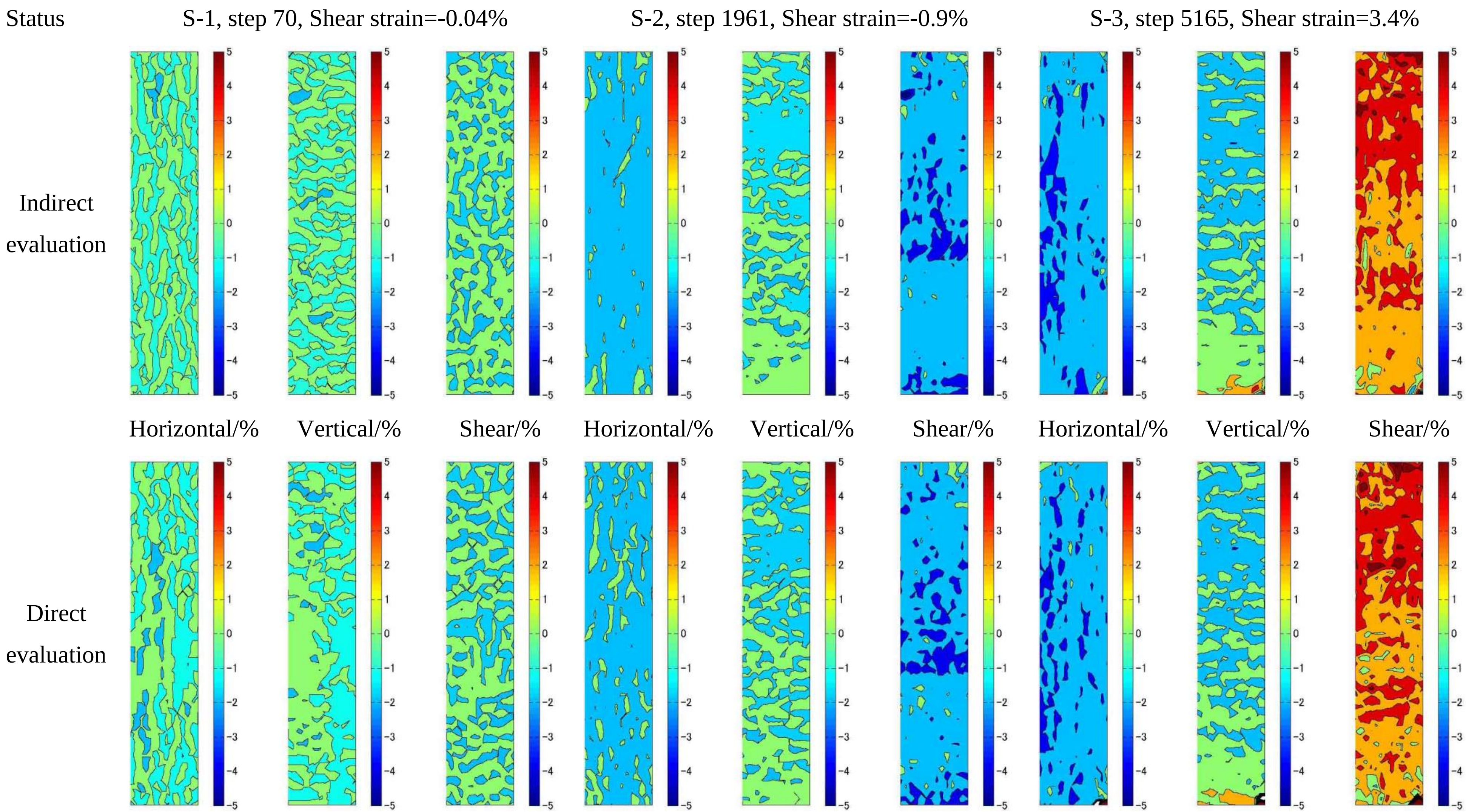

**Fig. 6.34 Local strain distributions from direct and indirect evaluations at selected statuses in test SAUC 10**

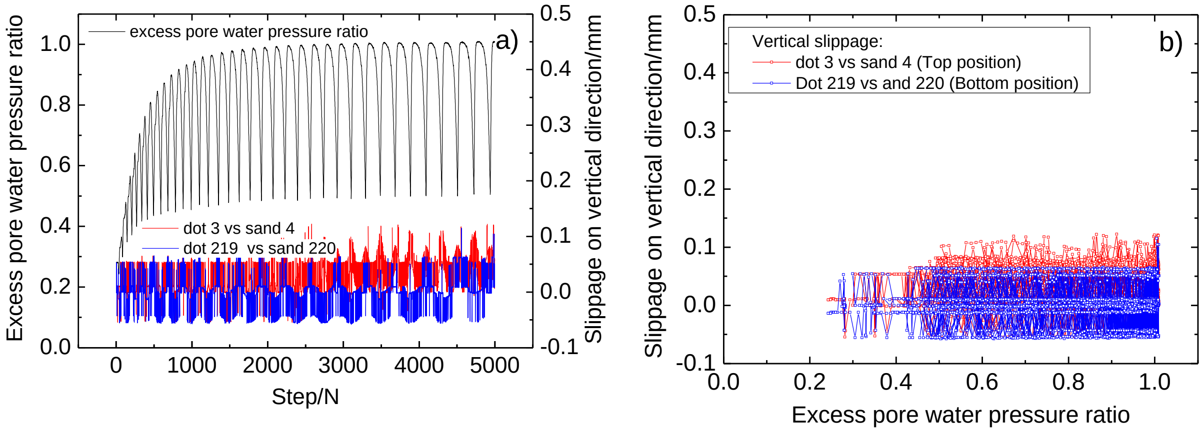

**Fig. 6.35 Relationships between excess pore water pressure ratio and vertical slippage at test SAUC10**

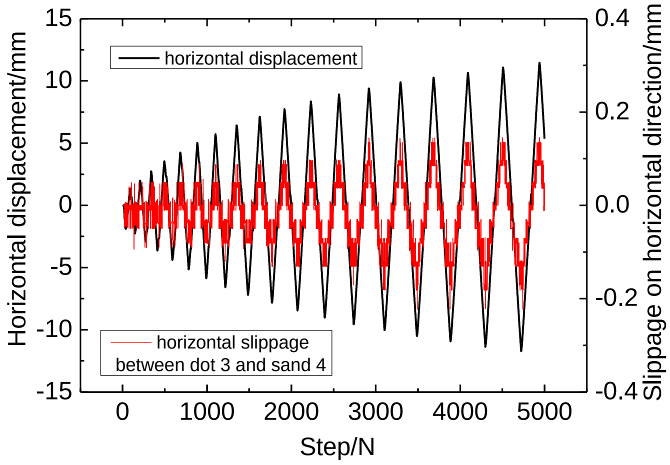

**Fig. 6.36 Step histories of horizontal displacement and horizontal slippage at top part of specimen in test SAUC10**

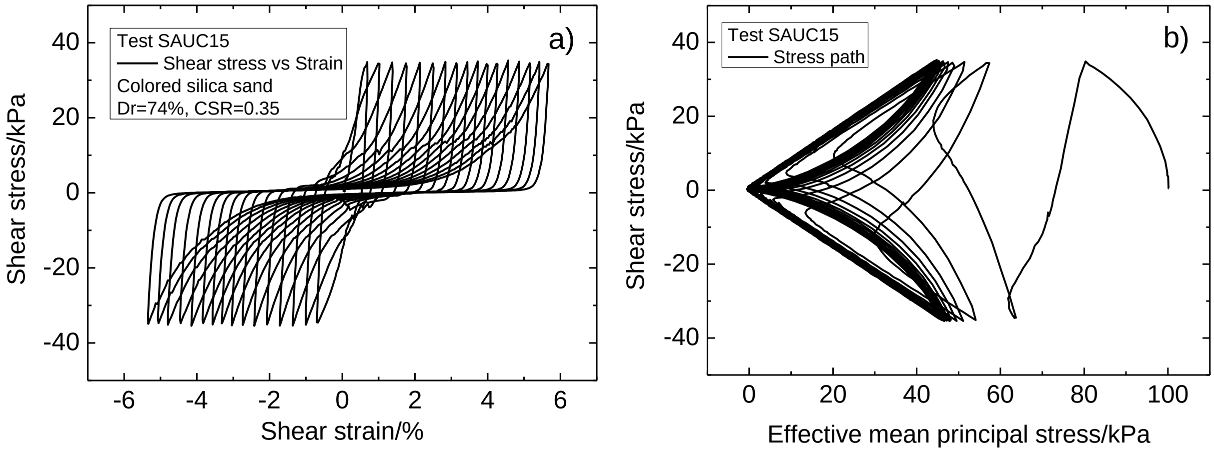

**Fig. 6.37 Results from test SAUC15**

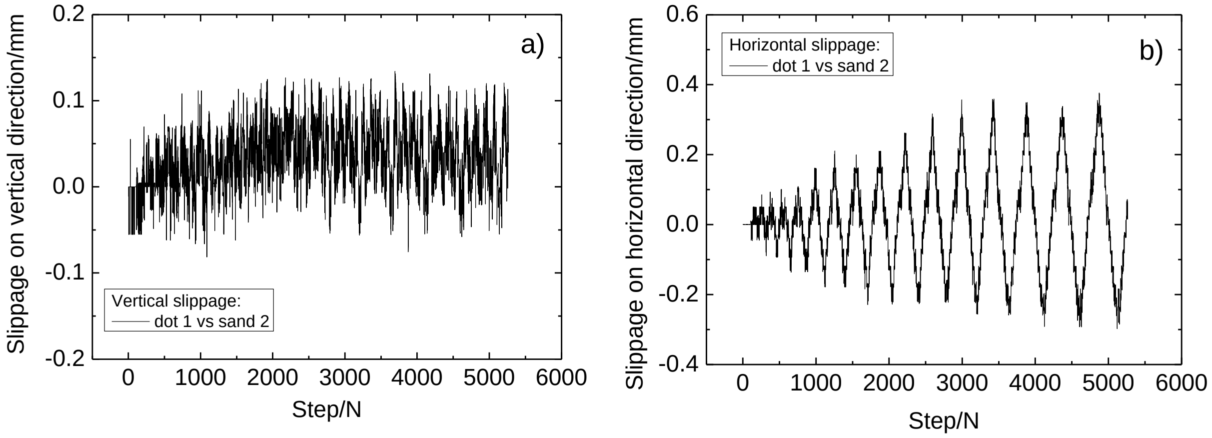

**Fig. 6.38 Step histories of vertical and horizontal slippages**

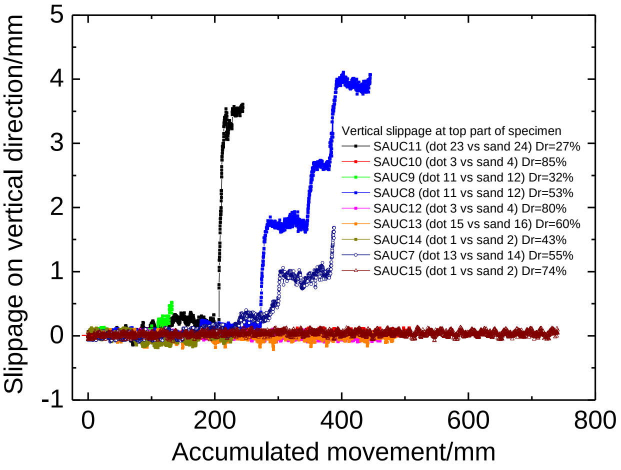

**Fig. 6.39 Relationships between vertical slippages and accumulated movements at top parts of specimens in different tests**

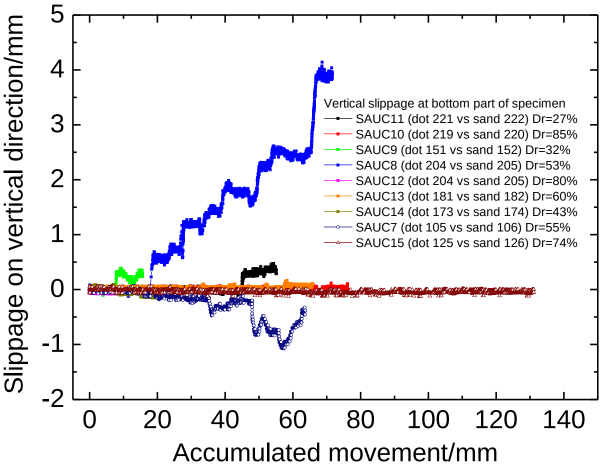

**Fig. 6.40 Relationships between vertical slippages and accumulated movements at bottom parts of specimens in different tests**

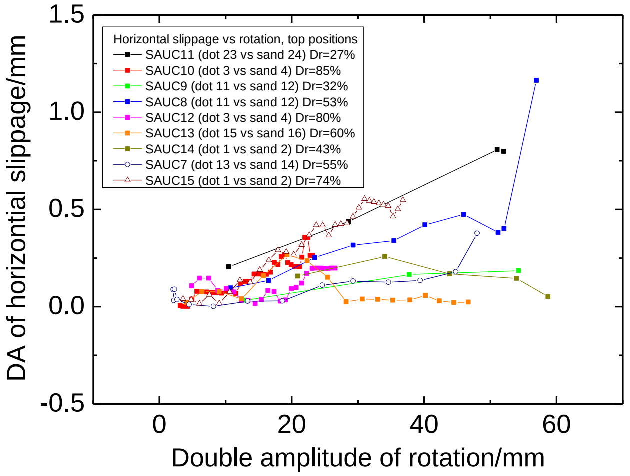

**Fig. 6.41 Relationships between double amplitudes of horizontal slippages and horizontal rotations at the top parts of specimens in different tests**

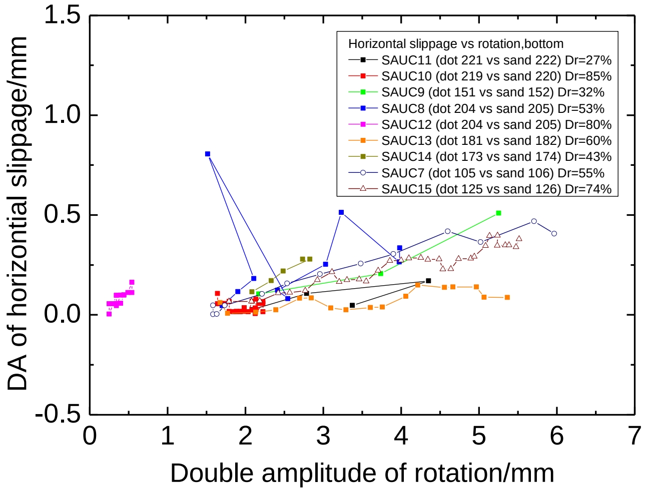

**Fig. 6.42 Relationships between double amplitudes of horizontal slippages and horizontal rotations at the bottom parts of specimens in different tests**

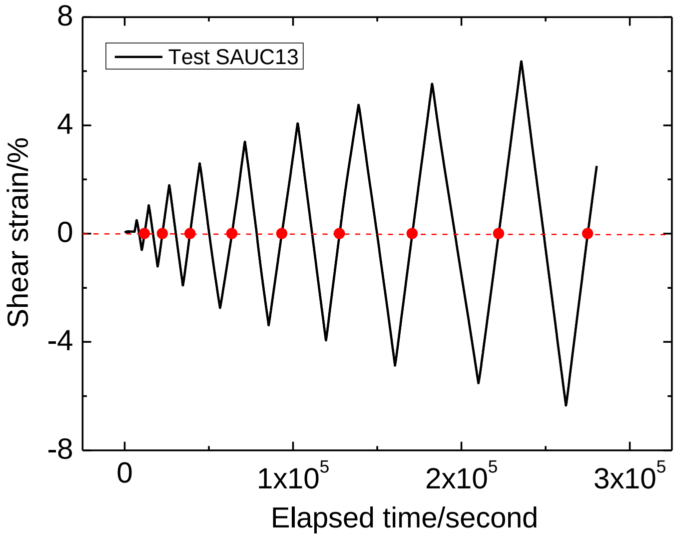

**Fig. 6.43 Time history of shear strain with selected statuses for slippage analysis in test SAUC13**

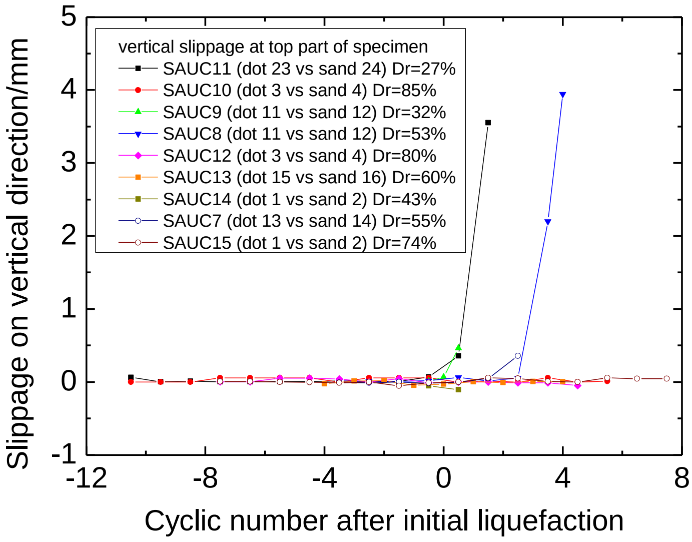

**Fig. 6.44 Relationships between vertical slippage at top part of specimen and cyclic number after initial liquefaction**

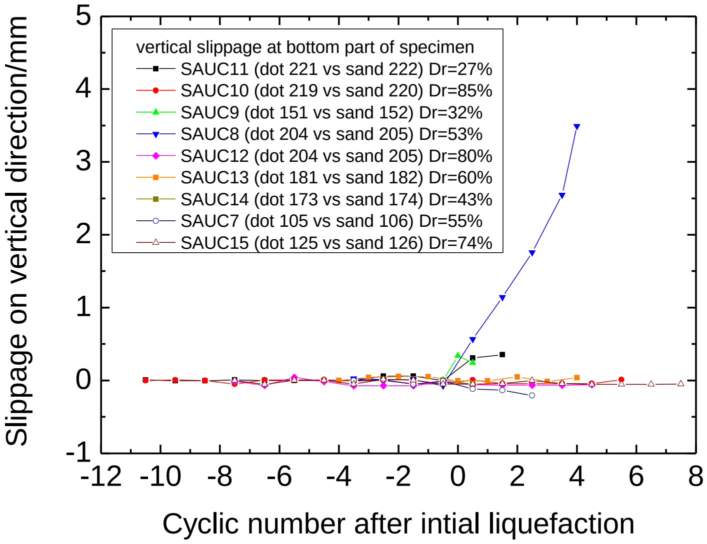

**Fig. 6.45 Relationships between vertical slippage at bottom part of specimen and cyclic number after initial liquefaction**

# 7. LOCAL DEFORMATIONS OF SEGREGATED SAND SPECIMENS IN UNDRAINED TORSIONAL SHEAR TESTS

## 7.1 Introduction

This chapter introduces the formation mechanism of layered deposits in reclaimed land and presents the related researches on layered deposits by element test, one column test, shading table test and dynamic centrifuge test. Additionally, this study divides the tests into two categories by the thickness of fine layers. One class is that the sand specimen is intercepted by three thin fine layers. The other class is that the sand specimen is intercepted by one thick fine layer. The local deformations of segregated sand specimens will be described by indirect and direct evaluation methods. Meanwhile, the local strains between fine layer and sand layer are compared. In order to observe sand particles and pore water migrations, the low capacity differential pressure transducer will be employed to measure the differential pore pressure between top and bottom of specimen.

## 7.2 Prior researches on local deformations of layered deposit

Reclaimed land is widely constructed by dredging and pumping method in recent years to meet the needs of economy development in the developed regions. The sand was dredged from the bottom of river or sea, and delivered to the reclaimed land by pumping. Since the reclaimed land was constructed near sea bay area, it was filled with seawater during construction. The sand sunk to the bottom to form the ground gradually. It should be noted that natural sand was not a uniform material which had various particle sizes. Certainly, different size of sand particles would had different velocities of settlement. Therefore, the natural sand would be separated by their particle sizes and stratification was formed. The layered deposit was actually intercepted by less permeable layers which consisted of fine and silt layers. Another geology condition was that the water table of reclaimed land was relatively high. The bottom layers were fully saturated. These reclaimed lands were highly liquefiable during earthquake.

Soil investigation was conducted by Kokusho (2002) for one reclaimed land along Tokyo bay area. Sieve analysis was employed along one line of the investigation excavation. Fig. 7.1 gives the vertical change in grain size distribution along the depth. The results indicated that the percent of soil was highly variable in terms of the particle size along the depth. In addition, one column test was used to investigate the water film formation by Kokusho (1999). It was found that a water film was generated beneath the silt layer which had a thickness of only few millimeters. Fig. 7.2 gives the photograph of water film beneath the silt seam. Moreover, Shaking table tests were also performed by Kokusho (2000) for the investigation of water film. A water film as thin as a hair appeared beneath the silt seam.

Additionally, dynamic centrifuge tests were performed by Maharjan and Takahashi (2014) to investigate the seismic performance of embankments by various liquefiable foundations.

Multiple layered sand foundation was intercepted by discontinuous low permeability layers. The results indicated that pore water was accumulated beneath the low permeability layer. Large shear strain was also found below the silty layer which might result into lateral spreading of non-homogeneous foundation. In could be concluded that low permeability layer acted as an important role on the stability of liquefiable foundations.

In order to obtain the mechanism of water film formation, a torsional shear apparatus was applied by changing the frequency of loading (Kokusho, 2003; Kokusho et al., 2002). Being similar as author's research, the vertical displacement was not allowed during the undrained cyclic loading. The settlement of sand particles was found during the tests. Water film under the top cap was observed. In chapter 6, the affection factors for water film formation has been introduced in detail. Moreover, segregated sand specimen was employed in the undrained torsional shear tests (Fauzi, 2015; Fauzi and Koseki, 2014). The sand used in the test was excavated from Katori city at Chiba prefecture in Japan. Sand specimen was intercepted by two fine layers which had relatively low permeability. Great efforts had been made to observe the water film by applying image analysis. The results indicated that pore water was concentrated beneath the fine layer. This phenomenon was confirmed by the expanded local vertical strains at the fine layer.

## 7.3 Local deformations of segregated sand specimen

The preparation method of segregated specimen has been introduced in chapter 2. As shown in Fig. 7.3, three low permeability layers were formed at the top of sand layers. In the method described by Fauzi, the top fine layer was cut off because the top fine layer would be affected by the top cap largely. Based on the results in chapter 6, the settlement of sand particles was accumulated finally at the top part of specimen, which meant the phenomenon of water film at top part was more instinct than the bottom positions. Therefore, the top fine layer was remained by slightly decreasing the thickness of each layer. At last, as shown in Fig. 7.4 (a), there were three fine layers intercepting the sand specimen. The top sand layer was only 2-3 cm which would eliminate the disturbance from top cap. This dispose would increase the potential to observe water film during testing. Another measure was the combination of fine layers without changing the global fine content. As shown in Fig. 7.4 (b), the thickness of top fine layer was increased by decreasing the thicknesses of bottom fine layers. Before testing, the Katori sand was sieved to obtain the fines whose diameter was less than 0.075 mm. Actually, One specimen needed around 10 Kg Katori sand. It was different to sieve out all the fines in the sand. Therefore, there were still fine layers at the bottom. Almost all the fines were used to obtain a thick fine layer at the top part of specimen.

Since the water filled in the acrylic pipes was domestic water without processing, there was much of air in the water. Even though de-aired water was used for the saturation, the fully saturated condition was difficult to achieve. In order to obtain a high B value, the saturation process was kept for a long time until the pore water in the specimen was fully replaced by the de-aired water. Finally, the B value obtained was larger than 0.95.

Fig. 7.5 shows the liquefaction resistance of Katori sand compared with the data from Fauzi (2015). It can be seen that the specimen prepared by water sediment method had a relatively larger liquefaction resistance than the one by moist tamping method. Based on the results, the specimen prepared by fine had the largest liquefaction resistance than others which including and excluding fines. Whereas, the specimen prepared by sand only was with the lowest liquefaction resistance. Even though the fine content was 15% in this study, the liquefaction resistance of specimen with a relative density of 24~26% was smaller than the one with a relative density of 28~29% and fine content of 5%. In addition, when the fine layers were combined into one fine layer at top part of specimen, the liquefaction resistance slightly increased.

### 7.3.1 Sand specimen intercepted by thin fine layers

The segregated specimen with three thin fine layers shown in Fig. 7.6 was consolidated to an initial effective confining stress of 100 kPa and subjected to undrained cyclic loading at a cyclic stress tress of 0.15. The observed behavior is shown in Fig. 7.7 (a) through (f) in which three statues are marked by read rectangles. S-1 is the status when the first time of phase transformation was reached. S-2 is the one when excess pore water pressure ratio was 0.97 at the first time. S-3 is the one when the shear strain was -10.6%. Their corresponding local strain distributions were analyzed and plotted in Fig. 7.8. It could be seen that the local strain distributions from indirect and direct evaluations were almost same with each other before status-2. In status-3, the strain localization could be recognized from the local strain distribution. Slight affection by fine layers could be observed by the local strain distributions. The distinct different of local strains between fine layer and nearby sand layer was found from the direct evaluation. Meanwhile, this difference also appeared on the local strain distributions from indirect evaluation.

In order to observe the values of local strains along the specimen, the central position of each row was selected. Fig. 7.9 gives the local strain comparisons from indirect evaluation between the three statuses and the status after consolidation. There was no difference of local vertical strains between the four statuses. Since the vertical displacement during testing was prohibited, the values of local vertical strains were reasonable. As for the local shear strain, non-uniform distributions occurred and there was no significant difference between sand layers and fine layers. Fig. 7.10 shows the local strains of central position at each row from direct evaluation. The results of local vertical strains were almost same as those from indirect evaluations. There was also no significant difference between the four statuses. Moreover, only slight affection on the local vertical strain was observed from the bottom fine layer. However, remarkable difference of local shear strains between fine layers and sand layers took place. It seemed that fine layers largely affected the local behavior near fine layers, especially under large shear strain condition.

The above analysis indicated that the local shear strain near fine layer had a sudden change at the selected statuses. The sudden change could be described by the opposite increments of shear strain on clockwise and anti-clockwise directions. The image analysis method employed in this study was based on the pattern of traced element. The distribution of gray color in the pattern was memorized and searched in the appointed region. As for the water sediment sample preparation method, sand particles were separated by their particle sizes. The particles in the fine layer were very small. In addition, the color of Katori sand was flat and quite different from the mixed colored silica sand introduced in chapter 6. It is still a tough task to make a large color contrast of Katori sand. Therefore, it can be seen in Fig. 7.11 that the traces of sand particles patterns in fine layer were not as steady as the traces in the nearby sand layers.

As shown in Fig. 7.12, five elements were selected near each fine layer. The two fine layers at middle and bottom positions of sand specimen had a thickness of around 5mm, respectively. Therefore, the data from element 3 of each part could represent the local behavior of corresponding fine layer. The step histories of local vertical and shear strains were plotted in Fig. 7.12. The local strains were not uniform even the measured points were neighboring to each other. Compared with the local strains from indirect evaluation, the local strains from direct evaluation were not steady. The fluctuation was quite distinct because color of Katori sand was flat. However, the change trend of the local strains was still coincident with those from indirect evaluations.

Observed behavior in test KWUC2 where the specimen was consolidated to an initial effective stress of 100 kPa and subjected to undrained cyclic loading at a cyclic stress ratio of 0.1 is shown in Fig. 7.13 (a) through (f). Compared with the result of test KWUC1, large number of cycles was undergone in test KWUC2. Three statues were selected and marked by red rectangles to show the local strain distributions. S-1 is the status when the shear strain was -1.36%. S-2 is the status when the excess pore water pressure ratio was 0.98 at the first time. S-3 is the one when shear strain was -7.12%. Their corresponding local strain distributions are plotted in Fig. 7.14. At step 948, it could be seen that the local strains from indirect evaluation were uniform. At the top part of the figure, there were two regions plotted by red and white colors. It was induced by the coordinate information of missing points. For example, when the dots in the region could not be traced, the coordinate of these lost points were not valid. Therefore, the local strain results from the two regions were not reliable. From the direct evaluation at step 948, strain localization was observed near the fine layers. At step 1027, the red arrows point to the position of fine layers. Extended local vertical strains were found at the fine layers from the indirect evaluation. This phenomenon was also observed by Fauzi (2015). It was explained by the reason that pore water was concentrated near the fine layers. Form the direct evaluation at step 1027, strain localization was found both from the vertical and shear strain distributions. At step 1135, the extended local vertical strain was also observed near the fine layers. In addition, the region of extended local vertical strain expanded when compared with the region at step 1027.

### 7.3.2 Sand specimen intercepted by thick fine layer

As introduced in Fig. 7.4, in order to observe the local behavior of fine layer, the three fine layers were combined into one layer. Additionally, the difference of pore water pressure between top and bottom of specimen was measured by one low capacity differential pressure transducer. As shown in Fig. 7.15, there was one thick fine layer under the top cap with the thickness about 25 mm. Fig. 7.16 shows the photo when the specimen was vacuumed at a negative pressure of 30 kPa. Since the settlement heights of sand and fine were same during preparation, the lower stiffness of fine layer might be the reason why membrane penetration occurred at fine layer.

Observed behavior in test KWUC3 where the segregated specimen was consolidated to an initial effective stress of 100 kPa and subjected to undrained cyclic loading at a cyclic stress ratio of 0.13 is shown in Fig. 7.17 (a) through (f). Three statuses were selected and marked by red rectangles to show the local strain distributions. S-1 is the status when the phase transformation was reached. S-2 is the status when the excess pore water pressure ratio was 0.97 at the first time. S-3 is the one when shear strain was 8.1%. Their corresponding local strain distributions were plotted in Fig. 7.18. The arrows in the figures point to the position of fine layer. It can be seen that most of the strain localization occurred near the fine layer. At first, the compressed vertical strains were observed only near the fine layer. It was due to the penetration of membrane when there was effective stress. At step 196, the penetration affection on the local strains almost disappeared. However, the strain localization from direct evaluation was irreversible. The local strains in fine layer became more serious than the local strains at status-1. At status-3, significant difference of local strains between sand layer and fine layer was not observed from the indirect evaluations. Another fact was that the local strains along the specimen at S-3 were not uniform. Based on the direct evaluation of local strains, distinct strain localization appeared near the fine layer. Compared with the local strains from indirect evaluation, it can be confirmed that considerable deformation took place at fine layer. In addition, since the color of fine layer was flat and the size of fine particle was very small, the image analysis results at fine layer were not valid when the shear strain was large. More efforts were needed to increase the accuracy of image analysis on the local deformation evaluation of segregated specimen.

In order to check the local strains near fine layer, Fig. 7.19 gives the local strains of the central position at each row from indirect evaluation. The curves of local vertical strains indicated that they were uniform throughout the test. However, the point just beneath the fine layer had a relative larger vertical strain than other positions after the consolidation. In the next cycles, the local vertical strain of this point was always smaller than the one after consolidation. This phenomenon might be influenced by the membrane penetration at first by increasing the effective stress from 30 kPa to 100 kPa. Subsequently, the concentration of pore water underneath the fine layer might decrease the affection of penetration. Based on the geometry relations between specimen surface and camera, membrane penetration induced the increasing of distance from membrane to camera lens. Therefore, the measured distance between two dots or sand particle patterns became shorter than the one before membrane penetration. Moreover, membrane penetration was induced by the compression of specimen. These two factors resulted in the red local strain strip in the local strain distribution at step 176. As for the local shear strain from indirect evaluation, significant strain localization was not observed. Moreover, the global shear strain measured by potentio-meter underestimated the shear deformation of specimen. For example, the global shear strain at status-3 was 8.1%. However, the average value of local shear strains at S-3 was 12% which was 1.5 times larger than the global shear strain.

As explained in the above section, the color of fine layer was flat and the particle size was very small, the local strains shown in Fig. 7.20 were not valid when the shear strain was large. During consolidation, the results of local strains were reliable. After that, the local strains at fine layer were not reliable. On the other hand, the local strains in sand layer were valid to some extent. Based on the above local strain analysis, the indirect evaluation method could be used to observe the local deformation of sand specimen. As for the direct evaluation, the local deformation of sand layer was valid and the local deformation of fine layer was reliable only when the shear strain was small.

In order to increase the tracing effect of sand particle pattern, the sand at the top part of specimen was mixed Katori sand by its original color and white color. Before specimen preparation, the original Katori sand was put into the oven to dry under the temperature of 50℃. After that, dry Katori sand was sieved by the sieves (4.75 mm and 0.075). All the sand passing through 4.75 mm and left over on the 0.075 mm sieve was separated into two parts. One was used to prepare the bottom part of specimen as shown in Fig. 7.21 (around 5 kg), only little fine was left inside of this part. The other part was around 2.3 kg which was used to make the upper sand layer. One fourth of this 2.3 kg Katori sand would be mixed with the white color (construction using pigment) and put into the oven to dry again. The white colored Katori sand was mixed with the left three fourth Katori sand. The speckled top part of specimen could be seen in Fig. 7.21. Image analysis results indicated that this measure increased the validity of deformations from direct evaluation.

Observed behavior in test KWUC4 where specimen was consolidated to an initial effective stress of 100 kPa and subjected to undrained cyclic loading at a cyclic shear stress ratio of 0.14 is shown in Fig. 7.22 (a) through (f). As explained in chapter 6, water film beneath the top cap was informed during the test. Therefore, there should be no deviator stress when the excess pore water pressure ratio was 1.0. However, the value of deviator stresses were around -3.0 kPa in all the tests. It was because the two top caps were hanged under the load cell. The deviator stress was updated to 0 kPa during the specimen preparation when the load cell was hanged in the air. It could be seen in figure (f) that the deviator stress was -3.3 kPa. Most of the deviator stress was from the self-weight of two top caps. Actually, the deviator stress between top cap and specimen was around 0 kPa during liquefaction. Three statuses were selected and marked by red rectangles to show the local strain distributions. S-1 is the status when the phase transformation was reached at the first time. S-2 is the status when the shear strain was -7.9%. S-3 is the one when the excess pore water pressure ratio was 0.99 at the first time.

In Fig. 7.23, the local strain distributions at selected statuses were compared between indirect and direct evaluation methods. At status-1, the excess pore water pressure ratio was around 0.85. As introduced in the above section, the red strain strip in the vertical strain distribution was induced by the membrane penetration. Along with the increasing of pore water pressure, the compressed vertical strain decreased gradually. In other words, the largest affection by membrane penetration occurred just after the consolidation. At status-2, it could be observed that non-uniform local strains were formed along the specimen. However, even though the shear strain was -7.9%, there was no wrinkles on the surface of membrane. The membrane wrinkles occurred when the load direction was reversed. The excess pore water pressure ratio increased sharply after the reversion of loading direction. At status-3, there was almost no effective stress. It can be seen that significant expanded vertical strain was induced near the fine layer. Relatively large local shear strain was also observed at the fine layer. Since the permeability of fine layer was remarkably lower than the sand layer, the expanded local vertical strain at fine layer might be affected by the pore water concentration. Based on the improvement of color contrast, the local strains from direct evaluation were reliable except for the positions near membrane wrinkles.

In Fig. 7.24, the local strains of the central position at each row are compared between the selected statues from indirect evaluation. It can be seen that the maximum value of compressed local vertical strain was reached at fine layer just after the consolidation. In addition, the significant extended local vertical strain appeared at status-3 when the excess pore water pressure ratio was almost 1.0. Based on the local vertical and shear strains, the affection of winkles also could be observed. Moreover, there was no large difference of local shear stain between sand layer and fine layer. The local strains of central position from direct evaluation are shown in Fig. 7.25. The same trend of local vertical strain in the direct evaluation was found. Differently, there were sudden changes of shear strain at the boundaries between sand layers and fine layer. Based on the results of Fauzi (2015), the liquefaction resistance of fine only specimen was significant larger than the sand only specimen when they were under the same experimental conditions. It could be seen from the direct evaluation of shear strains that smaller local shear strains were found at the fine layer before the excess pore water pressure ratio reaching 1.0. The considerable difference of local shear strain between sand layer and fine layer might be influenced by the concentration of pore water beneath fine layer.

## 7.4 Pore water and sand particles migrations

As explained above, the local behaviors of fine layer and sand layer are of difference during the undrained cyclic torsional shear tests. At first, the liquefaction resistances of them were different when they were under the same experimental conditions. Therefore, they might not liquefy (5% double amplitude of shear strain) at the same time. Secondly, the permeability of sand only specimen was around 63 times larger than the permeability of fine only specimen. The pore water would concentrate underneath the fine layer or in the fine layer when the segregated specimen was liquefied. The void ratios of sand layer and fine layer were different even their settlement heights during preparation were same. The compressibility of them would be not equal. There were also some other factors which contributed to the diverse local deformations between fine layer and sand layer. In chapter 6, water film beneath the top cap was formed. Slippages between membrane and sand particles also were observed during the test. Therefore, accompanied with the occurrence of membrane wrinkles, there might be pore water and sand particles migrations during the liquefaction tests on segregated sand specimens.

### 7.4.1 Pore water migration

It is well known that the pore water migration is triggered by the difference of pore water pressure without considering the hydrostatic pressure. If considered, the difference of pore water pressure should be based on the eliminating of hydrostatic pressure. As shown in Fig. 7.26, the different pore water pressure was measured by the low capacity differential pressure transducer. It can be seen that both the pore water pressures at position A and B had considered the hydrostatic pressure. The hydrostatic pressure at A was transmitted from the top porous-stone through the pipes directly. The one at B was transmitted from the top porous stone through pipes and specimen. Therefore, the physical value measured by LCDPT was the difference of excess pore water pressure between top and bottom of specimen. The pore water migration could be induced by this difference.

Fig. 7.27 gives the time histories of excess pore water pressure ratio and the different excess pore water pressure between top and bottom of specimen in test KWUC4. The results indicated that distinct difference of pore water pressure occurred after status-1. As introduced above, status-1 was the status when the phase transformation was reached at the first time. In order to describe the evolution of differential pore pressure, the relationships between shear stress and differential pore pressure are plotted in Fig. 7.28. Before status-1, the differential pore pressure increased when the shear stress increased both on clockwise and anti-clockwise directions. It decreased when the loading direction was reversed. However, after status-1, the different pore pressure stopped increased when the test reached step 474. After step 474, the different pore pressure changed to decrease until step 530 was reached. Fig. 7.29 shows the local strain distributions at step 474 and step 530 in test KWUC4 from indirect evaluation. Based on the observation of local strain distributions, strain localization of shear strain started from step 474. Since there was still effective stress at step 474, the compressed vertical strain at fine layer did not disappear. At step 530, the compressed vertical strain at fine layer almost disappeared. In addition, the significant local shear strain was found near the fine layer and it started to decrease. It was because the loading direction was reversed. Therefore, the differential pore pressure was affected by the strain localizations.

The Statuses of step 850 and step 1200 are marked in Fig. 2.27. Their corresponding local strain distributions and original photos are plotted in Fig. 7.30. At step 850, this was the first time of excess pore water pressure ratio reaching 1.0. The expanded vertical strain was observed near the fine layer at the first time. By the way, wrinkles appeared after the reversion of loading direction. At step 1200, the largest expanded vertical strain was induced at the fine layer. Wrinkles also appeared at this status. The expanded vertical strain at fine layer was triggered by the concentration of pore water. The radio recorded during test proved that the pore water flow passed through the fine layer along wrinkles. Fig. 7.31 gives the absolute values of excess pore water pressure at top and bottom of specimen, respectively. The increments of excess pore water pressures were almost same with each other during the test. Since the largest difference of excess pore water pressure was around 1.0 kPa between top and bottom of specimen, it could not be recognized in Fig. 7.31.

In order to compare the occurrence of differential pore water pressure (top vs bottom) of segregated specimen, Fig. 7.32 gives the evolution of differential pore water pressure of uniform specimen in test SAUC15. The uniform specimen prepared by colored silica sand was subjected to undrained cyclic loading by the same loading rate as the tests on segregated specimen. It can be seen that the maximum value of differential pore water pressure was less than 0.2 kPa. In figure (b), the differential pore pressure decreased with the increasing shear stress and suddenly increased after the loading direction was reversed. In addition, the loading direction affected the differential pore pressure. In figures (c) and (d), the differential pore pressure was zero when there was no effective stress. During the cyclic mobility, the contractive trend of specimen made the effective stress increase. By the way, limited differential pore pressure occurred and it would have a sudden leap when the loading direction reversed. It dissipated quickly after the liquefaction status was reached. It can be seen as a formation of non-uniform pore pressure after the reversion of loading direction. It might be affected by the inertia force of specimen. Therefore, most of the silica sand particles only sunk during the liquefaction status. In the liquefaction test on segregated specimen, not only settlement of Katori sand particles, but upward water flow was observed near the fine layer.

### 7.4.2 Sand particles migration

Accompanied with the formation of differential excess pore pressure between top and bottom of segregated specimen, sand particles migration was observed in the test with the water flow. As shown in Fig. 7.33, this was the specimen after three time of re-liquefaction tests. It can be seen that sand particles at the top part flowed down along the wrinkles. In Fig. 7.34, wrinkles occurred and developed from bottom to the upper part after the reversion of loading direction (near step 1200). This image was recorded at the backside of apparatus. At first, upward flow of sand particles was observed. After the dissipation of differential pore pressure, sand particle flowed back due to its gravity. When the wrinkles developed to the positions marked by red square, significant settlement of sand particles at here was observed. At the left side of this image, a small wrinkle developed from the top part to the lower part. When the wrinkle reached the fine layer, a local water film was observed in the wrinkle. Accompanied with the disappearance of this wrinkle, the water film also disappeared. For example, Fig. 7.35 shows the fully developed wrinkles at step 1200. The wrinkle marked by red arrow developed from bottom part to upper part. When the wrinkle reached one position, the raised membrane made the sand in the wrinkle become loose. Since the sand in the wrinkle became loose, pore water concentrated in the wrinkle. Based on the results in Fig. 7.27, there was a hydraulic gradient between top and bottom of specimen. Moreover, the permeability of fine layer was significantly lower than sand layer. Under such circumstance, the fine layer in the wrinkle blocked the route for pore pressure dissipation. Therefore, local water film was formed in the wrinkle. After the hydraulic gradient was dissipated, settlement of sand particles would be induced. This phenomenon happened several times during the re-liquefaction test. Differently, since the strength and stiffness of fine layer was very low during liquefaction status, the hydraulic gradient might break the fine layer. For example, the differential pore pressure near the middle wrinkle in Fig. 7.34 dissipated along the upward flow, there was no distinct water film.

Fig. 7.36 gives the photograph of pore water concentration beneath the fine layer in test KWUC3. Based on the procedure of experiment, there was a silt layer underneath the fine layer. The fine in the sand layer could not be sieved perfectly. After the water sediment, silt and fine in the sand layer accumulated at the top of sand layer. It can be seen from the photo that the colors of sand layer and fine layer were different. It was due to the reason that the sand was colored by black color agent before preparing the specimen. This method was tried to increase the color contrast for image analysis. Compared with image shown in Fig. 7.37 which was taken at the other side of specimen, the fine layer should be like this before testing. The silt layer beneath the fine layer shown in Fig. 7.36 might be eroded by the pore water concentration. More efforts should be paid on this in the future. In addition, significant settlement of sand particles was observed underneath the top cap. After three time of re-liquefaction tests, the specimen was cut off by layer from the top part. At the top of fine layer, sand particles were not found. However, sand particles were observed at relatively lower positions of fine layer. As shown in Fig. 7.38, the black colored Katori sand was observed. This sand particle migration was not adjacent to the membrane, it was at inside of the fine layer. It might be induced by the upward flow of pore water. This phenomenon was still unconfirmed, and more evidence was needed. Due to the non-uniformity characteristics of segregated specimen, the local behaviors along the specimen should be different. Therefore, the positions, where sand particle migration occurred, were un-predictable.

## 7.5 Observation of water films

Water film beneath low permeability layer without shear strength has aroused researchers and engineers' attention on the stabilities of embankments and foundations during seismic events. As introduced in section 7.2, water films have been observed in the one column and shaking table tests, respectively. In the torsional shear test, since sand particles sunk, water film beneath the top cap was found when the vertical displacement of top cap was prohibited. Some researchers considered the top cap as low permeability layer when compared with the shaking table test or one column test. Similar water films beneath the top cap had been observed in the undrained torsional shear tests on homogeneous sand specimen. However, they depended on the density and strain conditions during the liquefaction tests which had explained in chapter 6. In this chapter, the water films near the fine layer of segregated specimen will be introduced in details.

As shown in Fig. 7.36, due to the settlement of sand particles, a water film appeared underneath the top cap. This water film did not occupy all the cross section of specimen at top. Under the fine layer, author thought that the silt layer was affected and eroded by the water concentration. It also could be seen as an invisible water film. Fig. 7.39 gives the local water films in stage 1 and stage 2 of re-liquefaction test (KWUC4). Both of them were formed after the reversion of loading directions. The water film in stage one remained for a while until the membrane wrinkle disappeared. The left water film in the figure at stage 2 also kept until the wrinkle disappeared. The right one appeared only for several seconds. Actually, the loading rate in torsional shear test was far below the frequency of earthquake. It is still a tough task to observe the distinct water film beneath low permeability layer in torsional shear tests. More efforts are needed to investigate the information of water films.

## 7.6 Summary

Based on the direct and indirect evaluations of local deformation, the results from a series of undrained cyclic torsional shear tests on segregated sand specimens could be summarized as follows:

1. As for the Katori sand specimens intercepted by thin fine layers, the local deformations from indirect and direct evaluations were almost same with each other, except for large shear strain conditions. The local strains along the specimen were not uniform when the global shear strain was larger than 5%. After the excess pore water pressure ratio reached 0.8, expanded vertical strains at fine layer were observed from the vertical strain distributions by indirect and direct evaluations.
2. In order to observe the local behavior of segregated specimen affected by fine layer, the thickness of fine layer at top part of specimen increased by decreasing the thicknesses of other fine layers. Katori sand was colored by white and black colors to increase the accuracy of image analysis method. The results indicated that the validity of direct evaluation of local deformation was improved to some extent. Distinct difference of local strains between fine layer and sand layer was observed. Based on the local strain distributions, the largest affection by membrane penetration was observed after consolidation. This affection decreased gradually with the increasing of excess pore water pressure. The expanded

vertical strain at fine layer was observed when the excess pore water pressure ratio was around 1.0.

3. In order to prove the potential of pore water and sand particle migrations, the differential pore pressure was measured between the top and bottom of specimen. The results indicated that maximum differential pore pressure was reached when the excess pore water pressure ratio was around 1.0 at the first time. Moreover, pore water and sand particle migrations were observed during this status. Upward flows of pore water and sand particles were observed at the bottom of fine layer. In addition, the differential pore pressure was affected by the strain localization at fine layer. The concentration of pore water beneath fine layer was confirmed.
4. Significant water film beneath the top cap was observed in the liquefaction test on segregated sand specimen. The eroded silt layer underneath the fine layer might be induced by the concentration of pore water. After the reversion of shearing directions, small water films were observed in the wrinkles when the wrinkles passed through the fine layer. Small water films in wrinkles at fine layer were also observed in the second stage of re-liquefaction test.

# Reference

1. Fauzi, U. J. (2015). *Local Deformation and Repeated Liquefaction Properties of Segregated Sand Specimen in Hollow Cylindrical Torsional Shear Tests.* The University of Tokyo.
2. Fauzi, U. J. and Koseki, J. (2014). Local deformation properties of segregated sand specimen in hollow cylindrical torsional shear tests. *Bulletin of ERS*(47), 27-36.
3. Kokusho, T. (1999). Water film in liquefied sand and its effect on lateral spread. *Journal of Geotechnical and Geoenvironmental Engineering, 125*(10), 817-826.
4. Kokusho, T. (2000). Mechanism for water film generation and lateral flow in liquefied sand layer. *Soils and Foundations, 40*(5), 99-111.
5. Kokusho, T. (2003). Current state of research on flow failure considering void redistribution in liquefied deposits. *Soil Dynamics and Earthquake Engineering, 23*(7), 585-603.
6. Kokusho, T. and Kojima, T. (2002). Mechanism for postliquefaction water film generation in layered sand. *Journal of Geotechnical and Geoenvironmental Engineering, 128*(2), 129-137.
7. Kokusho, T., Toshikawa, T., Suzuki, K. and Takashi, K. (2002). Basic research on mechanism for water film generation by hollow cylindrical torsional shear apparatus. *Geotechnical Engineering Society of Japan, 37*, 565-566.
8. Maharjan, M. and Takahashi, A. (2014). Liquefaction-induced deformation of earthen embankments on non-homogeneous soil deposits under sequential ground motions. *Soil Dynamics and Earthquake Engineering, 66*, 113-124.

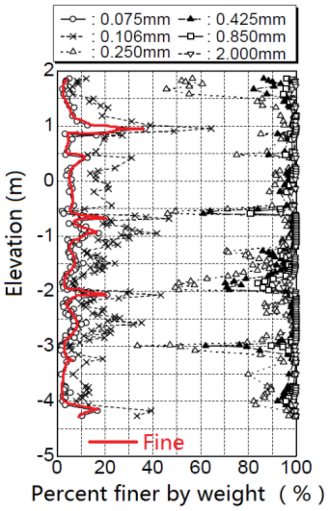

**Fig. 7. 1 Vertical change in grain size distribution along depth of reclaimed land (Kokusho and Kojima, 2002)**

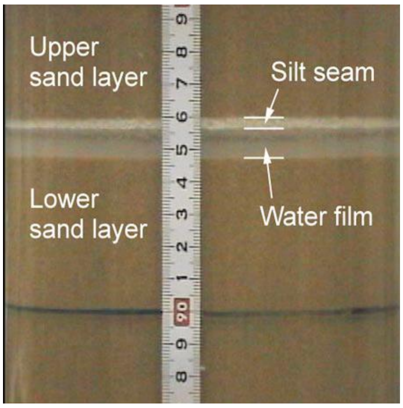

**Fig. 7. 2 Water film formation beneath the silt seam in one column test (Kokusho, 1999)**

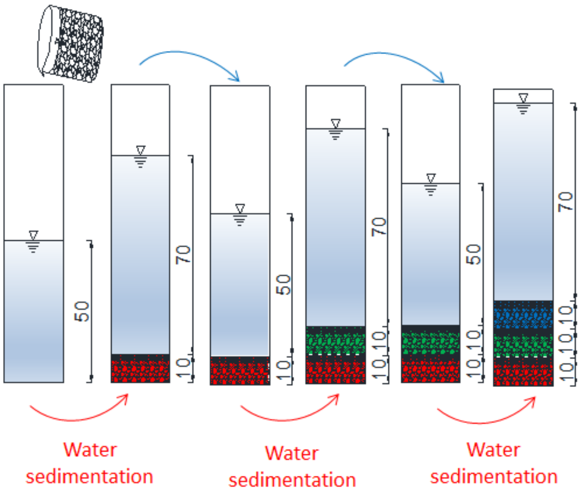

**Fig. 7. 3 Preparation method of segregated specimen (Fauzi, 2015)**

a) Intercepted by thin fine layer
b) Intercepted by thick fine layer

**Fig. 7. 4 Schematic diagrams of segregated specimens in this study**

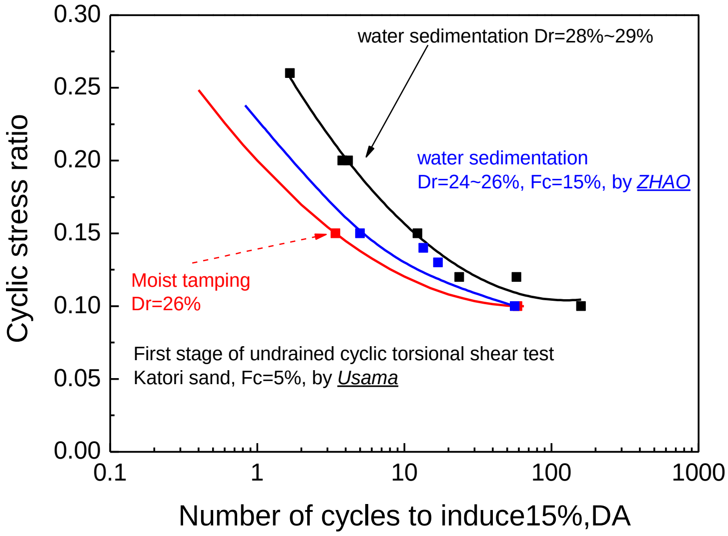

**Fig. 7. 5 Liquefaction resistance of Katori sand (Fauzi, 2015)**

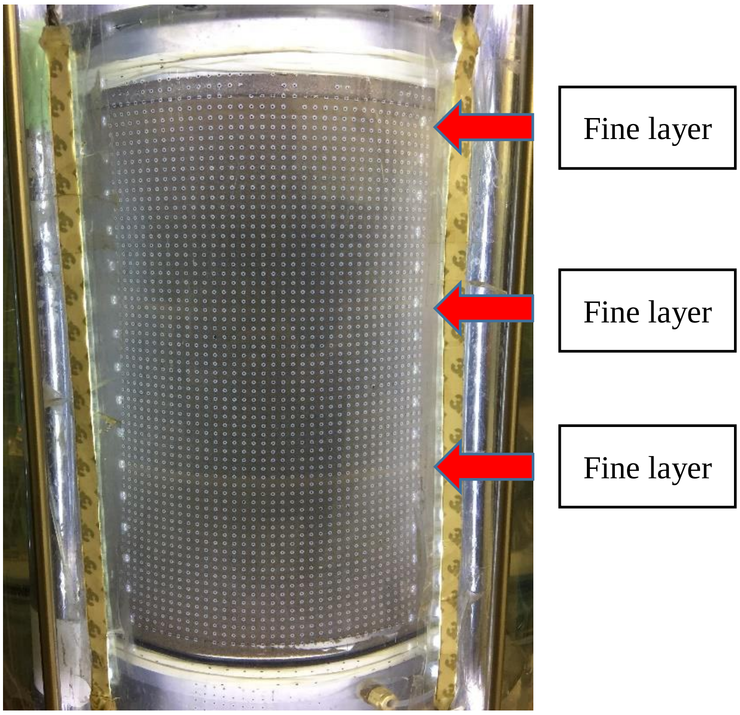

**Fig. 7. 6 Segregated specimen with three fine layers prepared by water sediment method**

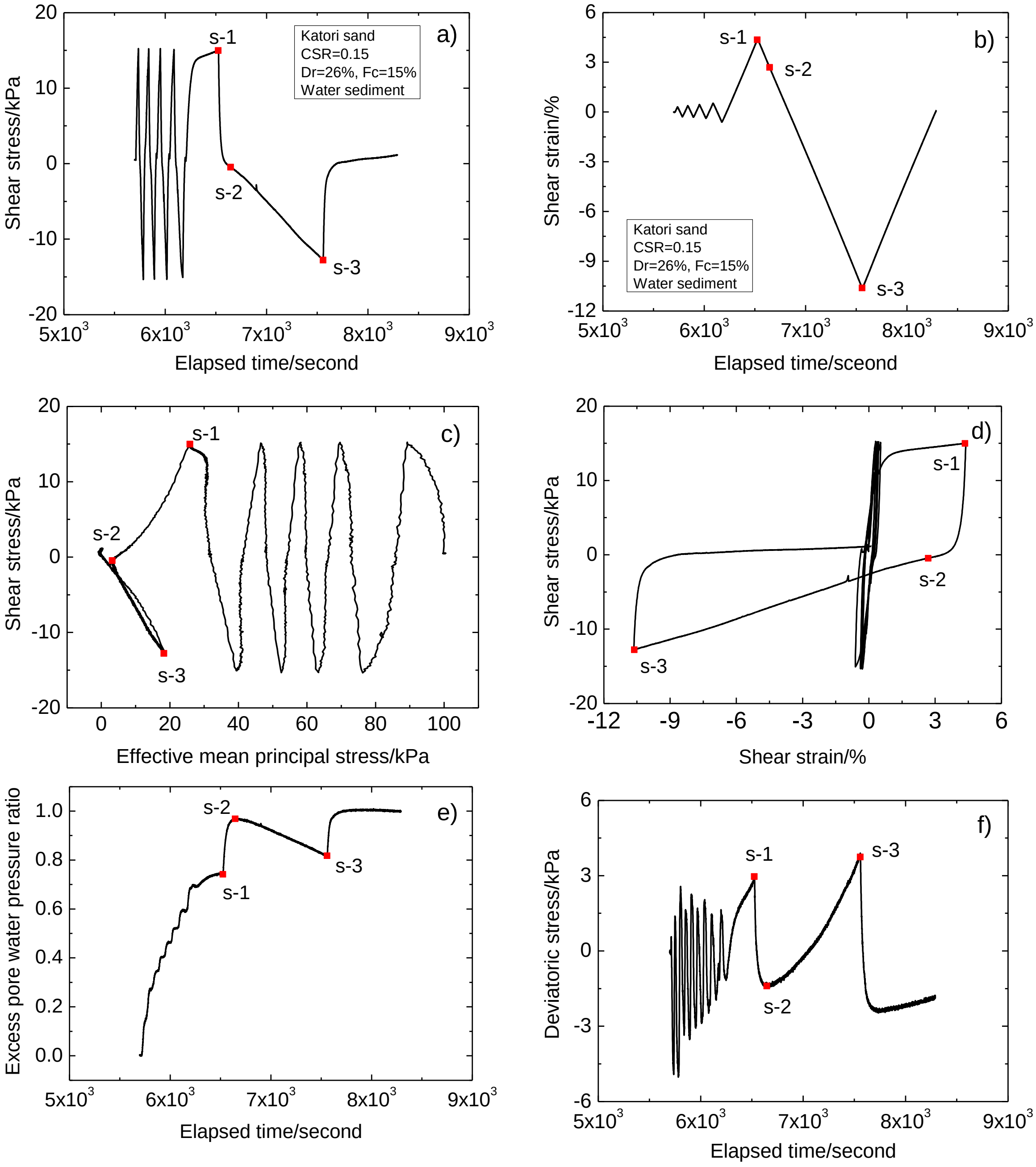

Fig. 7. 7 Results from test KWUC1

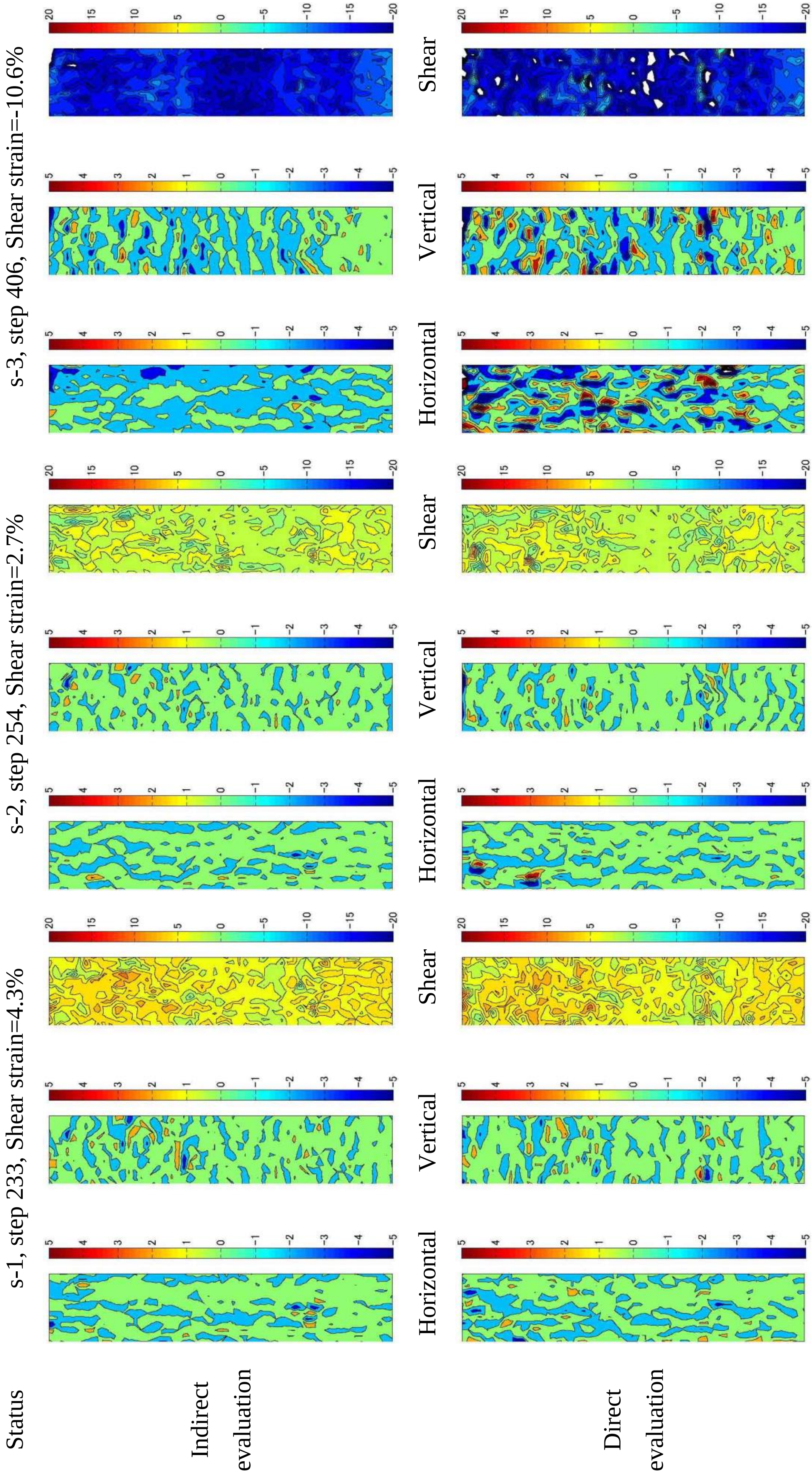

**Fig. 7. 8 Local strain distributions of selected statuses in test KWUC1**

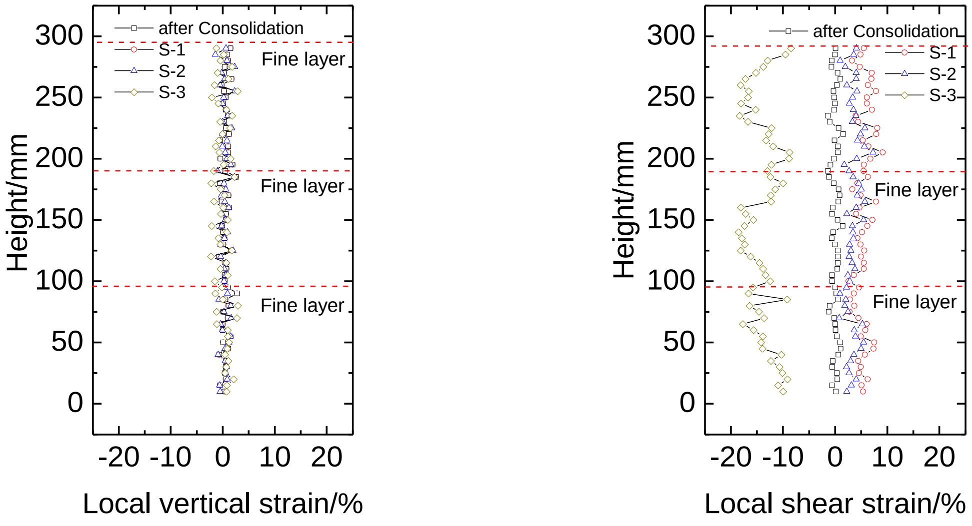

Fig. 7. 9 Local strains of the central position at each row from indirect evaluation

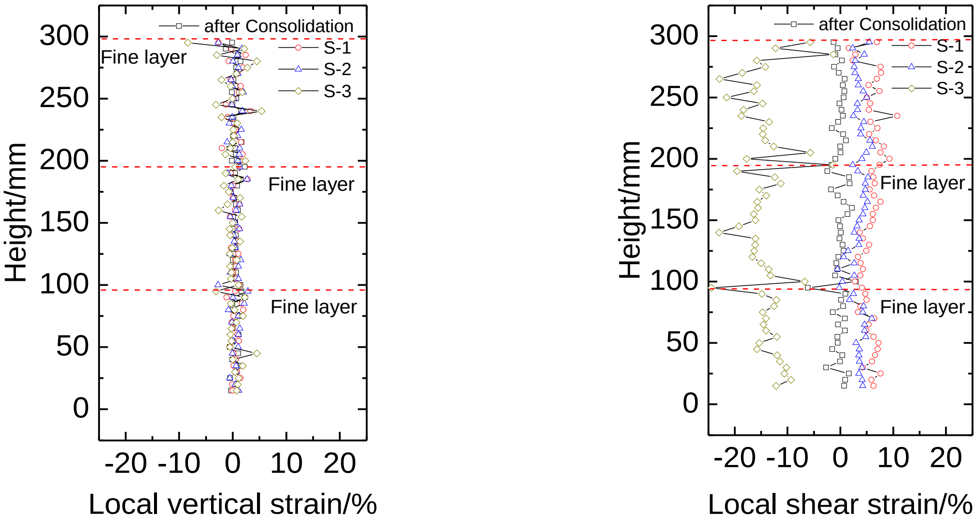

Fig. 7. 10 Local strains of the central position at each row from direct evaluation

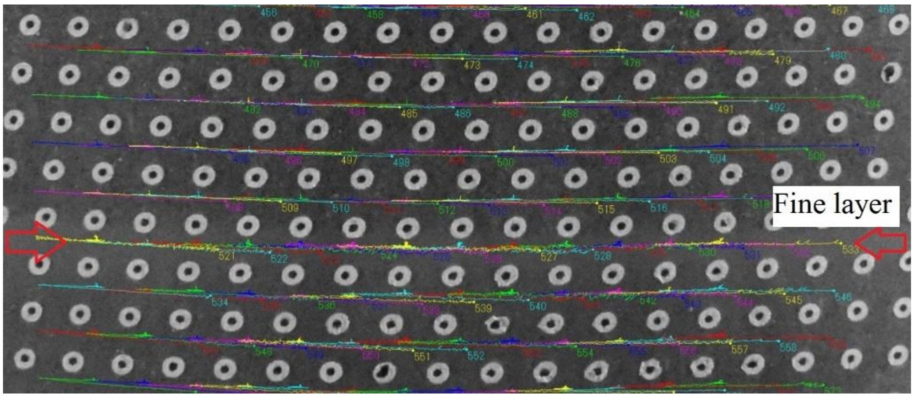

Fig. 7. 11 Trace photography of step 406 in test KWUC1

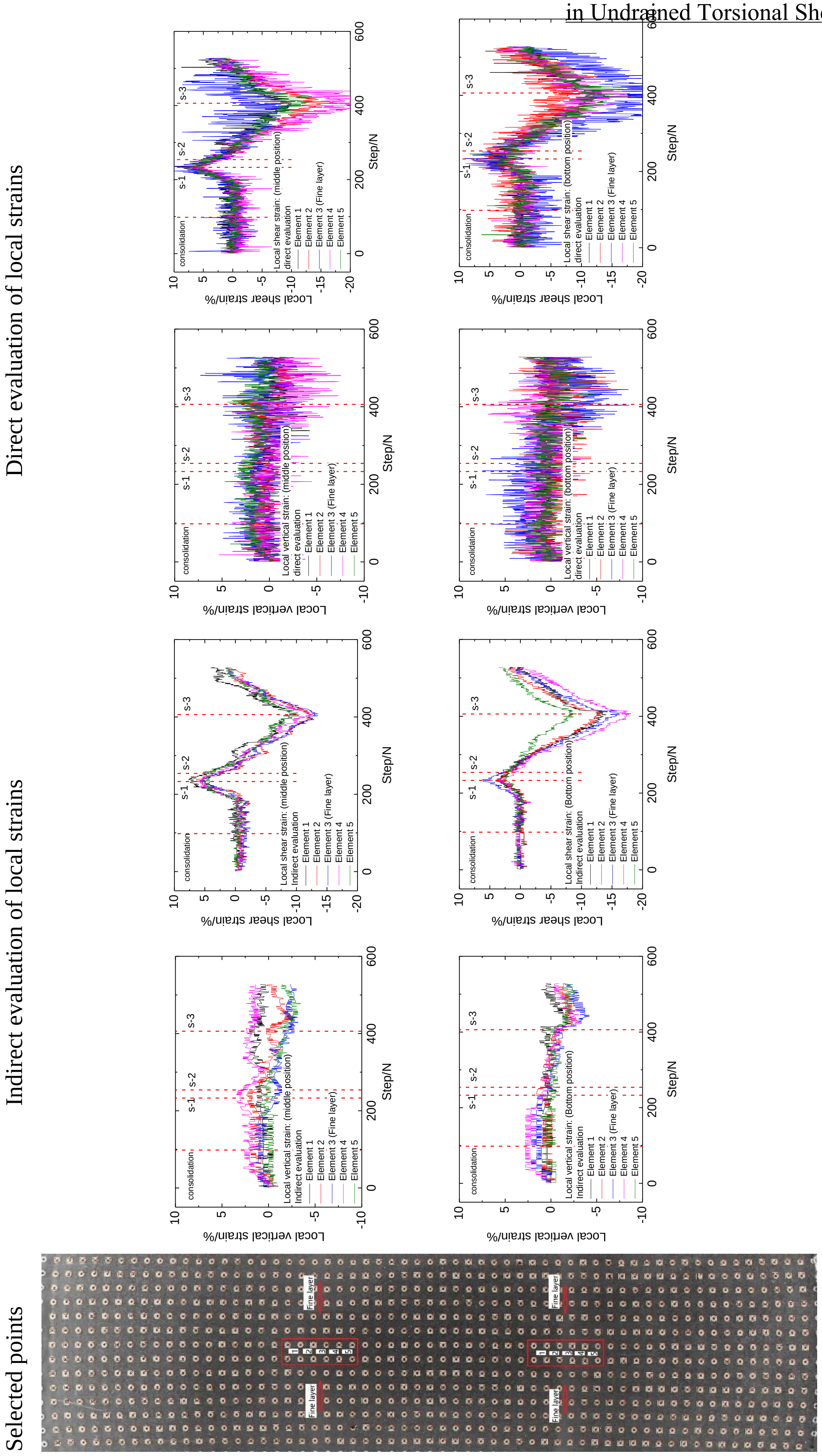

**Fig. 7. 12 Local strain comparisons at selected points in test KWUC1**

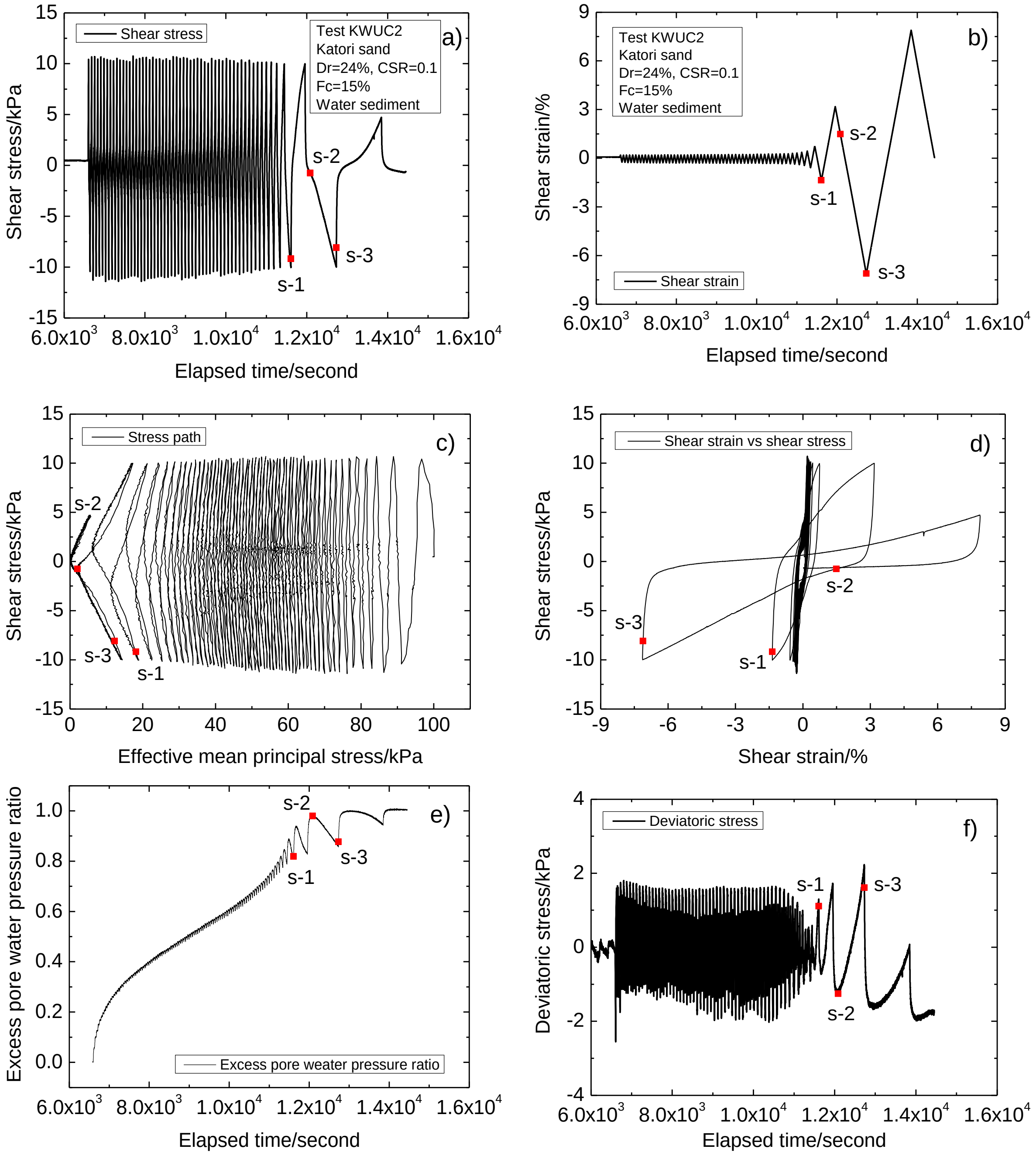

**Fig. 7. 13 Test results from KWUC2**

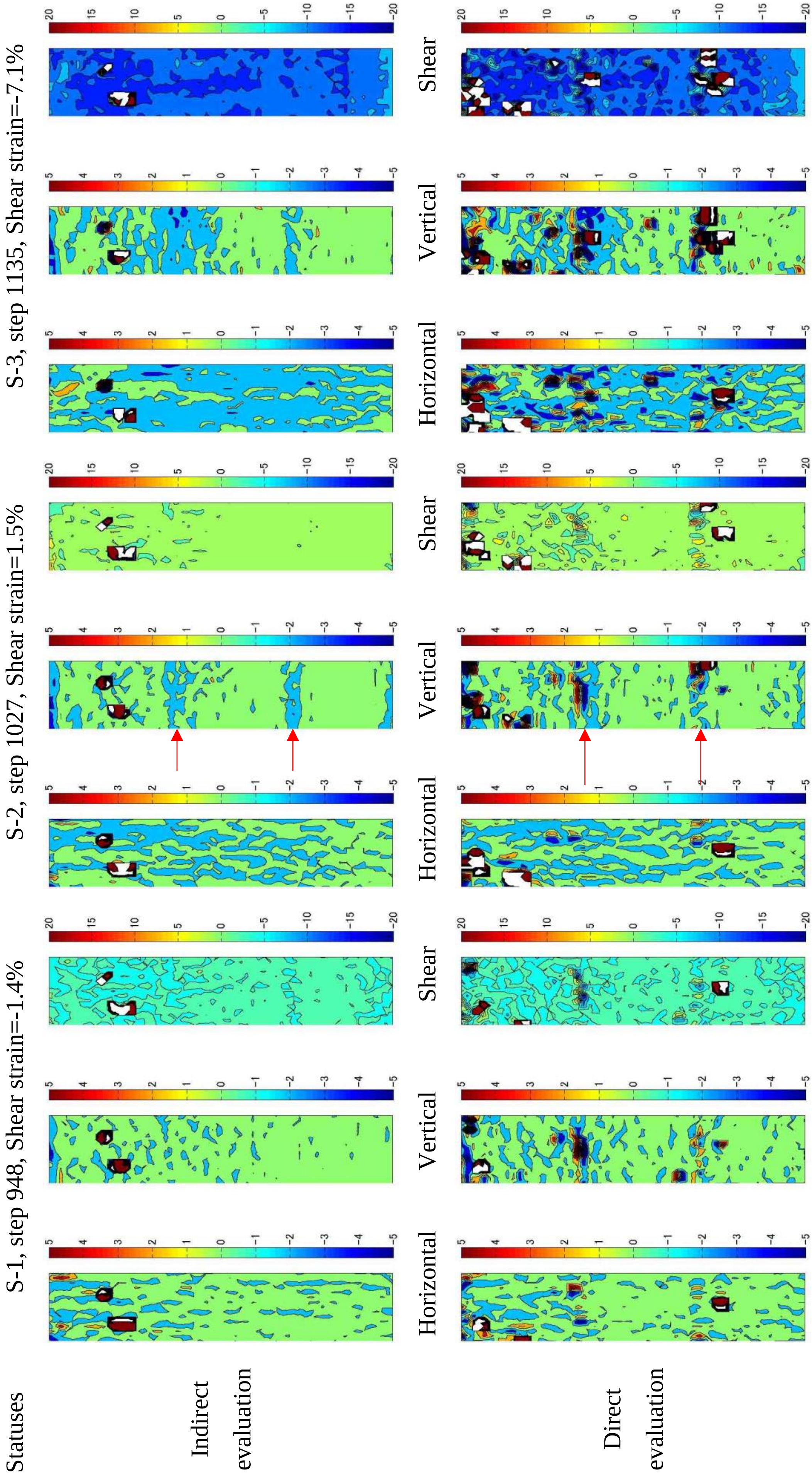

**Fig. 7. 14 Local strain distributions at selected statuses in test KWUC2**

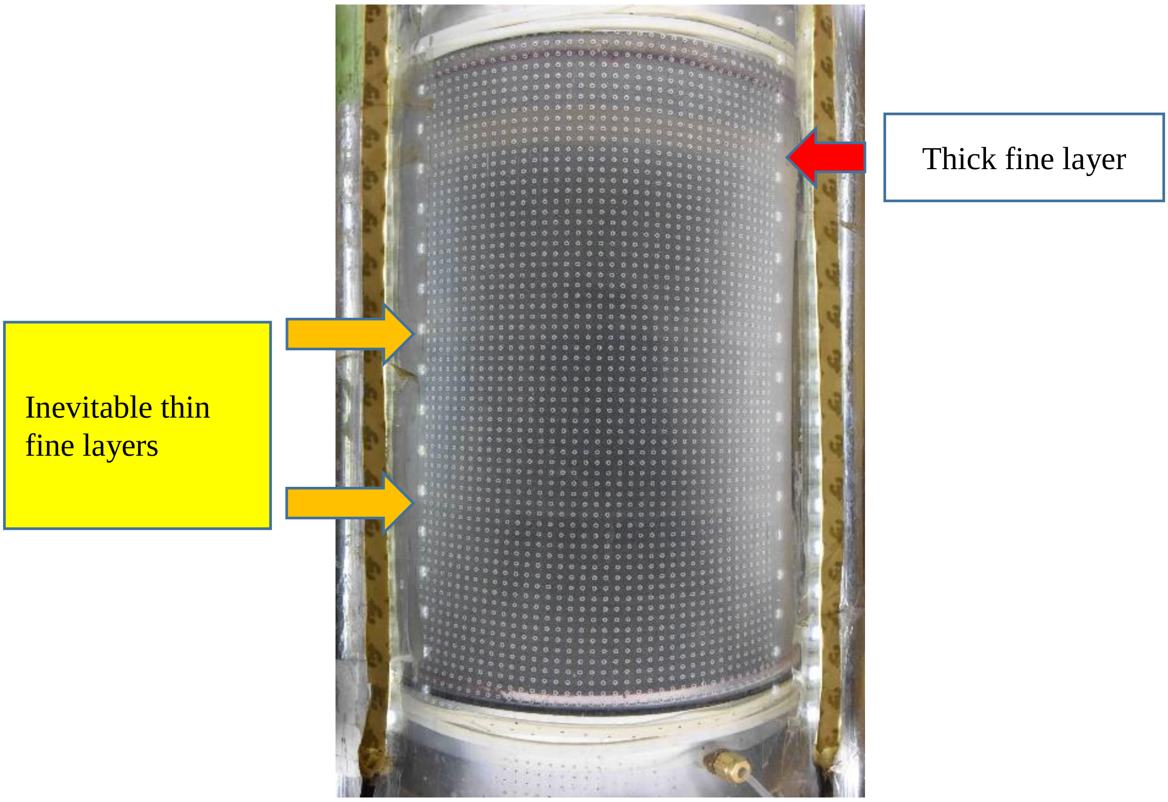

**Fig. 7. 15 Segregated specimen with one thick fine layer in test KWUC3**

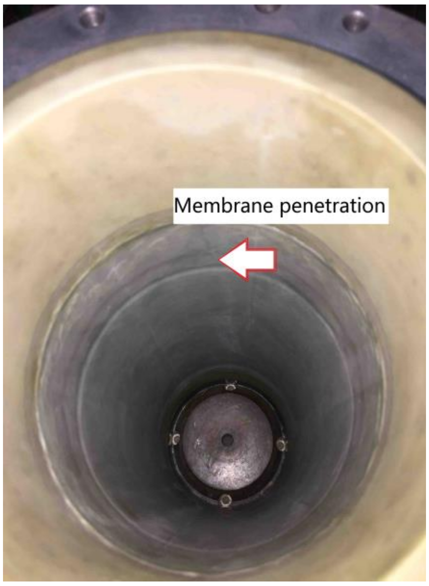

**Fig. 7. 16 Penetration of membrane at fine layer under 30 kPa negative pressure**

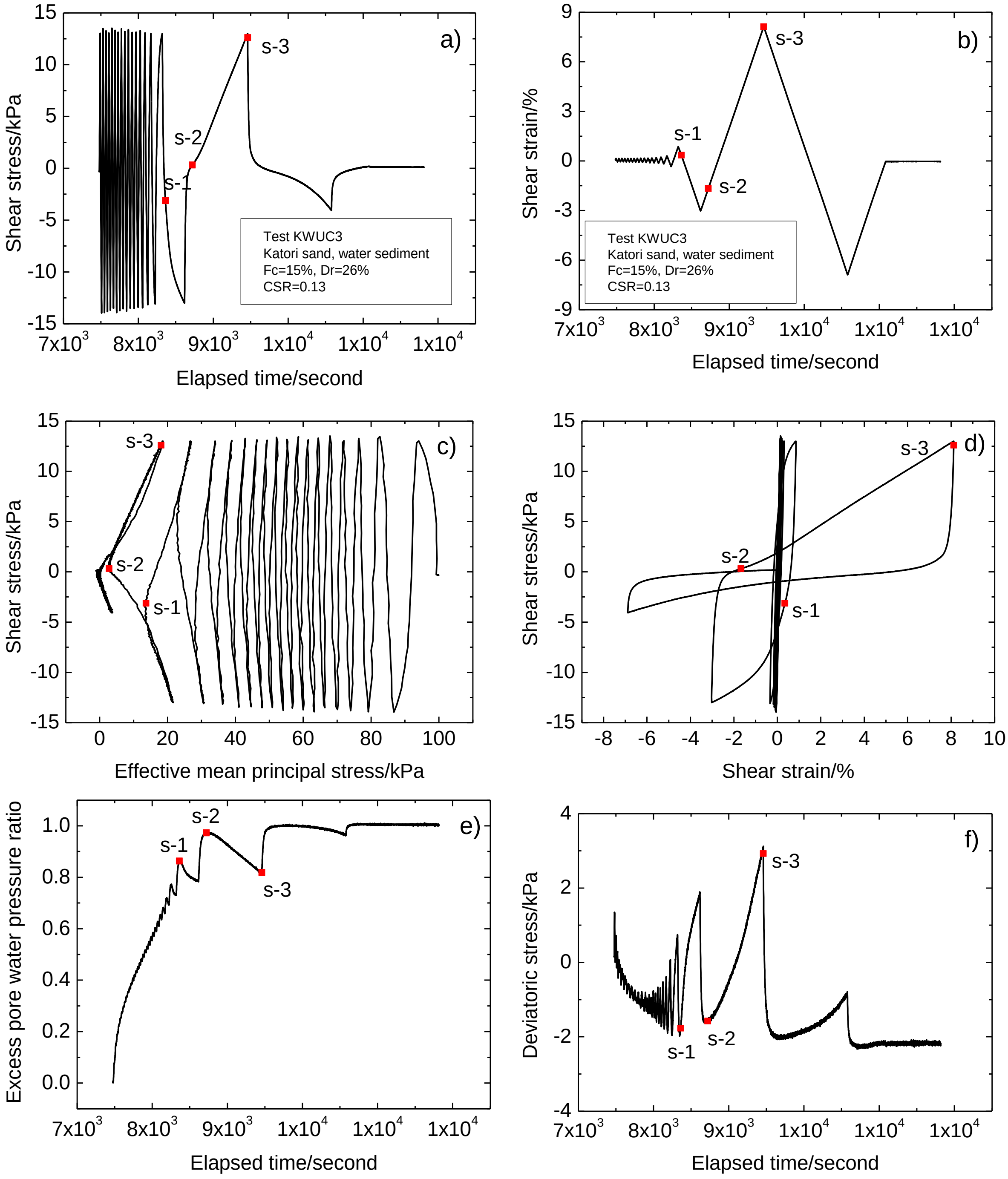

**Fig. 7. 17 Test results from KWUC3**

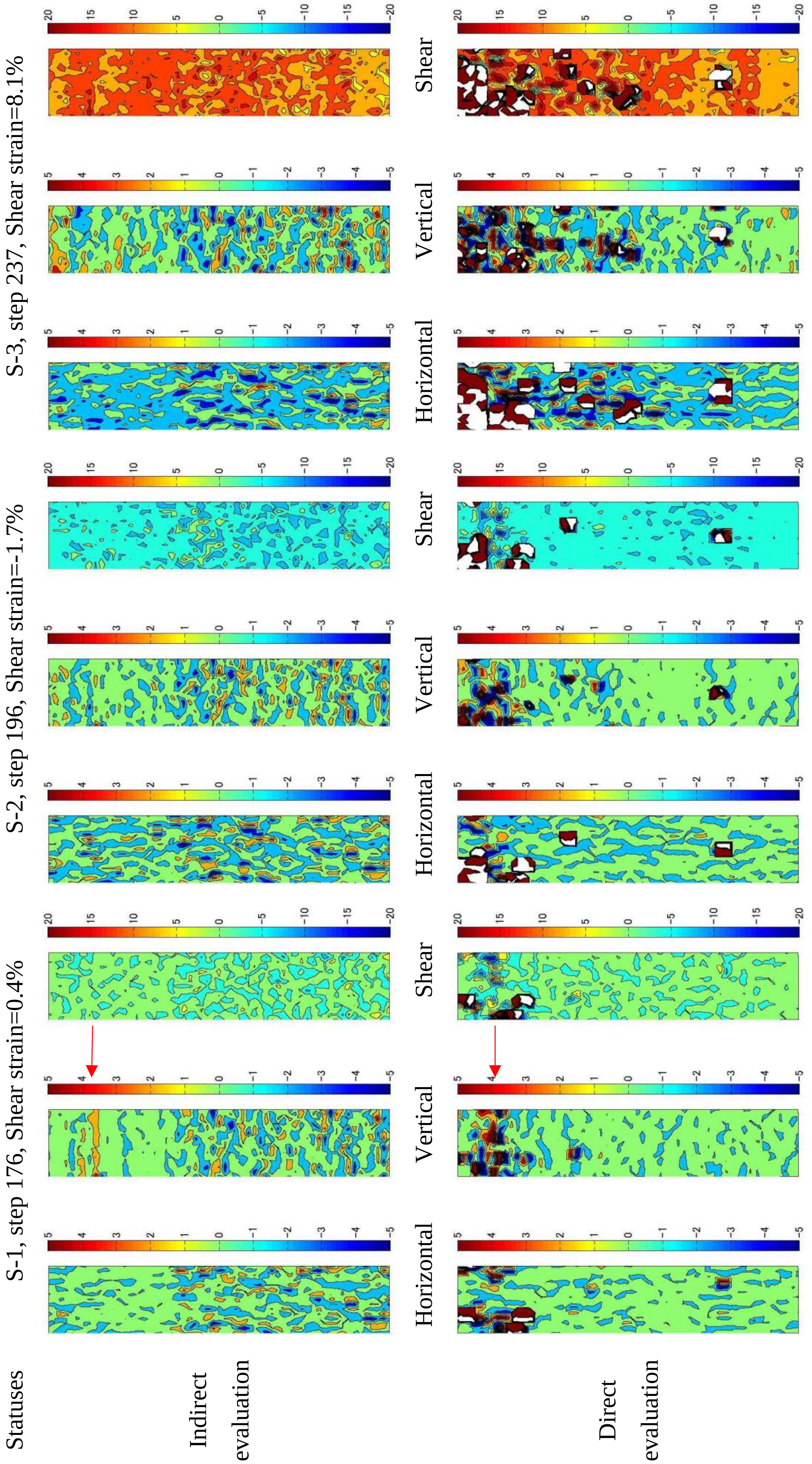

**Fig. 7. 18 Local strain distributions at selected statuses in test KWUC3**

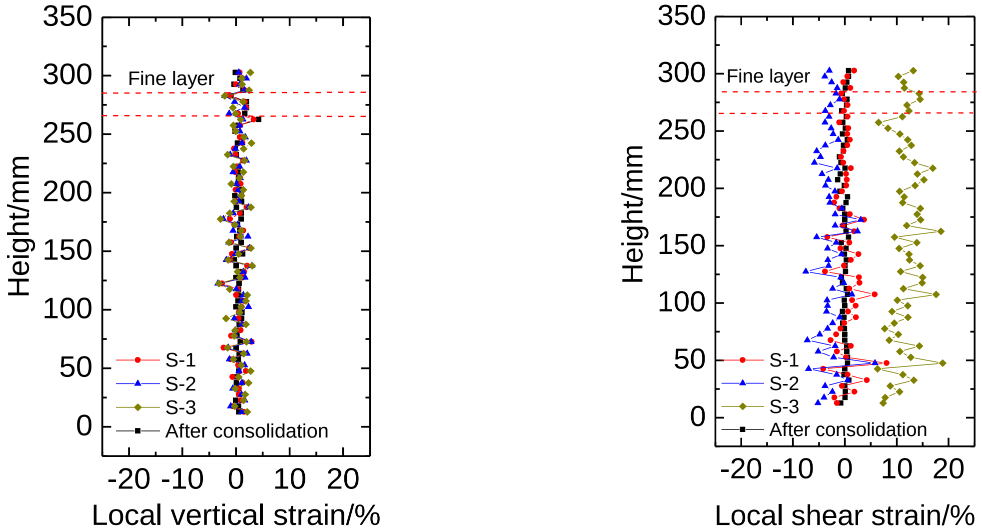

**Fig. 7. 19 Local strains of the central position at each row from indirect evaluation in test KWUC3**

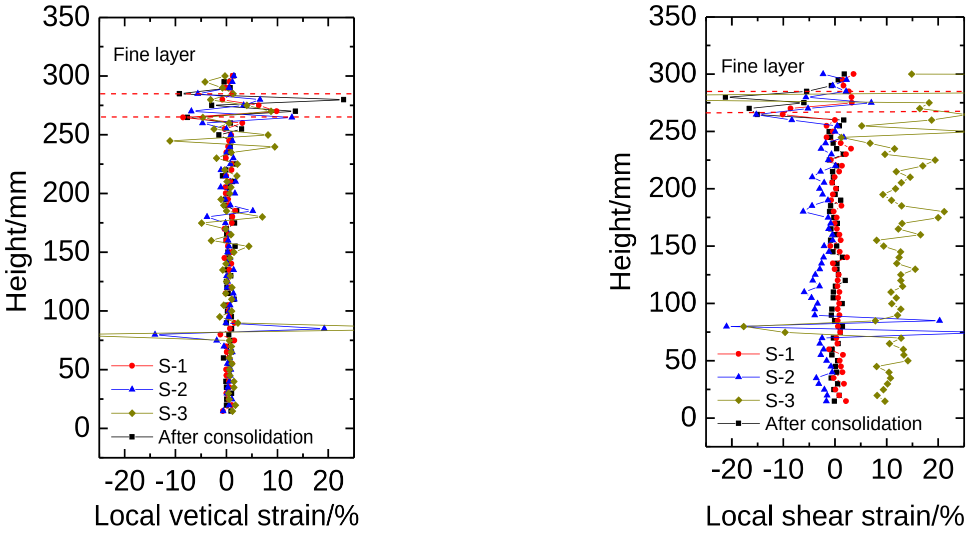

**Fig. 7. 20 Local strains of the central position at each row from direct evaluation in test KWUC3**

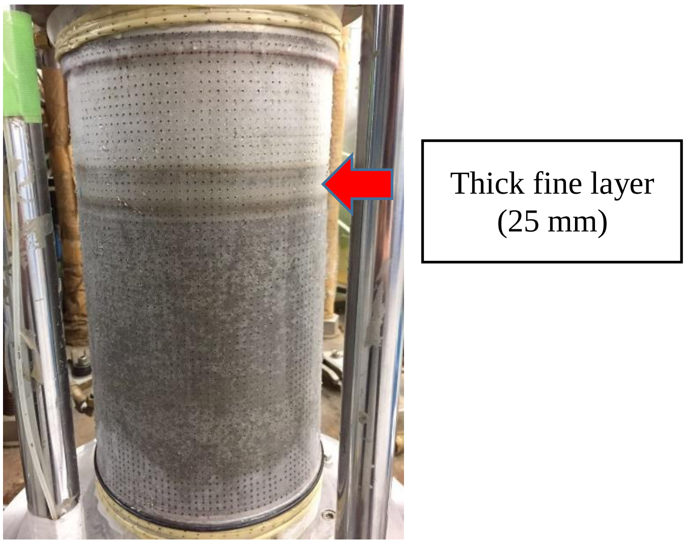

**Fig. 7. 21 Specimen prepared by water sediment in test KWUC4**

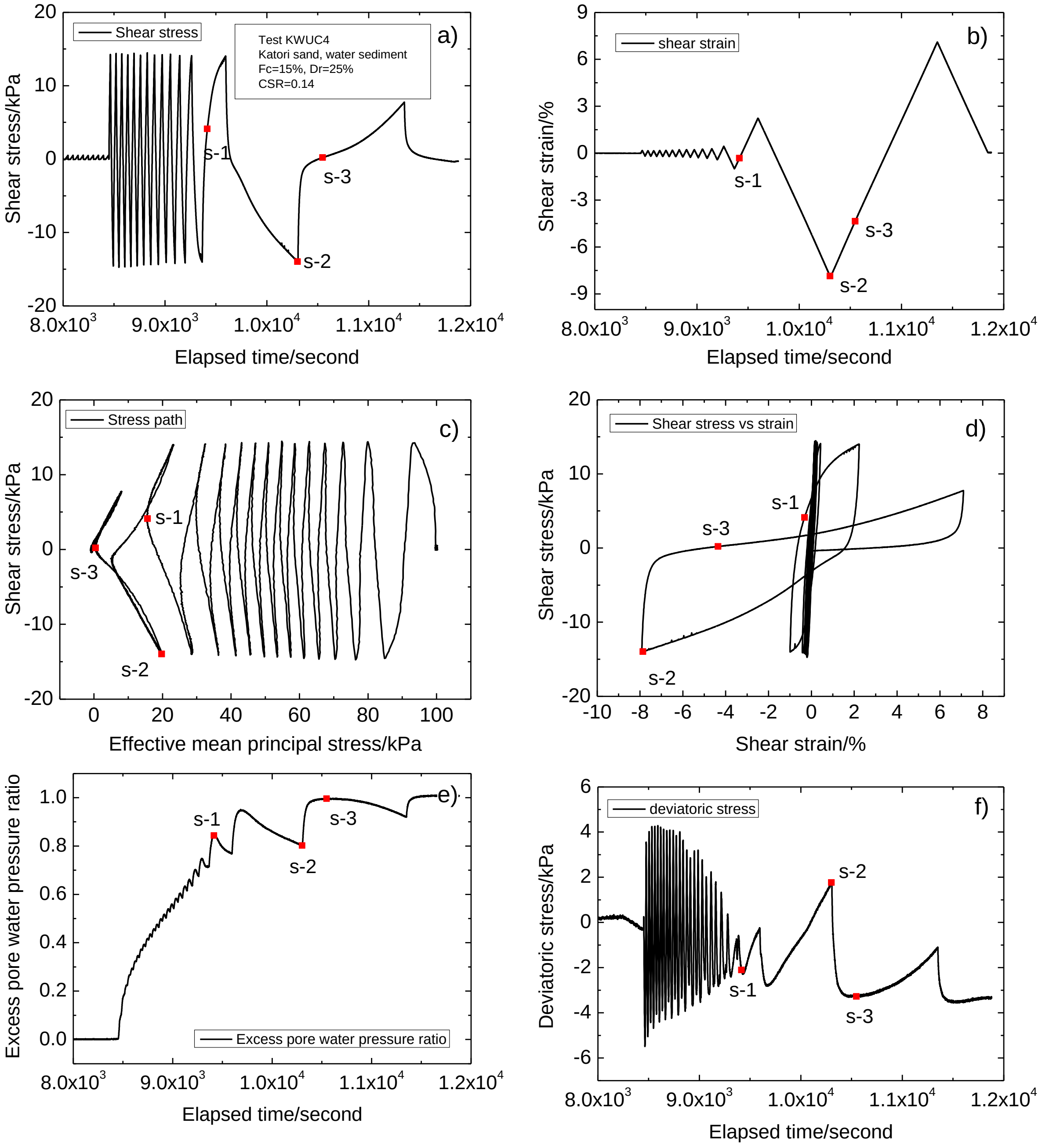

Fig. 7. 22 Test results from KWUC4

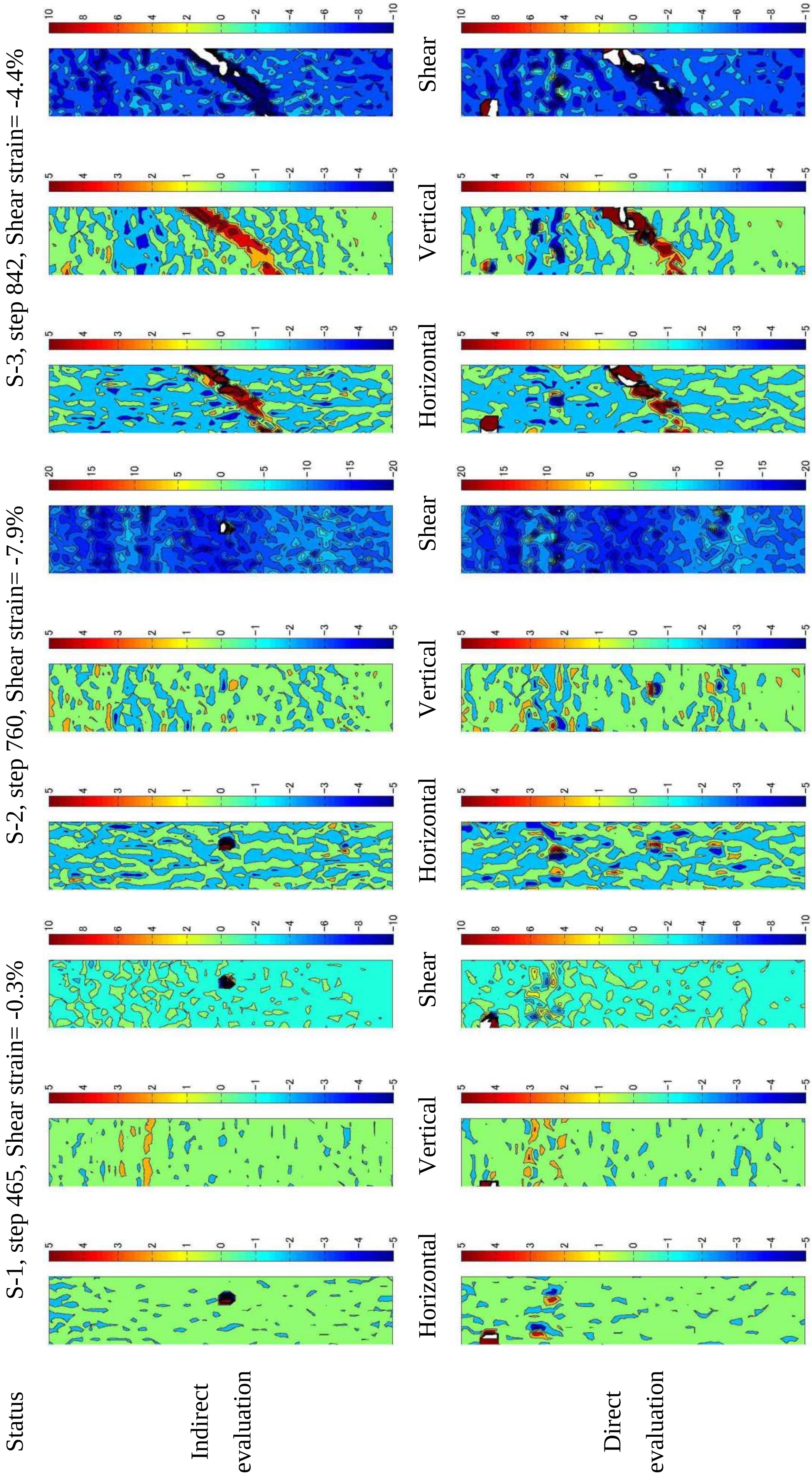

**Fig. 7. 23 Local strain distributions of selected statuses in test KWUC4**

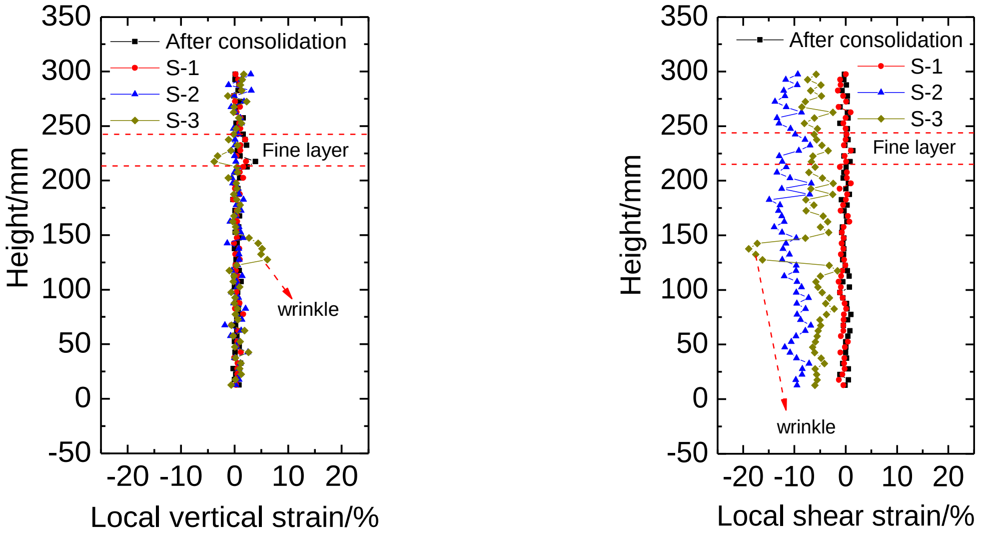

Fig. 7. 24 Local strains of the central position at each row from indirect evaluation in test KWUC4

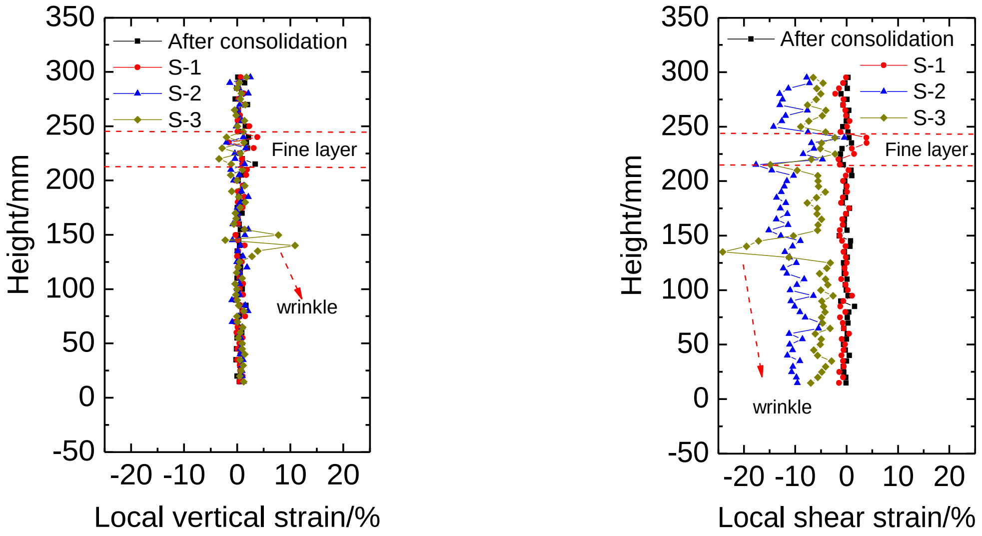

Fig. 7. 25 Local strains of the central position at each row from direct evaluation in test KWUC4

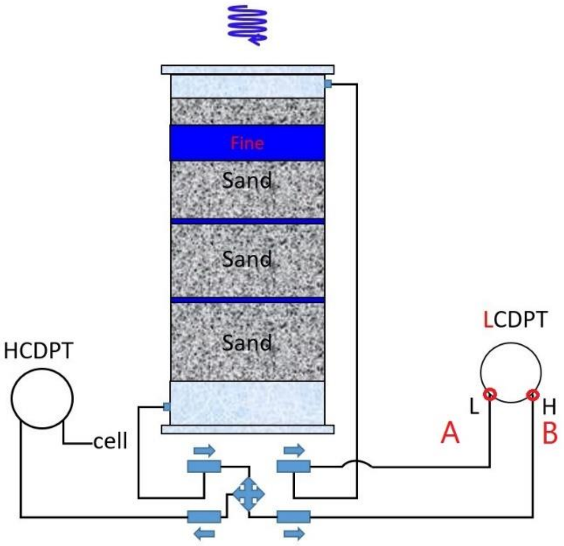

Fig. 7. 26 Schematic diagram of measuring the different pore water pressure between the top and bottom of specimen

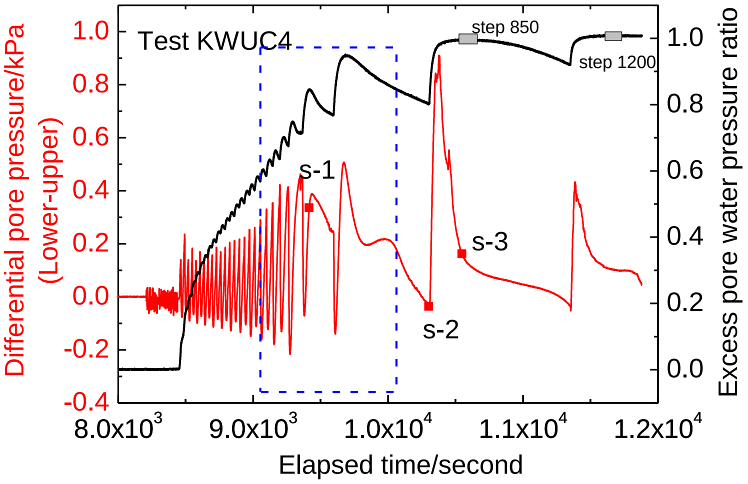

Fig. 7. 27 Time history of excess pore water pressure ratio and differential pore pressure between top and bottom of specimen in test KWUC4

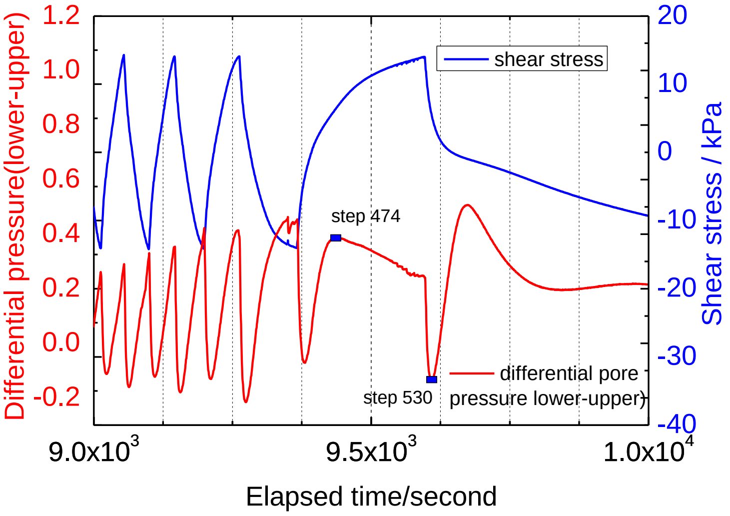

Fig. 7. 28 Time history of shear stress and differential pore water pressure between top and bottom of specimen

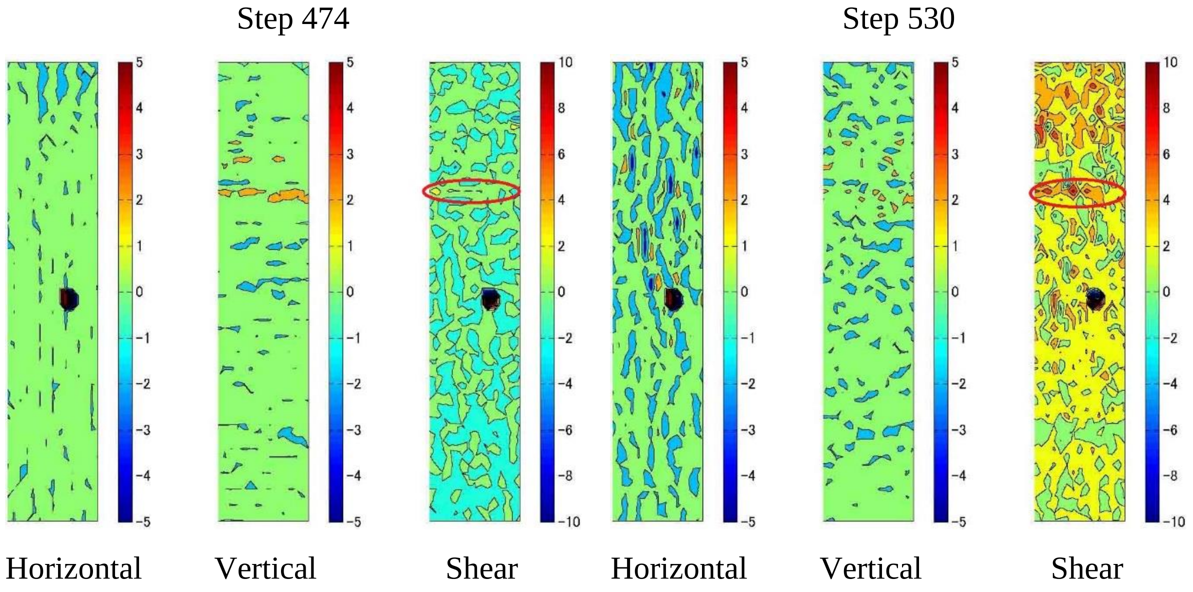

**Fig. 7. 29 Local strain distributions at step 474 and step 530 from indirect evaluation in test KWUC4**

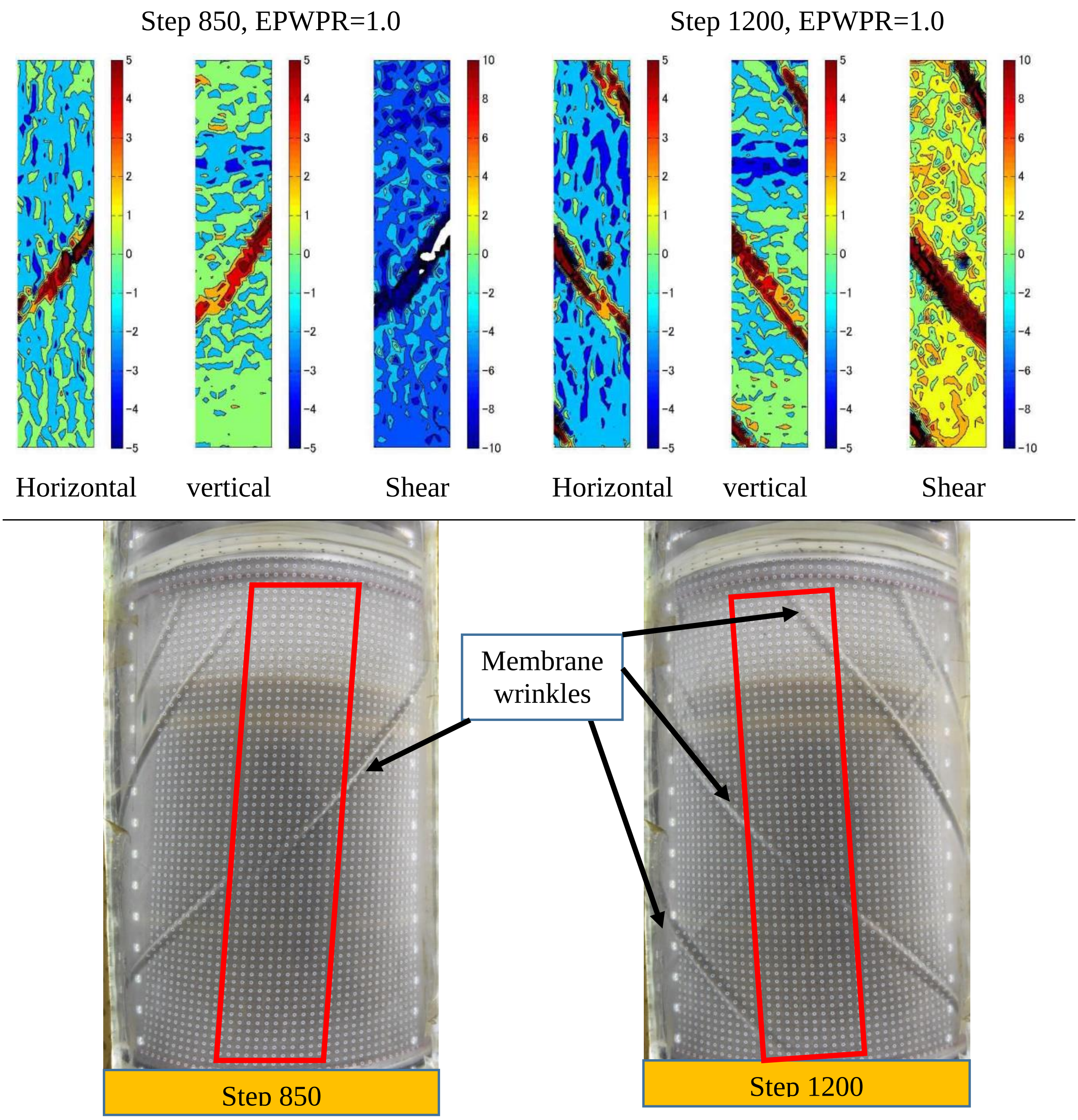

**Fig. 7. 30 Local strain distributions at step 850 and step 1200 from indirect evaluation and corresponding original photos in test KWUC4**

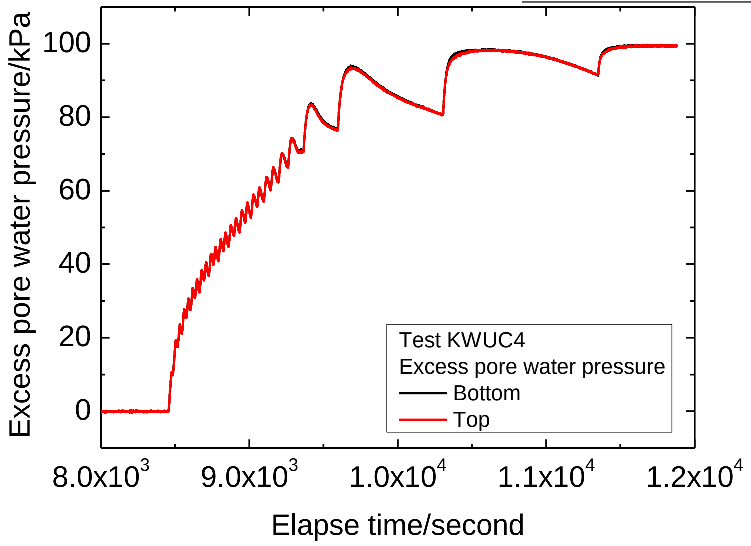

**Fig. 7. 31 Absolute values of excess pore water pressure at top and bottom of specimen in test KWUC4**

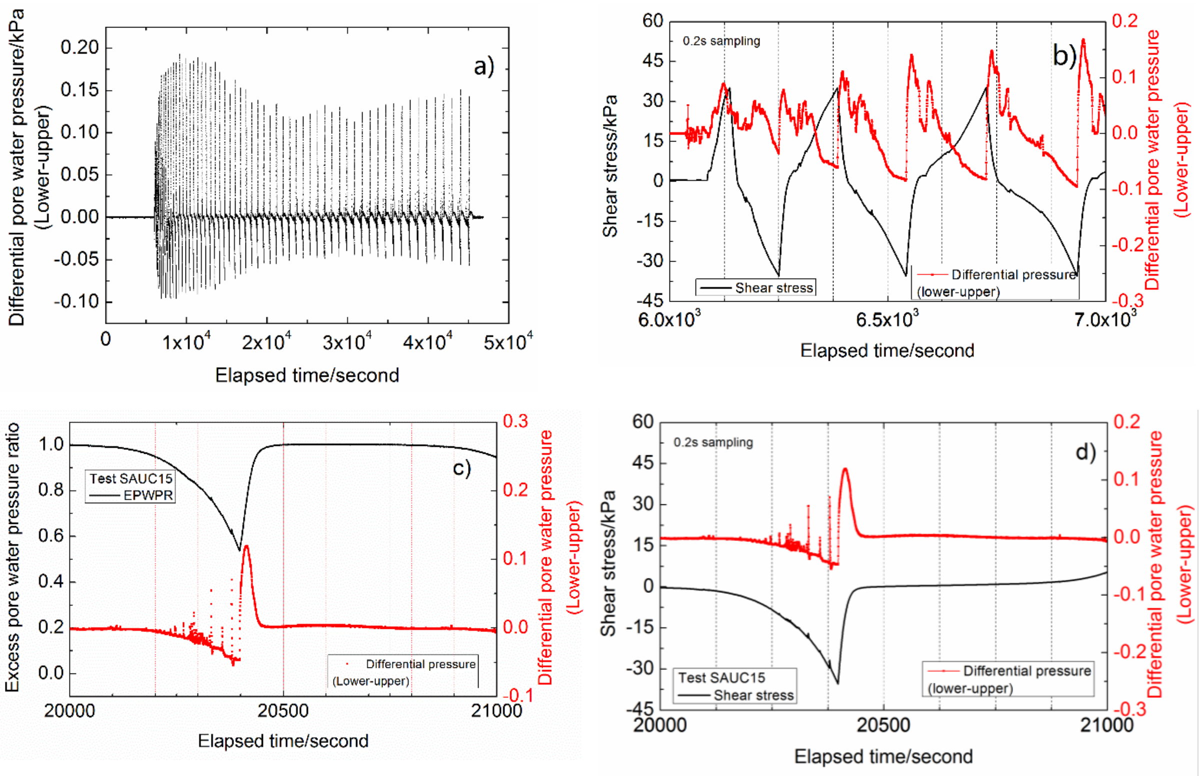

**Fig. 7. 32 Differential pore water pressure between top and bottom of specimen in test SAUC15**

**Fig. 7. 33 sand particle migration in test KWUC4**

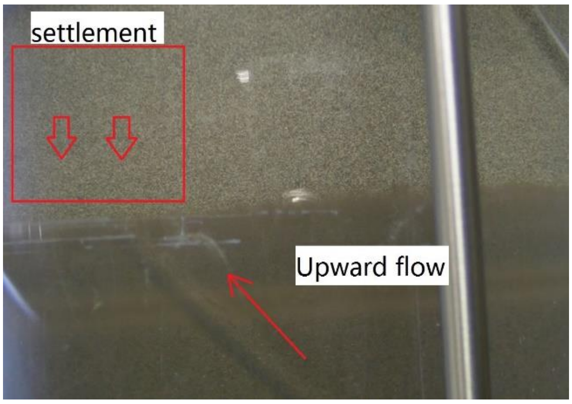

**Fig. 7. 34 Upward sand flow in test KWUC4**

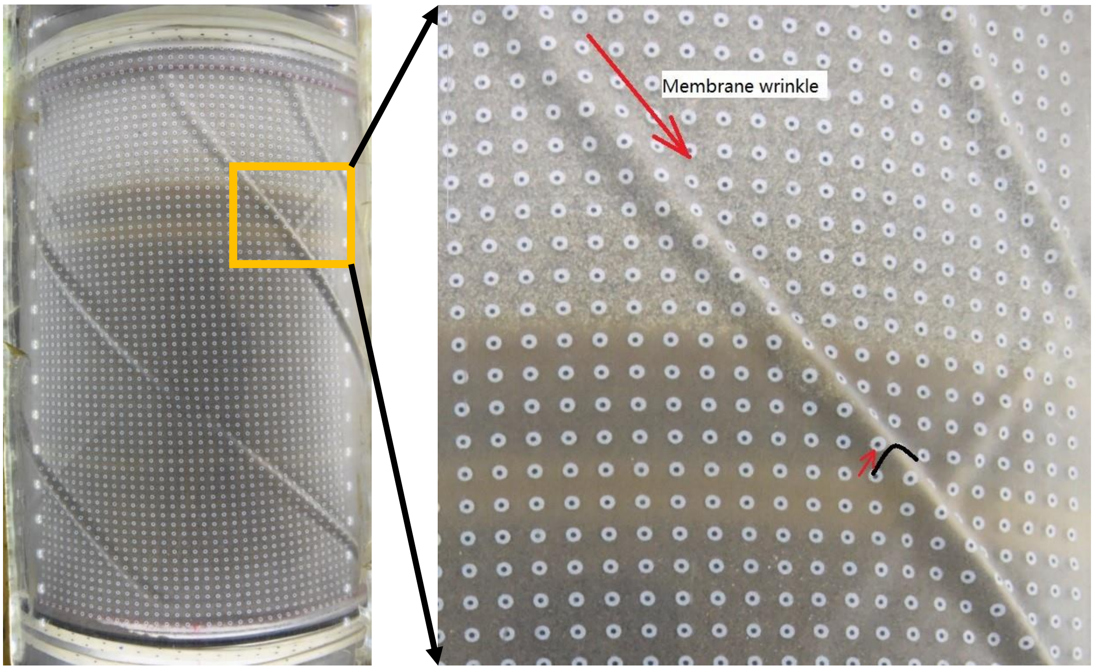

**Fig. 7. 35  Pore water and sand particles migrations affected by wrinkles**

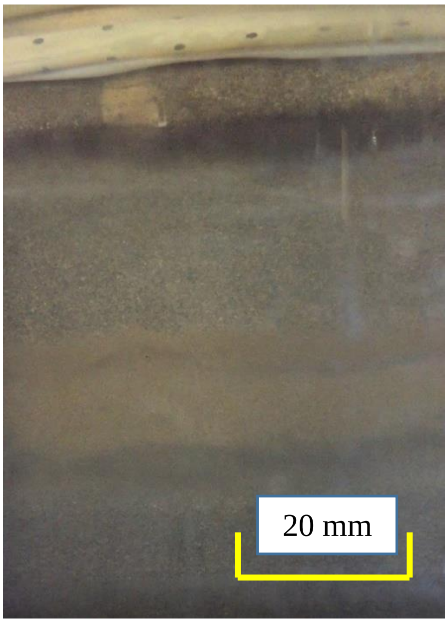

**Fig. 7. 36 Water concentration in test KWUC3**

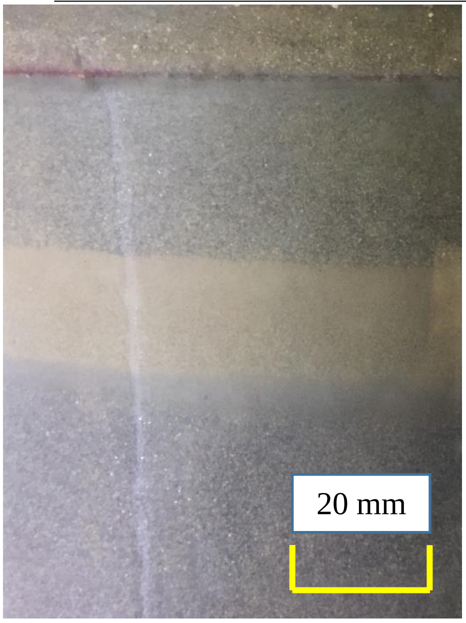

**Fig. 7. 37 photograph in test KWUC3 at other side of specimen**

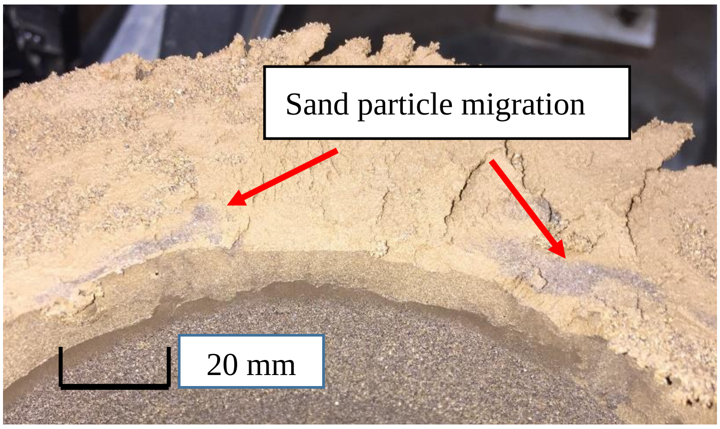

**Fig. 7. 38 Sand particle migration in test KWUC3**

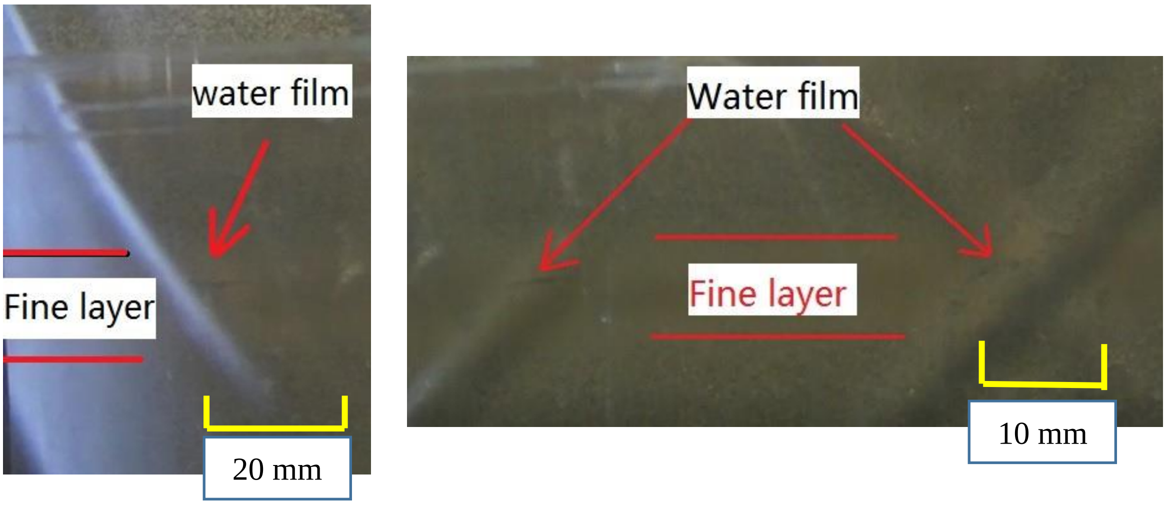

Stage 1 of re-liquefaction

Stage 2 of re-liquefaction

**Fig. 7. 39 Local water films in stage1 and stage 2 of test KWUC4**

# 8. CONCLUSIONS AND RECOMMENDATIONS

## 8.1 Conclusions

In this study, image analysis method was employed in the indirect and direct evaluations of local deformation. Transparent membranes were used in the undrained triaxial and torsional shear tests, respectively. The corresponding coordinate correction in the torsional shear test was developed and applied. Subsequently, the local deformations of uniform and segregated sand specimens were studied. Based on the obtained results, the following conclusions can be drawn:

**Image analysis technique applied in the undrained triaxial and torsional shear tests**

1. Through the transparent membrane, the movement of dots on membrane could be tracked and used for the indirect evaluation of local deformation, while sand particle patterns were for the direct evaluation of local deformation. Based on the geometry relation between specimen and camera, the resolutions were 0.025 mm/pixel in triaxial test and 0.05 mm/pixel in torsional shear test.
2. A coordinate correction method, by dividing the surface of specimen in torsional shear test into 2000 grids, was developed and verified by calibration test. Since the real and apparent coordinates of each dot were established directly and independently, it could be deemed that the affection by camera lens, light, refraction and other factors had been considered. Based on the theoretical analysis on two special planes, the errors induced by the replacement of real arc ratio to the length ratio in image for the bilinear-interpolation were less than 3%. This proof made the possibility of applying bilinear-interpolation method to compute the coordinate of dot or sand particle pattern, which was surrounded by dots in the reference image.
3. By applying calibration test in which a plastic mold was suspended under the top cap, the errors of the interval of two neighboring dots were less than 0.2 mm during the rotation. The maximum relative movements to the reference point were less than 0.3 mm even under the rotation displacement as large as 46 mm. The local strains could be displayed by local strain distributions visually and clearly.

**Local deformation observations in undrained triaxial tests**

1. Based on the indirect and direct evaluations of local deformations on Toyoura sand and Silica sand specimens in undrained triaxial tests, dot elements on membrane have the same local strains with the sand particle patterns except for the positions near wrinkles. Moreover, non-uniform local strains were formed along the specimen even when the axial strain was less than 2%.

2. The relative displacement between dot on membrane and neighboring sand particle named as slippage would not be zero and could not remain constant along the cyclic loading. When the global axial strain returned to zero, slippage was accumulated and increased with the cyclic number. No slippage before initial liquefaction proved the validity of previous researches which used the deformations of membrane to represent the sand behavior in drained test. Subsequently, the non-effective stress conditions induced the leap of vertical slippage during cyclic mobility.
3. Compared with the local strain distributions of Silica sand specimen prepared by moist tamping method, air pluviation method induced relatively uniform local strain distributions. Since the sand specimen was prepared by moist tamping method with five sand layers and four interfaces, necking phenomenon was recognized during extension stage at small axial strain. Loose specimen had a relatively larger potential than dense one to induce significant vertical slippage.

**Local deformations of uniform specimens in undrained torsional shear tests**

1. The local strains from indirect evaluation had the same change trends as those from direct evaluation except for the positions where membrane wrinkles occurred nearby. Moreover, almost same values of local strains at the same positions from direct and indirect evaluations were observed before the excess pore water pressure ratio reached 1.0. In general, both direct and indirect evaluations of local deformations were valid to some extent to represent the local behavior of sand specimen in undrained torsional shear tests. Another advantage of image analysis was that it eliminated the underestimation of shear strains measured by potentio-meter.
2. Before the initial liquefaction, the local strains along the specimen were relatively uniform. Meanwhile, non-uniform local strains occurred after the specimen was liquefied. After the reversion of loading direction during cyclic mobility, membrane wrinkles appeared and affected the deformations of neighboring sand particles. Distinct vertical slippage was observed when the excess pore water pressure ratio was around 1.0. Sand particle flowing was observed in the membrane wrinkles and pedestal of specimen. Since the sand particles sunk during liquefaction, water film beneath the top cap was formed at the end of test. The settlement of sand particle was also recognized by the extended local horizontal strains at the bottom part of specimen.
3. Regardless of high speed loading and pre-shearing, there was no significant vertical slippage in the test where specimen was dense. Based on the local strain distributions of dense specimen, non-uniform local strains took place after the initial liquefaction even when the

shear strain was small. In addition, several cycles after the onset of non-uniform deformation, the local shear strains at top and middle parts of specimen were significantly larger than those at bottom.

4. Liquefaction status was not the sufficient but necessary condition for the leap of vertical slippage. Significant vertical slippage was observed only in those tests where the specimens were relatively loose and the accumulated movements of measured points were large. Based on the results obtained, there was no remarkable vertical slippage when the relative density of specimen was larger than 60%. Meanwhile, slight vertical slippage was observed in test where the relative density of specimen was 55%. Therefore, relative density of 60% would be used as a threshold value for the significant vertical slippage. Beyond that there was no slippage either when the relative density of specimen was 43%. It was due to the fact that the test stopped quickly with limited rotation displacement. At present, there is no threshold of accumulated movement for the significant vertical slippage. The large accumulated movement is only considered as a factor which would increase the potential to trigger remarkable vertical slippage.
5. As for the horizontal slippage, it was dominated by the double amplitude of rotation displacement of measured point. Regardless of the relative density of specimen, the movements of dots on membrane were always larger than the movements of neighboring sand particles both on clockwise and anti-clockwise directions.

## Local deformations of segregated sand specimens in undrained torsional shear tests

1. As for the Katori sand specimens intercepted by thin fine layers, the local deformations from indirect and direct evaluations were almost same with each other, except for the large shear strain conditions. The local strains along the specimen were not uniform when the global shear strain was larger than 5%. After the excess pore water pressure ratio reached 0.8, expanded vertical strains at fine layer were observed from the vertical strain distributions by indirect and direct evaluations.
2. In order to observe the local behavior of segregated specimen affected by fine layer, the thickness of fine layer at top part of specimen increased by decreasing the thicknesses of other fine layers. Katori sand was colored by white and black colors to increase the accuracy of image method, respectively. The results indicated that the validity of direct evaluation of local deformation was improved to some extent. Distinct difference of local strains between fine layer and sand layer was observed. Based on the local strain distributions, the largest affection by membrane penetration was observed after the consolidation. This affection decreased gradually with the increasing of excess pore water pressure. The expanded

vertical strain at fine layer was observed when the excess pore water pressure ratio was around 1.0.

3. In order to prove the potential of pore water and sand particle migrations, the differential pore pressure was measured between the top and bottom of specimen. The results indicated that the maximum differential pore pressure was reached when the excess pore water pressure ratio was 1.0 at the first time. Moreover, pore water and sand particle migrations were observed during this status. Upward flows of pore water and sand particles were observed at the bottom of fine layer. In addition, the differential pore pressure was affected by the shear strain localization at fine layer. The concentration of pore water beneath fine layer was confirmed.
4. Significant water film beneath the top cap was observed in the liquefaction test on segregated specimen. The eroded silt layer underneath the fine layer might be induced by the concentration of pore water. After the reversion of shear directions, small water films were observed in the wrinkles when the wrinkles passed through the fine layer. Small water films in wrinkles at fine layer were also observed in the second stage of re-liquefaction test.

## 8.2 Recommendations

According to the results obtained in this study, several recommendations are made for the future investigations:

**Image analysis technique**

1. In this study, only one camera was employed by which the displacements of measured points were recorded. However, the displacement of one direction parallel to perpendicular line of camera lens was missed. Since the vertical displacement was prohibited in the undrained torsional shear test, the diameter of specimen was assumed to be constant during test. Therefore, the shape of specimen was remained during shearing. The coordinate correction method was only applicable in this condition. If the number of camera increased, the 3D coordinate of each measured point could be obtained. The accuracy of image analysis also will be increased.
2. Since the volume change of specimen was measured during the consolidation, a suitable calculation method for the volume change of specimen could be developed by image analysis.
3. The Matlab code could be improved to increase the computation speed.

**Uniform and segregated sand specimens (Silica no.5)**

1. Since the accuracy of image analysis before initial liquefaction is high, undrained monotonic loading test could be employed to obtain the evolution of local deformations until the steady state. The initial effective confining stress could be adjusted to investigate the local behavior near phase transformation.
2. Attention is needed to pay on the strain localization in re-liquefaction test. Moreover, the slippage at re-liquefaction could be compared with the one obtained in this study.
3. Artificial segregated specimen by different materials could be tried to observe strain localization and water film in undrained torsional shear test. For example, the Silica sand specimen intercepted by low permeability layer can be introduced. The significant vertical slippage has been observed in the liquefaction test on Silica specimen. When one low permeability layer is added at the top part of specimen, the potential of water film formation beneath the low permeability layer will be increased significantly.

### Segregated sand specimen (Katori sand)

1. The white-colored Katori sand could be prepared to increase the color contrast for the image analysis. Related measures are also needed to speckle the fine layer.
2. In order to investigate the formation mechanism of water film, more tests are needed by increasing the thickness of fine layer and the loading rate.

### Layered deposit model test with image analysis (Katori sand)

1. A model test on the shaking table could be performed with layered deposits. The layered deposit could be prepared similarly as the segregated specimen in torsional shear test. One fine layer at the top part intercepts the sand layer. Image analysis is also need to obtain the evolution of water film beneath the fine layer.

# Appendix

## Appendix I: Matlab code

### Coordinate correction and strain calculation

```
% --------------------------------------------
% Image Analysis for Torsional Apparatus
% --------------------------------------------
% by Chuang Zhao (37-147198)
%          Doctoral Student 3
%          Geo Laboratory, Hongo
%          The University of Tokyo
%          Date 11/09/2016
%---------------------------------------------
arange=input('   Range of next x-y coordinate = ');
disp(' ');
disp(' Please input Dot point information(x, y)');
b=input('   Number of rows = ');
c=input('   Number of column = ');
a=input('   Center point for inclination correction = ');
d=c-1;
e=input('   Number of total column for coordinate correction = ');
f=input('   Number of total rows for coordinate correction = ');
g=input('   Number of total photos = ');
% Xoc=zuobiao(:,1) type in Xoc directly
% Yoc=zuobiao(:,2)
% realx=zuobiaoafx(:,1)
% realy=zuobiaoafy(:,1)
Xo=koorx(:,1);
Yo=koory(:,1);
XoYo=[Xo Yo];
Xpt=koorx(:,(arange*1));
Ypt=koory(:,(arange*1));
tengah=zeros(b,2);
for i=1:b-1
    tengah(1,:)=XoYo(a,:);
    tengah(1+i,:)=XoYo(a+i*c,:);
end
figure(1);
plot (tengah(:,1),tengah(:,2));
p = polyfit(tengah(:,1),tengah(:,2),1); %persamaan inclinasi
```

```
rad=1/p(1,1); %sudut camera
Xi=Xo*cos(-rad)+Yo*sin(-rad);
Yi=Xo*sin(-rad)+Yo*cos(-rad);
Xpth=Xpt*cos(-rad)+Ypt*sin(-rad);
Ypth=Xpt*sin(-rad)+Ypt*cos(-rad);
Xoci=Xoc*cos(-rad)+Yoc*sin(-rad); %coordinate correction range
Yoci=Xoc*sin(-rad)+Yoc*cos(-rad);
XiYi=[Xi,Yi]; %koordinat baru
XociYoci=[Xoci,Yoci]
disp(' ');
disp(' Result:');

    Xafce=[];
    Yafce=[];
%zhao chuang new method

for i=1:c*b

   for k=1:(f-1)
       flgEndLoop = 0;
    for j=1:(e-1);

      xor=Xpth(i,1);
      yor=Ypth(i,1);

      yzs4=Yoci(j+(k-1)*e,1);
      yys3=Yoci(j+(k-1)*e+1,1);
      yyx2=Yoci(j+(k-1)*e+e+1,1);
      yzx1=Yoci(j+(k-1)*e+e,1);

      xzs4=Xoci(j+(k-1)*e,1);
      xys3=Xoci(j+(k-1)*e+1,1);
      xyx2=Xoci(j+(k-1)*e+e+1,1);
      xzx1=Xoci(j+(k-1)*e+e,1);

           yrzs4=realy(j+(k-1)*e,1);
           yrys3=realy(j+(k-1)*e+1,1);
           yryx2=realy(j+(k-1)*e+e+1,1);
           yrzx1=realy(j+(k-1)*e+e,1);
```

```
           xrzs4=realx(j+(k-1)*e,1);
           xrys3=realx(j+(k-1)*e+1,1);
           xryx2=realx(j+(k-1)*e+e+1,1);
           xrzx1=realx(j+(k-1)*e+e,1);

    % make sure one point in one area with four points
    xv=[xzx1 xyx2 xys3 xzs4 xzx1];
    yv=[yzx1 yyx2 yys3 yzs4 yzx1];
    in=inpolygon(xor,yor,xv,yv);
        if in==1
  %biliner interpolation method
  Xr1=(xyx2-xor)*xrzx1/(xyx2-xzx1)+(xor-xzx1)*xryx2/(xyx2-xzx1);
  Xr2=(xys3-xor)*xrzs4/(xys3-xzs4)+(xor-xzs4)*xrys3/(xys3-xzs4);
  %important
  Ytr1=(xyx2-xor)*yzx1/(xyx2-xzx1)+(xor-xzx1)*yyx2/(xyx2-xzx1);
  Ytr2=(xys3-xor)*yzs4/(xys3-xzs4)+(xor-xzs4)*yys3/(xys3-xzs4);

  Yr1=(xyx2-xor)*yrzx1/(xyx2-xzx1)+(xor-xzx1)*yryx2/(xyx2-xzx1);
  Yr2=(xys3-xor)*yrzs4/(xys3-xzs4)+(xor-xzs4)*yrys3/(xys3-xzs4);

  Xafc=(Ytr2-yor)*Xr1/(Ytr2-Ytr1)+(yor-Ytr1)*Xr2/(Ytr2-Ytr1);
  Yafc=(Ytr2-yor)*Yr1/(Ytr2-Ytr1)+(yor-Ytr1)*Yr2/(Ytr2-Ytr1);
 %summary final coordiante after correction in matrix

  Xafce=[Xafce;Xafc];
  Yafce=[Yafce;Yafc];
   flgEndLoop = 1 %use for jump out double cycles
          break
        end


    end
    if flgEndLoop == 1 % judge whether jump out or not
        break
    end
    end
end

% Displacement and strain calculation
Xc=[];
Yc=[];
```

```
% first photo coordinate correction
for i=1:c*b
     for k=1:(f-1)
         flgEndLoop = 0;
    for j=1:(e-1);

      xor=Xi(i,1);
      yor=Yi(i,1);

      yzs4=Yoci(j+(k-1)*e,1);
      yys3=Yoci(j+(k-1)*e+1,1);
      yyx2=Yoci(j+(k-1)*e+e+1,1);
      yzx1=Yoci(j+(k-1)*e+e,1);

      xzs4=Xoci(j+(k-1)*e,1);
      xys3=Xoci(j+(k-1)*e+1,1);
      xyx2=Xoci(j+(k-1)*e+e+1,1);
      xzx1=Xoci(j+(k-1)*e+e,1);

           yrzs4=realy(j+(k-1)*e,1);
           yrys3=realy(j+(k-1)*e+1,1);
           yryx2=realy(j+(k-1)*e+e+1,1);
           yrzx1=realy(j+(k-1)*e+e,1);

           xrzs4=realx(j+(k-1)*e,1);
           xrys3=realx(j+(k-1)*e+1,1);
           xryx2=realx(j+(k-1)*e+e+1,1);
           xrzx1=realx(j+(k-1)*e+e,1);

    % make sure one point in one area with four points
    xv=[xzx1 xyx2 xys3 xzs4 xzx1];
    yv=[yzx1 yyx2 yys3 yzs4 yzx1];
    in=inpolygon(xor,yor,xv,yv);
        if in==1

  %biliner interpolation method
  Xr1=(xyx2-xor)*xrzx1/(xyx2-xzx1)+(xor-xzx1)*xryx2/(xyx2-xzx1);
  Xr2=(xys3-xor)*xrzs4/(xys3-xzs4)+(xor-xzs4)*xrys3/(xys3-xzs4);
  %important
```

```
  Ytr1=(xyx2-xor)*yzx1/(xyx2-xzx1)+(xor-xzx1)*yyx2/(xyx2-xzx1);
  Ytr2=(xys3-xor)*yzs4/(xys3-xzs4)+(xor-xzs4)*yys3/(xys3-xzs4);

  Yr1=(xyx2-xor)*yrzx1/(xyx2-xzx1)+(xor-xzx1)*yryx2/(xyx2-xzx1);
  Yr2=(xys3-xor)*yrzs4/(xys3-xzs4)+(xor-xzs4)*yrys3/(xys3-xzs4);

  Xafc=(Ytr2-yor)*Xr1/(Ytr2-Ytr1)+(yor-Ytr1)*Xr2/(Ytr2-Ytr1);
  Yafc=(Ytr2-yor)*Yr1/(Ytr2-Ytr1)+(yor-Ytr1)*Yr2/(Ytr2-Ytr1);
 % summary final coordinate after correction in matrix

  Xc=[Xc;Xafc];
  Yc=[Yc;Yafc];
   flgEndLoop = 1 %use for jump out double cycles
         break
        end
    end
    if flgEndLoop == 1 % judge whether jump out or not
        break
    end
    end
end
% for i=1:c*b
% Xcs=realx(i,1);
% Xc=[Xc;Xcs];
% Ycs=realy(i,1);
% Yc=[Yc;Ycs];
% end
XcYc=[Xc Yc]; %coordinate of first photo after correection
XafceYafce=[Xafce Yafce]; % target photo coordinate after correction
DispArX=Xafce-Xc;
DispArY=Yafce-Yc;  % displacement of X and Y
DispArXY=(DispArX.^2+DispArY.^2).^0.5;
% complete=[Xafce Yafce DispArX DispArY DispArXY]; % Dispplacement analysis in complete
disp(' Displacement analysis on [Complete]=[Xpthc Ypthc DispArX DispArY DispArXY]');

K_element=c-1;
B_element=b-1;
N_element=K_element*B_element;

Xec=[]; %average coordiante of one element on X axies
```

```
Yec=[]; %average coordiante of one element on X axies
Ex=[];  %Horizontal Strain
Ey=[];  %Vertical Strain
gamma=[]; % engineering shear strain different from shear strain in torsional apparatus
(two times)
gammac=[] %academic shear strain with directions
Xecpthc=[]; %average coordinate of one element in target photo on X axies
Yecpthc=[]; %average coordinate of one element in target photo on Y axies
% 20161109 add the shape function to calculate the strains
xi=0; eta=0;
dN_dxi  = 0.25*[-(1-eta) (1-eta) (1+eta) -(1+eta)];
dN_deta = 0.25*[-(1-xi) -(1+xi) (1+xi) (1-xi)];

% caculation in one element, the order of four points in one element here
% is different from previous one when use biliner interpolation method, but
% it is still ok, between them there is no relationship

    for k=1:(b-1)
        for  j=1:(c-1)

      Xe=[Xc(j+(k-1)*c+c,1); Xc(j+(k-1)*c+c+1,1); Xc(j+(k-1)*c+1,1); Xc(j+(k-1)*c,1)];
      Ye=[Yc(j+(k-1)*c+c,1); Yc(j+(k-1)*c+c+1,1); Yc(j+(k-1)*c+1,1); Yc(j+(k-1)*c,1)];

    Xepthc=[Xafce(j+(k-1)*c+c,1); Xafce(j+(k-1)*c+c+1,1); Xafce(j+(k-1)*c+1,1);
Xafce(j+(k-1)*c,1)]
    Yepthc=[Yafce(j+(k-1)*c+c,1); Yafce(j+(k-1)*c+c+1,1); Yafce(j+(k-1)*c+1,1);
Yafce(j+(k-1)*c,1)]

    % 20161109 add the shape function to calculate strains
    u = Xepthc-Xe;
    v = Yepthc-Ye;

     j=[dN_dxi; dN_deta]*[Xepthc Yepthc];
    ji = [j(1,1) j(1,2); j(2,1) j(2,2)];
    def = [ji(2,2) -ji(1,2); -ji(2,1) ji(1,1)]/det(ji)*[dN_dxi;dN_deta]*[u v];

     Ex1= -[def(1,1)];
    Ex=[Ex;Ex1*100];
     Ey1= -[def(2,2)];
    Ey=[Ey;Ey1*100];
```

```
    gamma1= abs(-(def(1,2)+def(2,1)));% Should be engineering shear strain 20170213zhao
    gamma=[gamma;gamma1*100];
    gamma2=(-(def(1,2)+def(2,1)));%should be engineering shear strain with direction 20170213zhao
    gammac=[gammac;gamma2*100];

   % Ex1=(-1)*((((Xepthc(2,2)-Xepthc(2,1))-(Xe(2,2)-Xe(2,1)))/(Xe(2,2)-Xe(2,1)))+(((Xepthc(1,2)-Xepthc(1,1))-(Xe(1,2)-Xe(1,1)))/(Xe(1,2)-Xe(1,1))))/2;
   % Ex=[Ex;Ex1*100];
    % Ey1=(-1)*((((Yepthc(1,1)-Yepthc(2,1))-(Ye(1,1)-Ye(2,1)))/(Ye(1,1)-Ye(2,1)))+(((Yepthc(1,2)-Yepthc(2,2))-(Ye(1,2)-Ye(2,2)))/(Ye(1,2)-Ye(2,2))))/2;
    % Ey=[Ey;Ey1*100];
   % Ea=Ex+Ey;
   % A=-(Yepthc(2,2)-Yepthc(2,1))/(Xepthc(2,2)-Xepthc(2,1));
   % B=-(Yepthc(1,2)-Yepthc(1,1))/(Xepthc(1,2)-Xepthc(1,1));
   % C=-(Ye(2,2)-Ye(2,1))/(Xe(2,2)-Xe(2,1));
   % D=-(Ye(1,2)-Ye(1,1))/(Xe(1,2)-Xe(1,1));
   % E=-(Xepthc(1,1)-Xepthc(2,1))/(Yepthc(1,1)-Yepthc(2,1));
   % F=-(Xepthc(1,2)-Xepthc(2,2))/(Yepthc(1,2)-Yepthc(2,2));
   % G=-(Xe(1,1)-Xe(2,1))/(Ye(1,1)-Ye(2,1));
   % H=-(Xe(1,2)-Xe(2,2))/(Ye(1,2)-Ye(2,2));
   % gamma1=abs(((A+B)/2)-((C+D)/2)+((E+F)/2)-((G+H)/2)); %absolute value of engineering shear strain
  %  gamma2=0.5*(((A+B)/2)-((C+D)/2)+((E+F)/2)-((G+H)/2)); % academic shear strain with direction
   % gamma=[gamma;gamma1*100];
   % gammac=[gammac;gamma2*100];
    Xec1=(sum(sum(Xe)))/4;
    Xec=[Xec;Xec1]; %average coordiante of one element on X axies
    Xecpthc1=(sum(sum(Xepthc)))/4;
    Xecpthc=[Xecpthc;Xecpthc1]; %average coordinate of one element in target photo on X axies
    Yec1=(sum(sum(Ye)))/4;
    Yec=[Yec;Yec1]; %average coordiante of one element on Y axies
    Yecpthc1=(sum(sum(Yepthc)))/4;
    Yecpthc=[Yecpthc;Yecpthc1]; %average coordinate of one element in target photo on Y axies
        end
    end
Ea=Ex+Ey
```

```
e1=(1/2)*(Ex+Ey)+sqrt((1/4).*(Ex-Ey).^2+(1/4).*(gamma.^2));
e3=(1/2)*(Ex+Ey)-sqrt((1/4).*(Ex-Ey).^2+(1/4).*(gamma.^2));
gammamax = e1-e3;
Complete2=[Xec Yec Xecpthc Yecpthc Ex Ey Ea gamma e1 e3 gammamax];
Completet2=[Xec Yec Xecpthc Yecpthc Ex Ey Ea gammac e1 e3 gammamax];

%%for i=1:b-1
 %   Complete2(i*c,:)=1234567890;
  %  Completet2(i*c,:)=1234567890;
%end
% size it, maybe the dimentions are not always the same
[r, s] = size(Complete2);

% start a new row index for a new matrix
r2 = 1;

% check row by row
for i = 1:r
% if the x row has only positive values, copy the row to a new
% matrix and increment the row index of the new matrix
if max(Complete2(i,:)) ~= 1234567890
Complete3(r2,:) = Complete2(i,:);
r2 = r2+1;
end
end

[r, s] = size(Completet2);
r2 = 1;
for i = 1:r
if max(Completet2(i,:)) ~= 1234567890
Completet3(r2,:) = Completet2(i,:);
r2 = r2+1;
end
end
XYafce=[];
Complete4=[];
Completet4=[];
CompleteEx=[];
CompleteEy=[];
Completegamma=[];
```

```
Complete4=Complete3;
Completet4=Completet3;
CompleteEx=Complete4(:,5);
CompleteEy=Complete4(:,6);
Completegamma=Completet4(:,8);

disp(' Strain analysis on [Complete3]=[Xec Yec Ex Ey Ea gamma]');

fprintf('posisi = %d ¥n', arange);
answer=input('   Do you want to re-do (Y/N) = ', 's');
if (answer == 'Y')
    hitung2
elseif (answer == 'N')
    display (' Thank you');
else (answer ~= 'Y') && (answer ~= 'N')
    display (' Wrong Input');
end
```

## Contour plot

```
xlin =
linspace(min(min(Complete4(:,1),[],2)),max(max(Complete4(:,1),[],2)),length(Complete4(:,1)
));
ylin = linspace(min(Complete4(:,2)),max(Complete4(:,2)),length(Complete4(:,2)));
[X,Y] = meshgrid(xlin,ylin);

%aviobj = avifile('myPeaks2.avi', 'fps',1);

for i=2:2
Z = griddata(Complete4(:,1),Complete4(:,2),Complete4(:,(5+((i-2)*9))),X,Y,'linear');
Z2 = griddata(Complete4(:,1),Complete4(:,2),Complete4(:,(6+((i-2)*9))),X,Y,'linear');
Z3 = griddata(Completet4(:,1),Completet4(:,2),Completet4(:,(8+((i-2)*9))),X,Y,'linear');
figure(i)
subplot(1,3,1);
a=contourf(X,Y,Z,-10:2:10);
axis off;
set (gca,'CLim',[-10 10]);
colorbar;
subplot(1,3,2);
a=contourf(X,Y,Z2,-10:2:10);
axis off;
set (gca,'CLim',[-10 10]);
colorbar;
subplot(1,3,3);
a=contourf(X,Y,Z3,-20:4:20);
axis off;
set (gca,'CLim',[-10 10]);
colorbar;
filename=i
print('-djpeg', filename);
close(gcf)
%M(i)=getframe;
end
```

## Appendix II: Experimental setting (Digital Show Basic)

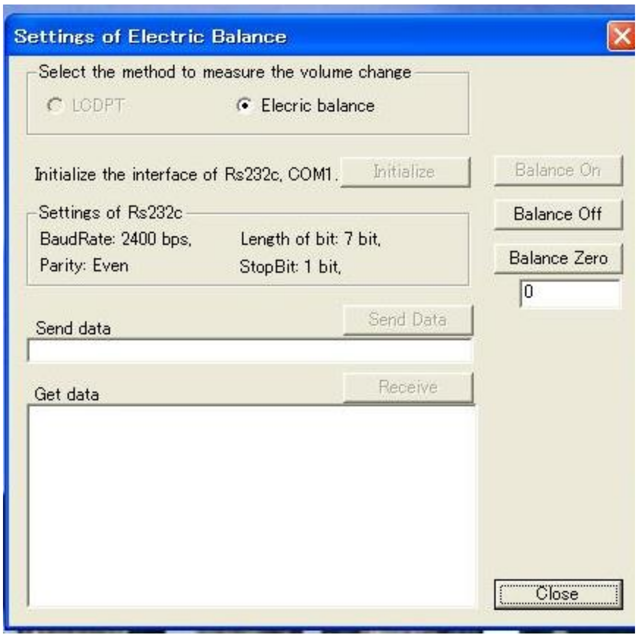

Select the method to measure the volume change
○ LCDPT ● Elecric balance

Initialize the interface of Rs232c, COM1.

Settings of Rs232c
BaudRate: 2400 bps, Length of bit: 7 bit,
Parity: Even StopBit: 1 bit,

0

Send data

Get data

① Select electric balance to measure the volume change of specimen

② Initialize the balance

③ Balance on

④ Balance zero

( It should be noted that the capacity of balance is 520g)

⑤ Close (Digital Show Basic will open automatically)

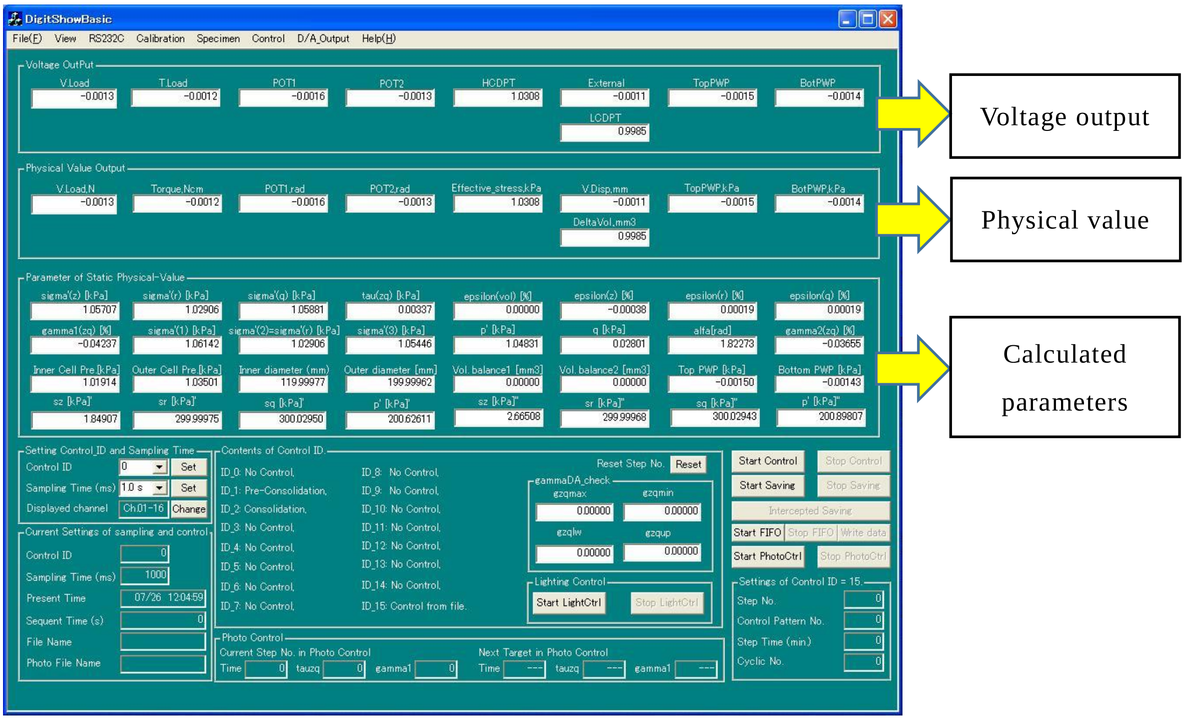

Voltage OutPut
V.Load -0.0013
T.Load -0.0012
POT1 -0.0016
POT2 -0.0013
HCDPT 1.0308
External -0.0011
TopPWP -0.0015
BotPWP -0.0014
LCDPT 0.9985

Physical Value Output
V.Load,N -0.0013
Torque,Ncm -0.0012
POT1,rad -0.0016
POT2,rad -0.0013
Effective_stress,kPa 1.0308
V.Disp,mm -0.0011
TopPWP,kPa -0.0015
BotPWP,kPa -0.0014
DeltaVol,mm3 0.9985

Parameter of Static Physical-Value
sigma'(z) [kPa] 1.05707
sigma'(r) [kPa] 1.02906
sigma'(q) [kPa] 1.05881
tau(zq) [kPa] 0.00337
epsilon(vol) [%] 0.00000
epsilon(z) [%] -0.00038
epsilon(r) [%] 0.00019
epsilon(q) [%] 0.00019
gamma1(zq) [%] -0.04237
sigma'(1) [kPa] 1.06142
sigma'(2)=sigma'(r) [kPa] 1.02906
sigma'(3) [kPa] 1.05446
p' [kPa] 1.04831
q [kPa] 0.02801
alfa[rad] 1.82273
gamma2(zq) [%] -0.03655
Inner Cell Pre.[kPa] 1.01914
Outer Cell Pre.[kPa] 1.03501
Inner diameter (mm) 119.99977
Outer diameter [mm] 199.99962
Vol. balance1 [mm3] 0.00000
Vol. balance2 [mm3] 0.00000
Top PWP [kPa] -0.00150
Bottom PWP [kPa] -0.00143
sz [kPa]' 1.84907
sr [kPa]' 299.99975
sq [kPa]' 300.02950
p' [kPa]' 200.62611
sz [kPa]" 2.66508
sr [kPa]" 299.99968
sq [kPa]" 300.02943
p' [kPa]" 200.89807

Setting Control_ID and Sampling Time
Control ID 0
Sampling Time (ms) 1.0 s
Displayed channel Ch.01-16

Current Settings of sampling and control
Control ID 0
Sampling Time (ms) 1000
Present Time 07/26 12:04:59
Sequent Time (s) 0
File Name
Photo File Name

Contents of Control ID.
ID_0: No Control,
ID_1: Pre-Consolidation,
ID_2: Consolidation,
ID_3: No Control,
ID_4: No Control,
ID_5: No Control,
ID_6: No Control,
ID_7: No Control,
ID_8: No Control,
ID_9: No Control,
ID_10: No Control,
ID_11: No Control,
ID_12: No Control,
ID_13: No Control,
ID_14: No Control,
ID_15: Control from file.

Reset Step No.

gammaDA_check
gzqmax 0.00000
gzqmin 0.00000
gzqlw 0.00000
gzqup 0.00000

Lighting Control

Photo Control
Current Step No. in Photo Control
Time 0 tauzq 0 gamma1 0
Next Target in Photo Control
Time --- tauzq --- gamma1 ---

Settings of Control ID = 15.
Step No. 0
Control Pattern No. 0
Step Time (min.) 0
Cyclic No. 0

Voltage output

Physical value

Calculated parameters

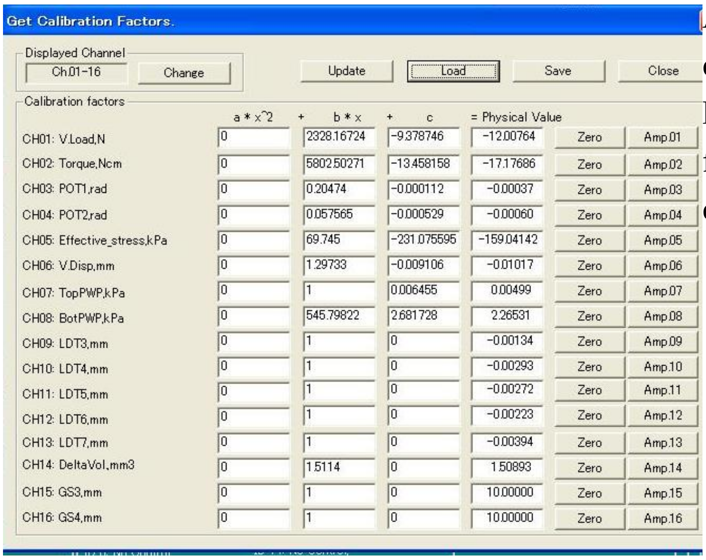

| | a * x^2 | + b * x | + c | = Physical Value | | |
|---|---|---|---|---|---|---|
| CH01: V.Load,N | 0 | 2328.16724 | -9.378746 | -12.00764 | Zero | Amp.01 |
| CH02: Torque,Ncm | 0 | 5802.50271 | -13.458158 | -17.17686 | Zero | Amp.02 |
| CH03: POT1,rad | 0 | 0.20474 | -0.000112 | -0.00037 | Zero | Amp.03 |
| CH04: POT2,rad | 0 | 0.057565 | -0.000529 | -0.00060 | Zero | Amp.04 |
| CH05: Effective_stress,kPa | 0 | 69.745 | -231.075595 | -159.04142 | Zero | Amp.05 |
| CH06: V.Disp,mm | 0 | 1.29733 | -0.009106 | -0.01017 | Zero | Amp.06 |
| CH07: TopPWP,kPa | 0 | 1 | 0.006455 | 0.00499 | Zero | Amp.07 |
| CH08: BotPWP,kPa | 0 | 545.79822 | 2.681728 | 2.26531 | Zero | Amp.08 |
| CH09: LDT3,mm | 0 | 1 | 0 | -0.00134 | Zero | Amp.09 |
| CH10: LDT4,mm | 0 | 1 | 0 | -0.00293 | Zero | Amp.10 |
| CH11: LDT5,mm | 0 | 1 | 0 | -0.00272 | Zero | Amp.11 |
| CH12: LDT6,mm | 0 | 1 | 0 | -0.00223 | Zero | Amp.12 |
| CH13: LDT7,mm | 0 | 1 | 0 | -0.00394 | Zero | Amp.13 |
| CH14: DeltaVol,mm3 | 0 | 1.5114 | 0 | 1.50893 | Zero | Amp.14 |
| CH15: GS3,mm | 0 | 1 | 0 | 10.00000 | Zero | Amp.15 |
| CH16: GS4,mm | 0 | 1 | 0 | 10.00000 | Zero | Amp.16 |

After open Digital Show Basic, the calibration factors should be loaded. Each factor is obtained from the corresponding calibration curve

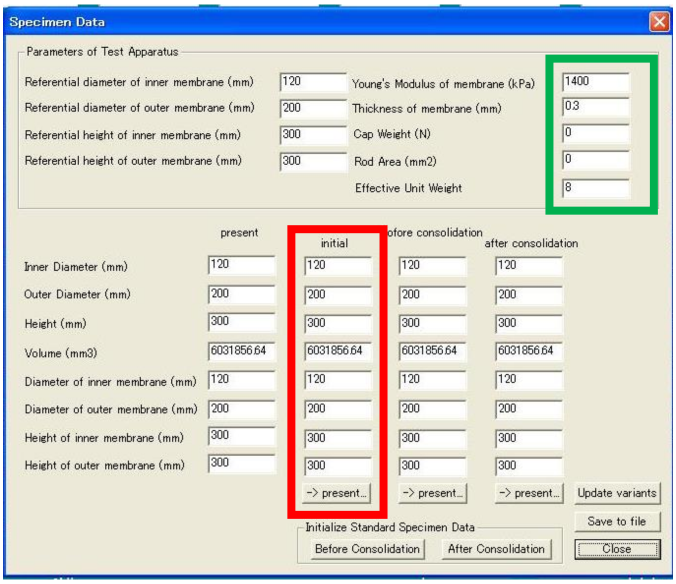

| | | | |
|---|---|---|---|
| Referential diameter of inner membrane (mm) | 120 | Young's Modulus of membrane (kPa) | 1400 |
| Referential diameter of outer membrane (mm) | 200 | Thickness of membrane (mm) | 0.3 |
| Referential height of inner membrane (mm) | 300 | Cap Weight (N) | 0 |
| Referential height of outer membrane (mm) | 300 | Rod Area (mm2) | 0 |
| | | Effective Unit Weight | 8 |

| | present | initial | ofore consolidation | after consolidation |
|---|---|---|---|---|
| Inner Diameter (mm) | 120 | 120 | 120 | 120 |
| Outer Diameter (mm) | 200 | 200 | 200 | 200 |
| Height (mm) | 300 | 300 | 300 | 300 |
| Volume (mm3) | 6031856.64 | 6031856.64 | 6031856.64 | 6031856.64 |
| Diameter of inner membrane (mm) | 120 | 120 | 120 | 120 |
| Diameter of outer membrane (mm) | 200 | 200 | 200 | 200 |
| Height of inner membrane (mm) | 300 | 300 | 300 | 300 |
| Height of outer membrane (mm) | 300 | 300 | 300 | 300 |

For membrane correction

Specimen size

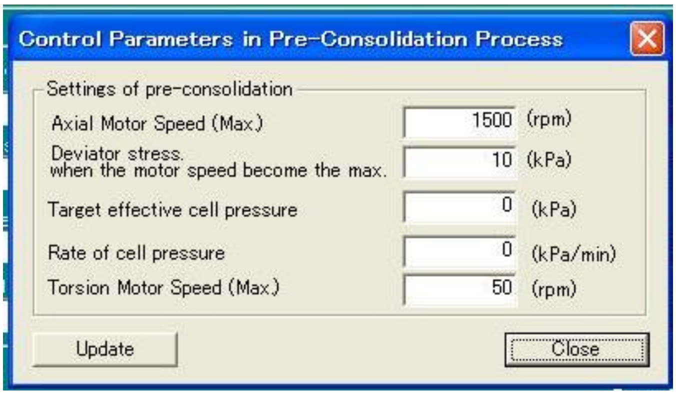

Axial Motor Speed (Max) 1500 (rpm)
Deviator stress when the motor speed become the max. 10 (kPa)
Target effective cell pressure 0 (kPa)
Rate of cell pressure 0 (kPa/min)
Torsion Motor Speed (Max) 50 (rpm)

In order to remain isotropic consolidation, the apparatus could adjust the stress by corresponding rate.

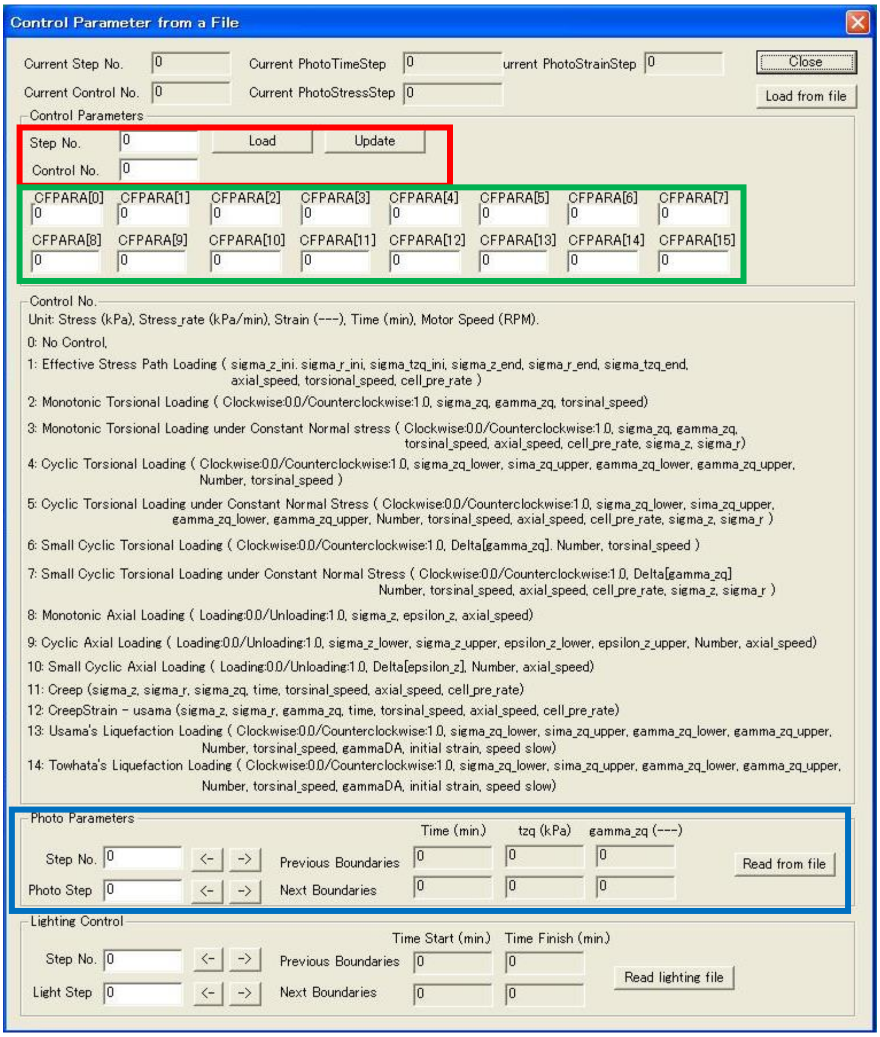

Current Step No. 0
Current PhotoTimeStep 0
urrent PhotoStrainStep 0
Current Control No. 0
Current PhotoStressStep 0

Control Parameters

Step No. 0
Control No. 0

| CFPARA[0] | CFPARA[1] | CFPARA[2] | CFPARA[3] | CFPARA[4] | CFPARA[5] | CFPARA[6] | CFPARA[7] |
|---|---|---|---|---|---|---|---|
| 0 | 0 | 0 | 0 | 0 | 0 | 0 | 0 |
| **CFPARA[8]** | **CFPARA[9]** | **CFPARA[10]** | **CFPARA[11]** | **CFPARA[12]** | **CFPARA[13]** | **CFPARA[14]** | **CFPARA[15]** |
| 0 | 0 | 0 | 0 | 0 | 0 | 0 | 0 |

Control No.

Unit: Stress (kPa), Stress_rate (kPa/min), Strain (---), Time (min), Motor Speed (RPM).

0: No Control,

1: Effective Stress Path Loading ( sigma_z_ini. sigma_r_ini, sigma_tzq_ini, sigma_z_end, sigma_r_end, sigma_tzq_end, axial_speed, torsional_speed, cell_pre_rate )

2: Monotonic Torsional Loading ( Clockwise:0.0/Counterclockwise:1.0, sigma_zq, gamma_zq, torsinal_speed)

3: Monotonic Torsional Loading under Constant Normal stress ( Clockwise:0.0/Counterclockwise:1.0, sigma_zq, gamma_zq, torsinal_speed, axial_speed, cell_pre_rate, sigma_z, sigma_r)

4: Cyclic Torsional Loading ( Clockwise:0.0/Counterclockwise:1.0, sigma_zq_lower, sima_zq_upper, gamma_zq_lower, gamma_zq_upper, Number, torsinal_speed )

5: Cyclic Torsional Loading under Constant Normal Stress ( Clockwise:0.0/Counterclockwise:1.0, sigma_zq_lower, sima_zq_upper, gamma_zq_lower, gamma_zq_upper, Number, torsinal_speed, axial_speed, cell_pre_rate, sigma_z, sigma_r )

6: Small Cyclic Torsional Loading ( Clockwise:0.0/Counterclockwise:1.0, Delta[gamma_zq]. Number, torsinal_speed )

7: Small Cyclic Torsional Loading under Constant Normal Stress ( Clockwise:0.0/Counterclockwise:1.0, Delta[gamma_zq] Number, torsinal_speed, axial_speed, cell_pre_rate, sigma_z, sigma_r )

8: Monotonic Axial Loading ( Loading:0.0/Unloading:1.0, sigma_z, epsilon_z, axial_speed)

9: Cyclic Axial Loading ( Loading:0.0/Unloading:1.0, sigma_z_lower, sigma_z_upper, epsilon_z_lower, epsilon_z_upper, Number, axial_speed)

10: Small Cyclic Axial Loading ( Loading:0.0/Unloading:1.0, Delta[epsilon_z], Number, axial_speed)

11: Creep (sigma_z, sigma_r, sigma_zq, time, torsinal_speed, axial_speed, cell_pre_rate)

12: CreepStrain - usama (sigma_z, sigma_r, gamma_zq, time, torsinal_speed, axial_speed, cell_pre_rate)

13: Usama's Liquefaction Loading ( Clockwise:0.0/Counterclockwise:1.0, sigma_zq_lower, sima_zq_upper, gamma_zq_lower, gamma_zq_upper, Number, torsinal_speed, gammaDA, initial strain, speed slow)

14: Towhata's Liquefaction Loading ( Clockwise:0.0/Counterclockwise:1.0, sigma_zq_lower, sima_zq_upper, gamma_zq_lower, gamma_zq_upper, Number, torsinal_speed, gammaDA, initial strain, speed slow)

Photo Parameters

Step No. 0
Photo Step 0

| | Time (min) | tzq (kPa) | gamma_zq (---) |
|---|---|---|---|
| Previous Boundaries | 0 | 0 | 0 |
| Next Boundaries | 0 | 0 | 0 |

Lighting Control

Step No. 0
Light Step 0

| | Time Start (min) | Time Finish (min) |
|---|---|---|
| Previous Boundaries | 0 | 0 |
| Next Boundaries | 0 | 0 |

Step order

Parameter setting for each step

Programs for different purposes

Prescribed photo controlling file can be loaded and the status can be checked

## Appendix III: The effects of pattern matching scale

Fig. 1 gives the original photos at step 2037 with the corresponding pattern settings in test SAUC11 (details have been introduced in chapters 2 & 6). It can be seen that some searching points are missing, especially in the right photo. If the pattern matching area is small, the color distribution inside may be flat. It becomes difficult to detect the same color pattern after deformation. Based on the right photo in Fig. 1, the color of missing point is relatively uniform. The large matching area is round 47*47 pixels, while the small matching area is around 40*38 pixels. Compared with the right photo, the tracking effects are improved by increasing the size of pattern matching area. However, there are still many missed points. As for the coordinate correction method introduced in appendix I, the lost points need to be corrected manually. Therefore, it is difficult to plot the local strain distributions of step 2037. Fig. 2 gives the local strain distributions at step 1566 by large and small matching areas, respectively. From the global view, they are almost same with each other. There is little difference at some local parts. For example, many error regions are observed at the top part of local strain distributions, which are evaluated by small matching area. Based on the theoretical understanding of image analysis, the center of matching area will represent the behavior of the matching area, the local characteristics inside the matching area are lost. By applying the large matching area, the deformation results become steady and follow the same variation with global deformation well. If the size of pattern matching area decreases, the errors associated with accuracy and precision will become larger. If the pattern matching area is very small, the gray scale distribution in the matching area will be flat, resulting into many missed points.

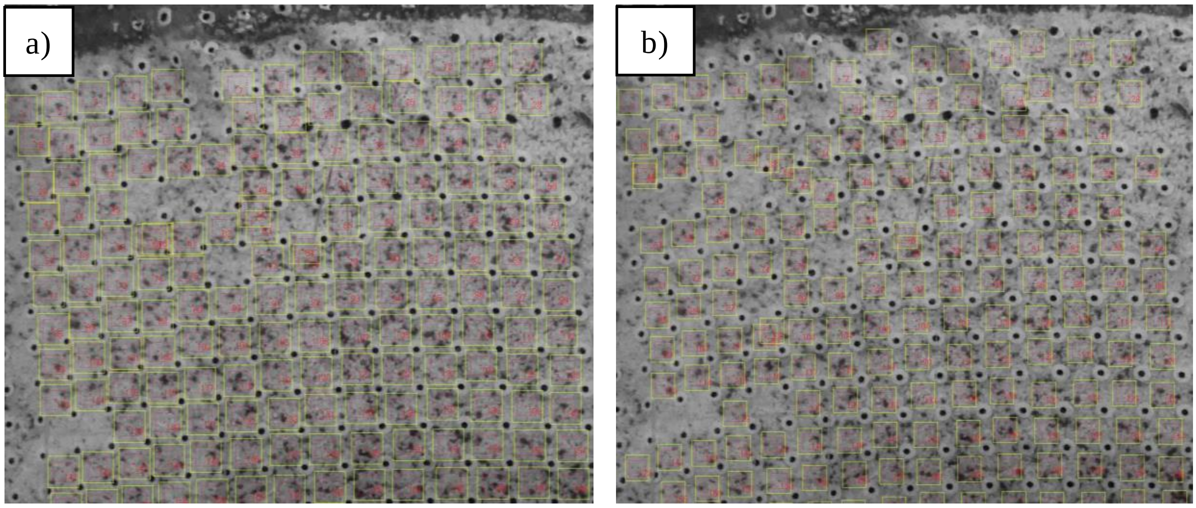

Large matching area Small matching area

Fig. 1 large and small pattern matching settings for the direct evaluations of local deformation in test SAUC11

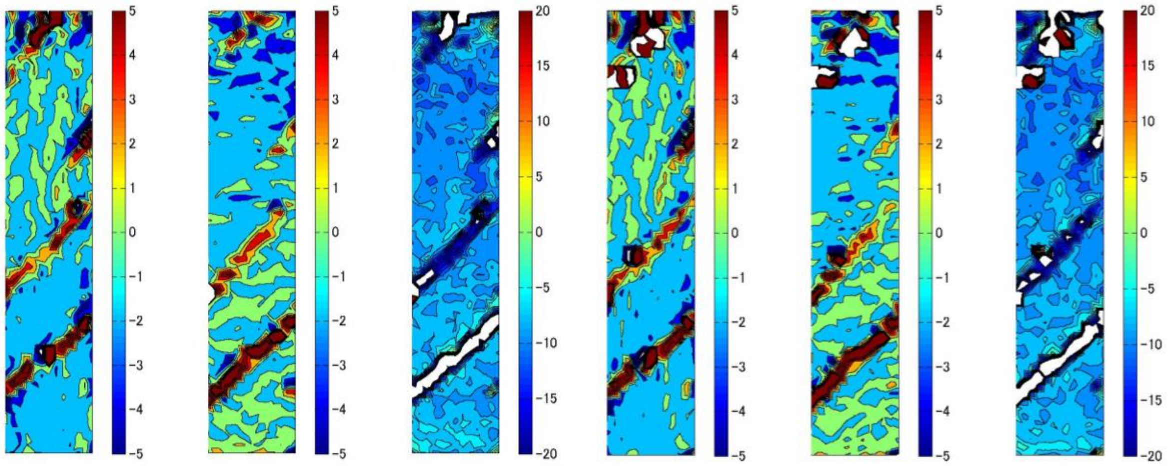

Horizontal strain/%, vertical strain/%, shear strain/% (Large matching area)

Horizontal strain/%, vertical strain/%, shear strain/% (Small matching area)

Fig. 2 Local strain distributions at step 1566 in test SAUC11

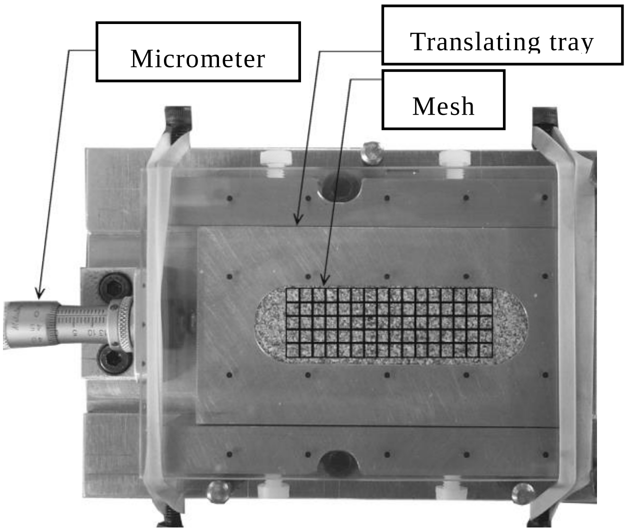

Fig. 3 Device including micrometer and translating tray to measure the accuracy of image analysis method (White et al., 2003)

Fig. 3 gives the device to measure the accuracy of applied image analysis introduced by White et al. (2003). The true displacement can be obtained by the micrometer. After comparing the displacements of patches with different size, the result indicated that the accuracy of image analysis increased with the increasing of patch size. This result is reasonable because the soil moves together without local deformation. In addition, the smaller patches allow the image to contain a large number of measured points. This is the situation of the above image analysis, which requires two conflicting interests to be balanced.

In the image analysis method applied in this study, the situation is different from the one mentioned by White. In Fig. 4, it shows the settings of pattern matching, only one pattern is tracked in each grid. Therefore, the number of tracked points is not increased by decreasing the size of pattern. In addition, small matching pattern is more appropriate to evaluate the local deformation of sand than large one. If the pattern is large, the properties of local deformation cannot be detected precisely. Namely, the ‘resolution’ for measuring local deformation will be reduced by large matching pattern. However, the complex distribution of gray scale results into the uniqueness of the color information inside of each matching area. If the size of pattern matching area decreases, the uniqueness will be reduced. Further, it will increase the potential to generate error.

In Fig. 4(a), it shows the gray scale distribution of the right photo. Like the large pattern matching area shown in figure (b), the large pattern matching area and the corresponding searching area are shown in figure (a). The gray scale distribution will be detected and recorded at the first photo. Subsequently, the same distribution will be searched in the yellow searching area in the next photo. Meanwhile, the position of yellow searching area will be updated continuously. As introduced before, the large matching area will generate steady coordinate data. With the decreasing of pattern matching size, the information considered in the next detection will be reduced. Since the sand used in this study is mixed colored sand at a mass ratio of 10 to 1 (white to black). It is inevitable to confront the flat gray distribution in some regions. The points at these regions are of potential to lose. With the decrease of pattern matching size, the potential and number of missed points will increase.

In Fig. 4, three kinds of matching sizes are applied to investigate the effects on accuracy and resolution of image analysis. The summarized results of the tracked points at position 2 are plotted in Fig. 5. Since the vertical displacement is prohibited during test, the displacements of tracked points at the same position should be same (without considering slippage). From the global view, they are overlapped with each other, except for the result by small pattern matching area after step 1800. Actually, some points at other positions are already lost at step 500 by the small matching pattern. Based on the relation between pixel and distance, each pixel accounts for 0.05 mm. Compared with the rotation displacement, the difference between these three types cannot be recognized easily. One local range from step 1470 to step 1520 is selected to show the evolutions of rotation on x direction. There is a linear relationship between step and rotation on x direction of measured point. It is reasonable because shearing rate is constant during the test. Compared with the fitting line of each, the data obtained from large matching pattern is steadier than those from middle and small pattern matching areas. In order to obtain the difference, Fig. 6 gives the step histories of rotation displacement on x direction of tracked points at position 2 during each step. Since the shearing rate is constant and the heights of tracked points are same, the rotation displacement of each at one step should be same. It can be seen that the values of rotation at each step are fluctuating. Even though the average values are similar, large error of rotation evaluated by small matching area occurs. Based on the standard deviations of the data evaluated by large, middle and small matching patterns, the degree of dispersion of the result from large matching pattern is lower than the middle and small matching patterns. In general, the results and above theoretical analysis are coincident with each other.

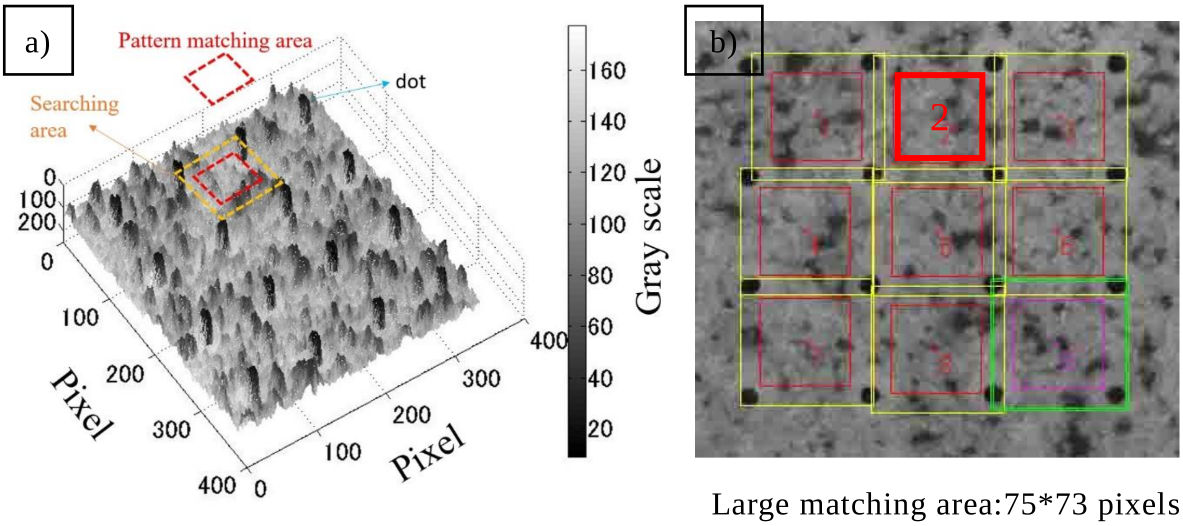

Gray scale distribution

Large matching area:75*73 pixels

Searching area:110*105 pixels

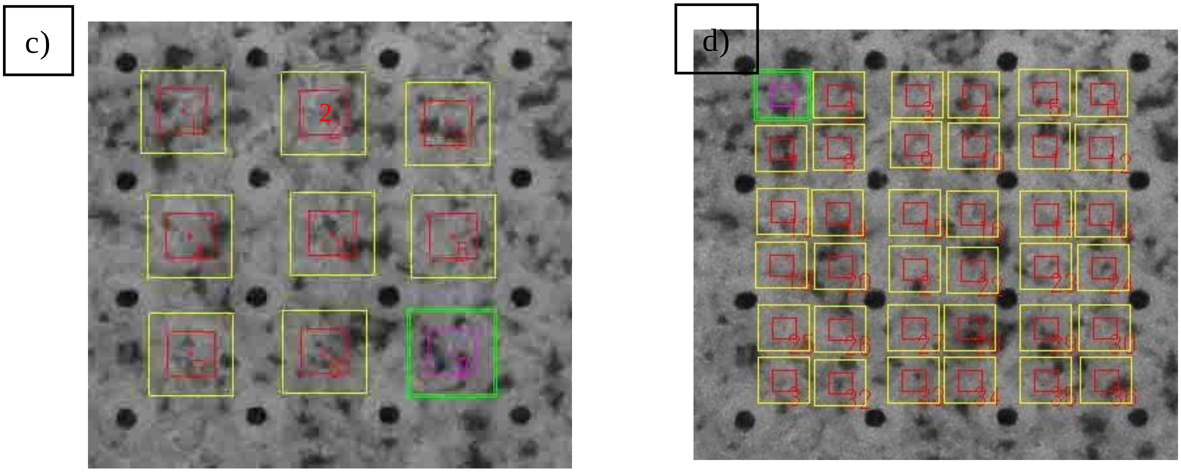

Middle matching area:37*35 pixels

Searching area:65*64 pixels

Small matching area:19*17 pixels

Searching area:40*36 pixels

a)Gray scale distribution, b)large pattern matching area, c)middle pattern matching area, d)small pattern matching area

Fig. 4 Pattern matching settings for the direct evaluations of local deformation in test SAUC11

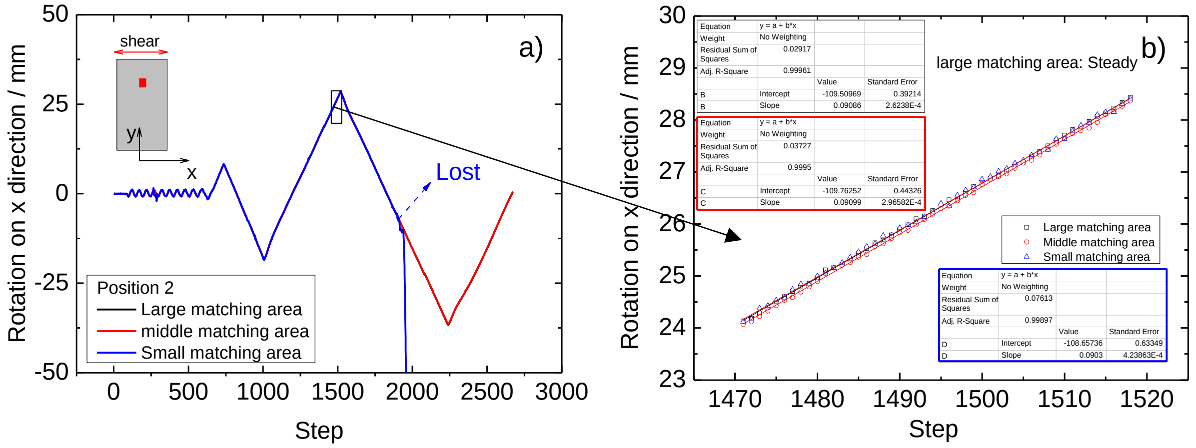

Fig. 5 Step histories of rotation on x direction of tracked points at position 2 by large, middle and small matching areas

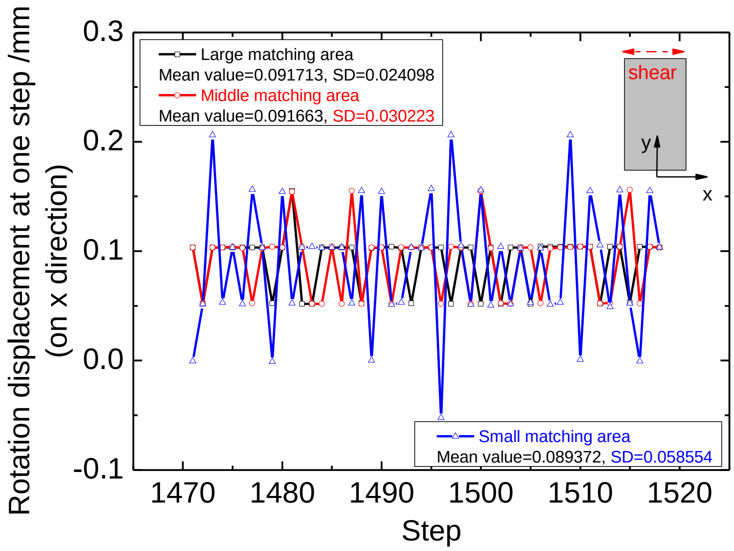

Fig. 6 Step histories of rotation displacement on x direction of tracked points at position 2 during each step

Similarly, Fig. 7 shows the step histories of displacement on y direction of tracked points at position 2 by large, middle and small matching areas. Fig. 8 gives the step histories of vertical displacement of tracked points at position 2 during each step. The same trend as displacement on x direction is obtained. It should be noted that the true displacement of tracked point is unknown. The rotation displacement calculated by potentio-meter is not accuracy to reflect the local deformation of tracked point. In general, the results evaluated by large, middle and small patterns are following the same trend. Therefore, the degree of dispersion is used to reflect the accuracy of the results. The ‘resolution’ used herein is for describing the local deformation of sand. Based on the above analysis, the accuracy of tracking will be better with larger matching pattern, while better ‘resolution’ of local deformation can be achieved with smaller matching pattern.

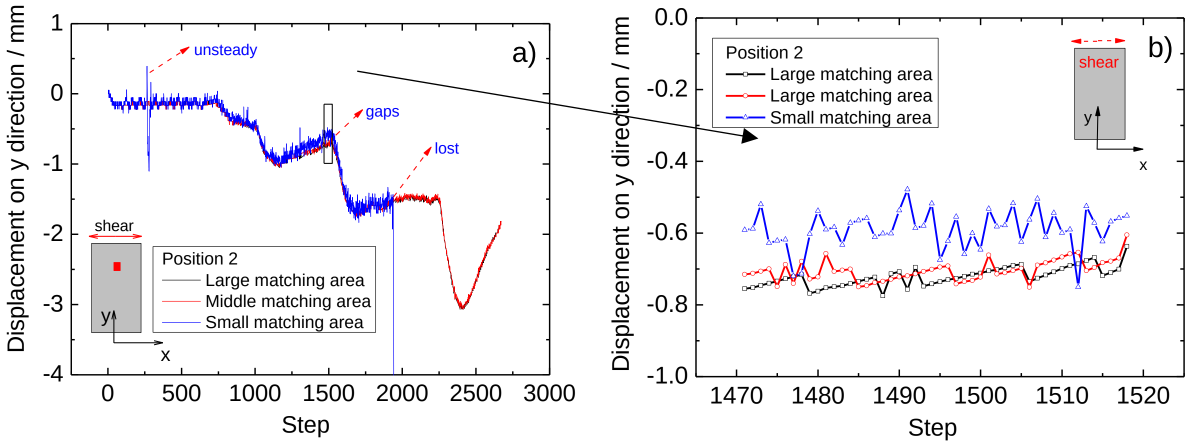

Fig. 7 Step histories of displacement on y direction of tracked points at position 2 by large, middle and small matching areas

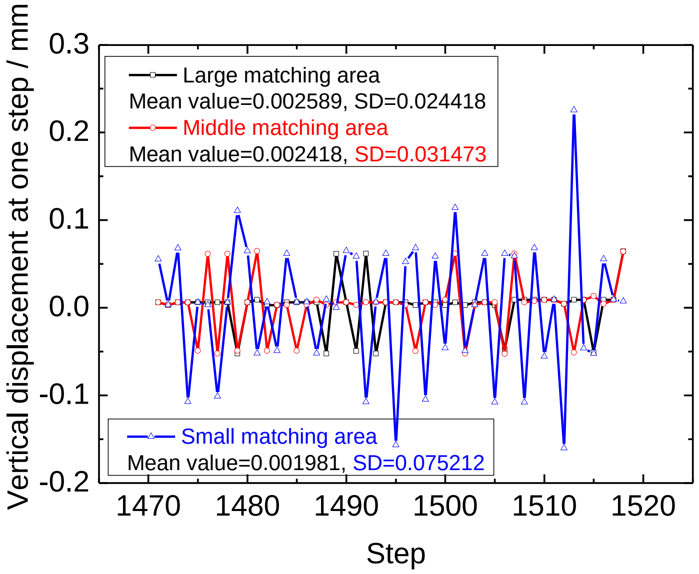

Fig. 8 Step histories of vertical displacement of tracked points at position 2 during each step

The selection of an optimum pattern size in this study requires the two conflicting interests to be balanced. Large matching pattern offers steady results, whereas small matching pattern is suitable for measuring the local deformation of sand. In this study, the size is determined by considering the particle size, speckled condition, shear strain and wrinkles. In author's opinion, half size of the dot grid (Fig. 1b) is always selected to track the movement of sand particle pattern. If it does not work well, 2/3 size of the grid (Fig. 1a) will be used.

1. White, D., Take, W. and Bolton, M. (2003). Soil deformation measurement using particle image velocimetry (PIV) and photogrammetry. *Géotechnique*, *53*(7), 619-631.